Universiteit Antwerpen

Faculteit Wetenschappen

Macroscopic X-ray powder diffraction in reflection mode: a new technique for chemical imaging of artworks

Macroscopische X-straal poederdiffractie in reflectiemodus: een nieuwe techniek voor chemische beeldvorming op kunstwerken

Proefschrift voorgelegd tot het behalen van de graad van doctor in de wetenschappen: chemie aan de Universiteit Antwerpen te verdedigen door

Steven De Meyer

Promotor:

prof. dr. Koen Janssens   Antwerpen, 2023

Cover image

MA-XRPD scanner with *The Night Watch*, 1642, Rembrandt van Rijn, Rijksmuseum.

Photo credit: Reinier Gerritsen.

Table of contents

Acknowledgements

I would like to sincerely thank my promotor Koen Janssens for providing me with the opportunity to pursue this fascinating research topic. Without his vision and guidance this PhD would not have been possible. When I started my thesis in 2017 the field of cultural heritage was very much unfamiliar territory for me yet having a supportive and experienced supervisor at my back made all the difference in this transition.

I immensely enjoyed working together with all my wonderful colleagues at the AXIS (formerly AXES) research group. I would like to especially thank my former mentor Frederik Vanmeert for introducing me to the magical world of XRPD and for sharing his extensive knowledge on the subject. I also want to thank Stijn Legrand for his support during our shared scanning campaigns and for his technical know-how. And of course thank you as well to all the other group members for making AXIS such a welcoming and warm workplace and for all the amazing memories we made over the years: Alba Alvarez Martin, Ermanno Avranovich Clerici, Iryn Bijker, Nina Deleu, Kirsten Derks, Hernan Fernandez Garcia, Arthur Gestels, Gert Nuyts, Annelies Rios-Casier, Teresa Scovacricchi, Geert Van der Snickt, Ehab Al-Emam, Olivier Voet, Piet Van Espen and Ana Cabal. Even beamtimes can be fun with the right company.

The instrument development in this thesis would not have happened without the expertise of Gilles Van Loon, Jaroslav Jordan and Eddie Schild from the technical workshop at the University of Antwerp. My sincere gratitude for all the help you provided over the years.

Chapter 1   Introduction

Painted works of art are widely considered to be immensely valuable to society, be it for their historical importance, cultural impact or aesthetically pleasing outlook. As paintings are also sensitive objects that can change (or have changed) over time due to internal or external factors, proper conservation and restoration procedures are crucial. For this reason, close collaboration between conservators, restorers, art historians and scientists is key towards gaining a better understanding of the condition of the painting.

From a historical point of view, conservation strategies were strongly reliant on observational data, overlooking the physicochemical interactions occurring at the nanoscopic or microscopic scale. These interactions can strongly impact the physical integrity of the paint materials and the macroscopic appearance of the painting through phenomena such as discoloration or crust formation. Chemical analysis is essential to explain the underlying causes for these changes and provides conservators and restorers with additional objective information in order to design effective conservation and treatment strategies. Not only does chemical analysis greatly benefit conservators and restorers in developing their treatment strategies, it also gives insight into the history and painterly style of the artwork itself. To understand the original intentions of the artist, differentiating between original materials and non-original materials (restorations or formed *in situ*) is an essential step. Characterizing an artists' palette in this manner also provides clues about historical production processes used to synthesize the paint or the geographical origins of a mineral pigment. And finally, the chemical composition of a painting can also be used to verify its authenticity. Many paint materials were

used within specific time periods and their presence can be used to date the painting, an important metric to distinguish genuine from counterfeit artworks.

In the past decades, the importance of scientific analysis within the field of cultural heritage has grown, in particular the use of macroscopic imaging techniques. There are several valuable advantages offered by macroscopic imaging: (1) they are non-invasive and thus damage to the painting through sampling is avoided, (2) the information obtained is more representative of the painting as a whole than the information obtained from a micrometric paint fragment and (3) many macroscopic imaging techniques are mobile and can be brought to the museum for *in situ* analysis.

IR and UV imaging modalities are routinely employed and can provide a basic level of material characterization on the macroscopic scale.[1] UV imaging is used to visualize the presence of organic materials as well as changes (e.g. damage, retouches) to the surface composition while infrared reflectography (IRR) is widely used for the examination of preparatory drawings in paintings as infrared radiation can penetrate the upper paint layers. The specificity of infrared imaging can be improved by scanning the painting over a spectral range, leading to stacks of images. Visible and near infrared (VNIR), short-wave (SWIR) reflectance imaging and macroscopic reflection fourier transform infrared scanning (MA-rFTIR) are several examples of recently developed techniques that allow for the identification of (some) pigments on the molecular level.[2–5] The VNIR spectral region is more sensitive to colors (due to electronic transitions) and gives information about materials present on the surface, while SWIR has a higher depth of penetration into the paint layers and provides more information on e.g. scattering from particles, the ground layer and infrared-absorbing pigments such as carbon blacks.[6]

Just as infrared-based techniques rely on the absorption of infrared radiation by vibrational modes to discriminate between functional groups, so too do X-ray based techniques exploit the (sub)nanoscopic wavelengths to provide information on the atomic and crystallographic level. The oldest X-ray imaging method (and still frequently used) in cultural heritage is X-ray radiography which relies on the absorption contrast between low-Z and high-Z elements; it can also be used to reveal paintings hidden beneath the surface.[7,8] More specific information can be gathered by employing a spectroscopic-based technique such as X-ray fluorescence, which can discriminate not just between low-Z and high-Z areas on a painting but between individual elements. By combining a spectrometer with an XY scanner, distribution images can be created for every element identified in the painting. As macroscopic X-ray fluorescence (MA-XRF) is a fast, non-invasive and highly informative technique that can be employed *in situ*, it has rapidly evolved from early prototype to commercialized instrument that is used by art historians and conservation scientists all over the world.[8,9] From the elemental distributions, (indirect) conclusions can be drawn about the presence of certain pigments. Additionally, the penetrative power of X-rays allows for a measure of depth selectivity. High energy emission lines (e.g. Pb-L) can emerge from deeper within the paint stratigraphy than low energy emission lines (e.g. Pb-M), allowing for discrimination between lead used in the ground layer and lead used in the pictorial layer(s). This depth selectivity also means that MA-XRF can be used to visualize overpainted areas and subsurface modifications, including underdrawings and hidden paintings.[8,10,11] Many artworks have been scanned in this manner, ranging from works by Da Vinci to paintings by Mondrian, in order to gain new insights into the artistic history of the painting and the state of conservation.[12–14]

The major limiting factor of XRF is that it only provides information on the elemental content of a painting. The technique cannot differentiate between molecular compounds that share the same elemental composition or differ only in low-Z elements such as oxygen, carbon or sulphur. This presents a problem, not just for distinguishing primary pigments such as azurite [$Cu_3(CO_3)_2(OH)_2$] from malachite [$Cu_2CO_3(OH)_2$] but also for the identification of secondary compounds that can form over time from the oxidation or sulfidation of the primary pigment. MA-XRF cannot distinguish between azurite, malachite or cupric oxide as all three compounds contribute to the Cu-K fluorescence signal. A second limitation of XRF is that the sampling depth of the collected XRF signals is strongly energy-dependent. While advantageous when considering different emission lines from the same element (e.g. Pb-L and Pb-M), interpretation becomes more complex when comparing emission lines from different elements. Low energy emission lines only convey superficial (e.g. several microns) information while high energy emission lines can come from much deeper (e.g. several hundreds of microns) in the stratigraphy. Potassium (K-K) and arsenic (As-K) signals originate from different depths, further complicating the interpretation of the fluorescence data.

An X-ray based analysis method that provides a significantly higher specificity than XRF is X-ray powder diffraction (XRPD). X-ray diffraction is a physical process that involves the constructive interference of elastically scattered X-rays at an angle 2θ after interaction with the atoms of a crystalline structure. When the sample consists of many crystallites positioned in random orientations, it is considered to be a powder and Debye-Scherrer rings are obtained on a diffraction camera during analysis. From the diffraction angle 2θ the characteristic interplanar spacing d can be calculated from the peak positions using Bragg's Law: $n\lambda = d \sin 2\theta$ with wavelength λ and diffraction order n. The set of

characteristic *d*-values can then be used to identify the crystal structure and corresponding molecular composition for the compound in question. In this manner XRPD can be used to obtain molecular information rather than just elemental information, provided the material is crystalline. XRPD has been extensively used in the field of cultural heritage on paint samples using synchrotron radiation (SR), both for the imaging of samples with a micrometric beam and for high angular resolution bulk analysis with a millimetric beam.[15–18]

SR-XRPD has been frequently used to identify primary pigment materials and their secondary degradation products.[19–22] Yet as previously discussed, significant disadvantages and limitations are associated to sampling an artwork. Non-invasive portable instruments for *in situ* XRPD analysis exist but are limited by long acquisition times (tens of minutes per point), restricting their usefulness for imaging purposes.[23] More recently, the potential of a macroscopic XRPD (MA-XRPD) scanner has been explored, resulting in an instrument capable of analyzing small works of art in transmission mode.[24]

In this thesis the possibilities and limitations of mobile MA-XRPD in reflection mode will be explored. MA-XRPD in transmission mode has previously been shown to have important applications in the field of cultural heritage. Transmission MA-XRPD has been used to identify the primary pigments of Van Gogh's Sunflowers and differentiate between two types of chrome yellow, a light-sensitive and light-resistant type.[25] Finally, MA-XRPD in transmission mode has also been used to differentiate between the recto and verso side of an illuminated sheet of parchment, illustrating the potential for depth-selective analysis.[26]

In Chapter 2 the potential of a MA-XRPD scanner in reflection mode is investigated and a comparison is made with MA-XRPD in transmission mode.

This includes an instrumental study of different X-ray sources and geometries in order to obtain the best combination of characteristics for scanning purposes as well as a case study on a 17th century oil painting in order to highlight the advantages (and limitations) of both transmission and reflection MA-XRPD.

Subsequent chapters will focus on the application of reflection mode MA-XRPD on oil paintings, often combined with other techniques (e.g. transmission MAXRPD, SR-XRD or MA-XRF) in order to shed light on several topics of interest in the field of cultural heritage. Chapter 3 revolves around the pigment lead white with case studies focused on the paintings *Girl with a Pearl Earring* (1655) by Johannes Vermeer and *The Night Watch* (1642) by Rembrandt van Rijn. More specifically, the presence of multiple lead white pigments within the paintings will be discussed in detail using semi-quantitative analysis, providing insight into the painterly styles of Vermeer and Rembrandt. The potential for the depth-specific extraction of information with reflection MA-XRPD will also be highlighted.

In Chapter 4 MA-XRPD scanning in reflection mode is used to investigate the presence of secondary degradation products in oil paintings. Several case studies will be presented, covering different examples of degradation phenomena: lead-containing degradation compounds that were identified in Vermeer's *Girl with a Pearl Earring*, the susceptibility of arsenic(III)-based pigments to oxidize over time and form As(V) species, demonstrated on *Still life with Quinces, Medlars and a Glass* (c. 1669-1719) by Martinus Nellius and *Still Life with Flowers and a Watch* (c. 1660-1679) by Abraham Mignon, and an investigation into the prevalence of metal oxalates in early Netherlandish oil paintings of the 15th – 17th century in which fourteen paintings by eleven different artists were investigated

in an attempt to draw representative conclusions about the correlation between the formation of metal oxalate formation and specific pigments.

References

(1) Trentelman, K. Analyzing the Heterogeneous Hierarchy of Cultural Heritage Materials: Analytical Imaging. *Annu. Rev. Anal. Chem.* **2017**, *10*, 247–270.

(2) Ricciardi, P.; Delaney, J. K.; Facini, M.; Zeibel, J. G.; Picollo, M.; Lomax, S.; Loew, M. Near Infrared Reflectance Imaging Spectroscopy to Map Paint Binders in Situ on Illuminated Manuscripts. *Angew. Chem.* **2012**, *51* (23), 5607–5610.

(3) Legrand, S.; Alfeld, M.; Vanmeert, F.; De Nolf, W.; Janssens, K. Macroscopic Fourier Transform Infrared Scanning in Reflection Mode (MA-RFTIR), a New Tool for Chemical Imaging of Cultural Heritage Artefacts in the Mid-Infrared Range. *Analyst* **2014**, *139*, 2489–2498.

(4) Dooley, K. A.; Conover, D. M.; Glinsman, L. D.; Delaney, J. K. Complementary Standoff Chemical Imaging to Map and Identify Artist Materials in an Early Italian Renaissance Panel Painting. *Angew. Chem. Int. Ed.* **2014**, *53*, 13775–13779.

(5) Gabrieli, F.; Dooley, K. A.; Zeibel, J. G.; Howe, J. D.; Delaney, J. K. Standoff Mid-Infrared Emissive Imaging Spectroscopy For Identification and Mapping of Materials in Polychrome Objects. *Angew. Chem.* **2018**, *57*, 7341–7345.

(6) Gabrieli, F.; Delaney, J. K.; Erdmann, R.; Gonzalez, V.; Van Loon, A.; Smulders, P.; Berkeveld, R.; Van Langh, R.; Keune, K. Reflectance Imaging Spectroscopy (RIS) for Operation Night Watch: Challenges and Achievements of Imaging Rembrandt's Masterpiece in the Glass Chamber at the Rijksmuseum. *Sensors* **2021**, *21*, 6855.

(7) Kirsch, A.; Levenson, R. S. *Seeing Through Paintings: Physical Examination in Art Historical Studies*; Yale University Press: New Haven, 2002.

(8) Dik, J.; Janssens, K.; Van der Snickt, G.; Van der Loeff, L.; Rickers, K.; Cotte, M. Visualization of a Lost Painting by Vincent van Gogh Using Synchrotron Radiation Based X-Ray Fluorescence Mapping. *Analytical Chemistry* **2008**, *80*, 6433–6442.

(9) Alfeld, M.; Janssens, K.; Dik, J.; De Nolf, W.; Van der Snickt, G. Optimization of Mobile Scanning Macro-XRF Systems for the in Situ Investigation of Historical Paintings. *J. Anal. At. Spectrom.* **2011**, *26*, 899–909.

(10) Van der Snickt, G.; Legrand, S.; Slama, I.; Van Zuien, E.; Gruber, G.; Van der Stighelen, K.; Klaassen, L.; Oberthaler, E.; Janssens, K. In Situ Macro X-Ray Fluorescence (MA-XRF) Scanning as a Non-Invasive Tool to Probe for Subsurface Modifications in Paintings by P.P. Rubens. *Microchem. J.* **2018**, *138*, 238–245.

(11)   Derks, K.; Van der Snickt, G.; Legrand, S.; Van der Stighelen, K.; Janssens, K. The Dark Halo Technique in the Oeuvre of Michael Sweerts and Other Flemish and Dutch Baroque Painters. A 17th c. Empirical Solution to Mitigate the Optical 'Simultaneous Contrast' Effect? *Herit. Sci.* **2022**, *10*, 5.

(12)   Van der Snickt, G.; Dooley, K. A.; Sanyova, J.; Dubois, H.; Delaney, J. K.; Gifford, M.; Legrand, S.; Laquiere, N.; Janssens, K. Dual Mode Standoff Imaging Spectroscopy Documents the Painting Process of the Lamb of God in the Ghent Altarpiece by J. and H. Van Eyck. *Sci. Adv.* **2020**, *6*, eabb3379.

(13)   Martins, A.; Albertson, C.; McGlinchey, C.; Dik, J. Piet Mondrian's Broadway Boogie Woogie: Non Invasive Analysis Using Macro X-Ray Fluorescence Mapping (MA-XRF) and Multivariate Curve Resolution-Alternating Least Square (MCR-ALS). *Herit. Sci.* **2016**, *4*, 16.

(14)   Bicchieri, M.; Biocca, P.; Caliri, C.; Romano, F. P. Complementary MA-XRF and µ-Raman Results on Two Leonardo Da Vinci Drawings. *X-Ray Spectrom* **2021**, *50*, 401–409.

(15)   Janssens, K.; Alfeld, M.; Van der Snickt, G.; De Nolf, W.; Vanmeert, F.; Radepont, M.; Monico, L.; Dik, J.; Cotte, M.; Falkenberg, G.; Costanza, M.; Brunetti, B. The Use of Synchrotron Radiation for the Characterization of Artists' Pigments and Paintings. *Annu. Rev. Anal. Chem.* **2013**, *6* (1), 399–425.

(16)   Salvado, N.; Pradell, T.; Pantos, E.; Papiz, M. Z.; Molera, J.; Vendrell-Saz, M. Identification of Copper-Based Green Pigments in Jaume Huguet's Gothic Altarpieces by Fourier Transform Infrared Microspectroscopy and Synchrotron Radiation X-Ray Diffraction. *J. Synchrotron Radiat.* **2002**, *9*, 215–222.

(17)   Janssens, K.; Dik, J.; Cotte, M.; Susini, J. Photon-Based Techniques for Nondestructive Subsurface Analysis of Painted Cultural Heritage Artifacts. *Acc. Chem. Res.* **2010**, *43*, 814–825.

(18)   Gonzalez, V.; Wallez, G.; Calligaro, T.; Cotte, M.; De Nolf, W.; Eveno, M.; Ravaud, E.; Menu, M. Synchrotron-Based High Angle Resolution and High Lateral Resolution X-ray Diffraction: Revealing Lead White Pigment Qualities in Old Masters Paintings. *Anal. Chem.* **2017**, *89* (24), 13203–13211.

(19)   Monico, L.; Janssens, K.; Hendriks, E.; Vanmeert, F.; Van der Snickt, G.; Cotte, M.; Falkenberg, G.; Brunetti, B.; Costanza, M. Evidence for Degradation of the Chrome Yellows in Van Gogh's Sunflowers: A Study Using Noninvasive In Situ Methods and Synchrotron-Radiation-Based X-Ray Techniques. *Angew. Chem.* **2015**, *54* (47), 13923–13927.

(20)   Gonzalez, V.; Calligaro, T.; Pichon, L.; Wallez, G.; Mottin, B. Leonardo Da Vinci's Drapery Studies: Characterization of Lead White Pigments by µ-XRD and 2D Scanning XRF. *Appl. Phys. A* **2015**, *121* (3), 849–856.

(21)   De Keyser, N.; Broers, F.; Vanmeert, F.; De Meyer, S.; Gabrieli, F.; Hermens, E.; Van der Snickt, G.; Janssens, K.; Keune, K. Reviving Degraded Colors of Yellow Flowers in 17th Century Still Life Paintings with Macro- and Microscale Chemical Imaging. *Sci. Adv.* **2022**, *8*, abn6344.

(22)   Simoen, J.; De Meyer, S.; Vanmeert, F.; De Keyser, N.; Avranovich Clerici, E.; Van der Snickt, G.; Van Loon, A.; Noble, P.; Keune, K.; Janssens, K. Combined Micro- and Macro Scale X-Ray Powder Diffraction Mapping of Degraded Orpiment Paint in a 17th Century Still Life Painting by Martinus Nellius. *Herit. Sci.* **2019**, *7*, 83.

(23)   Nakai, I.; Yoshinari, A. Portable X-Ray Powder Diffractometer for the Analysis of Art and Archaeological Materials. *Applied Physics A* **2012**, *106* (2), 279–293.

(24)   Vanmeert, F.; De Nolf, W.; De Meyer, S.; Dik, J.; Janssens, K. Macroscopic X-Ray Powder Diffraction Scanning, a New Method for Highly Selective Chemical Imaging of Works of Art: Instrument Optimization. *Anal. Chem.* **2018**, *90*, 6436–6444.

(25)   Vanmeert, F.; Hendriks, E.; Van der Snickt, G.; Monico, L.; Dik, J.; Janssens, K. Chemical Mapping by Macroscopic X-Ray Powder Diffraction of Van Gogh's Sunflowers: Identification of Areas with Higher Degradation Risk. *Angew. Chem.* **2018**, *57*, 7418–7422.

(26)   Vanmeert, F.; De Nolf, W.; Dik, J.; Janssens, K. Macroscopic X-Ray Powder Diffraction Scanning: Possibilities for Quantitative and Depth-Selective Parchment Analysis. *Anal. Chem.* **2018**, *90*, 6445–6452.

Chapter 2   Instrumentation
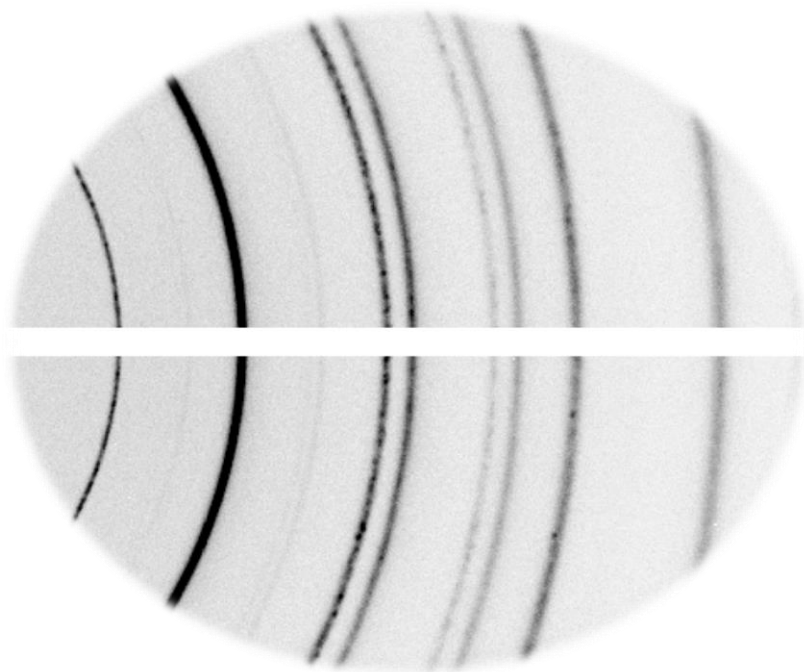
In the past decade the application of MA-XRF (macroscopic X-ray fluorescence) scanning, one of the non-invasive methods for hyperspectral imaging of works of art, has become increasingly popular with art historians and conservation scientists.[1,2] While microscopic XRF (μ-XRF) scanning has been used for a long time at synchrotron facilities, it is only from 2008 on that the microscopic technique was converted into a mobile macroscopic analogue.[3,4] MA-XRF offers a higher specificity for material analysis than traditional X-ray radiography as it provides information on the local elemental composition of the artwork rather than the density of the irradiated material. Not only can the presence of certain inorganic pigments be inferred from this elemental information, the additional depth-sensitive information provided by MA-XRF allows for the localization of

overpainted areas (original or restored) and even the detection of hidden underdrawings[5,6]. While the emergence of these mobile MA-XRF instruments has had a remarkable effect on cultural heritage research in general, the technique is still limited to providing elemental information.[7,8]

To differentiate between compounds with a similar elemental composition (for example the two most prevalent components of lead white: cerussite, $PbCO_3$ and hydrocerussite, $2PbCO3.Pb(OH)_2$) several molecular imaging techniques have been developed for cultural heritage analysis in the wake of MA-XRF scanning, ranging from visible and infrared reflectance imaging spectroscopy (RIS) to macroscopic reflection FTIR scanning (MA-rFTIR).[9–12] Recently, the potential of a macroscopic X-ray powder diffraction (MA-XRPD) scanner has also been successfully explored, resulting in the construction of an instrument capable of analyzing small works of art in transmission geometry.[13–15]

While transmission MA-XRPD offers useful information regarding the depth-averaged composition of the artwork, more superficial information representing the pictorial state of the painting (e.g., restorations, pentimenti, degradation products) gets lost due to the dominant contributions of diffraction emerging from thick paint layers and the ground layer to the total diffraction signal. A second limitation of transmission MA-XRPD is that the painting dimensions need to be taken into consideration for analysis. X-ray attenuation will limit how thick the artwork in question can be and analyzing paintings on a wooden panel or with a thick lead white ground layer presents a significant challenge. As the X-ray source and detector are positioned on opposite sides of the artwork, the painting must also be moved relative to the equipment, which excludes the investigation of large, heavy, immobile or sensitive artworks. Paintings also need

to be removed from the showroom walls, a decision that museum curators are usually reluctant to make.

For these reasons a new reflection geometry configuration of the MA-XRPD scanner is proposed to take advantage of the increased superficial sensitivity and to expand the catalogue of paintings available for analysis. This chapter will outline the possibilities and limitations of both transmission and reflection MA-XRPD and justify the choices made for the instrumentation and configuration of the individual components used in a reflection MA-XRPD scanner.

2.1 Fundamentals of transmission and reflection XRPD

2.1.1 Transmission-XRPD
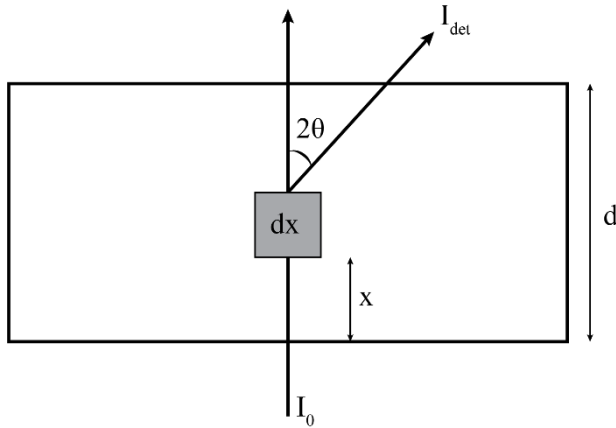
Figure 2-1 Schematic for the diffraction process in transmission geometry

Due to the importance of attenuation effects, X-ray powder diffraction in transmission geometry is usually limited to thin samples as the detected diffraction intensity I_{det} is proportionally related to the X-ray absorption A of the material.

$$I_{det} \propto \lambda^2 I_0 \left(\frac{F_{hkl}^2 m_{hkl}}{V^2} \right) \left(\frac{1 + cos^2 2\theta}{sin^2 \theta \, cos\theta} \right) A$$

The intensity further depends on the wavelength λ, the intensity I_0 of the primary X-ray beam, the structure factor F, the multiplicity m and Bragg angle θ of the irradiated crystal plane, the volume V of the unit cell and the absorption factor A.

To predict the impact of the object thickness on the detected diffraction intensity a model was created based on Figure 2-1. In this model it is assumed the primary bundle impinges upon the sample surface under an angle of 90° (transmission). After traveling a distance x through a sample with thickness d, the intensity I_x of

the primary beam can be described using the law of Lambert-Beer with μ being the mass attenuation coefficient and ρ the density of the material.

$$I_x = I_0 e^{-\mu\rho x}$$

Only a small fraction of the primary beam will undergo diffraction in the element dx.

$$\mathrm{d}I_{diff} = \alpha \mathrm{d}x I_x$$

The remaining pathway for the X-rays after diffraction is defined by the Bragg angle θ.

$$\mathrm{d}I_{det} \propto e^{-\mu\rho\frac{d-x}{\cos 2\theta}} \mathrm{d}I_{diff}$$

After substitution the expression for I_{det} is given as follows.

$$I_{det} \propto \alpha I_0 e^{-\mu\rho\frac{d}{\cos 2\theta}} \int_0^d e^{-\mu\rho x\left(1-\frac{1}{\cos 2\theta}\right)} \mathrm{d}x$$

Solving the integral leads to the following expression for the intensity of the detected diffraction beam.

$$I_{det} \propto \alpha I_0 \frac{e^{-\mu\rho\frac{d}{\cos 2\theta}}}{\mu\rho\left(\frac{1}{\cos 2\theta}-1\right)}\left[e^{-\mu\rho d\left(1-\frac{1}{\cos 2\theta}\right)}-1\right]$$

Using this expression, the detected diffraction intensity can be plotted as a function of the thickness d of the sample.
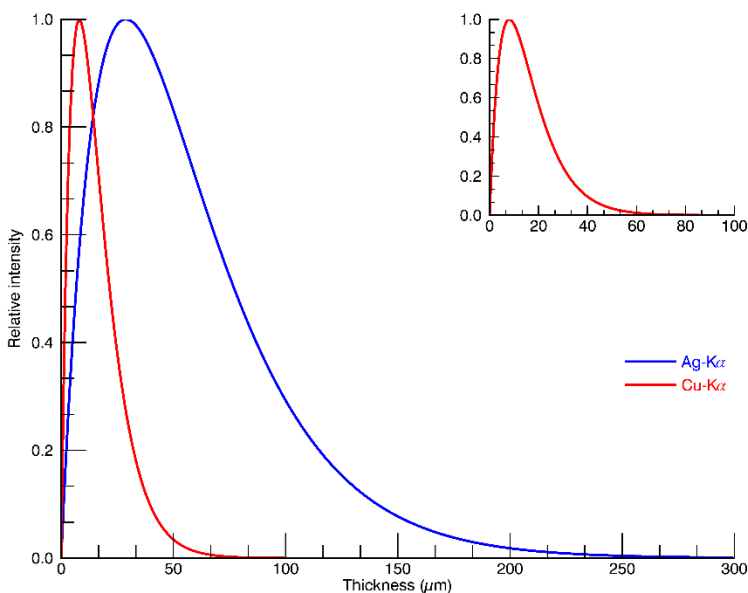
Figure 2-2 Variation in intensity of the 111 reflection of $PbCO_3$ as a function of the thickness d in transmission geometry for a Cu-K_α and a Ag-K_α X-ray source.

In Figure 2-2 an example is shown with cerussite ($PbCO_3$), a component of the pigment lead white, to illustrate the absorption effect for two commonly used types of X-ray sources. For Ag-K_α radiation (22 keV) the maximum intensity is obtained at a thickness of 29 µm. For very thin samples the diffraction intensity will increase in a linear fashion with the thickness as more crystals are irradiated, leading to more diffraction. For thicker samples the absorption effect will be dominant, causing an exponential decrease in the detected diffraction intensity. For Ag-K_α radiation (22 keV), the maximum intensity is obtained at a thickness of 29 µm. At a thickness of 150 µm only 10% of the maximum intensity remains.

For Cu-K_α radiation (8 keV), the maximum intensity is achieved at a value of only 8 µm. While Cu-K_α radiation is more likely to undergo diffraction, low energy X-ray radiation is also much more likely to be absorbed as shown in Table 2-1. Additionally, the characteristic diffraction angle 2θ is energy-dependent and

26

increases with decreasing energy. A larger diffraction angle will increase the pathway length along which the diffracted X-rays can be absorbed.

Table 2-1 Influence of the primary energy on the cross-section for coherent scattering and absorption for the 111 plane of $PbCO_3$.

	Diffraction ($cm^2 g^{-1}$)	Absorption ($cm^2 g^{-1}$)	Diffraction angle (°)
Ag-K_α	1.62	52.5	8.93
Cu-K_α	4.73	180	24.8

Based on this absorption model it is clear that macroscopic transmission XRPD is only suitable for the analysis of artworks with a limited thickness d and that ideally a high energy X-ray source is used to ensure sufficient transmission of the diffracted X-rays. For paintings with a thick lead white ground layer or with a wooden support the absorption effects will be too strong to obtain sufficiently intense diffraction signals.

Additionally, transmission MA-XRPD is also only suitable for the analysis of the bulk composition of works of art. The contribution of thin superficial (degraded) paint layers that are several microns thick to the averaged diffraction signal representing the entire >100 µm paint stratigraphy is so small that often neither identification nor quantification is possible. This presents a serious issue because the surface is not only representative of the visual outlook of a painting, but also because many relevant chemical processes are initiated at the exposed surface – air interphase.

2.1.2 Reflection-XRPD
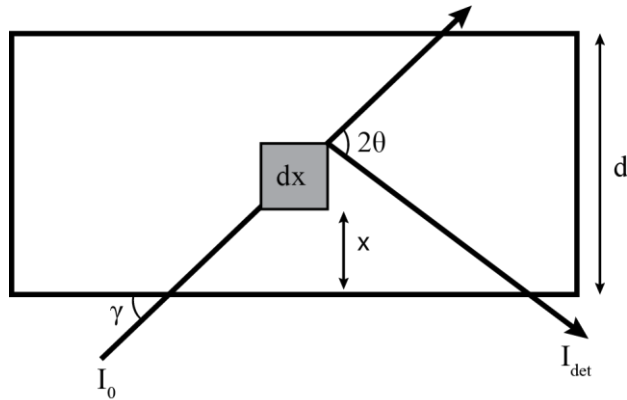
Figure 2-3 Schematic for the diffraction process in reflection geometry

A similar absorption model can be created for XRPD in reflection geometry. In this geometry the primary X-ray beam impinges under an angle $\gamma < 90°$ upon the sample surface. The smaller the angle, the longer the pathway and the stronger the primary bundle will be attenuated.

$$I_x = I_0 e^{-\mu\rho\frac{x}{\sin\gamma}}$$

A fraction of the primary X-ray beam diffracts in the element dx under an angle 2θ and leaves the sample at the surface.

$$dI_{det} \propto \alpha I_0 e^{-\mu\rho x\left(\frac{1}{\sin(2\theta-\gamma)} + \frac{1}{\sin\gamma}\right)}dx$$

After integration an expression is obtained for the diffracted intensity registered in reflection mode.

$$I_{det} \propto \alpha I_0 \frac{1}{\mu\rho}\left(\frac{1}{\sin(2\theta-\gamma)} + \frac{1}{\sin\gamma}\right)\left[1 - e^{-\mu\rho d\left(\frac{1}{\sin(2\theta-\gamma)} + \frac{1}{\sin\gamma}\right)}\right]$$

Analogous to the transmission model the variation of the diffraction intensity is described as a function of the sample thickness in Figure 2-4.
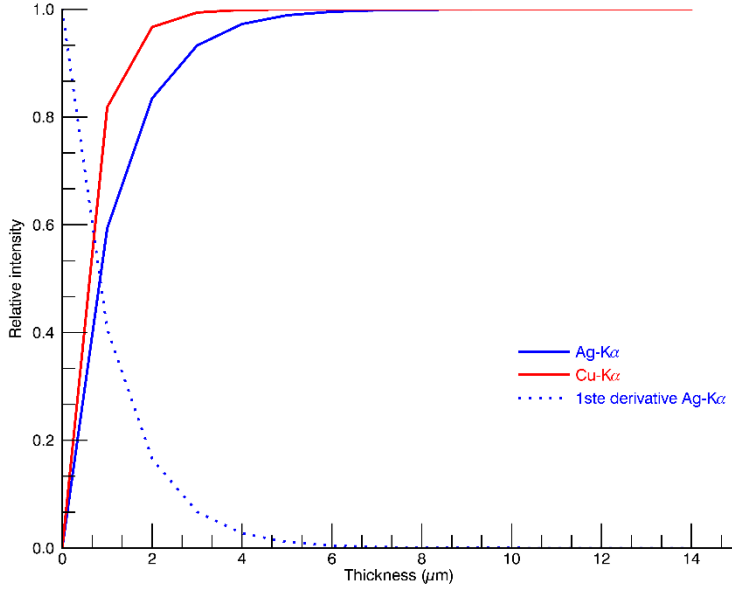
Figure 2-4 Variation in intensity of the 111 reflection of PbCO$_3$ as a function of the thickness in transmission geometry for two types of X-ray sources for an incident angle of 5°.

Contrary to the intensity profile in transmission geometry, the diffraction intensity in reflection geometry only increases with a higher thickness. This can be explained by calculating the first derivative of the expression for the diffracted intensity in reflection mode.

$$\frac{\mathrm{d}I_{det}}{\mathrm{d}d} \propto \left[\alpha I_0 \frac{1}{\mu\rho} \left(\frac{1}{\sin(2\theta - \gamma)} + \frac{1}{\sin\gamma} \right) \right]^2 e^{-\mu\rho d \left(\frac{1}{\sin(2\theta - \gamma)} + \frac{1}{\sin\gamma} \right)}$$

The continuously downward trend of this function means that the increase in diffraction intensity slows down with increasing thickness of the sample. As the intensity of the primary beam decreases the further it penetrates into the sample, less and less diffraction signals are generated. Additionally, the pathway for the generated diffraction signals becomes longer when the X-rays penetrate deeper into the sample. This means that from a certain thickness the maximum

diffraction intensity is achieved and no more additional diffraction signals are registered by the diffraction detector; this thickness is referred to as d_{thick}. In the example of Figure 2-4 d_{thick} is achieved at approximately 2 µm for Cu-K$_\alpha$ and at 4 µm for Ag-K$_\alpha$.

The diffraction intensity profiles for reflection geometry also show that the difference between Ag-K$_\alpha$ and Cu-K$_\alpha$ is less pronounced than it is for transmission geometry. One would expect that the higher energy Ag-K$_\alpha$ radiation would penetrate much deeper within the sample than the Cu-K$_\alpha$ radiation and thus have a much larger value for d_{thick}. However, this effect is counteracted by the energy-dependence of the diffraction angles. Higher energies will cause the 2θ angles to shift to lower values and from Figure 2-3 it can be visualized that lower 2θ angles cause an increase in the pathway length of the diffracted X-rays.

The sampling depth is derived from the expression for the diffraction intensity in reflection mode and, for the purposes of this thesis, is defined as the depth at which 99% of maximum diffracted intensity has been measured. This depth is also called the infinite thickness d_{thick}. Diffraction signals coming from deeper within the sample will not contribute to the registered diffraction intensity.

A thickness d is considered to be infinitely thick on the condition that the registered diffraction intensity at this thickness is equal to or larger than the diffraction intensity at infinite thickness.

$$I_{det}(d) \geq 0.99\, I_{det}(d_\infty)$$

Substitution leads to the following expression.

$$1 - e^{\mu\rho d\left[\frac{1}{sin(2\theta-\gamma)}+\frac{1}{\sin\gamma}\right]} \geq 0.99$$

The infinite thickness d can subsequently be expressed as follows.

$$d \geq \frac{\ln 100}{\mu\rho\left[\frac{1}{sin(2\theta - \gamma)} + \frac{1}{sin\,\gamma}\right]} = d_{thick}$$

As shown in the example of Figure 2-4 the obtained diffraction signals reflect the composition of only the upper 2 – 4 µm of the paint stratigraphy. Note that this calculation has been performed for pure cerussite powder while actual oil paint is approximately a 50:50 mixture of inorganic pigment and organic binding medium. Depending on the pigment, the sampling depth can range from approximately 5 µm (pigments containing 'heavy' elements such as Pb, As or Hg) to 50 µm (pigments containing 'light' elements such as Si or C).

While the absorption model proposed in this chapter has highlighted the possibilities and limitations of reflection MA-XRPD compared to the already existing transmission MA-XRPD setup, many questions still remain about the ideal configuration for this reflection setup. In what follows in this chapter several crucial parameters and concepts will be discussed in more detail in order to justify the hardware choices made. The X-ray beam spot size will determine the level of detail (spatial resolution) the MA-XRPD scanner is capable of delivering. The sampling depth d_{thick} has been defined in the previous equation and needs to be sufficiently low to ensure superficial sensitivity. The angular range determines the range of 2θ Bragg angles that can be detected by the X-ray diffraction detector and is an important parameter for identification purposes. The angular resolution describes the width of the diffraction signals and is an important parameter to assess the quality of the diffractogram.

2.2 X-ray sources

2.2.1 X-ray beam profile

Three different commercially available X-ray microsources (Incoatec GmbH, DE) were considered for incorporation within the reflection MA-XRPD scanner: IµS-Cu, IµS-Cu[HB] and IµS-Ag[HB]. The specifications of the X-ray sources are listed in Table 2-2. The values for flux and weight were provided by the manufacturer. The IµS Incoatec sources are equipped with Montel optics, consisting of two W/C multilayered perpendicular mirrors capable of energy discrimination and focusing the X-ray beam in two dimensions.[16] In order to compare the X-ray sources parameters such as the focal distance (d_F), the divergence (Θ) and the beam width ($FWHM$) were experimentally determined.
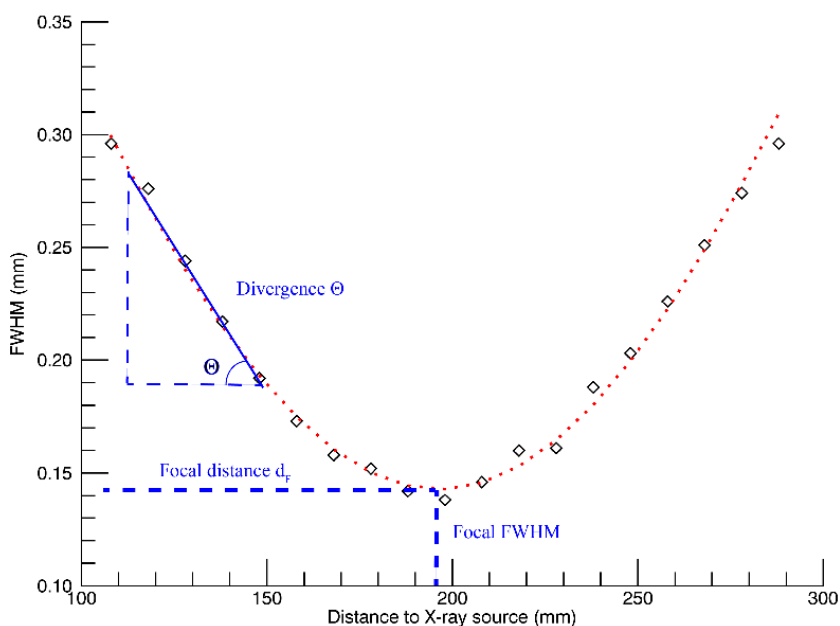
Figure 2-5 Beam profile for IµS-Cu[HB] showing the beam width as a function of the distance from the source.

The beam profiles were created by performing knife-edge scans across a thin wire of Fe (25 µm) or Zr (25 µm) at different source – wire distances, registering the intensity of the Fe-K or Zr-K fluorescence and creating a plot of the fluorescence intensity as a function of the scan range.[17] The resulting *FWHM* values were used as an approximation of the beam spot size. The obtained data points were fitted with a Gaussian profile. In Figure 2-5 the beam profile for the IµS-Cu^{HB} X-ray source is shown. Using the Gaussian profile, the focal distance d_F can be defined as the distance where the *FWHM* reaches its minimum value. Similarly, the divergence Θ can be calculated from the slope of the linear fit of the Gaussian profile.

Table 2-2 X-ray source specifications

	IµS-Cu	IµS-Cu^{HB}	IµS-Ag^{HB}
Primary energy (keV)	8 (Cu-K$_\alpha$)	8 (Cu-K$_\alpha$)	22 (Ag-K$_\alpha$)
Focal distance d$_F$ (cm)	39.8 (1)	19.6 (1)	21.6 (1)
Spot size FWHM (µm)	313 (5)	142 (2)	112 (3)
Divergence Θ (mrad)	2.6 (4)	2.4 (1)	3.8 (3)
Flux (photons s^{-1})	7.0 x 10^8	2.9 x 10^8	1.1 x 10^7
Flux density (photons s^{-1} m^{-2})	2.2 x 10^{12}	2.0 x 10^{12}	9.8 x 10^{10}
Mass (kg)	6.6	7.2	7.2

2.2.2 X-ray beam spot size

While the beam spot size values provided in Table 2-2 are sufficiently low for high resolution spatial imaging of artworks with XRPD, in reflection mode the footprint of the X-ray beam on the sample is elongated significantly in the horizontal dimension, depending on the value of the incident angle as shown in Figure 2-6. The result is a beam footprint with an elliptical profile.

$$d_1 = \frac{d_0}{\sin \gamma}$$

For example, an incident angle of 10° would increase the horizontal beam footprint of the IµS-Cu source from 313 µm to 1802 µm. The corresponding footprints for the IµS-Cu^{HB} and IµS-Ag^{HB} sources would increase to 818 µm and 645 µm respectively. This means that despite the higher total flux of the IµS-Cu source, its large spot size would significantly worsen the spatial image quality of 2D imaging experiments. Typically, a spot size of 1 mm or lower is desired for imaging purposes.
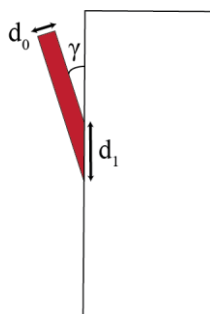
Figure 2-6 Impact of the incident angle on the beam footprint in reflection mode.

2.2.3 X-ray beam primary energy

The selected primary energy impacts several important parameters: the sampling depth (d_{thick}), the angular range and the capability for simultaneous XRF acquisition.

Sampling depth

While for transmission geometry the choice for a high energy X-ray source is required for sufficient X-ray transmission, for reflection geometry there is only a minor difference in sampling depth between low energy Cu-K$_\alpha$ (8 keV) and high energy Ag-K$_\alpha$ (22 keV) radiation as shown by Figure 2-4.

In Figure 2-7 the sampling depth is calculated for the range of $8 - 22$ keV. Across this range the impact of the primary energy on the sampling depth is minimal and the sampling depth remains largely constant at approximately 5 µm. The increase of the sampling depth at 12 keV is due to the proximity of the Pb-L$_3$ edge, significantly decreasing the mass attenuation coefficient of hydrocerussite at this energy.

Figure 2-7 Sampling depth as a function of the primary energy, calculated for a 50:50 mixture of linseed oil and hydrocerussite (10-5 reflection) at an incident angle of 8°.

Two compensating effects explain why the primary energy has a limited impact on the sampling depth in reflection geometry. While a higher primary energy decreases the attenuation of the primary and diffracted X-ray beams, it also shifts the 2θ diffraction angles to smaller values. From the model in Figure 2-3 it can be deduced that a smaller diffraction angle causes the pathway length of the

diffracted X-rays to increase, thereby increasing the attenuation. The net effect is that the total amount of attenuation is not strongly affected by a change in primary energy. The relationship between the primary energy and sampling depth will therefore not influence the choice of X-ray source.

Simultaneous XRF acquisition

XRF signals can be collected simultaneously during a MA-XRPD experiment, providing additional information for identifying amorphous compounds or for easier interpretation of the diffraction data. However, a primary energy of 8 keV is insufficient to excite fluorescence radiation from many relevant elements, ranging from zinc (Zn-K) to lead (Pb-L). For Ag-K$_\alpha$ (22 keV) radiation this is not an issue; commercial MA-XRF instruments employ a rhodium source that is similar in its maximum energy output (20 keV).[18]

Angular range

A higher primary energy shifts the 2θ Bragg angles to lower values. An angular range of $2\theta = 10° - 40°$ at 8 keV corresponds with an angular range of $2\theta = 4° - 13°$. This presents an important limitation in regards to the incident angle. Figure 2-3 shows that if $2\theta \leq \gamma$ the diffracted X-rays travel parallel to or away from the sample surface and cannot be registered by the detector. Therefore, in order to collect diffraction signals within the proposed angular range, using Ag-K$_\alpha$ radiation mandates a very shallow incident angle; this significantly impacts the size of the footprint of the X-ray beam.

While the use of Ag-K$_\alpha$ radiation in reflection mode offers an advantage for the simultaneous collection of XRF signals, the limitations imposed by the angular shift to lower values require a compromise that will either negatively impact the spot size of the beam or the starting value of the angular range. The use of Cu-K$_\alpha$

radiation does not require such a compromise and the IµS-Cu^{HB} source is therefore the better choice for implementation in the MA-XRPD scanner. The higher flux relative to the IµS-Ag^{HB} source is an additional advantage.

2.2.4 X-ray beam incident angle

The incident angle γ between the X-ray beam and the paint surface influences both the sampling depth d_{thick}, the spot size and the angular range (see 2.2.3).

In Figure 2-8 the sampling depth has been calculated for different values of the incident angle ranging from 2° to 26° for the (10-5) reflection of hydrocerussite at $2\theta = 27°$. The graph profile is explained by two competing effects. As Figure 2-3 shows, for shallow angles the path length of the primary beam is increased, causing more attenuation and a smaller sampling depth. For large incident angles, the path length of the diffracted beam increases as the angle $2\theta - \gamma$ becomes smaller and the sampling depth decreases as well. At intermediate values for the incident angle both effects are less pronounced. Despite that, the difference in sampling depth between an incident angle of 2° (2 µm) and 14° (8 µm) remains limited in absolute value. Both values are still considered to be very superficial within the context of a paint stratigraphy. Therefore, the sampling depth is not considered an important factor for deciding the incident angle.
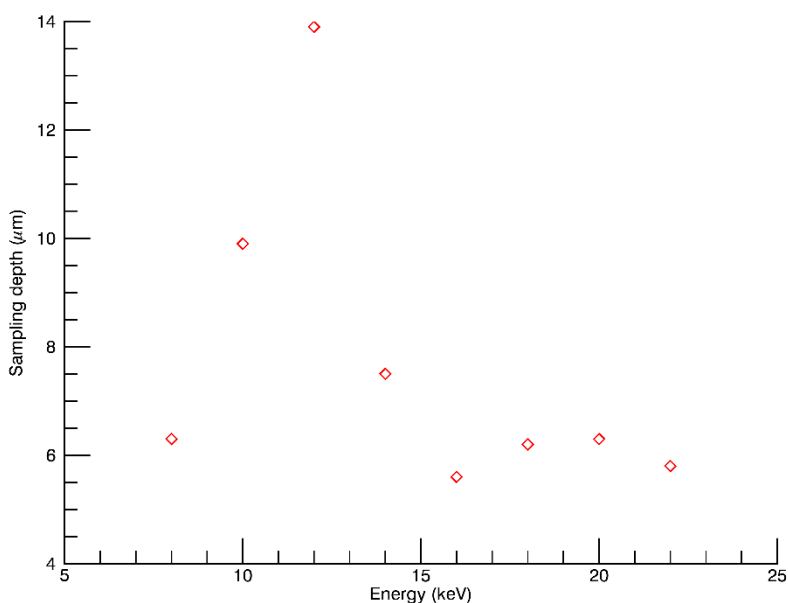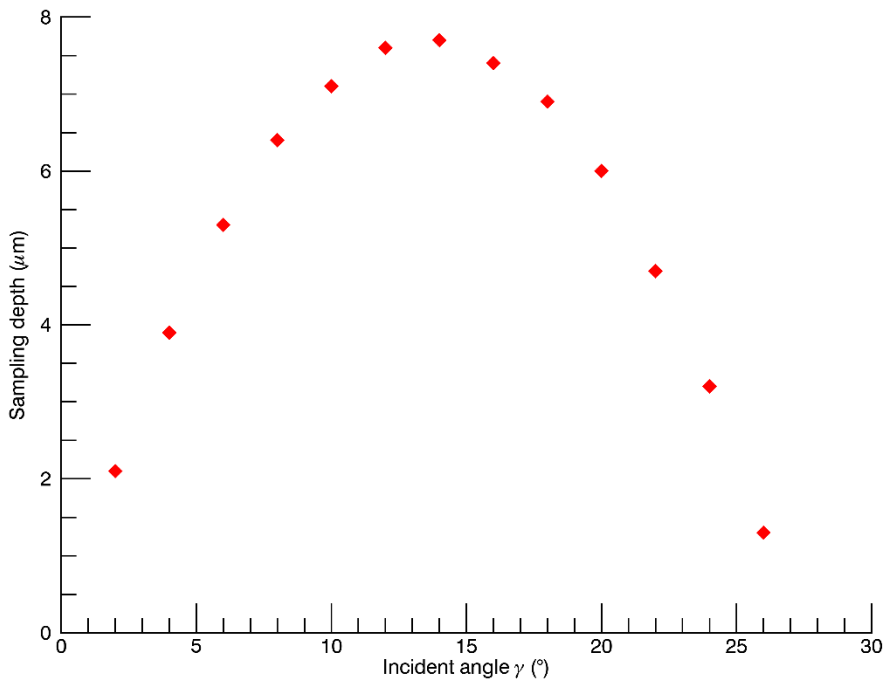
Figure 2-8 Sampling depth as a function of the incident angle γ, calculated for a 50:50 mixture of linseed oil and hydrocerussite (10-5 reflection) for a primary energy of 8 keV.

As stated in 2.2.2 the incident angle directly impacts the size of the beam footprint. The horizontal diameter of the beam for the IµS-Cu^{HB} source ranges from 4.1 mm for an angle of 2° to 0.32 mm for an angle of 26°. As the beam is only elongated in the horizontal direction, the vertical diameter remains constant at 0.15 mm. As a spot size of 1 mm or lower is desired for high spatial resolution imaging experiments, a compromise between spot size and angular range is desired. Additionally, due to physical constraints imposed by the dimensions of the IµS-Cu^{HB} source, a minimum incident angle of 8° is required for safety reasons. At lower angles the distance between the source and painting would be

too small to guarantee a safe analysis of the artwork. For this reason, an incident angle of $\gamma = 10°$ is chosen, ensuring a safe operating distance between source and painting while keeping the spot size (0.82 mm) and angular range within acceptable boundaries.

2.3 X-ray diffraction detector

2.3.1 Technical specifications

A commercial PILATUS 200K (Dectris Ltd., CH) X-ray diffraction detector was made available for implementation in the MA-XRPD scanner. The PILATUS 200K is a two-dimensional hybrid pixel array detector (HPAD). Major advantages of HPADs are their single photon counting capabilities (low noise), short readout time and high dynamic range.[19] Its specifications are listed in Table 2-3. The (relatively) small dimensions, low weight and mild operating conditions ensure that the detector does not undermine the mobility of the MA-XRPD scanner. Cooling is performed through a built-in air fan, eliminating the need for N_2. Only an additional dry air pump is required to satisfy the relative humidity conditions (<30%). Additionally, the improved detector efficiency at lower energies strengthens the choice for the use of the IμS-Cu^{HB} X-ray source.

Table 2-3 Technical specifications for the PILATUS 200K area detector

Active area size (mm^2)	83.8 x 67	**Sensor thickness** (μm)	1000
Sensor material	Si	**Det. efficiency 8 keV**	96%
Pixel size ($μm^2$)	172 x 172	**Det. efficiency 22 keV**	50%
Pixel amount	198 029	**Dimensions** (mm^3)	156 x 155 x 284
Max. frame rate (Hz)	20	**Operating humidity**	< 30%
Readout time (ms)	7	**Operating temp.** (°C)	20 - 35
Point-spread function	1 pixel	**Weight** (kg)	5.4

2.3.2　XRPD data processing

Processing of the diffraction data in this thesis was performed using the XRDUA software package.[20] XRDUA provides the necessary tools for extracting crystalline-specific distributions from large numbers of diffraction patterns obtained during imaging experiments. 2D diffraction patterns are azimuthally integrated to obtain 1D diffractograms, which show the diffraction intensity as a function of the 2θ angle. The compounds present in the diffractogram are then identified by cross-referencing with a database. After identification a Rietveld model containing the individual contributions of the identified compounds is created to perform whole pattern fitting on the 1D data. The crystallographic data required for constructing the models was obtained from the American Mineralogist Crystal Structure Database.[21]

$$I_R(2\theta) = I_{BG}(2\theta) + \sum_i S_i \sum_H F_{iH}^2 \, C_{iH} \Omega_i(2\theta - 2\theta_{iH})$$

In this equation S_i denotes the total peak intensity scaling factor for every identified phase, F_{iH} denotes the structure factor and C_{iH} the part of the Lorentz-Polarization factor not removed during azimuthal integration. The contribution of I_{BG} was modelled using a built-in strip function. A Gaussian peak shape Ω_i was used for modeling. In this manner refined values for the intensity scaling parameter, the position and the width of the diffraction signal are obtained. Constraints can be set on the peak position and peak width to exclude solutions without physical meaning. MA-XRPD distribution images are obtained by plotting the intensity scaling parameter values for every scanned pixel in the 2D array.

The diffraction intensity is commonly shown as a function of the diffraction angle 2θ (°). However, for comparing diffraction patterns registered at different

energies use of the energy-independent scattering vector Q (reciprocal space) is preferable.

$$Q = \frac{4\pi}{\lambda}\sin\theta$$

2.3.3 Angular range

The captured angular range depends on the distance and position of the 2D diffraction detector to the sample. Positioning the detector closer to the sample will increase the angular range captured by the detector surface and vice versa. As an increase in the angular range negatively impacts the angular resolution, the angular range should be limited to low Q-values, at which the most common pigments (and secondary products) can be identified. Very low Q-values cannot be captured because of the incident angle limitation while large Q-values are excluded because of increasing FWHM values and subsequently more peak overlap.

2.3.4 Angular resolution

The angular resolution is an important parameter for distinguishing diffraction signals, especially in complex paint mixtures where signal overlap can cause significant difficulties for unambiguously identifying unknown compounds. To determine the source – sample – detector geometry that leads to the best angular resolution, a diffraction standard (LaB_6) was analyzed at different positions and the integrated diffraction patterns were fitted using the method described in 2.3.2. Initially the sample – detector distance was set at 11.5 cm, corresponding to a Q-range of 11 nm^{-1} – 39 nm^{-1}.
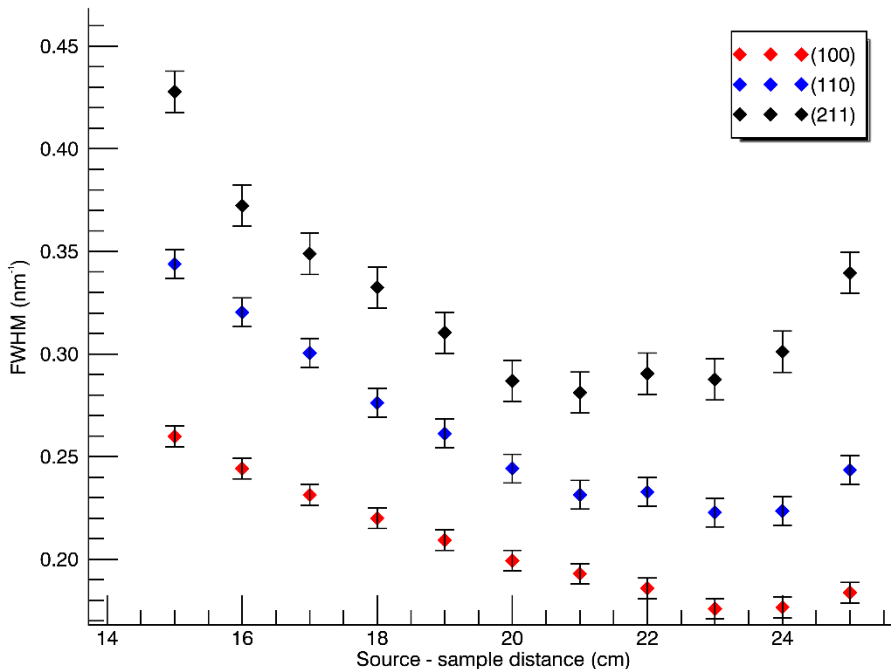
Figure 2-9 FWHM for three LaB$_6$ diffraction signals at different source – sample distances. The FWHM values were calculated by fitting averaged patterns from 10 measurements.

The source – sample distance was incrementally increased with steps of 1 cm. Three of the six captured reflections are shown in Figure 2-9, including the (100) and (211) reflections close to the start and end of the angular range.

The lowest *FWHM* values are obtained within the source – sample distance range of 21 – 24 cm (0.18 nm^{-1} – 0.29 nm^{-1}), close to the focal distance of the IµS-Cu^{HB} X-ray source (see Table 2-2). This is ideal as it allows for analysis combining a high spatial and a high angular resolution. The differences within this range are small, likely due to the parabolic shape of the beam profile (see Figure 2-5).

The *FWHM* value increases significantly from the (100) to the (211) reflection. Solely taking the detector into account, the opposite phenomenon would be expected. The *Q*-range coverage of a Pilatus 200K detector pixel decreases with increasing *Q*-value. A pixel for reflection (100) covers a *Q*-range of 0.06 nm^{-1} while a pixel for reflection (211) covers a *Q*-range of only 0.04 nm^{-1}. However, given that the minimum *FWHM* of reflection (100) is 0.11 nm^{-1} lower than for reflection (211) there is a second, more dominant, factor at play. Cu-K$_\alpha$ radiation is not monochromatic but consists of two separate contributions: Cu-K$_{\alpha1}$ (8.05 keV, 67% contribution) and Cu-K$_{\alpha2}$ (8.03 keV, 33% contribution). While the Montel optics are sufficient to separate the Cu-K$_\beta$ (8.91 keV) contribution from the generated Cu-K X-rays, the energy difference between Cu-K$_{\alpha1}$ and Cu-K$_{\alpha2}$ is too small to allow for separation. Table 2-4 shows the increase in angular separation for Cu-K$_{\alpha1}$ and Cu-K$_{\alpha2}$. $\Delta 2\theta$ is nearly three times larger at higher angles.

Table 2-4 Higher diffraction angles give cause to a higher FWHM due to peak separation of Cu-K$_{\alpha1}$ and Cu-K$_{\alpha2}$.

	(100)	(211)
2θ Cu-K$_{\alpha1}$ (nm^{-1})	21.354	53.995
2θ Cu-K$_{\alpha2}$ (nm^{-1})	21.406	54.135
$\Delta 2\theta$ (°)	0.052	0.140

In the final design of the MA-XRPD scanner the sample – detector distance was increased to 22.0 cm in order to safely capture lower *Q*-values related to compounds of interest. Due to the increased sample detector distance, also the angular resolution improves significantly. For the (100) reflection the improved *FWHM* is 0.108 nm^{-1}, for the (110) reflection 0.133 nm^{-1} and the (211) reflection is now outside the captured angular range. The downside is a narrowing of the

Q-range for higher angles, from 11 nm^{-1} – 38 nm^{-1} to 10 nm^{-1} – 34 nm^{-1}. Additionally, the increased sample – detector distance causes more attenuation by the air of the diffracted X-rays: from 13% attenuation at 11.5 cm to 22% attenuation at 22.0 cm. The attenuation of the primary X-ray beam is negligible due to the use of a vacuum-sealed flight tube that covers most of the distance between the beryllium exit window of the X-ray source and the point of impact on the painting.

2.3.5 Azimuthal range

In reflection geometry only part of the azimuthal range is captured by the X-ray diffraction detector. The captured azimuthal range is approximately -5° to 35° and decreases for high Q-values: 0° to 25°. Due to the rectangular shape of the detector, for very small or very high Q-values the azimuthal coverage can be as low as several degrees. This means that in practice only about 5 – 10% of a diffraction ring is captured by the detector. For powders that give rise to homogenous Debye rings this is not an issue. However, for crystallites subject to preferred orientation effects it is possible that their diffraction signals are outside the azimuthal range captured by the detector.
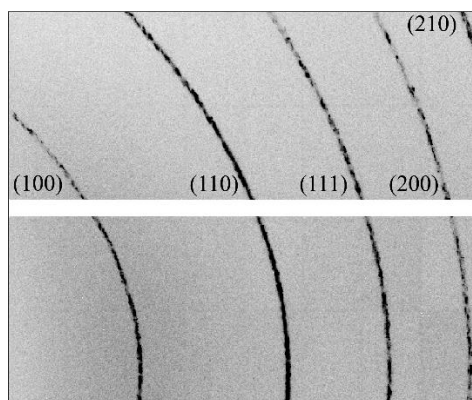
Figure 2-10 Diffraction pattern of LaB$_6$ captured in reflection geometry.

2.4 MA-XRPD scanner hardware

While the X-ray source and X-ray diffraction detector configuration choices have already been discussed, the other hardware components that constitute the MA-XRPD scanner have yet to be introduced. Figure 2-11 shows the MA-XRPD scanner in action accompanied by a schematic detailing its components.

The scan platform consists of a IμS-Cu^{HB} X-ray source and a PILATUS 200K detector. To ensure that the artwork remains in focus during the scanning procedure an optical distance laser, linked to a 10 cm motor stage, is used with a diameter of 1 mm and a distance resolution of 50 μm. This is necessary as paintings are often not completely flat and different phenomena (e.g. pentimenti, retouches, damage, etc.) can introduce topographical variations in the paint surface. For shiny (e.g. metallic) or poorly-reflecting (e.g. dark) surfaces the accuracy of the distance correction can decrease significantly however, causing variations in the measurement positions.

A Vortex silicon drift detector (Hitachi, Japan) can also be positioned on the platform to simultaneously collect fluorescence data although, as mentioned in 2.2.3, the primary energy is too low to excite most elements with a high atomic number (e.g. Hg or Pb) while fluorescence radiation from elements with a low atomic number (e.g. S or K) suffers from attenuation by the air.[22]

The scan platform itself is mounted on a set of three motor stages (Newport Corp., USA) which can move in three directions (X,Y,Z). The motor stages can cover 30 cm x 30 cm on the XY imaging plane and 10 cm towards and away from the painting, regulated by the laser distance sensor. Both the motor stages and the distance sensor contribute to the dead time, which is approximately 2.5 s pt^{-1}.
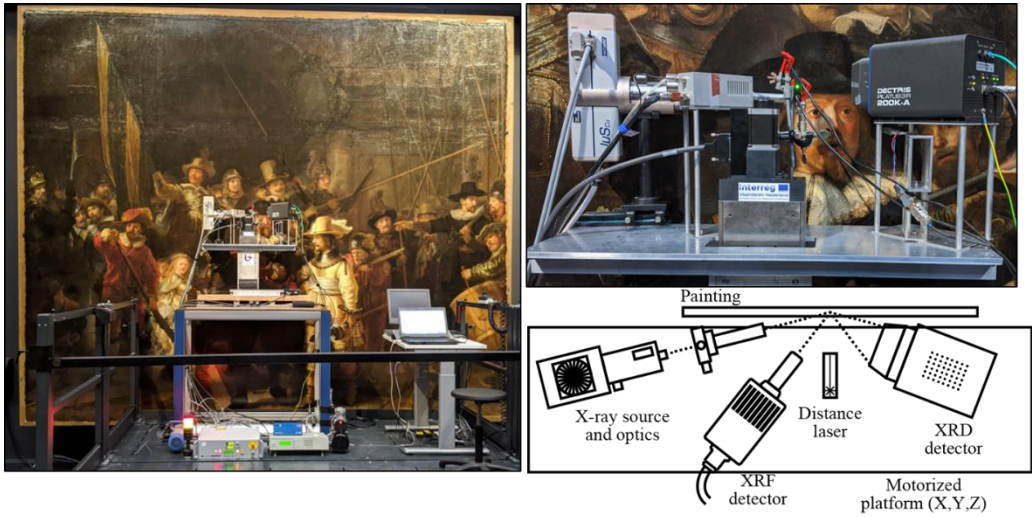
Figure 2-11 Left: MA-XRPD scanner in front of *The Night Watch* (Rembrandt, 1642). Right: Zoomed in image of the scan platform with corresponding schematic display. Photo credit: Frederik Vanmeert

2.5   Case study: *Portrait of Pope Innocent X*

To demonstrate the advantages of a MA-XRPD scanning instrument in reflection geometry, scans were performed on a painting (48 x 63 cm^2) from a private collection depicting Pope Innocent X. The painting has been dated to the 17th century and was likely created by the Spanish artist Diego Velázquez or one of his students. The portrait would have served as an early version for one of Velázquez' most famous works: *Portrait of Pope Innocent X* (1650).

Figure 2-12 Left: Private painting (17th century) analyzed with MA-XRPD, Right: *Portrait of Pope Innocent X* (1650, Doria Pamhilj Gallery, Rome)

Part of the painting was initially scanned in transmission mode using a IµS-Ag^{HB} X-ray source with a total scan size of 267 x 380 mm^2, a step size of 1 x 1 mm^2 and an exposure time of 10 s pt^{-1}. Seven crystalline compounds were identified and their attenuation-corrected distribution images are shown in Figure 2-13.
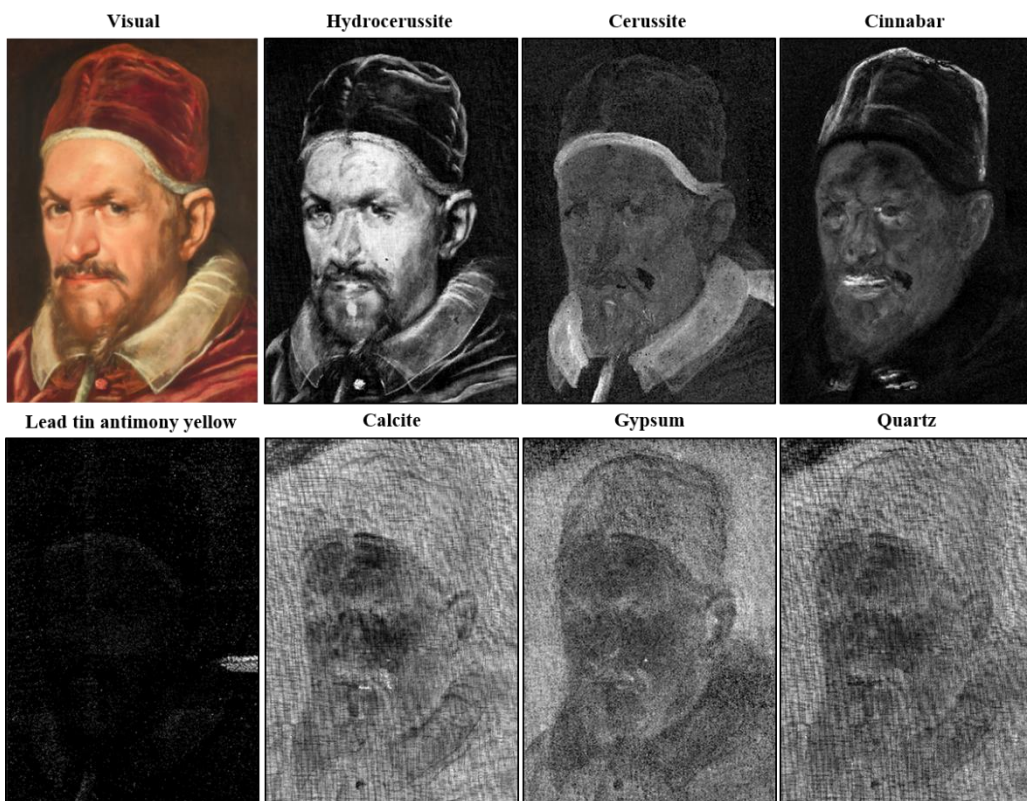
Figure 2-13 Compound-specific distribution images obtained with MA-XRPD in transmission mode

The pink flesh tones in the face of Pope Innocent X are the result of a paint mixture containing lead white (hydrocerussite and cerussite) and vermilion (cinnabar, HgS). As MA-XRPD can only identify crystalline materials, the presence of other red pigments here cannot be excluded. The vermilion is more strongly present in the red lips and in the bright red tones of the felt hat. No vermilion is identified in the dark red regions of the papal clothing, suggesting that an amorphous organic red lake was extensively used there. The hydrocerussite distribution also reveals the presence of a second pair of eyes that was overpainted at a later stage. A rare lead antimony yellow pigment ($Pb_2SbSnO_{6.5}$) was also identified in the background of the painting. This rare

pigment was sometimes used in 17th century Roman paintings to paint golden decorations.[23] The ground layer for this portrait was created with a mixture of chalk (calcite, $CaCO_3$) and quartz (SiO_2) with small amounts of gypsum ($CaSO_4 \cdot 2H_2O$). The presence of chalk together with quartz has been identified in previous works by Vélazquez such as *Kitchen Scene* or *Forge of Vulcan*.[24,25] As MA-XRF identified Fe-K in the background of the painting, the presence of quartz is likely linked to the usage of a red earth pigment in the background. As expected, transmission-geometry provides information on pigments that are abundantly present, both original paint layers and the ground layer.

A similar part of the painting was scanned in reflection mode using a IµS-Cu[HB] X-ray source in the configuration described in the previous subchapters. An area of 250 x 384 mm^2 was scanned with steps of 1.5 x 1.5 mm^2 and an exposure time of 10 s pt^{-1}. Thirteen crystalline compounds were identified and their distribution images are shown in Figure 2-14.

With the exception of lead antimony yellow, all of the compounds that were identified in transmission mode were also identified in reflection mode: hydrocerussite, cerussite, cinnabar, calcite, quartz and gypsum. While the two distributions of hydrocerussite look similar, there are subtle differences: the overpainted eyes and the neck are almost completely invisible in reflection mode. The cinnabar distributions are comparably similar, implying that both cinnabar and hydrocerussite are primarily present at the surface of the stratigraphy. The difference is more outspoken for cerussite, which is strongly localized in the white mantle embroidery but absent from the brim of the hat or the mantle collar in reflection mode. In transmission mode a strong cerussite signal is encountered in these latter two areas, suggesting the presence of a cerussite-rich layer below a hydrocerussite-rich top layer. This hypothesis is further reinforced by the fact

that in areas with less hydrocerussite at the surface, a very faint signal of cerussite is detected in reflection mode. We also hypothesize that this cerussite-rich underlayer is likely not uniform in thickness; the transmission intensity of cerussite in the brim of the papal hat is significantly higher than in the facial area even though the hydrocerussite signal detected in both areas is of the same magnitude.

Similarly, the gypsum distribution also differs strongly from its transmission counterpart. The intensity in the background areas has disappeared while only localized gypsum-rich areas remain, co-localized with calcite. For calcite and quartz, the background intensity is still present, suggesting that there is a gypsum layer underneath the calcite and quartz layer(s). It is also important to note that the sampling depth is not uniform across the painting. In the face of Pope Innocent X, the X-rays will sample only approximately the first 10 μm due to the lead- and mercury-rich paint. Much less absorption occurs in the background areas where the elemental composition is dominated by carbon, calcium and silicon. Nevertheless, no lead tin antimonate could be detected.

Six additional compounds were detected compared to the transmission analysis: lazurite ($(Na,Ca)_8[(S,Cl,SO_4,OH)_2|(Al_6Si_6O_{24})]$), zincite ($ZnO$), barite ($BaSO_4$), rutile ($TiO_2$), palmierite ($K_2Pb(SO_4)_2$), anglesite ($PbSO_4$) and finally a type of organic wax. Lazurite, the main crystalline component of ultramarine, was identified in the background of the painting. As it was not identified in transmission, it is likely only present at the surface. Zincite, barite and rutile are all compounds found in modern paints such as zinc white and titanium white. They are strongly localized at the surface in retouched areas in the face. Finally, two crystalline compounds were identified that do not relate to pigments commonly found in literature: palmierite and anglesite. These compounds are

secondary products formed as a result of reactions between pigments, binding media and/or the environment.

Visual | **Hydrocerussite** | **Cerussite** | **Cinnabar**

Calcite | **Quartz** | **Gypsum** | **Lazurite**

Wax | **Zincite** | **Barite** | **Rutile**

Palmierite | **Anglesite**
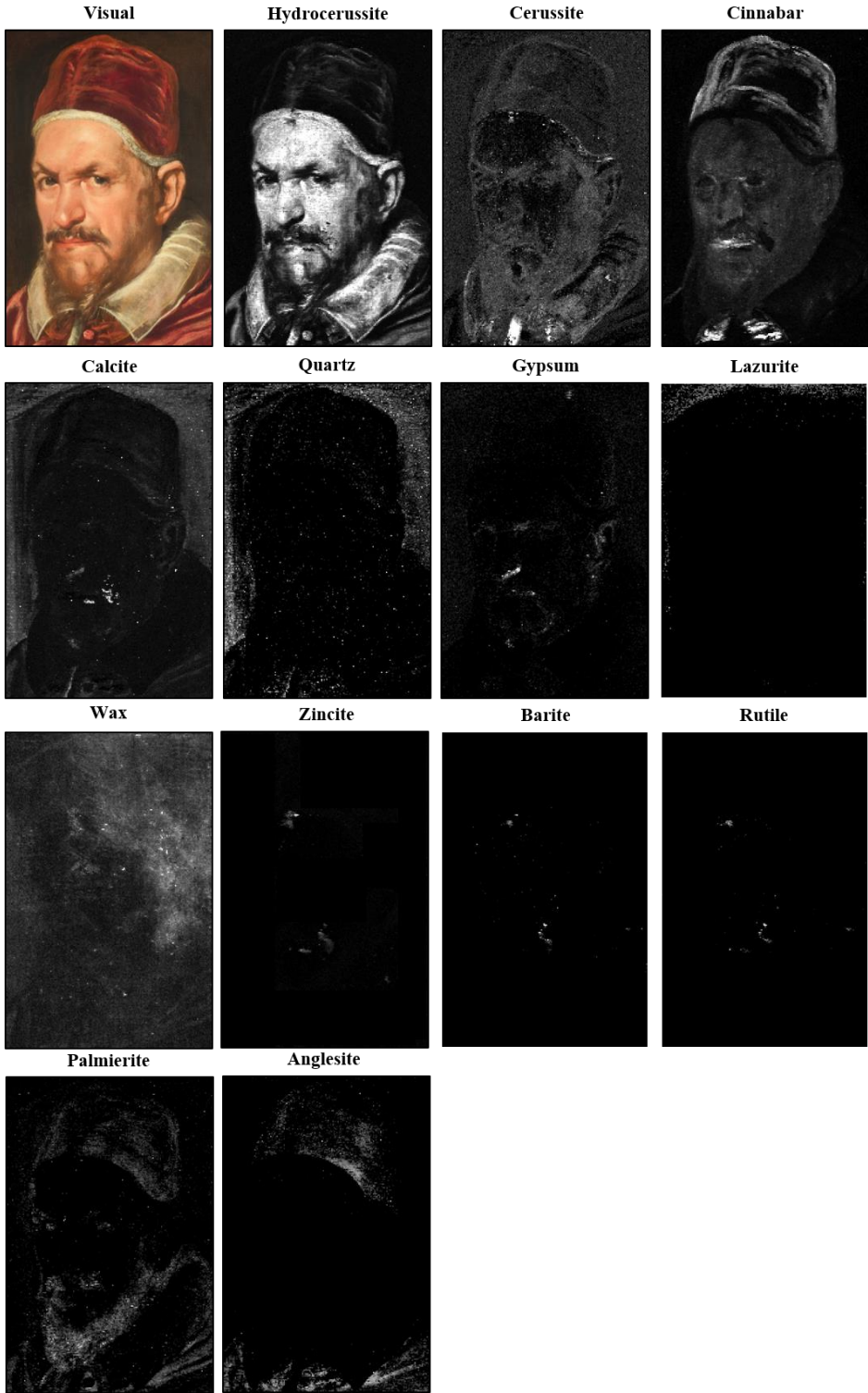
Figure 2-14 Compound-specific distribution images obtained with MA-XRPD in reflection mode

2.6 Conclusions

In this chapter the advantages and limitations of MA-XRPD in reflection mode were outlined. A configuration of a reflection MA-XRPD scanner was proposed taking into account several relevant parameters: the beam spot size, the sampling depth, the angular range and the angular resolution. The IµS-Cu^{HB} source was chosen for its small spot size (good spatial resolution) and low primary energy. The latter is important for shifting the diffraction angles to higher values, so the cutoff in the angular range caused by the incident angle is limited to only low Q-values. For the detector position a compromise was made between the angular resolution and the angular range as identification of most paint materials is possible and preferable at low Q-values due to peak broadening at higher Q-values.

As demonstrated by the absorption model and the presented case study, reflection MA-XRPD is highly sensitive to superficial phenomena. This includes not only pictorial paint layers but also secondary products that are formed over time or retouches made by the artist or later conservators. Information pertaining to deeper paint layers or to the ground layer cannot be (easily) acquired in reflection mode; transmission MA-XRPD is more suited for that purpose. Combining both techniques will lead to a more complete understanding of the crystalline paint stratigraphy.

Several important limitations need to be highlighted. As X-ray powder diffraction is a technique reserved for the analysis of crystalline materials, other techniques that can visualize the distribution of amorphous compounds (e.g. organic lakes, smalt, etc.) remain very relevant. While reflection MA-XRPD is a superficial technique, the sampling depth varies depending on the paint composition and there is no certainty on how many paint layers are sampled at any given point.

Therefore, conclusions about the stratigraphy of the painting can only be inferred indirectly. For this reason, synchrotron-based techniques for the microscopic investigation of stratified paint samples remain highly relevant and reflection MA-XRPD can help guide conservators to areas relevant for sampling.

References

(1) Van der Snickt, G.; Dooley, K. A.; Sanyova, J.; Dubois, H.; Delaney, J. K.; Gifford, M.; Legrand, S.; Laquiere, N.; Janssens, K. Dual Mode Standoff Imaging Spectroscopy Documents the Painting Process of the Lamb of God in the Ghent Altarpiece by J. and H. Van Eyck. *Sci. Adv.* **2020**, *6*, eabb3379.

(2) Derks, K.; Van der Snickt, G.; Legrand, S.; Van der Stighelen, K.; Janssens, K. The Dark Halo Technique in the Oeuvre of Michael Sweerts and Other Flemish and Dutch Baroque Painters. A 17th c. Empirical Solution to Mitigate the Optical 'Simultaneous Contrast' Effect? *Herit. Sci.* **2022**, *10*, 5.

(3) Dik, J.; Janssens, K.; Van der Snickt, G.; Van der Loeff, L.; Rickers, K.; Cotte, M. Visualization of a Lost Painting by Vincent van Gogh Using Synchrotron Radiation Based X-Ray Fluorescence Mapping. *Analytical Chemistry* **2008**, *80*, 6433–6442.

(4) Alfeld, M.; Janssens, K.; Dik, J.; De Nolf, W.; Van der Snickt, G. Optimization of Mobile Scanning Macro-XRF Systems for the in Situ Investigation of Historical Paintings. *J. Anal. At. Spectrom.* **2011**, *26*, 899–909.

(5) da Silva, A. T.; Legrand, S.; Van der Snickt, G.; Featherstone, R.; Janssens, K.; Bottinelli, G. MA-XRF Imaging on René Magritte's La Condition Humaine: Insights into the Artist's Palette and Technique and the Discovery of a Third Quarter of La Pose Enchantée. *Herit. Sci.* **2017**, *5*, 37.

(6) De Keyser, N.; Van der Snickt, G.; Van Loon, A.; Legrand, S.; Wallert, A.; Janssens, K. Jan Davidsz. de Heem (1606-1684): A Technical Examination of Fruit and Flower Still Lifes Combining MA-XRF Scanning, Cross-Section Analysis and Technical Historical Sources. *Herit. Sci.* **2017**, *5*, 38.

(7) Dooley, K. A.; Conover, D. M.; Glinsman, L. D.; Delaney, J. K. Complementary Standoff Chemical Imaging to Map and Identify Artist Materials in an Early Italian Renaissance Panel Painting. *Angew. Chem. Int. Ed.* **2014**, *53*, 13775–13779.

(8) Romano, F. P.; Caliri, C.; Nicotra, P.; Di Martino, S.; Pappalardo, L.; Rizzo, F.; Santos, H. C. Real-Time Elemental Imaging of Large Dimension Paintings with a Novel Mobile Macro X-Ray Fluorescence (MA-XRF) Scanning Technique. *J. Anal. At. Spectrom.* **2017**, *32*, 773–781.

(9) Ricciardi, P.; Delaney, J. K.; Facini, M.; Zeibel, J. G.; Picollo, M.; Lomax, S.; Loew, M. Near Infrared Reflectance Imaging Spectroscopy to Map Paint Binders in Situ on Illuminated Manuscripts. *Angew. Chem.* **2012**, *51* (23), 5607–5610.

(10) Cucci, C.; Delaney, J. K.; Picollo, M. Reflectance Hyperspectral Imaging for Investigation of Works of Art: Old Master Paintings and Illuminated Manuscripts. *Acc. Chem. Res.* **2016**, *49*, 2070–2079.

(11)   Gabrieli, F.; Dooley, K. A.; Zeibel, J. G.; Howe, J. D.; Delaney, J. K. Standoff Mid-Infrared Emissive Imaging Spectroscopy For Identification and Mapping of Materials in Polychrome Objects. *Angew. Chem.* **2018**, *57*, 7341–7345.

(12)   Legrand, S.; Alfeld, M.; Vanmeert, F.; De Nolf, W.; Janssens, K. Macroscopic Fourier Transform Infrared Scanning in Reflection Mode (MA-RFTIR), a New Tool for Chemical Imaging of Cultural Heritage Artefacts in the Mid-Infrared Range. *Analyst* **2014**, *139*, 2489–2498.

(13)   Vanmeert, F.; De Nolf, W.; De Meyer, S.; Dik, J.; Janssens, K. Macroscopic X-Ray Powder Diffraction Scanning, a New Method for Highly Selective Chemical Imaging of Works of Art: Instrument Optimization. *Anal. Chem.* **2018**, *90*, 6436–6444.

(14)   Vanmeert, F.; De Nolf, W.; Dik, J.; Janssens, K. Macroscopic X-Ray Powder Diffraction Scanning: Possibilities for Quantitative and Depth-Selective Parchment Analysis. *Anal. Chem.* **2018**, *90*, 6445–6452.

(15)   Vanmeert, F.; Hendriks, E.; Van der Snickt, G.; Monico, L.; Dik, J.; Janssens, K. Chemical Mapping by Macroscopic X-Ray Powder Diffraction of Van Gogh's Sunflowers: Identification of Areas with Higher Degradation Risk. *Angew. Chem.* **2018**, *57*, 7418–7422.

(16)   Montel, M. In *X-ray Microscopy and Microradiography*; Academic Press: New York, 1957; pp 177–185.

(17)   Sun, T.; Ding, X. Study on the Measurement of Properties of Polycapillary X-Ray Lens. *Nucl. Instr. Meth. Phys. Res.* **2004**, *226*, 651–658.

(18)   Alfeld, M.; Pedroso, J. V.; van Eikema Hommes, M.; Van der Snickt, G.; Tauber, G.; Blaas, J.; Haschke, M.; Erler, K.; Dik, J.; Janssens, K. A Mobile Instrument for in Situ Scanning Macro-XRF Investigation of Historical Paintings. *J. Anal. At. Spectrom.* **2013**, *28*, 760–767.

(19)   Manolopoulos, S.; Bates, R.; Bushnell-Wye, G.; Campbell, M.; Derbyshire, G.; Farrow, R.; Heijne, E.; O'Shea, V.; Raine, C.; Smith, K. M. X-Ray Powder Diffraction with Hybrid Semiconductor Pixel Detectors. *J. Synchrotron Rad.* **1999**, *6*, 112–115.

(20)   De Nolf, W.; Vanmeert, F.; Janssens, K. XRDUA: Crystalline Phase Distribution Maps by Two-Dimensional Scanning and Tomographic (Micro) X-Ray Powder Diffraction. *J. Appl. Crystallogr.* **2014**, *47*, 1107–1117.

(21)   Downs, R. T.; Hall-Wallace, M. The American Mineralogist Crystal Structure Database. *Am. Mineral.* **2003**, *88*, 247–250.

(22)   Barkan, S.; Iwanczyk, J. S.; Patt, B. E.; Feng, L.; Tull, C. R. Vortex^TM - A New High Performance Silicon Drift Detector for XRD and XRF Applications. *Adv. X-ray Anal.* **2003**, *46*, 332–337.

(23)   Ruiz-Moreno, S.; Perez-Pueyo, R.; Gabaldon, A.; Soneira, M. J.; Sandalinas, C. Raman Laser Fibre Optic Strategy for Non-Destructive

Pigment Analysis. Identification of a New Yellow Pigment (Pb, Sn, Sb) from the Italian XVII Century Painting. *J. Cult. Herit.* **2003**, *4*, 309–313.

(24)   Brown, J.; Garrido, C. *Velázquez: The Technique of Genius*; Yale University Press: New Haven, 1998.

(25)   McKim-Smith, G.; Anderson-Bergdoll, G.; Newman, R. *Examining Velázquez*; Yale University Press: New Haven, 1998.

Chapter 3   Lead white pigments
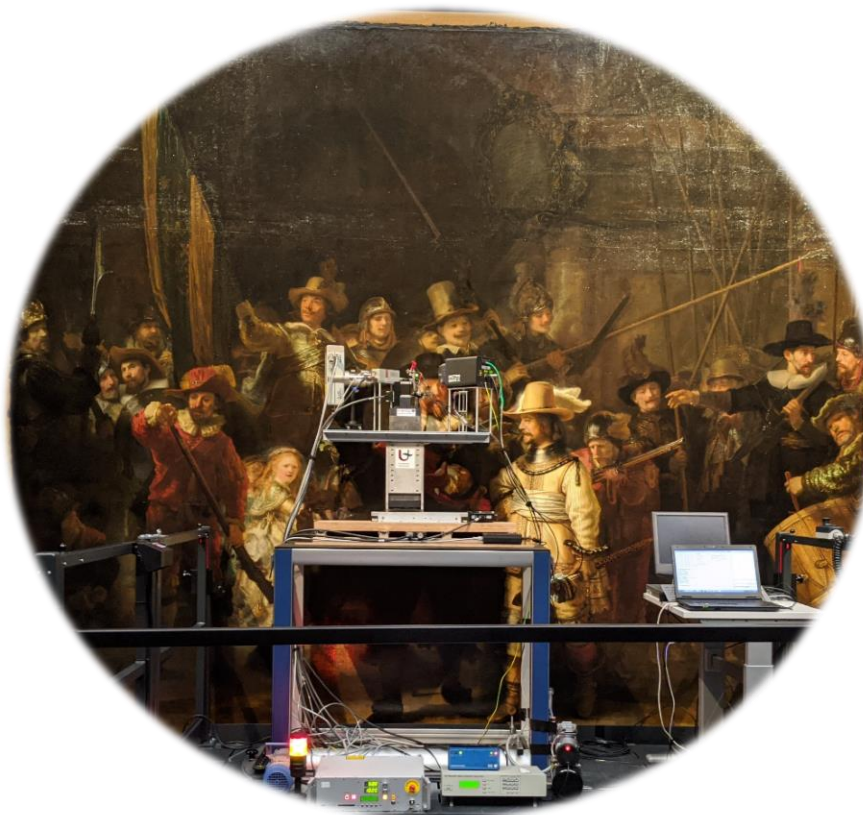
In this chapter, the unique potential of MA-XRPD for the chemical speciation and quantification of lead white pigments and associated lead-based compounds is demonstrated by means of two case studies.

In the first case study Johannes Vermeer's usage of lead white in the painting *Girl with a Pearl Earring* (c. 1665) is investigated with a multitude of analytical techniques, including reflection and transmission MA-XRPD. Lead white is typically composed of two crystalline lead carbonates: hydrocerussite ($2PbCO_3 \cdot Pb(OH)_2$) and cerussite ($PbCO_3$). Depending on the ratio between these

two compounds, lead white can be classified into different subtypes, each with different optical properties. Traditional methods to investigate lead white subtypes involve invasive sampling on a microscopic scale, which introduces problems of paint damage and representativeness. Different subtypes of lead white were identified using non-invasive MA-XRPD and their presence was confirmed with μ-XRD, implying that Vermeer was highly discriminatory in his use of lead white.

The second case study concerns *The Night Watch* (1642) by Rembrandt. Reflection MA-XRPD revealed the unusual presence of lead(II) formate, $Pb(HCOO)_2$ in lead white-rich areas. Until now, this compound was never reported in historical oil paints. To gain insight into the presence of this rare compound, a chemical pathway was explored through model oil paint media prepared by heating linseed oil and lead(II) oxide (PbO) drier as described in 17th century recipes. Both lead(II) formate and lead(II) formate hydroxide $Pb(HCOO)(OH)$ were detected in these model samples, which strengthens the hypothesis of lead drier reactivity in oil paintings and provides an explanation for the identification of lead(II) formate by MA-XRPD in lead white-containing areas of *The Night Watch*.

3.1 Macroscopic X-ray powder diffraction imaging reveals Vermeer's discriminating use of lead white pigments in *Girl with a Pearl Earring*

Adapted from <u>De Meyer, S.</u>; Vanmeert, F.; Vertongen, R.; van Loon, A.; Gonzalez, V.; Delaney, J.; Dooley, K.; Dik, J.; van der Snickt, G.; Vandivere, A.; Janssens, K. Macroscopic X-ray powder diffraction reveals Vermeer's discriminating use of lead white pigments in Girl with a Pearl Earring. *Sci. Adv.* **2019**, *5*, aax1975.

Contributions of the thesis author: SDM wrote the manuscript with input from all co-authors. SDM performed the MA-XRPD and SR-µ-XRD data acquisition and analysis together with FV.

3.1.1 Introduction

Girl with a Pearl Earring is an iconic oil painting created by the 17th century artist Johannes Vermeer in the collection of the Mauritshuis, The Hague (Figure 3.1-1A). One of the most well-documented (and often recurring) features in Vermeer's paintings is the delicate blend between light and shadow.[1,2] In *Girl with a Pearl Earring*, there is a stark contrast between the bright facial tones and the dark background, while within the *Girl*'s face, a smooth transition from light to dark is present. A pigment used by Vermeer to accentuate this contrast is lead white. Historically, lead white was the most important white pigment used in easel paintings until the 19th century, after which zinc white and titanium white became more dominant.[3] Before the 19th century, lead white was usually produced by the stack process, in which sheets of lead were exposed to vinegar and horse manure.[4] The resulting lead white is typically composed of two crystalline compounds: cerussite (C) ($PbCO_3$) and hydrocerussite (HC) [$2PbCO_3 \cdot Pb(OH)_2$].[5] Adjustments to the synthesis parameters or additional postsynthesis treatments may cause the mass ratio of these two phases to change, leading to a pigment with different physicochemical and optical properties.[6]

Differences in the lead white ratio have an influence on the opacity and brightness of the pigment, while a change in particle size will substantially influence a pigment's covering power, making it either more transparent or opaque. Consequently, investigating the lead white ratio provides insight into both the production process of the pigment and the optical effects the artist intended to express, which is highly relevant information for art historians and conservators. Previous microscopical analysis has already shown that Vermeer (and other artists, e.g., Grünewald) used different types of lead white in their paintings.[7,8]
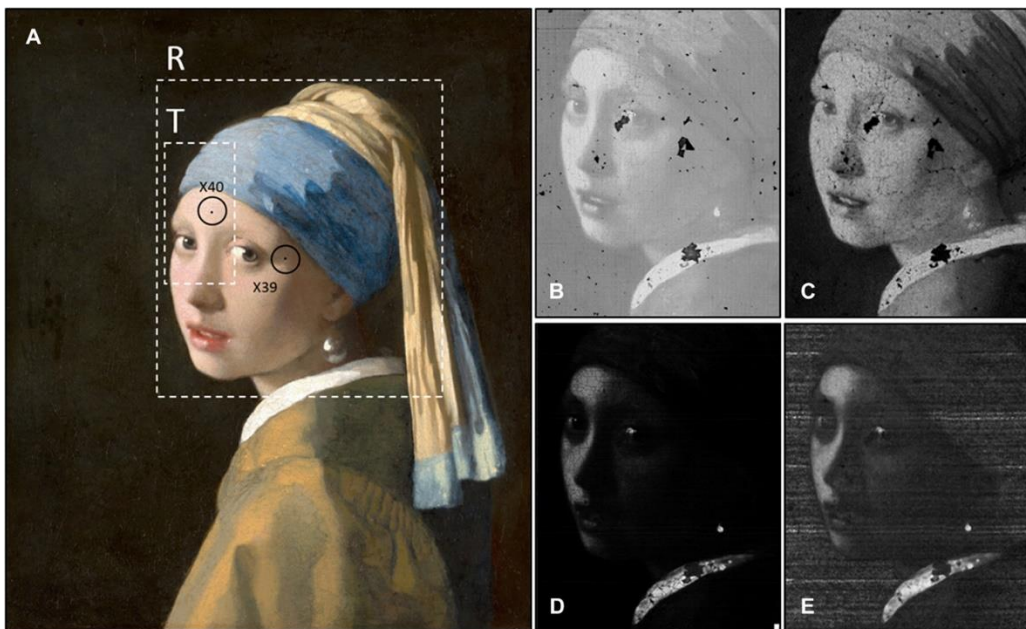
Figure 3.1-1 Comparison of various macroscopic imaging techniques. (**A**) Visual photograph of *Girl with a Pearl Earring* marked with the areas scanned with transmission (T) and reflection MA-XRPD (R). The locations where the paint cross sections X39 and X40 were taken are marked with a circle. (**B**) MA-XRF distribution for Pb-L and (**C**) MA-XRF distribution for Pb-M. (**D**) NIR reflectance imaging spectroscopy distribution displaying the integrated area of the narrow ─OH absorption feature associated with hydrocerussite, centered near 1447 nm, in reflectance units. (**E**) Pseudo absorption of the narrow ─OH absorption feature. Photo credit: René Gerritsen, Art & Research Photography and Mauritshuis.

In the recent past, several synchrotron-based methods of analysis have been used to gain insight into the various types of lead white pigments used by painters. With high-resolution x-ray diffraction, it is possible to precisely estimate the crystal phase composition of paint samples; high lateral resolution x-ray powder diffraction (μ-XRPD) allows for spatial imaging of crystalline phases present in complex multilayered cross sections of paint samples.[6,9] However, the major drawback of these two techniques is that they require invasive sampling on the original painting, an undertaking that either is not permitted or is limited to those locations on the painting where the paint layer already shows signs of damage. Solely relying on a limited number of samples of micrometric dimensions to obtain information on a painting's material composition as a whole introduces problems of representativeness.

To bypass these problems of invasive sampling and representativeness, non-invasive and non-destructive mobile methods of analysis, capable of imaging paintings on the macroscopic scale, have been developed in recent years. Macroscopic x-ray fluorescence (MA-XRF), for example, has been extensively used as an imaging technique to obtain two-dimensional (2D) elemental distributions.[10,11] While MA-XRF is capable of visualizing the presence of the element lead both at the surface and deeper within the painting, it is unable to differentiate between compounds of a similar or identical elemental composition that feature a different crystal structure, such as cerussite and hydrocerussite. Macroscopic imaging spectroscopy techniques that have been used in the field of cultural heritage to provide information on the molecular level include macroscopic reflectance Fourier transform infrared (MA-rFTIR) spectroscopy (4000 to 400 cm^{-1}) and near-infrared (NIR) reflectance imaging spectroscopy (14,285 to 4000 cm^{-1}).[12,13] Unfortunately, the applicability of MA-rFTIR is strongly limited when a varnish layer is present, while NIR reflectance imaging

spectroscopy cannot detect the presence of cerussite. Raman spectroscopy has been previously used to investigate the presence of lead carbonates.[14] The application of Raman spectroscopy on oil paintings is, however, limited due to the interference from molecular fluorescence signals originating from the oil.

A relatively unknown technique in the field of cultural heritage is macroscopic x-ray powder diffraction (MA-XRPD). MA-XRPD scanning provides the option of faster imaging compared to previously developed portable XRPD instruments. These portable devices can be considered as an adequate alternative to sampling for investigating immovable objects such as mural paintings or outdoor sculptures, but their long acquisition time (20 to 60 min) limits their use to point-by-point investigations.[15,16] While its microscopic analog (μ-XRPD) is mostly used at synchrotron facilities to examine minute paint samples, MA-XRPD exploits low-power x-ray sources and can be used for non-invasive in situ analysis.[17,18] MA-XRPD combines the high specificity and imaging capabilities of μ-XRPD with the macroscopic scale of the aforementioned techniques, making it a suitable method for differentiating and quantifying various types of lead white on large artworks. MA-XRPD has been used in the recent past for visualizing the distributions of two types of chrome yellow, $PbCrO_4$ and $PbCr_{1-x}S_xO_4$, on the painting *Sunflowers* by Vincent Van Gogh.[19] It has also been used for obtaining quantitative information on a 15th century illuminated manuscript (in transmission mode) and a small mock-up painting (in reflection mode).[20,21]

This study aims to shed light on the different types of lead white Vermeer used in *Girl with a Pearl Earring* and to demonstrate the capabilities of MA-XRPD for providing quantitative information on different paint layers in a multilayered painting. For this purpose, next to the painting as a whole, two paint cross

sections were analyzed at a synchrotron facility by means of μ-XRPD, facilitating a direct comparison and interpretation of the macroscopic and microscopic data. The MA-XRPD analysis was conducted as part of an interdisciplinary project to examine *Girl with a Pearl Earring*. The research project *The Girl in the Spotlight* is a joint project of the Mauritshuis and a team of internationally recognized specialists working within the collaborative framework of the Netherlands Institute for Conservation + Art + Science + (NICAS). Within this project, the painting was analyzed with a multitude of techniques, including MA-XRF, NIR reflectance imaging spectroscopy, and MA-XRPD.

The MA-XRPD scanner was used in two different measurement modes: transmission and reflection. In transmission mode (MA-tXRPD), information on the entire stratigraphy of the painting is obtained, while reflection mode (MA-rXRPD) is more sensitive to compounds located close to the surface of the painting (Figure S 3.1-1). A small angle between the incident X-ray beam and the surface of the painting is chosen, resulting in a shallow probing depth that varies strongly depending on the paint matrix: from 10 μm or less for a paint matrix dominated by heavy elements (Pb, Hg, …) up to 50 μm for a matrix mainly composed of light elements (C, O, Ca, Si, …). The advantage of this technique is that only diffraction signals from the superficial layers will substantially contribute to the diffraction pattern. Information from deeper within the paint stratigraphy is blocked by the upper layers. By exploiting the complementary nature of these two measurement modes, a clear estimation of the buildup and composition of the various lead white–containing layers could be attained. This information allowed us to formulate a hypothesis about the way Vermeer overlaid opaque and transparent paint layers to create the face of the *Girl*.

3.1.2 Results and discussion

MA-XRF analysis of the face

MA-XRF imaging was used to obtain elemental maps, including those of Pb-L (Figure 3.1-1B) and Pb-M (Figure 3.1-1C), that visualize the presence of lead throughout the painting. The Pb-L X-ray fluorescence signals are higher in energy and come from deeper within the lead white paint stratigraphy (<200 μm), while the lower energy Pb-M signals originate from layers close to the surface (<10 μm). The Pb-L distribution shows the omnipresence of lead throughout the painting (with the exception of some retouchings). The Pb-M distribution, on the other hand, shows a lower lead abundance in the background area, meaning that most of the lead is located beneath the surface. The stratigraphy of a painting typically consists of a ground layer on which the artist would apply one or more paint layers and a varnish layer. In this case, the low Pb-M and high Pb-L intensity in the dark background implies the presence of a lead-rich ground layer. The Pb-M distribution also shows that there are superficial lead-containing compounds present in every part of the face.

NIR reflectance imaging spectroscopic analysis of the face

NIR reflectance imaging spectroscopy (967 to 1680 nm) enabled mapping of hydrocerussite within the painting, down to (but not including) the ground layer by using the first overtone of ─OH stretching (Figure S 3.1-2).[22] This narrow absorption feature is centered near 1447 nm and, if present, was fitted with a Gaussian function. Figure 3.1-1D shows the integrated area of the hydroxyl group absorption. To more readily compare the NIR reflectance imaging results with those obtained with MA-XRPD and MA-XRF, we converted the map from reflectance (R) to pseudo absorbance (A') units by applying the function $A' = \log(1/R)$ (Figure 3.1-1E). The clear contrast between the left, hydrocerussite-rich

and the right, hydrocerussite-poor part of the face already suggests a relevant difference in composition between both parts of the face. However, since the Pb-M intensity in these areas is similar, the data suggest that the left side of the face contains significantly more hydrocerussite at the paint surface than the right side. Another lead-containing compound must be present in the right part of the face, balancing the total amount of lead in both areas. This hints at the presence of either a cerussite-rich paint and/or secondary Pb-containing product(s) caused by the degradation of lead white. Detection of hydrocerussite by NIR reflectance in the background areas is hindered by a high level of noise, likely caused by the presence of carbon black, which substantially absorbs the hydrocerussite ─OH band.

Synchrotron μ-XRPD analysis of paint cross-sections

Two paint samples were taken from the *Girl*, prepared as cross sections and analyzed with μ-XRPD at beamline P06 of the PETRA III facility: one sample (X40; see Figure 3.1-1A) originated from a bright pink flesh tone area, rich in hydrocerussite and a second sample (X39; see Figure 3.1-1A) came from a shadow tone area, poor in hydrocerussite. The sample locations were carefully selected on the basis of the results obtained from the macro-imaging techniques to support and complement the findings of MA-XRPD. In Figure 3.1-2, the distribution maps of the most relevant identified crystalline phases are shown for both samples. The scan parameters and the dimensions of the scanned area for both cross sections are listed in Table S 3.1-1.

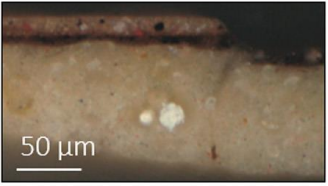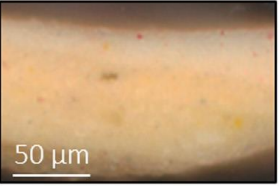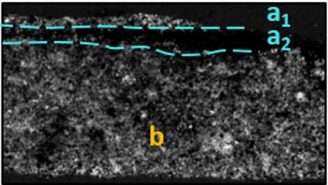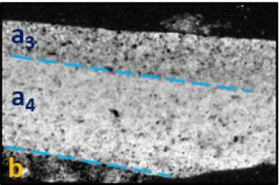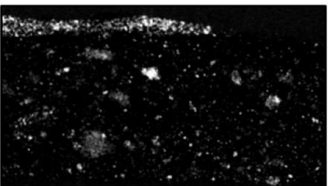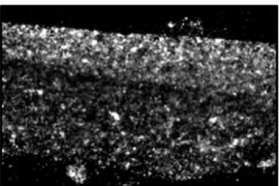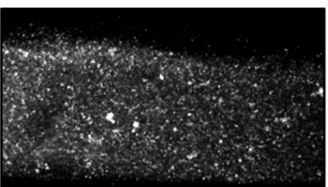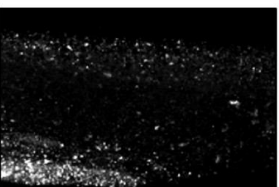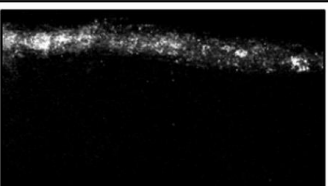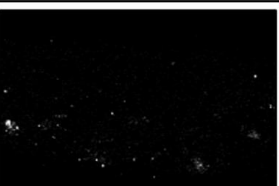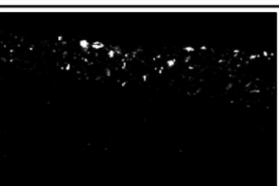|	X39 Shadow tones	X40 Bright tones
Photograph		
Hydrocerussite weight fraction		
Cerussite weight fraction		
Calcite scaling		
Palmierite scaling		
Cinnabar scaling		

Figure 3.1-2 Crystalline phase distributions obtained by μ-XRPD for two paint cross-sections collected from the *Girl's* face. For hydrocerussite and cerussite, the weight fractions were calculated in every pixel of the image. For calcite, palmierite, and cinnabar, a scaling parameter is displayed instead to improve the qualitative readability of the maps. Brighter areas indicate a higher weight fraction or scaling parameter value. The intensity was scaled independently for each image to improve readability: Intensities should not be directly compared. The scan parameters and size of the scanned areas are shown in Table S 3.1-1.

In sample X39, from a shadow tone on the cheek of the *Girl*, three layers could be identified by μ-XRPD. The top layer (a_1) is very thin (~10 μm) and appears to be rich in lead white with some traces of vermillion (cinnabar, HgS). Beneath this upper paint layer, a second layer (a_2) consisting mainly of palmierite ($PbSO_4 \cdot K_2SO_4$) is present: This is a secondary reaction product that can be associated with the degradation of lead white in the presence of lake pigment substrates that contain sulfur.[23,24] Below these two thin layers, the ground layer (b, ~100 μm in thickness) is present, which contains a mixture of mostly chalk (calcite, $CaCO_3$) with some lead white (both hydrocerussite and cerussite).

To determine whether Vermeer used the same lead white paint for the upper paint layers and ground layers, we required a quantitative approach. By using whole-pattern fitting, the relative abundance of hydrocerussite within the lead white was calculated as $w_{HC}/(w_{HC} + w_C)$ by using the relative weight fractions (w) of hydrocerussite (HC) and cerussite (C). The relatively large size of the hydrocerussite and cerussite particles with respect to the incoming X-ray beam leads to diffraction patterns that are dominated by intense diffraction spots; this prevents us from reliably calculating the weight fractions of the different components in each individual pixel. Averaging the XRPD response of multiple grains over tens or hundreds of pixels, however, leads to a cumulative powder-like diffraction pattern with a more uniform orientation, significantly increasing the accuracy of the calculated weight fraction to within an error of 10%. By

repeating this procedure for every layer, the $w_{HC}/(w_{HC} + w_C)$ ratio for every lead white–containing layer in the stratigraphy can be obtained. In the case of sample X39, a ratio value of 0.48 ± 0.05 is obtained for the top layer (a_1), while the ground layer (b) contains a lead white paint with a $w_{HC}/(w_{HC} + w_C)$ ratio of 0.83 ± 0.08.

A similar qualitative and quantitative analysis was made for sample X40, taken from a bright area on the forehead of the *Girl*. Initially, only two separate layers were observed with μ-XRPD: a fairly thick (~100 μm) top layer (a) consisting of mostly lead white with some vermillion, while underneath part of the ground layer (b) is present, consisting of a mixture of mostly calcite and some lead white. In this sample, no palmierite was found, aside from a few grains deep inside layer (a_4). After calculating the weight fractions of the lead carbonates, it became clear that layer (a) can be further subdivided in a thin top layer (a_3, ~30 μm) and a thicker bottom layer (a_4, ~70 μm). The upper layer has a $w_{HC}/(w_{HC} + w_C)$ ratio of 0.65 ± 0.07, while the lower layer features a ratio of 0.79 ± 0.08. In this sample, the ratio for the ground layer (b) could not be accurately estimated because of the limited amount of lead white present in the small part of this layer that was analyzed. A clear contrast between the layers a_1 and a_2, found in sample X39, is visible in the distribution maps of hydrocerussite and cerussite (Figure 3.1-2). These microscopic distribution maps are consistent with the hypothesis that Vermeer painted the left (bright) and right (shadow) parts of *the Girl*'s face using a different (combination of) lead white paint.

Reflection mode MA-XRPD analysis of the face

Figure 3.1-3B-F shows the distributions of the compounds identified by means of MA-rXRPD (see Table S 3.1-1 for details of the reflection scan). It is clear that hydrocerussite and cerussite are prominently present in the upper layers of

the face, whereas in the dark background of the painting, calcite and palmierite are the dominant species. However, a small amount of hydrocerussite and cerussite is still detectable in the dark background areas. Furthermore, vermillion was used extensively in the *Girl*'s lips and only sparsely in the pink flesh tones of her face. Closer inspection of the hydrocerussite and cerussite images reveals some clear differences: The presence of hydrocerussite is more prominent on the left (bright) side of the face than on the right (shadow) side, while cerussite has a mostly uniform distribution across her entire face.
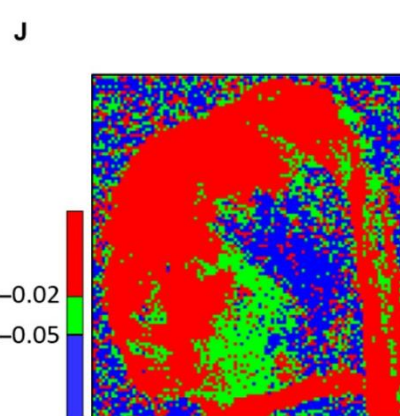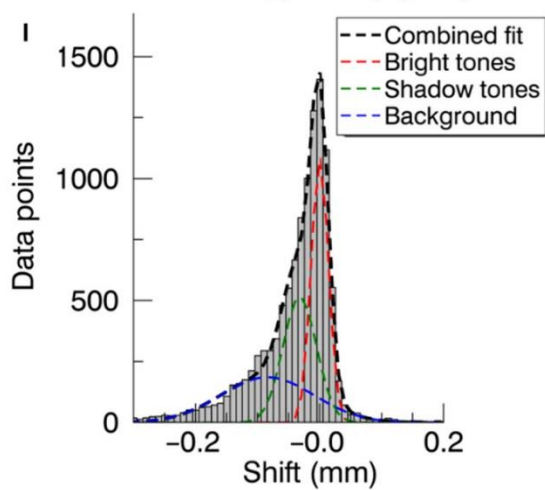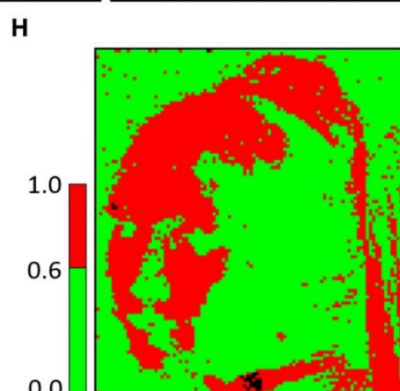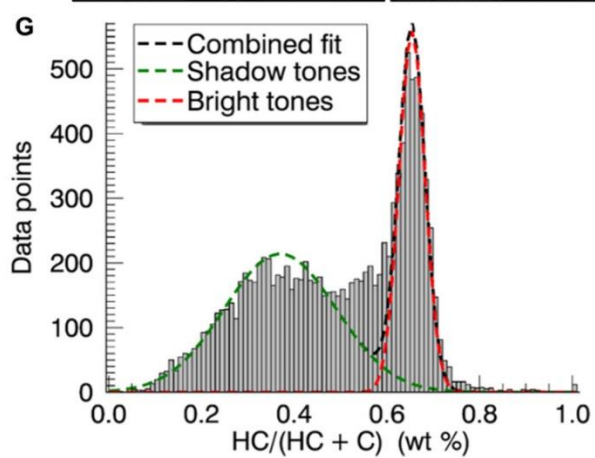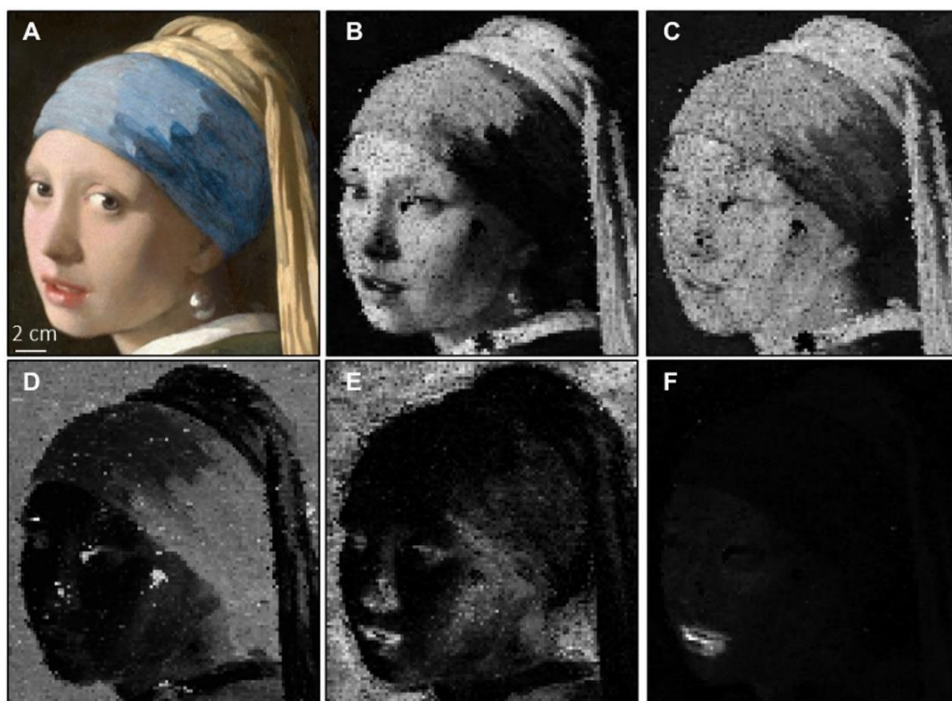
Figure 3.1-3 Results obtained with MA-XRPD reflection mode. (**A**) Optical photograph of the analyzed area. (**B** to **F**) Distribution images obtained with reflection MA-XRPD showing the scaling parameter for every pixel. Higher scaling parameter values are represented by a brighter color. (B) Hydrocerussite, (C) cerussite, (D) calcite, (E) palmierite, and (F) cinnabar. (**G**) Histogram for the $w_{HC}/(w_{HC} + w_C)$ ratios. The black dashed line represents the combined contribution of both Gaussian curves. (**H**) Corresponding RGB image for (G). (**I**) Histogram for the average depth of hydrocerussite relative to the average depth of cerussite. (**J**) Corresponding RGB image for (I). Images were scaled independently of each other: Intensities should not be directly compared. Photo credit: René Gerritsen, Art & Research Photography and Mauritshuis.

Again, the weight fractions for both components were calculated to obtain a more quantitative understanding of the lead white ratios in the scanned area. Another advantage MA-rXRPD has over synchrotron μ-XRPD is that a relatively large X-ray beam (1 mm × 0.2 mm) is used for imaging. In this way, many crystals are irradiated at once, resulting in powder-like patterns. The weight ratio calculated for each individual pixel will therefore be less prone to errors than is the case for the μ-XRPD data; however, an error of approximately 5 to 10% on the individual weight fractions should still be considered, especially in the dark background areas that only show low quantities of both hydrocerussite and cerussite.

In Figure 3.1-3G, a histogram of $w_{HC}/(w_{HC} + w_C)$ for every pixel of the scanned area is shown. A clear bimodal distribution is visible: a broad distribution with a mean $w_{HC}/(w_{HC} + w_C)$ ratio of 0.37 (as estimated using the Gaussian curve shown in green) and a narrow distribution with a mean $w_{HC}/(w_{HC} + w_C)$ ratio of 0.65 (as estimated using the Gaussian shown in red). When visualizing the location of these two groups in the distribution image (Figure 3.1-3H), it becomes apparent that they are linked to distinct features in the *Girl*'s face. The broad distribution with a lower mean $w_{HC}/(w_{HC} + w_C)$ ratio (0.37) is correlated with the shadow tones in the face and the background of the painting, while the narrow group with a higher mean $w_{HC}/(w_{HC} + w_C)$ ratio (0.65) matches with the brighter tones. The large distribution width of the lead white ratios in the background originates from

the large error induced by the small quantities of both hydrocerussite and cerussite in this region and because of strongly differing contributions of the hydrocerussite-rich ground layer to the collected diffraction data. Where the thickness of the upper paint layer varies laterally, either a larger (where the paint layer is thin) or smaller (where the paint layer is thick) volume of the ground layer will be probed, increasing the width of the Gaussian distribution in the shadow region.

These findings strongly suggest that there might be a cerussite-rich layer present at the surface in the shadow areas that causes the low $w_{HC}/(w_{HC} + w_C)$ ratio, as evidenced in sample X39. Further evidence to support this claim can be found by considering the displacement parameter of the XRPD patterns obtained after whole-pattern fitting. This displacement is indicative of a slightly larger or smaller distance of the diffracting material relative to the paint surface; this information can be used to roughly estimate the relative depth below the painting surface of individual compounds within a multilayered stack of paint strata.[20] This phenomenon is visualized and explained in more detail in Figure S 3.1-3. In this case, the average depth of the center of mass for hydrocerussite is considered relative to the average depth of the center of mass for cerussite. Figure 3.1-3I shows a histogram for the depth of hydrocerussite relative to that of cerussite for every data point in the scan. The negative values indicate that, within the probed region, the average depth at which cerussite is located is closer to the surface of the painting than the average depth at which hydrocerussite is present. The histogram data can be described by three Gaussian contributions: one corresponding to no difference in depth (red), another representing a medium depth difference (green), and a third one showing a large depth difference (blue). These three distributions are shown in the RGB map (Figure 3.1-3J). The bright parts of the *Girl*'s face correspond to a relative depth of approximately 0,

meaning that cerussite and hydrocerussite are located at a similar depth within the probed region. When taking the μ-XRPD results from this region (sample X40; Figure 3.1-2) into account, it can be assumed that only the upper layer was probed by MA-rXRPD in which hydrocerussite and cerussite are homogeneously mixed. For the shadow part of the *Girl*'s face, the relative depth becomes more negative, indicating that cerussite is, on average, located closer to the surface than hydrocerussite. When compared to the corresponding μ-XRPD results (sample X39; Figure 3.1-2), it can indeed be envisioned that not only the very thin upper layer but also the poorly attenuating organic layer below and the upper part of the hydrocerussite-rich ground layer were probed with MA-rXRPD. The attenuation coefficient of the upper layer is estimated to be 50 to 100 $cm^2\, g^{-1}$ (dependent on the organic fraction within the upper layer: binding medium, red lakes, carbon black, …), which translates to a probing depth of approximately 10 to 20 μm, i.e. larger than the size of the upper layer itself. In the shadows, the center of mass of hydrocerussite will therefore be deeper within the sample than in the bright parts. In addition, in the dark background, the relative depth is negative. This is consistent with the presence of cerussite in the upper glaze layer (Figure 3.1-3G), a thick black organic layer and a hydrocerussite-rich ground layer. The prior observations suggest that the paint layer buildup in the bright areas differs from the shadow areas of the *Girl*'s face and from the dark background area surrounding the face: In the shadow tones, a thin upper layer containing cerussite-rich lead white is present, while in the bright areas, hydrocerussite and cerussite are homogeneously mixed.

Transmission MA-XRPD analysis of the face

In transmission mode (MA-tXRPD), the x-ray beam probes the entire depth of the paint stratigraphy. The resulting diffraction patterns are consequently

dominated by diffraction signals from crystalline materials with a high abundance in the probed volume (usually components from the thick ground layer) and a high scattering power (usually Pb- and Hg-containing pigments). Thus, MA-tXRPD is less sensitive than MA-rXRPD for identifying superficial compounds (present in thin paint layers or resulting from degradation phenomena at the surface), as the obtained diffraction signals are averaged out over the entire depth of the painting. Hence, MA-tXRPD is well suited for obtaining quantitative information on the composition of the ground layer.

The details of the MA-tXRPD scan are summarized in Table S 3.1-1. By means of MA-tXRPD, only hydrocerussite, cerussite, and calcite are detected in the analyzed area (Figure 3.1-4A-D). These three compounds make up most of the ground and paint layers and therefore dominate the transmission diffraction data. In Figure 3.1-4D, the calcite shows a (mostly) uniform presence over the entire analyzed area, confirming the presence of a calcite-rich ground layer. Although the exact thickness and buildup of the paint layers are only precisely known at the locations where samples were taken, it is assumed that the bright and shadow areas feature a stratigraphy similar to their corresponding samples. The MA-tXRPD images of hydrocerussite and cerussite (Figure 3.1-4B-C) suggest that more lead white paint is present in the bright parts of the face (such as in the forehead) than in the shadow tones of the face (e.g., around the eyes) and the dark background. The $w_{HC}/(w_{HC} + w_C)$ ratio in these three areas only seems to vary slightly, ranging from an average value of 0.75 ± 0.05 in the bright tones to 0.82 ± 0.06 in the shadow tones and 0.88 ± 0.04 in the background (Figure 3.1-4E). The histogram of the $w_{HC}/(w_{HC} + w_C)$ ratio can be resolved into four separate contributions: a pixel group (red) representing the bright tones, a second group (green) corresponding to the shadow areas, a third group (blue) linked to the

background, and finally, a black group indicating a damaged area under the *Girl*'s left eye.
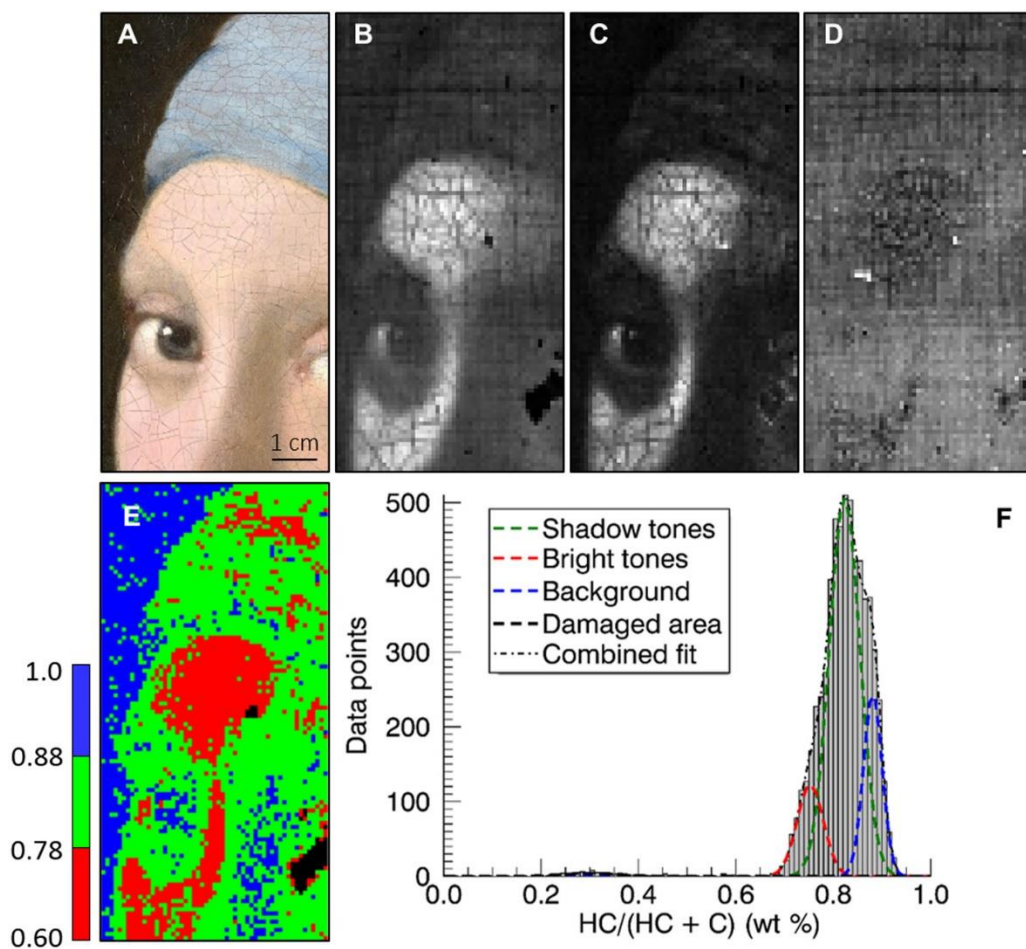
Figure 3.1-4 Results obtained by MA-XRPD transmission mode. (**A**) Optical photograph of the analyzed area (B to D) Distribution images obtained with MA-tXRPD showing the scaling parameter for every pixel. Higher scaling parameters are represented by a brighter color. Images were scaled independently of each other: Intensities should not be directly compared. (**B**) hydrocerussite, (**C**) cerussite, and (**D**) calcite. (E) False color image and (**F**) Histogram showing the $w_{HC}/(w_{HC} + w_C)$ ratio. Photo credit: René Gerritsen, Art & Research Photography and Mauritshuis.

At first sight, these findings seem to conflict with the results derived from the MA-rXRPD data. The lead white paint used for the bright areas of the face was

found to be rich in hydrocerussite [$w_{HC}/(w_{HC} + w_C) = 0.65 \pm 0.06$] in reflection mode compared to transmission mode (0.75 ± 0.05). For the shadow tones and background, lead white rich in cerussite was found in reflection mode (0.37 ± 0.20), while in transmission mode, a lead white rich in hydrocerussite was found for the shadow tones (0.82 ± 0.06) and for the background (0.88 ± 0.04). It is, however, important to take into account that MA-rXRPD probes the paint stratigraphy in a superficial manner (i.e., the upper 5 to 10 μm for concentrated lead white paint), while the complete paint stratigraphy (including the ca. 150-μm-thick ground layer) is probed in transmission mode. Thus, the fairly thin (10 μm or less) cerussite-rich upper paint layer in the shadow tones only has a minor contribution to the transmission diffractogram, resulting in a $w_{HC}/(w_{HC} + w_C)$ ratio that largely mirrors that of the hydrocerussite-rich ground layer. On the other hand, in the bright areas of the face, the contribution of the thick top layer [with $w_{HC}/(w_{HC} + w_C) = 0.65 \pm 0.06$] is much more substantial. Given the fact that this thick layer has a lower $w_{HC}/(w_{HC} + w_C)$ ratio than the ground layer, the resulting $w_{HC}/(w_{HC} + w_C)$ ratio of the entire stratigraphy in the bright areas will be lower than in the shadow areas.

Combining μ- and MA-XRPD

By combining the transmission and reflection $w_{HC}/(w_{HC} + w_C)$ ratios obtained with XRPD imaging at the macroscopic and microscopic scale, a lead white layer structure can be proposed for three different regions in *Girl with the Pearl Earring*: the bright and shadow flesh tone areas and the background area. Furthermore, the μ-XRPD analyses allow us to verify our assumptions based on the MA-XRPD data and elucidate the possibilities and limitations of this technique (Figure 3.1-5 and Table 3.1-1).

A

Shadow tones	Bright tones	Background
	0.65 ± 0.07	
0.37 ± 0.20 **Palmierite**	0.81 ± 0.08	0.37 ± 0.20 (Incl. palmierite)
0.88 ± 0.04 Ground	0.88 ± 0.04 Ground	0.88 ± 0.04 Ground

B

$w_{HC}/(w_{HC} + w_C)$

0   1
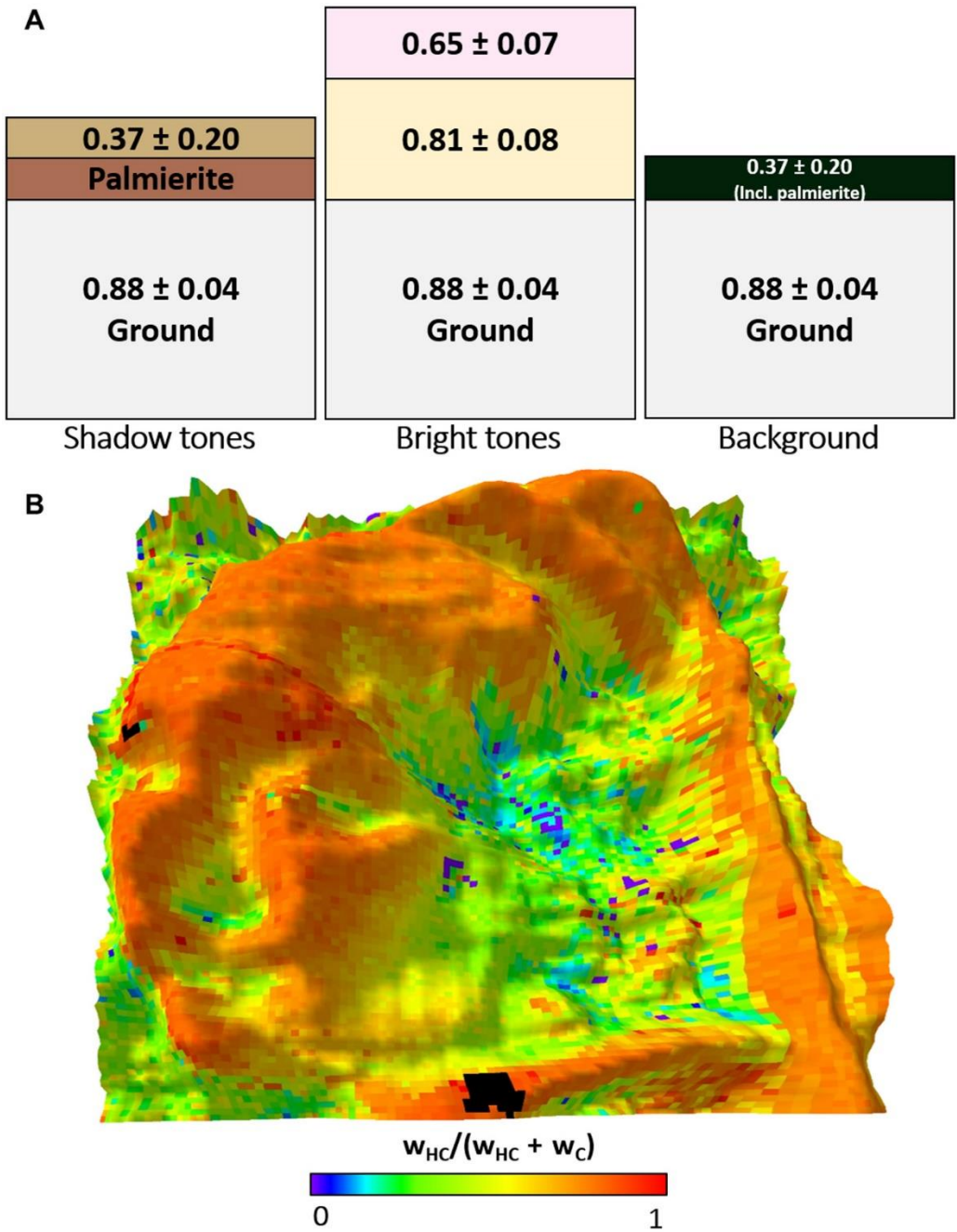
Figure 3.1-5 Combined results of macro- and micro-XRPD. (**A**) Proposed stratigraphy for the lead white paint and ground layers based upon the MA-XRPD (transmission and reflection) and μ-XRPD data for the shadow flesh tones, bright flesh tones, and dark background. In each layer, the corresponding $w_{HC}/(w_{HC} + w_C)$ ratio is indicated.

Layer thickness is not to scale. (**B**) 3D image showing the relation between $w_{HC}/(w_{HC} + w_C)$ ratio (ranging from 0 to 1, black indicates areas without lead white) and the relative depth of hydrocerussite compared to cerussite based on the MA-rXRPD data. A larger height indicates a smaller to no measured difference in depth between hydrocerussite and cerussite (and thus the presence of a homogeneous lead white mixture at the surface), while a lower height indicates the presence of a larger difference between hydrocerussite and cerussite (and thus the presence of a hydrocerussite-rich layer below a cerussite-rich layer).

Table 3.1-1 Overview of the lead white ratios for every (set of) layer(s) analyzed with the different XRPD methods. For MA-XRPD an error of $\pm 2\sigma$ is used, for μ-XRPD a relative uncertainty value of $\pm 10\%$ is cited (see Materials and Methods).

Area	Technique	Layer(s)	$w_{HC}/(w_{HC}+w_C)$
Bright flesh tones	μ-XRPD	Upper (a3)	0.65 ± 0.07
		Lower (a4)	0.79 ± 0.08
		Ground (b1)	-
	MA-tXRPD	All layers	0.75 ± 0.05
	MA-rXRPD	Superficial	0.65 ± 0.06
Shadow flesh tones	μ-XRPD	Upper (a1)	0.48 ± 0.05
		Lower (a2)	-
		Ground (b2)	0.83 ± 0.08
	MA-tXRPD	All layers	0.82 ± 0.06
	MA-rXRPD	Superficial	0.37 ± 0.20
Background	MA-tXRPD	All layers	0.88 ± 0.04
	MA-rXRPD	Superficial	0.37 ± 0.20

The dark background was analyzed with MA-tXRPD to gain insight into the composition of the ground layer. The lead white in the ground layer is heavily diluted within a calcite matrix, and the MA-tXRPD results show that the average ratio of chalk to lead white is 0.75 ± 0.08, a composition that is assumed to be constant throughout the entire painting. The average $w_{HC}/(w_{HC} + w_C)$ ratio of the ground layer is estimated to be 0.88 ± 0.04. In reflection mode, it was shown that the paint layers in the background contain a very small amount of cerussite-rich lead white. The contribution of these paint layers to the $w_{HC}/(w_{HC} + w_C)$ ratio obtained in transmission mode can therefore be neglected. Therefore, we consider the $w_{HC}/(w_{HC} + w_C)$ ratio obtained in transmission mode for the background to be a good estimate of the lead white composition used for the ground layer of the painting.

In the shadow tones of the face, a lead white top layer of $w_{HC}/(w_{HC} + w_C) = 0.37 \pm 0.20$ can be distinguished by means of MA-rXRPD, while MA-tXRPD provides a ratio of 0.82 ± 0.06 for the entire stratigraphy. This latter ratio is similar to that of the ground layer, indicating that the upper cerussite-rich layer must be thin. This is confirmed by the μ-XRPD analysis (Figure 3.1-2). Given that the typical $w_{HC}/(w_{HC} + w_C)$ ratio for lead white obtained from a 17th century stack synthesis is approximately 0.70, the presence of this thin cerussite-rich paint layer is noteworthy.[6]

In the literature, two hypotheses have been proposed through which enrichment of cerussite can take place in lead white pigments: Either a longer corrosion time was used during the synthesis of lead white (allowing for the conversion of hydrocerussite to cerussite) or a postsynthesis treatment of the lead white in an acidic environment has taken place.[6] Despite the fact that a hydrocerussite-rich

paint is easier to apply and creates a sharper impasto, Vermeer seems to have consciously used a cerussite-rich paint.[25]

The most important factor in determining the optical properties of lead white paint, however, is the particle size, which is strongly linked to the opacity of the paint. A larger particle size ensures a higher covering power and a higher opacity, while a smaller particle size achieves a more transparent effect. One method used in the 17th century to allow for particle size selection involves washing and decanting.[25] A different 17th century procedure for obtaining lead white paint with a small particle size was an acidic postsynthesis treatment carried out by washing and grinding the pigment in vinegar.[6] Preexisting crystallites are dissolved and recrystallized as small cerussite particles. This process not only causes a reduction in the particle size but it also increases the proportion of cerussite due to the instability of hydrocerussite in an acidic environment. As the proportion of hydrocerussite decreases, so do the opacity and brightness, albeit slightly. Hydrocerussite crystals, shaped like hexagonal platelets, recline better under brush strokes than the elongated rhombohedra cerussite crystals, forming a reflective layer of similarly oriented platelets. This results in a higher covering power of the pigment and, consequently, in a (slightly) higher opacity of hydrocerussite-rich paint[26,27]. The combination of these two effects may have motivated Vermeer to use a cerussite-rich paint to accentuate the contrast between the darker, cerussite-rich zones and the brighter, hydrocerussite-rich areas of the painting. Previous analysis of cross sections from the clothing has also indicated that Vermeer applied a thick dark underlayer and a thin transparent upper layer in the dark areas, while in the bright areas, he made use of a thin dark underlayer and a thick opaque upper layer.[28] It is well known that Vermeer intentionally varied his underlayers to achieve a variety of color effects in his paintings, explaining his use of transparent materials at the surface.[29] A

stratigraphy of all the lead-containing layers in the shadow areas is suggested in Figure 3.1-5A.

A similar hypothesis can be suggested for how Vermeer created the dark background. Besides the ground layer, a small amount of lead white in the top layer [with $w_{HC}/(w_{HC} + w_C) = 0.37 \pm 0.20$] is present in this area along with the secondary formation product palmierite. These findings align well with an earlier paint sample examination of *Girl with a Pearl Earring*, in which it was found that the background areas consist of a superficial transparent glaze layer, containing organic dyes (indigo and weld), chalk, alum, lead white, and red ochre, on top of a dark underpaint.[28] It is assumed that Vermeer originally created a translucent dark green background, made darker and given depth by the underpaint. This would explain the presence of the cerussite-rich lead white in the glaze layer, which is associated with more translucent optical properties. A possible lead white stratigraphy for the background area is suggested in Figure 3.1-5A.

In the bright flesh tones of the *Girl* (Figure 3.1-5A), MA-rXRPD confirms the presence of a top layer with a lead white ratio of 0.65 ± 0.06 (Figure 3.1-3G, red curve). The MA-tXRPD analysis yields a ratio of 0.75 ± 0.06. A logical conclusion based on these data would be that the paint stratigraphy consists of a layer with $w_{HC}/(w_{HC} + w_C) = 0.65$ on top of one with $w_{HC}/(w_{HC} + w_C) = 0.88$. The μ-XRPD analysis, however, revealed the presence of a third layer, in between the top (pink) and ground layers, with a similar lead white ratio as the ground layer in the absence of calcite (Figure 3.1-5A).

Figure 3.1-5B highlights the spatial correlation between the hydrocerussite/cerussite ratio in the upper paint layer(s) (indicated by a false color range) and the average depth difference between hydrocerussite and

cerussite, both types of information obtained with MA-rXRPD, (indicated by the height of the relief). In the elevated areas, the relative depth is zero, which means that hydrocerussite and cerussite are mixed homogeneously and present at the surface. A hydrocerussite-rich lead white paint has been applied in these areas. In the low-lying areas, which indicate a large difference in depth between hydrocerussite and cerussite, a cerussite-rich lead white paint has been applied on top of a hydrocerussite-rich layer. These observations are fully consistent with the stratigraphy and the μ-XRPD maps of hydrocerussite and cerussite shown in Figure 3.1-2.

As already pointed out, an important limitation of MA-XRPD in its present form is that it is unable to resolve complex layer sequences into individual contributions. The top layer can be analyzed directly in reflection mode, but in transmission mode, only information on the sum of all the layers becomes available. This highlights the need for other, more discriminatory techniques such as μ-XRPD to differentiate between individual layers. The question remains, of course, why Vermeer decided to use two different types of hydrocerussite-rich paint in the bright part of the face. One possible explanation is that Vermeer opted for a higher-quality lead white for the surface paint by using a pigment that was more intensely washed and ground after its synthesis, increasing the proportion of cerussite.

3.1.3   Conclusion

In this study, the information obtained with non-invasive and in situ MA-XRPD in transmission and reflection modes was used to propose a stratigraphy for the different lead white layers present in the various regions of Girl with a Pearl Earring, providing both qualitative and quantitative information on the macroscopic scale. An accurate and representative estimation of three different

types of lead white used by Vermeer was obtained using MA-XRPD. To verify and complement the findings from the macroscopic analysis, we analyzed several microscopic cross sections with μ-XRPD. While μ-XRPD provides less accurate and representative quantitative information, it proved necessary in revealing additional layers that could not be detected with MA-XRPD for complex multilayered paint systems. Consequently, a combination of both μ-XRPD and MA-XRPD proved to be highly useful in proposing a hypothesis about how Vermeer used different types of lead white in *Girl with a Pearl Earring*.

At least four distinct types of lead white paint have been used in the analyzed areas of *Girl with a Pearl Earring*. The ground layer consists of lead white paint with a hydrocerussite-rich composition in a matrix of chalk. The bright parts of the face contain two hydrocerussite-rich paints: one hydrocerussite-rich paint mixed with vermillion and one very hydrocerussite-rich paint in the layer below. Last, in the shadow areas and in the background, Vermeer used a transparent lead white paint rich in cerussite, presumably to induce a sense of contrast with the bright parts of the painting. This suggests that Vermeer was well aware of the distinctive optical properties of various types of lead white and was highly discriminating in using them in his paintings.

3.1.4   Materials and methods

MA-XRF imaging

MA-XRF maps of the entire painting were collected in two scan sessions using the Bruker M6 Jetstream.[11] The instrument consists of a measuring head equipped with a 30 W rhodium-target microfocus x-ray tube, a polycapillary lens, and an XFlash silicon drift detector with a beryllium window (energy resolution of <145 eV at Mn-K$_\alpha$). By slowly moving the measuring head on the XY motorized stage, the painting was scanned pixel by pixel, line by line. By

recording the emitted x-ray fluorescence radiation, the chemical elements present in the paint (associated with specific pigments) can be identified. With the Bruker M6, only elements heavier than silicon can be detected. Scans were carried out at 50 kV and a current of 600 μA, with a 400-μm step size and a dwell time of 125 ms. The distance between the scanning head and the paint surface was set at c. 1 cm, corresponding to an x-ray spot size of c. 300 μm. All data were collected with the Bruker M6 Jetstream software package. The acquired data cubes were then exported as raw files and processed and stitched using PyMca and the in-house developed Datamuncher software.[30,31]

Reflectance imaging spectroscopy

Infrared hyperspectral reflectance image cubes were collected with an optimized whisk broom line-scanning imaging spectrometer (SOC720, Surface Optics Corporation) that uses an InGaAs array (SUI 640SDV, Sensors Unlimited) operating from 967 to 1680 nm with 3.4 nm sampling at an integration time of 33 ms per line.[13] The painting was illuminated with two 125 W 3000 K halogen lamps whose voltage was regulated with a rheostat such that the effective color temperature was approximately 1000 K, giving a light level of approximately 700 lux at the artwork. The image cubes were dark-corrected, flat-fielded, and calibrated to apparent reflectance using diffuse reflectance standards (Labsphere Inc.). The calibrated image cubes were spatially registered using a point-based algorithm, and the resulting spatial sampling was 0.17 mm per pixel.[13,32] The image cubes were processed using MATLAB custom software and ENVI.

MA-XRPD imaging

The imaging experiments on the painting *Girl with the Pearl Earring* were carried out using a laboratory scanning MA-XRPD/MA-XRF scanner, both in reflection and in transmission mode. In transmission mode, a high-brilliance low-

power x-ray microsource (44 W; IµS-Ag^{HB}, Incoatec GmbH, Germany) was used to generate a monochromatic Ag-K$_\alpha$ (22 keV) x-ray beam with a photon flux of 1.1×10^7 photons s^{-1}; a focal diameter of 112 (3) µm, a focal distance of 22 (1) cm, and a divergence of 3.8 (3) mrad. Diffraction signals were recorded using a 2D diffraction detector (PILATUS 200K, DECTRIS Ltd., Germany). The detector was placed perpendicular to the x-ray source with the painting in between. The distance between the x-ray source and the PILATUS detector was set at 22 cm to attain the best possible angular resolution. The distance between the painting and the detector was set at 11 cm, ensuring a sufficiently wide coverage of the angular range. At a distance of 11 cm between the x-ray source and the painting, a beam diameter of approximately 0.4 mm was obtained. Calibration of the setup was performed with a hydrocerussite paint layer on a mock-up panel. The diffraction data collected in transmission mode were corrected for attenuation effects.

In reflection mode, a monochromatic Cu-K$_\alpha$ (8 keV) x-ray source was used. Because of geometrical limitations dictated by the dimensions of the x-ray source, it is undesirable to use an incident angle lower than 10°. The lower primary energy of the Cu source causes diffraction signals to shift toward higher 2θ angles. Low-energy x-rays were also more easily attenuated by the sample, rendering the scanner more sensitive for superficial phenomena. This x-ray source generates a photon flux of 2.9×10^8, has a focal diameter of 142 (2) µm, a focal distance of 20 (1) cm, and a divergence of 2.4 (1) mrad. The painting was placed at a distance of 20 cm from the x-ray source, while the distance between the painting and area detector was <0.5 cm. An incident angle of 10° was chosen to maximize the sensitivity for superficial compounds, leading to a beam with an elliptical footprint of approximately 1×0.2 mm^2. The PILATUS 200K detector was positioned on the same side of the painting as the x-ray source and at an

angle of 40° with the painting surface. To account for topographical variations and curvatures on the painting surface, a laser distance sensor (Baumer Hold., CH) was used to automatically adjust the distance between the x-ray source and the painting for every point of the scan. Calibration of the setup was performed with a calcite paint layer on a mock-up panel.

In both geometries, x-ray fluorescence data can be simultaneously acquired by means of a Vortex silicon drift detector (Hitachi, Japan). A set of three motor stages (25 cm × 10 cm × 10 cm; Newport Corp., USA) are responsible for the movements during the scanning procedure. The x-ray source, PILATUS 200K detector, and Vortex detector were placed on a motorized platform, capable of moving the setup in the XY plane. The artwork was placed on a motorized easel, capable of moving the painting in the vertical (Z) direction.

The regions scanned on the painting in reflection and transmission modes are shown in Figure 3.1-1A. In reflection mode, an area encompassing the entirety of the *Girl*'s face (200 mm × 224 mm) was scanned with an exposure time of 10 s point^{-1} and a step size of 2 mm × 2 mm, chosen larger than the actual beam size (1 mm × 0.2 mm) because of time constraints. In transmission mode, a smaller area (49.5 mm × 99.9 mm) was scanned with an exposure time of 10 s point^{-1} but with a reduced step size of 0.9 mm × 0.9 mm to attain a better spatial resolution.

<u>Microsample analysis</u>

Microscopic paint samples were collected from a light, pink flesh tone (forehead, sample X40) and a shadow tone (cheek, sample X39) from the *Girl*'s face to investigate stylistic and chemical differences. The paint samples were embedded in Technovit 2000 LC mounting resin (Heraeus Kulzer GmbH, Germany) and polished using a sample holder and Micromesh sheets up to grade 12000 (Micro-Surface Finishing Products Inc., Wilton, Iowa, USA).[33] A Zeiss Axio

Imager.A2m microscope equipped with a Zeiss AxioCam MRc5 digital camera was used to examine the polished cross sections, before scanning electron microscopy–energy-dispersive x-ray analysis.

Synchrotron µ-XRPD

To gain more insight into the lead white stratigraphy of the painting, the two cross-sectioned samples (described above) were analyzed with µ-XRPD. The samples were analyzed at beamline P06 (PETRA III, DESY, Germany), a hard x-ray micro- and nanoprobe beamline suited for XRPD imaging experiments on the microscale. A Kirkpatrick-Baez optical system focuses the beam to a diameter of 0.5 µm and a flux of 10^{10} photons s^{-1} with a primary energy of 21 keV. The samples were placed in a sample holder that could be moved in the *XYZ* dimensions across several millimeters. An EIGER X 4M detector (DECTRIS Ltd., Germany) was used to collect the diffraction signals. The sample was placed at a distance of 18 cm in front of the detector, ensuring a sufficiently wide angular range. The collected diffraction data were corrected for attenuation effects.

XRPD data processing

The in-house developed software package XRDUA was used for the processing of all XRPD data. XRDUA provides the necessary tools for extracting crystalline-specific distributions from the large number of 2D diffraction patterns obtained during XRPD imaging experiments.[34] The procedure to obtain compound-specific images from raw diffraction data is visualized in Figure S 3.1-4. The acquired diffraction patterns were converted into 1D diffractograms by means of azimuthal integration after which the crystalline phases present in the diffractogram were identified. After integration, whole-pattern fitting was performed on the 1D diffractograms using a Rietveld model containing all the

identified crystalline phases. The structural information was obtained from the American Mineralogist Crystal Structure Database.[35] The relative positions and intensities of the diffraction peaks for every compound were kept fixed during the fitting, while the angle-independent parameter W of the Caglioti width function was used to model the peak width. Refined values for the scaling, displacement, and width parameters were obtained for each compound. The intensity scaling parameters obtained in each point of the image were used to visualize the spatial distribution of the different compounds (Figure S 3.1-4). A more detailed explanation of the modeling procedure and the functionalities of XRDUA is offered elsewhere[34,36]. Weight fractions were calculated using the aforementioned scaling parameters (Figure S 3.1-4). The 2D distributions shown throughout this work are either based on the global scaling factor or the weight fraction data obtained from this fitting procedure. For the average μ-XRPD weight ratios, an estimated error of ± 10% was used on the basis of the analysis of model samples with a known composition and the SD calculated for different microscopic areas within the same cross-sectional layer. These model samples were created by mixing known amounts of hydrocerussite and cerussite into a homogeneous powder, after which the aforementioned fitting procedure was applied to calculate the weight ratios. For the average weight ratios obtained with MA-XRPD, an error of ±2σ, derived from the Gaussian profiles used in the histograms, was used.

3.1.5   Supporting information
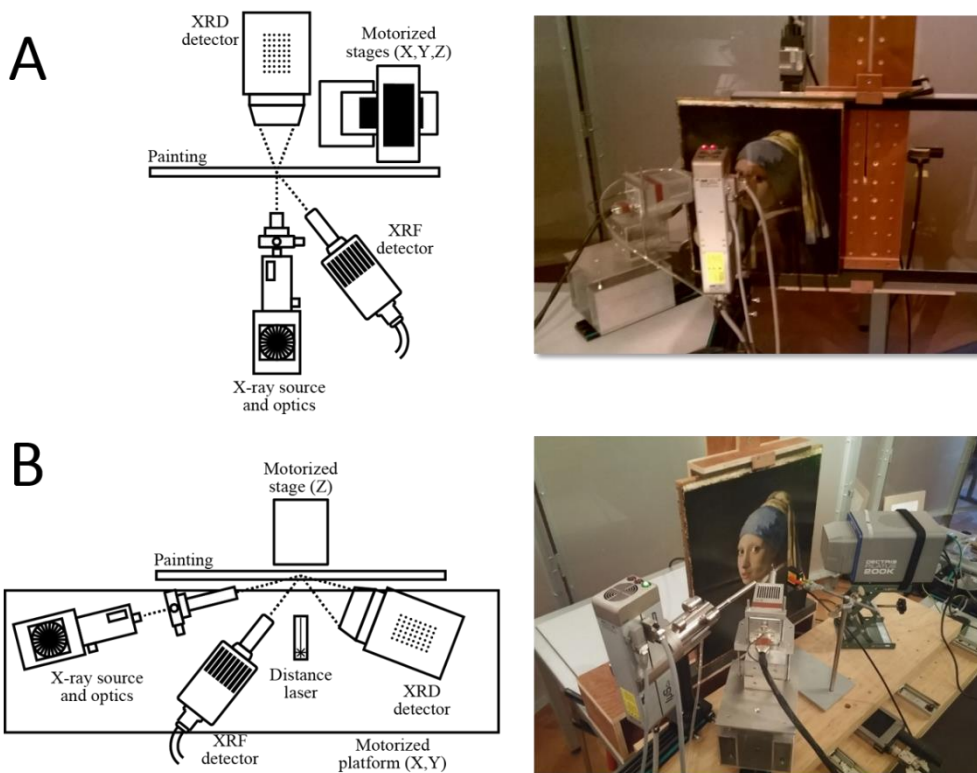
Figure S 3.1-1 Schematics and corresponding visual photographs of the MA-XRPD scanner in (A) transmission mode (B) reflection mode
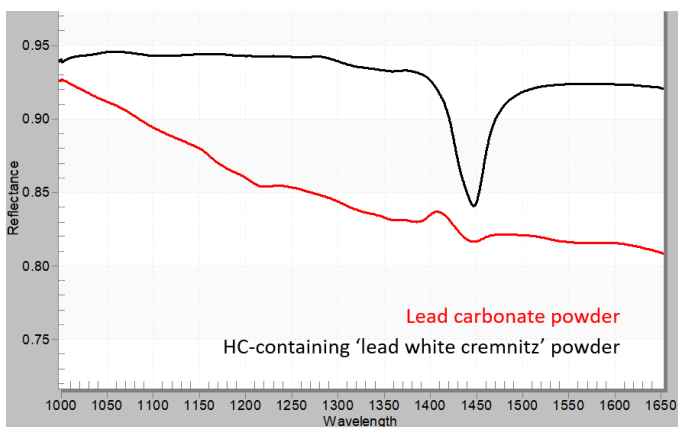
Figure S 3.1-2 NIR reflectance spectra for cerussite (lead carbonate powder) and hydrocerussite (lead white cremnitz)
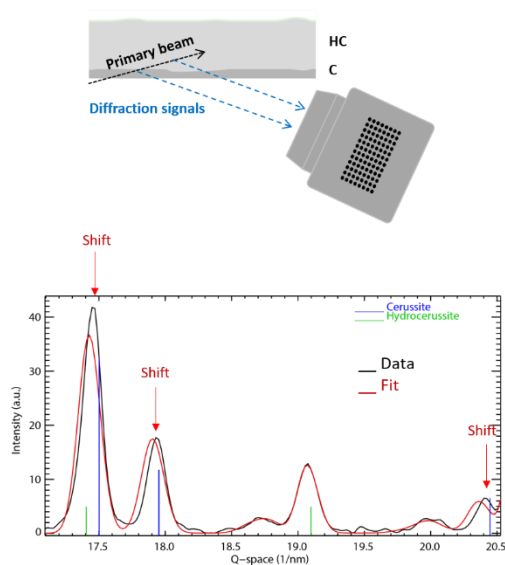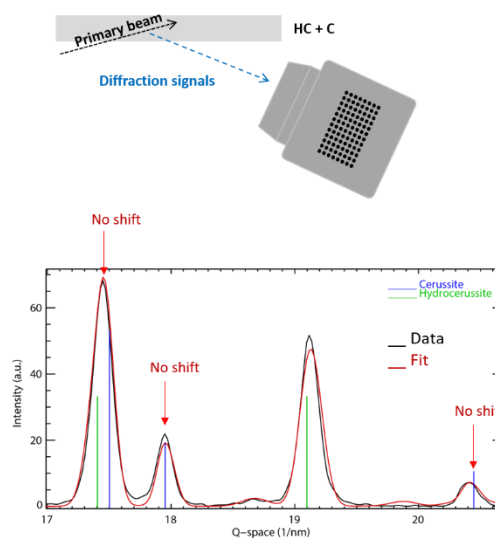
Figure S 3.1-3 Obtaining information on the depth difference of hydrocerussite and cerussite (A) when two different layers are probed (B) when one layer is probed.

The X-ray powder diffraction experiments in this study were performed assuming a single (calibrated) distance between the diffracting material and the detector. This calibration is therefore valid for diffraction signals emerging from the surface. If the signals originate from two different compounds, a relative shift in the diffractogram will occur between the two compounds coming from different depths. If the signals originate from the same compound present at different depths below the surface, peak broadening in the diffractogram will occur.

A displacement parameter can be used in the refinement model to take this diffraction peak shift into account. The displacement value (d_i) is defined as the distance from the calibrated depth, i.e. the sample surface, to the diffraction depth, parallel to the primary beam. By comparing the displacement values of the two compounds, it becomes possible to obtain information on the average

difference in depth (ΔD). γ denotes the incident angle of the X-ray beam with the surface.

$$\Delta D = \sin \gamma . (d_{HC}\text{-}d_C)$$

In this manner the actual depth difference between the center of mass for hydrocerussite and the center of mass for cerussite can be calculated.

In Figure S 3.1-3 two situations relevant to this research are highlighted. In situation A a two-layer system is probed by the X-ray beam: one layer contains cerussite and the other contains hydrocerussite. The diffractogram shows that the diffraction peaks of cerussite are shifted relative to those of hydrocerussite due to the different depths from which those signals originate. The XRPD refinement model can be improved by including the displacement parameter. The values of this parameter (d_{HC} and d_C) can then be used to calculate ΔD.

In situation B only one thick homogeneous layer is probed. No clear shift can be detected, which means the displacement parameters d_{HC} and d_C are equal and ΔD will be 0. This indicates that hydrocerussite and cerussite originate from the same depth.
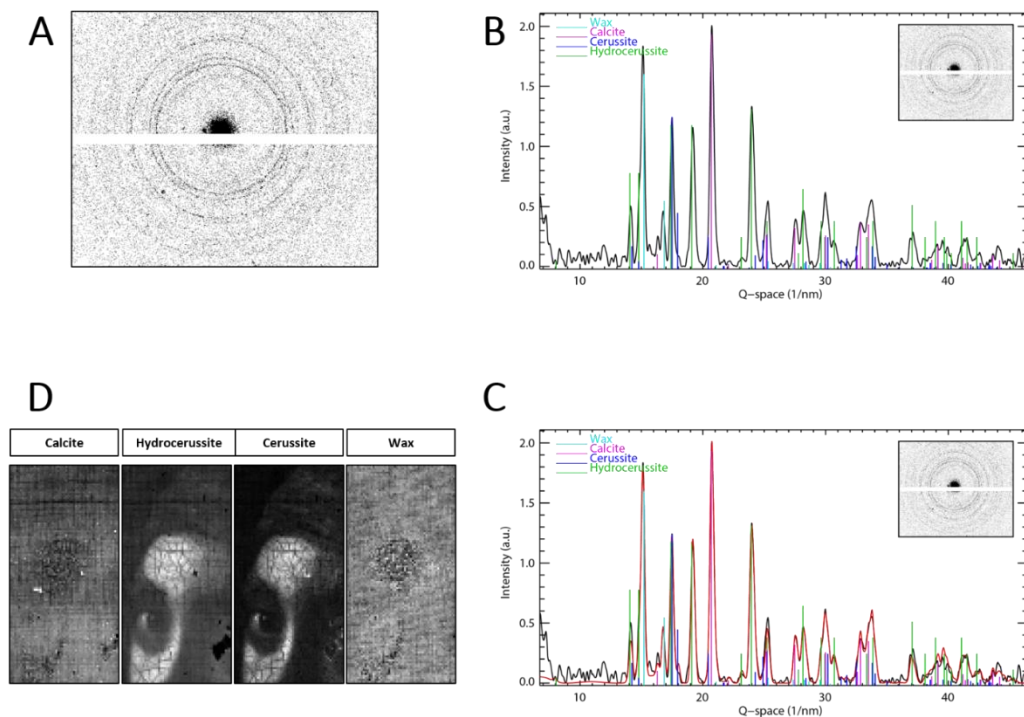
Figure S 3.1-4 From raw diffraction data to intensity scaling parameter distributions (A) 2D diffraction pattern (B) 1D diffractogram (C) 1D diffractogram after performing whole pattern fitting. The red curve indicates the refinement model. (D) Compound-specific scaling parameter distributions.

The compound-specific distribution images shown in this study display the intensity scaling factor obtained after performing whole pattern fitting on every diffractogram.

$$I_{\text{Riet}}(2\theta)=I_{\text{bkg}}(2\theta)+\sum_i S_i \sum_H F_{iH}^2 C_{iH}\Omega_i(2\theta-2\theta_{iH})$$

In this equation S_i denotes the total peak intensity scaling factor of every identified crystalline phase, F_{iH} denotes the structure factor and C_{iH} the part of the Lorentz-polarization factor not removed during azimuthal integration. A Gaussian peak shape (Ω_i) was used for modelling.

In some cases, weight fractions are used in the distribution images instead of intensity scaling factors. The weight fraction w_i relates to the scaling factor S_i as follows.

$$w_j = \frac{S_j U_j M_j}{\sum_j S_j U_j M_j}$$

In this equation the weight fraction of a phase j is related to scaling factor S_j, unit cell volume U_j and molar mass M_j.

Table S 3.1-1 Overview of the scans performed with μ-XRPD and MA-XRPD

Area	Scan size (mm²)	Step size (mm²)	Dwell time (s point⁻¹)
Sample X39	0.250 x 0.140	0.001 x 0.0005	0.5
Sample X40	0.175 x 0.115	0.001 x 0.0005	0.5
MA-rXRPD	200 x 224	2 x 2	10
MA-tXRPD	49.5 x 99.9	0.9 x 0.9	10

Acknowledgments

References

(1)   Wadum, J. Contours of Vermeer. In *Vermeer Studies*; Gaskell, I., Jonker, M., Eds.; Studies in the History of Art; National Gallery of Art: Washington, 1998; pp 201–223.

(2)   Gifford, M. Painting Light: Recent Observations on Vermeer's Technique. In *Vermeer Studies*; Gaskell, I., Jonker, M., Eds.; Studies in the History of Art; National Gallery of Art: Washington, 1998; pp 184–199.

(3)   Gettens, R.; Kühn, H.; Chase, W. Lead White. *Stud. Conserv.* **1967**, *12*, 125–139.

(4)   Harley, R. *Artists Pigments c. 1600-1835: A Study in English Documentary Sources*, 2nd ed.; Butterworth Scientific: London, 1982.

(5)   Welcomme, E.; Walter, P.; Van Elslande, E.; Tsoucaris, G. Investigation of White Pigments Used as Make-up during the Greco-Roman Period. *Appl. Phys. A.* **2006**, *83*, 551–556.

(6)   Gonzalez, V.; Wallez, G.; Calligaro, T.; Cotte, M.; De Nolf, W.; Eveno, M.; Ravaud, E.; Menu, M. Synchrotron-Based High Angle Resolution and High Lateral Resolution X-ray Diffraction: Revealing Lead White Pigment Qualities in Old Masters Paintings. *Anal. Chem.* **2017**, *89* (24), 13203–13211.

(7)   Kühn, H. A Study of the Pigments and the Grounds Used by Jan Vermeer. *Report and Studies in the History of Art* **1968**, *2*, 154–175.

(8)   Welcomme, E.; Walter, P.; Bleuet, J.-L.; Hodeau, E.; Dooryhee, E.; Martinetto, P.; Menu, M. Classification of Lead White Pigments Using Synchrotron Radiation Micro X-Ray Diffraction. *Applied Physics A* **2007**, *89* (4), 825–832.

(9)   Gonzalez, V.; Calligaro, T.; Wallez, G.; Eveno, M.; Toussaint, K.; Menu, M. Composition and Microstructure of the Lead White Pigment in Masters Paintings Using HR Synchrotron XRD. *Microchem. J.* **2016**, *125* (5), 43–49.

(10)   Alfeld, M.; Janssens, K.; Dik, J.; De Nolf, W.; Van der Snickt, G. Optimization of Mobile Scanning Macro-XRF Systems for the in Situ Investigation of Historical Paintings. *J. Anal. At. Spectrom.* **2011**, *26*, 899–909.

(11)   Alfeld, M.; Pedroso, J. V.; van Eikema Hommes, M.; Van der Snickt, G.; Tauber, G.; Blaas, J.; Haschke, M.; Erler, K.; Dik, J.; Janssens, K. A Mobile Instrument for in Situ Scanning Macro-XRF Investigation of Historical Paintings. *J. Anal. At. Spectrom.* **2013**, *28*, 760–767.

(12)   Legrand, S.; Alfeld, M.; Vanmeert, F.; De Nolf, W.; Janssens, K. Macroscopic Fourier Transform Infrared Scanning in Reflection Mode (MA-RFTIR), a New Tool for Chemical Imaging of Cultural Heritage Artefacts in the Mid-Infrared Range. *Analyst* **2014**, *139*, 2489–2498.

(13)   Dooley, K. A.; Conover, D. M.; Glinsman, L. D.; Delaney, J. K. Complementary Standoff Chemical Imaging to Map and Identify Artist Materials in an Early Italian Renaissance Panel Painting. *Angew. Chem. Int. Ed.* **2014**, *53*, 13775–13779.

(14)   Brooker, M. H.; Sunder, S.; Taylor, P.; Lopata, V. J. Infrared and Raman Spectra and X-Ray Diffraction Studies of Solid Lead(II) Carbonates. *Canadian Journal of Chemistry* **2011**, *61* (3), 494–502.

(15)   Chiari, G.; Sarrazin, P. C.; Gailhanou, M. Portable XRD/XRF Instrumentation for the Study of Works of Art. *Powder Diffr* **2008**, *23* (2), 175–186.

(16)   Nakai, I.; Yoshinari, A. Portable X-Ray Powder Diffractometer for the Analysis of Art and Archaeological Materials. *Applied Physics A* **2012**, *106* (2), 279–293.

(17)   De Nolf, W.; Dik, J.; Wallert, A.; Janssens, K.; Van der Snickt, G. High-Energy X-Ray Powder Diffraction for the Imaging of (Hidden) Paintings. *J. Anal. At. Spectrom.* **2011**, *22*, 910–916.

(18)   Vanmeert, F.; De Nolf, W.; De Meyer, S.; Dik, J.; Janssens, K. Macroscopic X-Ray Powder Diffraction Scanning, a New Method for Highly Selective Chemical Imaging of Works of Art: Instrument Optimization. *Anal. Chem.* **2018**, *90*, 6436–6444.

(19)   Vanmeert, F.; Hendriks, E.; Van der Snickt, G.; Monico, L.; Dik, J.; Janssens, K. Chemical Mapping by Macroscopic X-Ray Powder Diffraction of Van Gogh's Sunflowers: Identification of Areas with Higher Degradation Risk. *Angew. Chem.* **2018**, *57*, 7418–7422.

(20)   Vanmeert, F.; De Nolf, W.; Dik, J.; Janssens, K. Macroscopic X-Ray Powder Diffraction Scanning: Possibilities for Quantitative and Depth-Selective Parchment Analysis. *Anal. Chem.* **2018**, *90*, 6445–6452.

(21)   De Meyer, S.; Vanmeert, F.; Janssens, K.; Storme, P. A Mobile Scanner for XRPD-Imaging of Paintings in Transmission and Reflection Geometry. In *6th Interdisciplinary ALMA conference*; Academy of Fine Arts in Prague: Brno, 2017.

(22)   Bacci, M.; Picollo, M.; Trumpy, G.; Tsukada, M.; Kunzelman, D. Non-Invasive Identification of White Pigments on 20th Century Oil Paintings by Using Fiber Optic Reflectance Spectroscopy. *J. Am. Inst. Conserv.* **2007**, *46*, 27–37.

(23)   Van Loon, A.; Noble, P.; Boon, J. J. White Hazes and Surface Crusts in Rembrandt's Homer and Related Paintings. In *ICOM Committee for Conservation 16th Triennial Conference*; Lisbon, 2011.

(24)   Boon, J. J. Chemistry Underneath the Painting Surface: Palmierite Formation in/on a Painting by Johannes Vermeer and by Jacob Jordaens

Using Laboratory- and Synchrotron-Aided Spectroscopic Methods. In *Proceedings of Microscopy & Microanalysis*; Indianapolis, 2013.

(25)   Stols-Witlox, M. J. N.; Megens, L.; Carlyle, L. "To Prepare White Excellent...": Reconstructions Investigating the Influence of Washing, Grinding and Decanting of Stack-Process Lead White on Pigment Composition and Particle Size. In *The artist's process: technology and interpretation*; Eyb-Green, S., Townsend, J. H., Clarke, M., Nadolny, J., Kroustallis, S., Eds.; Archetype: London, 2012; pp 112–129.

(26)   Shahwan, T.; Zunbul, B.; Akar, D. Study of the Scavenging Behavior and Structural Changes Accompanying the Interaction of Aqueous Pb2+ and Sr2+ Ions with Calcite. *Geochem. J.* **2005**, *39* (4), 317–326.

(27)   Sánchez-Navas, A.; López-Cruz, O.; Velilla, N.; Vidal, I. Crystal Growth of Lead Carbonates: Influence of the Medium and Relationship between Structure and Habit. *J. Cryst. Growth.* **2013**, *376*, 1–10.

(28)   Groen, K.; Van der Werf, I.; Van den Berg, K.; Boon, J. Scientific Examination of Vermeer's "Girl with a Pearl Earring." In *Vermeer Studies*; Gaskell, I., Jonker, M., Eds.; Studies in the History of Art; National Gallery of Art: Washington, 1998; pp 168–183.

(29)   Costaras, N. A Study of the Materials and Techniques of Johannes Vermeer. In *Vermeer Studies*; Gaskell, I., Jonker, M., Eds.; Studies in the History of Art; National Gallery of Art: Washington, 1998; pp 144–167.

(30)   Alfeld, M.; Janssens, K. Strategies for Processing Mega-Pixel X-Ray Fluorescence Hyperspectral Data: A Case Study on a Version of Caravaggio's Painting Supper at Emmaus. *J. Anal. At. Spectrom.* **2015**, *30*, 777–789.

(31)   Solé, V. A.; Papillon, E.; Cotte, M.; Walter, P.; Susini, J. A Multiplatform Code for the Analysis of Energy-Dispersive X-Ray Fluorescence Spectra. *Spectrochim. Acta Part B* **2007**, *62*, 63–68.

(32)   Conover, D. M.; Delaney, J. K.; Loew, M. H. Automatic Registration and Mosaicking of Technical Images of Old Master Paintings. *Appl. Phys. A.* **2015**, *119*, 1567–1575.

(33)   Van Loon, A.; Keune, K.; Boon, J. J. Improving the Surface Quality of Paint Cross Sections for Imaging Analytical Studies with Specular Reflection FTIR and Static-SIMS. In *Proceedings of Art Conference on Nondestructive Testing and Microanalysis for the Diagnostics and Conservation of the Cultural and Environmental Heritage*; Lecce, 2005.

(34)   De Nolf, W.; Vanmeert, F.; Janssens, K. XRDUA: Crystalline Phase Distribution Maps by Two-Dimensional Scanning and Tomographic (Micro) X-Ray Powder Diffraction. *J. Appl. Crystallogr.* **2014**, *47*, 1107–1117.

(35)   Downs, R. T.; Hall-Wallace, M. The American Mineralogist Crystal Structure Database. *Am. Mineral.* **2003**, *88*, 247–250.

(36)   De Nolf, W. Imaging of Crystalline Phase Distributions by Means of Scanning and Tomographic X-Ray Powder Diffraction. PhD thesis, University of Antwerp, Antwerp, 2013.

3.2 Lead(II) Formate in Rembrandt's *Night Watch*: Detection and Distribution from the Macro- to the Micro-scale

Contributions of the thesis author: SDM performed the MA-XRPD and SR-µ-XRD data acquisition and analysis together with FV and AG.

3.2.1 Introduction

Rembrandt van Rijn (1606–1669) is one of the most innovative Dutch 17th-century painters. *The Night Watch*, painted in 1642, today displayed in the Rijksmuseum, Amsterdam, is one of his most important masterpieces. It is the largest extant work of art he ever painted, measuring 3.79×4.53 m. Rembrandt showcased his virtuosity, not only by achieving a bold composition with striking light and shadow effects, but also by his constant search for novelty in painting materials and techniques. In 2019, *Operation Night Watch*, the largest research and conservation project ever undertaken for Rembrandt's masterpiece was initiated.[1] The research questions were threefold: i) How did Rembrandt paint *The Night Watch*? ii) What is the condition of the painting? iii) How can we best preserve it for future generations? These questions were addressed in a multidisciplinary manner in close collaboration with conservators, art historians and scientists. The materiality of the painting was chemically investigated using various complementary analytical techniques, in particular chemical imaging methods that operate at multiple length scales. Paintings are highly heterogeneous materials, both along the surface of the painting and in depth (from

varnish to support). Accordingly, the composition and the distribution of materials were determined from the macro-scale -via large maps acquired directly on *The Night Watch*- to the micro-scale -via various (sub)microscopic modalities on minute samples taken from the artwork. This helps assessing the original paint components, conservation and degradation products, and the painting technique. In this research, our attention is focused on the identification and mapping of the various lead compounds. Lead-based pigments have been abundantly used by Rembrandt in his paintings, the most common form being lead white (LW), a synthesized pigment typically containing lead carbonates, hydrocerussite $Pb_3(CO_3)_2(OH)_2$ (HC) and cerussite $PbCO_3$ (C). A list of abbreviations can be found in Table S 3.2-1.[2] Besides LW, lead can also be found in other pigments (e.g. lead-tin yellow Pb_2SnO_4, LTY), in drying agents (lead(II) oxide PbO, red lead or minium, Pb_3O_4) or in degradation products (e.g. lead sulfates, notably palmierite, $K_2Pb(SO_4)_2$, the latest being extensively present in *The Night Watch*). X-ray powder diffraction (XRPD) techniques have proven to be highly efficient to simultaneously detect and discriminate these various lead compounds, and were applied both at the macro-scale via macro-XRPD (MA-XRPD) and at the micro-scale via SR-µ-XRPD.[3,4] This study reports on the detection of the very unusual compound lead(II) formate, $Pb(HCOO)_2$ (LF) in the paint layers of *The Night Watch*, and discusses its specific distribution from the macro- to micro-scale. This, together with a study of mock-ups, allows us to propose hypotheses regarding the origin of this unusual compound.

3.2.2   Results and discussion

<u>Analysis of The Night Watch</u>

In total, about 0.55 m^2 of the painting surface (corresponding to 26 small area maps) were scanned using a MA-XRPD prototype laboratory instrument.[5] Briefly, the X-ray beam (Cu-Kα anode, ca. 140 µm diameter X-ray

source spot) impinged on the painting under an angle of 10°. XRPD patterns were collected in reflection geometry by raster scanning the surface of the painting. In this case, the painting remained stationary while the X-ray instrument performed the scanning movements (details in Supporting Information). Unsurprisingly, HC and C were identified in many parts of the painting. Much more remarkably, LF was occasionally detected by MA-XRPD. Careful assessment of the 26 collected MA-XRPD maps revealed its presence in 12 maps. As illustrated in Figure 3.2-1 and detailed in Table S 3.2-2, some trends can be observed:

- LF is systematically found in light-coloured, LW-rich (and in one case also containing LTY) areas of the painting.

- In 10 of the 12 maps, plumbonacrite (PN), $Pb_5(CO_3)_3O(OH)_2$, another relatively rare lead carbonate, is also found co-localized with LF. PN was previously identified in other Rembrandt's paintings, in LW *impasto* areas (thickly applied paint with a clear three-dimensional morphology).[4]

- HC is always present in the regions where LF and PN are detected. In some regions (e.g. Figure 3.2-1), HC is mainly in LF regions; in other regions, HC is more concentrated outside LF regions.

- In the latter regions, HC is usually associated with C. C is less concentrated in the LF regions (Figure 3.2-1).
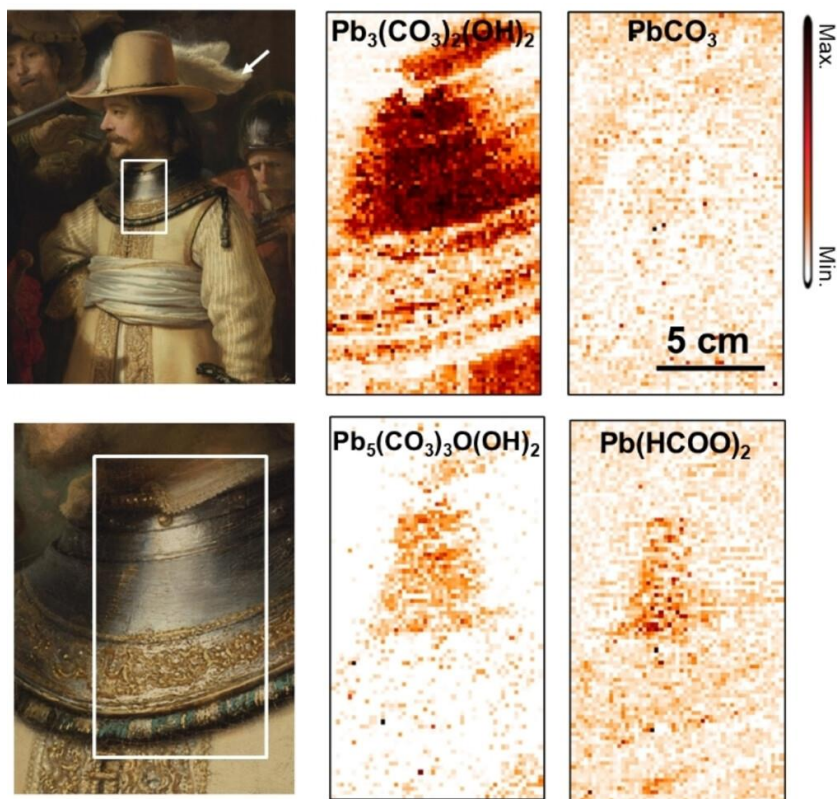
Figure 3.2-1 MA-XRPD crystalline phases distribution on the area of the steel gorget of Willem van Ruytenburch on *The Night Watch* (1642) by Rembrandt van Rijn (1606-1669). White rectangles indicate the area scanned using MA-XRPD. The white arrow indicates the location of sample SK-C-5_1457.

MA-XRPD maps of LF are often noisy (Figure 3.2-1 and Figure S 3.2-1), because of their low detected intensity, in particular when compared to the HC map in Figure 3.2-1. To confirm the presence of LF in The Night Watch, and gain insight into its distribution at the micro-scale, SR-μ-XRPD mapping was performed on paint micro-fragments. During Operation Night Watch, about 50 paint samples were taken to address different research questions. Maps were acquired in transmission geometry by raster scanning of the resin-embedded cross-sections in front of a micrometric X-ray beam (see details in Supporting Information).[6] LF was detected in three of these paint cross-sections. One of

these samples (SK-C-5_070), was purposely taken from a LF-rich area as identified by MA-XRPD, in the girl's light yellow dress (Figure S 3.2-1D14).

Sample SK-C-5_070 (Figure 3.2-2A) shows a LTY+LW layer (as shown by the distribution of LTY, cassiterite SnO_2 and HC). The near absence of C (only a few grains visible), combined with the detection of PN throughout the paint layer suggest that a non-standard LW is present here. In addition, a ≈80 μm diameter lead soap protrusion (a globular lump that has formed in situ in the paint layers) is visible in the middle of the map (red circular shape), in which crystalline mixed lead soaps (identified as approximately a mixture of palmitate/stearate soaps with a 1:1 ratio through their peaks at 1.28, 2.62 and 3.93 nm−1) were found.[7,8] Interestingly, HC diffraction signals were broader in the protrusion than in the surrounding LW layer (full-width at half maximum (FWHM) of peak HC (012) of 0.16° and 0.11° respectively as measured with the ID13 setup, Figure S 3.2-2). This suggests that part of the HC was formed or re-crystallized in situ in the protrusion. LF was detected near the top surface of the paint, mainly inside but also outside the protrusion.
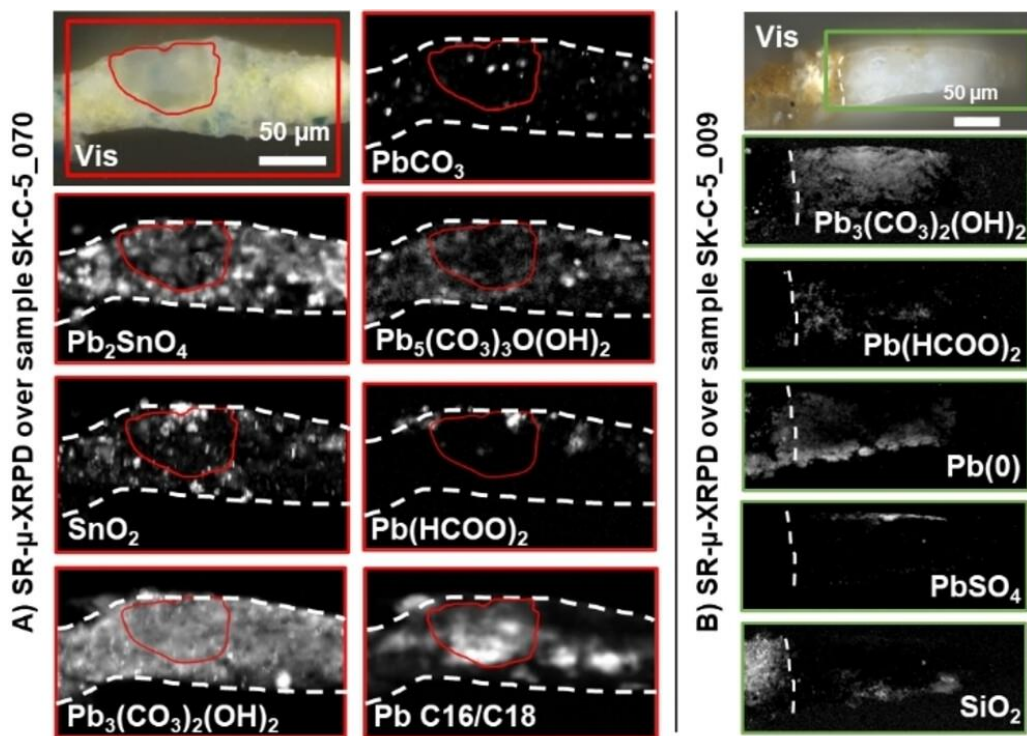
Figure 3.2-2 SR-μ-XRPD crystalline phases distribution on samples A) SK-C-5_070 from the girl's light yellow dress (the circular red shape indicates the protrusion) and B) SK-C-5_009 (the white dotted line represents the interface between the protrusion and the ground layer). The red and green rectangles indicate the area scanned on each sample. The intensities scale from min (black) to max (white).

Sample SK-C-5_009 (Figure 3.2-2B) shows part of a protrusion that formed within the clay-based ground - the preparatory layer that was used by Rembrandt for The Night Watch. The sample was taken in a degraded area from the dog in the lower right of the painting (Figure S 3.2-3). In this region, no Pb-compounds could be observed above the detection limits of MA-XRPD. However, with SR-μ-XRPD, LF was found throughout the protrusion. HC is homogeneously present in the protrusion, while no C was detected. A thin layer of anglesite (PbSO4), a degradation compound was detected at the surface of the sample.[9] Surprisingly, metallic lead was also detected throughout the map that we interpret as the result

of SR beam-induced alteration of LF as observed by following the evolution of the diffraction intensities under repeated acquisitions (Figure S 3.2-4). Indeed, we have recently reported the formation of Pb0 in LW-based paint layers under high-intensity X-ray beams.6 Even more recently, the formation of Pb0 from LF solutions upon electron beam irradiation was described possibly opening up future lines of enquiry about the treatment of heavy metals-contaminated water.[10] Here again, the FWHM of HC (012) estimated on the P06 data was broader (0.16°) than the one of the original HC pigment (0.06°) measured on another sample not shown here.

Sample SK-C-5_1457 was taken from an impasto area (feather of the hat of lieutenant Willem van Ruytenburch) (Figure S 3.2-5). The paint layer is homogeneously white and mostly contains HC and some C. Both PN and LF are present (mainly in the lower part of the section), but not co-localized at the micro-scale (Figure S 3.2-5).

In addition, micro-Fourier transform infrared spectroscopy in attenuated total reflectance mode (μ-FTIR-ATR) maps were acquired on the first two samples, to evaluate its potential as an alternative technique to SR-μ-XRPD to detect and map LF and to gain complementary molecular characterization (technical details available in Supporting Information). The formal identification of LF is made very difficult by the overlapping signals of other lead carboxylates and lead carbonates. However, in the central part of the protrusion of SK-C-5_009, the average FTIR spectrum shows a signal compatible with the presence of LF (Figure S 3.2-6).[11,12]

Results obtained with SR-μ-XRPD confirm some of the trends observed with MA-XRPD: when LF is detected, this is in the light-coloured or white areas; PN and HC are present as well, but these three lead phases are not co-localised at the

micro-scale; C always shows a lower amount, when detected at all. In two of the three samples, LF is detected in a protrusion, in addition to the surrounding paint.

The fact that MA-XRPD and SR-µ-XRPD did not systematically detect the same phases in the same area, (e.g. sample SK-C-5_009), can be ascribed to the different instrumental configurations (in addition of the beam size, X-ray energy and corresponding penetration depth (≈10 µm in a LW layer in the MA-XRPD configuration), source intensity, detector, geometry), leading to different limits of detection, to the intrinsic heterogeneity of paint at both scales, and the limited representativity of few ≈300 µm samples in a >15 m^2 painting.

To our knowledge, this is the first report of the presence of LF in an historical painting. There are few occurrences of metal formates in cultural heritage materials, most often associated with degradation of glass, calcareous materials, cements and sandstones, or metals and alloys.[13] Concerning historical paintings, only zinc formate has been reported so far: in Jack Chambers' *Summer Visito]* and in Salvador Dalí's *Couple with Clouds in their Heads*, where zinc formate dihydrate ($Zn(HCOO)_2 \cdot 2\,H_2O$) was found associated with $Zn(CH_3COO)_2 \cdot 2\,H_2O$ and ZnS.[14] In both cases, authors proposed that zinc formate was a degradation product of zinc white (ZnO), possibly reacting with formic acid ($HCOOH$) produced by the alkyd medium or from the wooden frame.[14,15] So far, lead formate has only (recently) been reported in model paints, forming at the end of oxidative polymerization of model paint films prepared by mixing red lead (Pb_3O_4) and four common drying oils (linseed, walnut, poppy-seed and stand oil).[16,17] In brief, in these studies by Švarcová et al., LF was detected within one day, by transmission XRPD but not in reflection geometry. [13]C, ^{1}H and [207]Pb solid state nuclear magnetic resonance spectroscopy confirmed the formation of LF. However, bulk FTIR (in transflectance mode on

thin paints applied on aluminium-coated glass slides) failed to detect them, which was ascribed to the overlap of the most intense IR peak of LF at 1537 cm^{-1} [v_4 asym. C−O stretch] with signals from oil and metal soaps.[11] Pb^{II} (from Pb_3O_4) reacts with oil, while the local chemical environment of Pb^{IV} atoms was found intact. The formation of formic acid in oils was also proven by gas chromatography-mass spectrometry, and LF was shown to form on Pb_3O_4 powder exposed to volatile formic acid released during the autoxidation of oils, demonstrating the crucial role of oxygen in the process. Reactions crucial for the formation of formic acid, and subsequently LF, are the formation and decomposition of unsaturated ester hydroperoxides as primary oxidation products. Decomposition of hydroperoxides leads to the formation of secondary oxidation products, such as aldehydes, which further decompose to formic acid. A detailed chemical mechanism for the formation of formic acid and LF was proposed in the literature.[16] Among the different oils tested, linseed oil is the most reactive towards the formation of LF, which would be due to its three isolated double bonds and their position near the methyl end in α-linolenic acid.[16] The scarcity of LF in historical paintings made Švarcová et al. suggest that these formate salts would not be stable and would only be an intermediate compound in the conversion of Pb_3O_4 to lead soaps and/or lead carbonates. Therefore, the presence of LF in a 380-years-old painting calls for a reconsideration of this hypothesis. Also, beyond LF, there is an on-going controversy about the effect(s) (positive or negative) of lead carboxylates in general in paintings.[18] Lead carboxylates are involved in many degradation processes but they also play a major role in the rheological and drying properties of oil paints. Consequently, a better understanding of the possible origins of LF is highly desirable. It not only offers clues on painters' techniques and materials but also guides conservators towards developing better treatment methods for the preservation of artworks.

To explore a possible scenario for the presence of LF in The Night Watch we investigated a series of model samples, representative of historical paint layers, made with linseed oil (LO), the most common organic binder used in the 17th century. The occurrence of PN, stable only in alkaline conditions (pH>10), as well as the presence of newly formed HC, led us to further explore the interactions of LO with lead(II) oxide (PbO), an alkaline lead compound frequently used by 17th-century Dutch artists as an oil siccative.[4] Model "cooked oils" were prepared following the "huile de litharge" recipe reported by Turquet De Mayerne in 1633.[15] This recipe describes mixing and heating of oil and PbO (4:1 w/w) and adding hot water to the reacting mixture. In our model, 12 g of linseed oil (Kremer pigmente 73020) was cooked with 2.25 g (i.e. 75 % of the recipe 4:1 weight ratio) of PbO (Alfa AEsar, 99.9 %, 23 w % litharge, α-PbO, 77 w % massicot, β-PbO) for 3 h at 100 °C, with or without 12 g of water (named PaWet and PaDry, respectively). The linseed oil was also heated without PbO and water for comparison (LO). As previously discussed, such preparations result in the saponification of oil triglycerides and the formation of lead soaps (complexes of lead and fatty acids; in the case of LO, mainly triply unsaturated α-linolenic acid, saturated palmitic and stearic acid, monounsaturated oleic acid and doubly unsaturated linoleic acid). This reaction is favored by the introduction of water.[19] To simulate an incomplete dissolution/reaction of PbO as described in some historical texts, additional PbO particles (0.75 g per 4 g of heated medium, i.e. the remaining 25 % of the 4 : 1 weight ratio) were added and lightly mixed at room temperature (RT) to the cooked media (noted PaWetPbO and PaDryPbO), leading to the formation of large globules within the oil matrix (Figure 3.2-3). The appearance of these globules spans from orange to white and sometimes translucent when observed as a thin section (Figure 3.2-4). Finally,

additional samples mimicking LW paints were prepared by mixing the above media (without and with the additional 25 % of PbO) with LW (Kremer, HC:C ratio of 90:10 w %, noted with the suffix _LW). The list of model samples relevant to this work is presented in Table S 3.2-3. The different model paints were spread on glass slides and left to dry for 3 years at RT. The optical microscope (OM) observation of the paint films revealed the formation of crystals from the first days of curing.
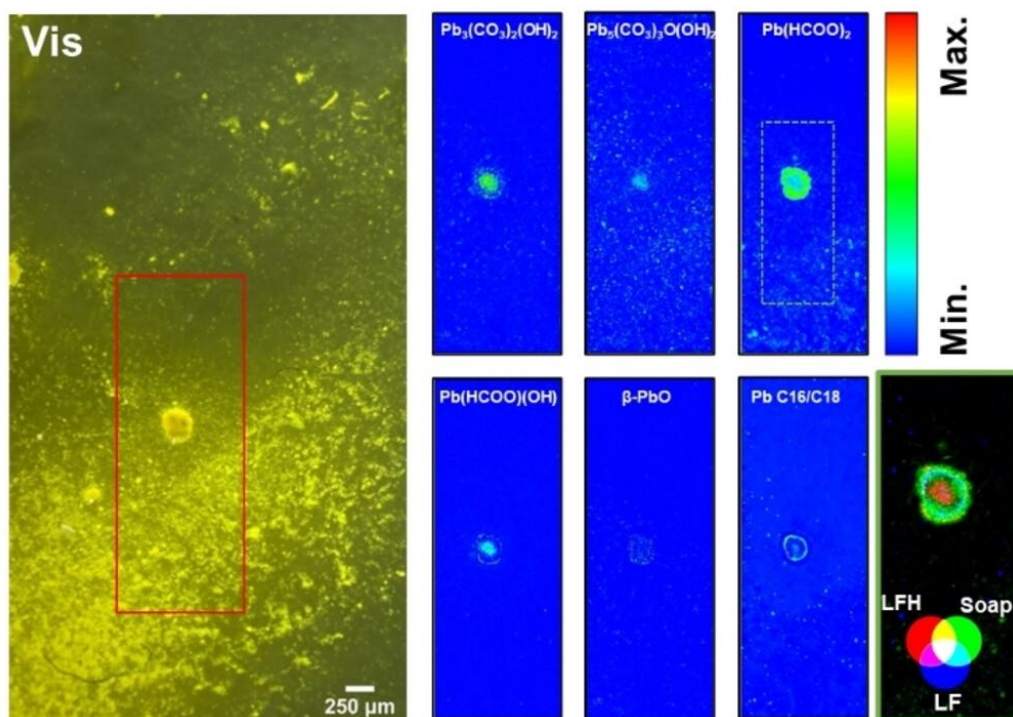
Figure 3.2-3 SR-µ-XRPD crystalline phases distribution on sample PaDryPbO, droplet laid on a glass slide. The red rectangle indicates the area scanned via SR-µ-XRPD, around a globule. In the bottom right corner, the RGB composite map displays a zoom around the globule (highlighted by the dotted green rectangle on LF map), with LFH (red), Pb-soaps with a 16- and 18-carbon chain (green) and LF (blue).
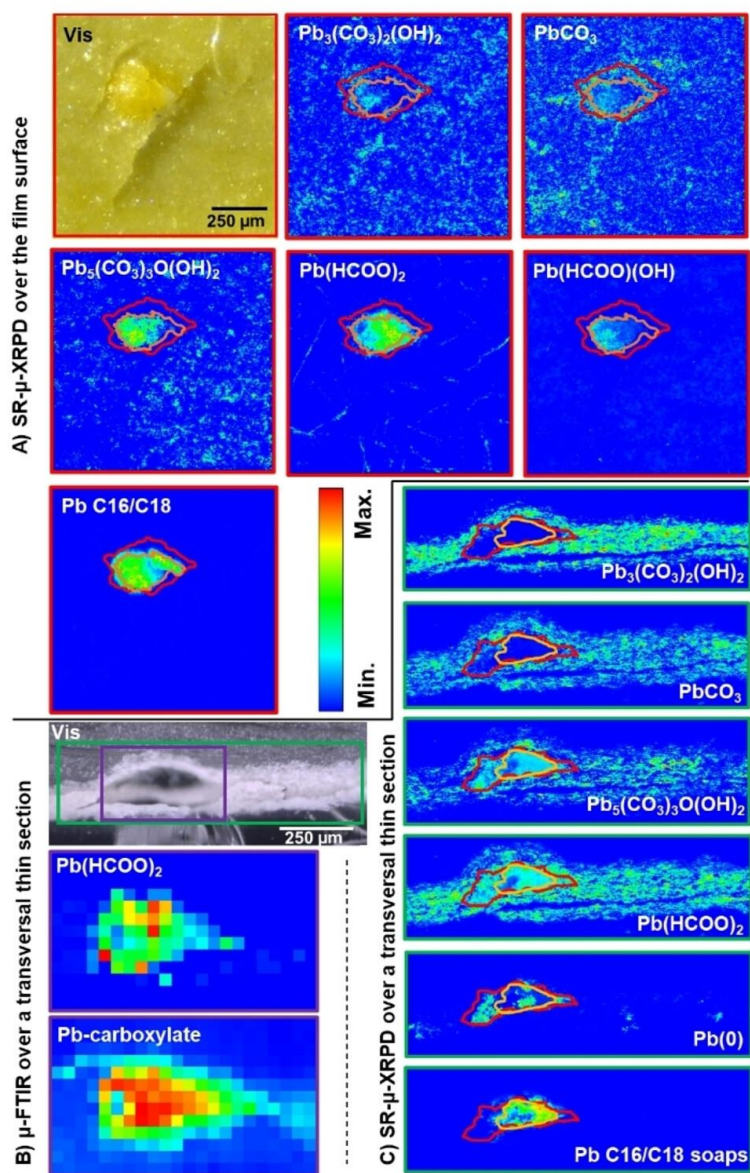
Figure 3.2-4 SR-μ-XRPD crystalline phases distribution and μ-FTIR molecular groups distribution around a lead soap globule, in sample PaWetPbO_LW. A) SR-μ-XRPD map over the film surface (red square); B), C) Maps over a thin section (resin embedded). Purple rectangle: μ-FTIR; green rectangle: SR-μ-XRPD. The μ-FTIR distributions were calculated by integrating the signal of the [v_5 in-plane C−H bend] band (1365–1385 cm^{-1}) for the LF; and of the [v asym. C−O stretch] band (1502–1564

cm^{-1}) for the lead carboxylates. In A) and C), the color lines have been added to ease the comparison between the maps.

The precise kinetics of the formation of LF crystals will be the subject of a dedicated publication. The discussion here focuses on the macro- and micro-localization of crystals. Interestingly, a highly heterogeneous distribution of crystals was observed, with crystals (sometimes as needles >100 μm, Figure 3.2-4A and Figure S 3.2-7) strongly concentrated in thick regions and absent in the edges of the PaWet and PaDry films (above Figure 3.2-3, Figure S 3.2-8). These crystals were identified as LF thanks to SR-μ-XRPD (Figure 3.2-3, Figure 3.2-4A, Figure 3.2-4C). It is noteworthy that during the first SR-μ-XRPD experiments (at high dose) the transformation of LF into metallic lead was observed with Pb^0 co-localized with the LF crystals (Figure S 3.2-7B). From then on, low X-ray dose conditions were favored to mitigate the reduction of lead(II).[6] Small (<1 μm) PN particles were also detected in the paint media (Figure 3.2-3, Figure 3.2-4A). In samples where LW was not added, small particles of newly formed HC were sometimes detected, usually more concentrated in LF rich regions (Figure 3.2-3). In these cases, C was not detected. In the samples prepared with LW pigment, LF crystals were not visible under the OM but could be clearly identified with SR-μ-XRPD (e.g. Figure 3.2-4A).

To assess the depth distribution of LF crystals in the models, transversal thin sections (5–10 μm) of cured films were prepared (Table S 3.2-4). OM and SR-μ-XRPD highlighted in most cases a lower concentration of crystals in the upper part (50 μm) of the cross-sections (Figure S 3.2-7B). This observation could explain why Švarcová et al. observed LF with XRPD in transmission mode but not in reflection and supports their hypothesis of the influence of particle sedimentation on the distribution of LF. The μ-FTIR map acquired on a thin section of cured PaDry succeeded in the detection of LF crystals, after non-

negative matrix approximation calculations using the PyMCA ROI imaging software package (Figure S7C).[20]

To further assess the relationship between the paint film thickness and the LF distribution, additional PaDry and PaWet films of controlled thickness (15, 30, 60 and 90 µm) were prepared using a paint applicator. Thin sections (10 µm) of these samples were analyzed with SR-µ-XRPD after four months of natural aging. LF was not detected in this case (not shown). In addition, PaDry films of variable thickness were prepared using microscope glass slides with concave depression (Figure S 3.2-10A). They revealed the absence of LF crystals in the thinner regions (Figure S 3.2-10). This result may explain why Švarcová et al. did not detect LF with FTIR spectroscopy. Based on our above observations, it is probable that in such thin layers, LF did not form. In our work, ATR-FTIR spectroscopy of thick (>0.3 mm) drops of PaDry was successful in the detection of LF, upon curing (Figure S 3.2-9C).

A further complexity and heterogeneity of the system is reached when introducing additional PbO particles to the prepared cooked oil. 2D SR-µ-XRPD maps were acquired over the formed globules, both over the films surface (Figure 3.2-3,Figure 3.2-4A and Figure S 3.2-11), and over thin-sections (Figure 3.2-4C). When mapped over the films surface, the globules usually present a complex onion-like structure with different Pb-based products distributed as successive layers. The composition of these core/shell structures varies from one sample to another and from one globule to another. However, some trends can be observed and are illustrated with maps acquired on sample PaDryPbO (Figure 3.2-3) and PaWetPbO_LW (Figure 3.2-4). PbO, when detected, was present at the core of the globule (Figure 3.2-3). The internal parts of the layered spheres (mixed with or just around the PbO core region) often contained a mixture of newly formed

PN, HC and in some cases, lead formate hydroxide Pb(HCOO)(OH) (LFH, Figure 3.2-3 and Figure S 3.2-12B). LF was usually more concentrated in the second layer of the spherical mass (Figure 3.2-3 and Figure S 3.2-12A), together or surrounded by other lead carboxylates. In some cases, mixed lead soaps (palmitate/stearate) were sufficiently crystallized to be firmly identified (Figure 3.2-3, Figure S 3.2-12C).

A thin section (5 μm) was prepared from one of these lead soap globules (sample PaWetPbO_LW) (Figure 3.2-4B and Figure 3.2-4C). SR-μ-XRPD maps show that in this globule, PbO has fully reacted away; the core of the globule contained crystallized mixed lead soaps, similar to The Night Watch sample SK-C-5_070 (Figure 3.2-4C). LF and Pb^0 were colocalized around the core of the globule, forming the first onion-like layer (Figure 3.2-4C). Unlike in the PaDry and PaWet samples, LF was detected all over the film depth, including the upper parts. HC, C, and PN (Figure 3.2-4C) were found, spreading from the edge of the globule throughout the paint matrix. Previously observed LFH was not detected in this map, demonstrating a high heterogeneity and variability of the composition of these paints. In this thin section, LF was also detected with μ-FTIR mapping (Figure 3.2-4B).

To investigate the direct reaction of PbO with oil, a simplified model system was prepared, consisting of cooked LO spread as a film on glass slides, and to which additional PbO particles were deposited (LO_PbO). Two films were left to cure, at RT and at 60 °C. This second sample was analyzed after 45 days and reanalyzed 2 years after the synthesis (after a first year at 60 °C and a second year at RT) (Figure S 3.2-11). LF, LFH and PN were all detected in the vicinity of PbO, successfully demonstrating that these compounds can form following the direct reaction of PbO with the oil. Finally, even though the long-term stability

of LF will be the subject of a future publication, it should be noted that LF crystals were still present in paint films aged for three years at ambient conditions, and after two days of immersion of oil film (PaDry) samples in water.

Results obtained on the model paints can be summarized as follows:

LF crystals formed during the curing of films of oil cooked with PbO (in both wet and dry conditions), sometimes in the form of needles up to ≈100 µm in length.

In LW-free samples, LF concentration decreased with film depth and film thickness, leading to extremely heterogeneous systems and the absence of LF in some parts of the paint layer.

LF was more concentrated around unreacted PbO particles, in the three systems (PaWet, PaDry, LO), and can also be present in an alkaline form: LFH (detected only in the _PbO samples).

LF (and its reduced Pb^0 form) was detected in a lead soap-rich globule (protrusion) prepared as a thin section.

Newly formed PN and HC were detected both throughout the paint films and in the vicinity of the unreacted PbO particles.

In addition to the lead soaps formed during the synthesis of the cooked oils, some additional soaps sometimes formed at RT and organized themselves as crystalline phases around PbO particles.

Figure 3.2-5 proposes two schemes to explain some of our findings on the model systems. The symbols used in the sketches follow the description of lead ionomer by Hermans et al.[21] Figure 3.2-5A is a model for the distribution of LF in curing oil films, while Figure 3.2-5B describes the more complicated case of the

additional presence of unreacted PbO particles in the medium. In Figure 3.2-5A, LF is proposed to form from the substitution of formic acid (formed during oxidative curing of oil) with the different lead carboxylate groups:[16] those formed during the preparation of the lead medium by saponification of oil triglycerides; but also those formed during the oil autoxidative drying, and the radical polymerization reactions.[21] Two hypotheses can explain the depth profile of LF crystals and their absence in thin films: 1) the evaporation of formic acid, in particular in thin paint layers or close to the paint surface (top part of Figure 3.2-5A); 2) the diffusion of small molecules of LF, assembling into crystals(middle part of Figure 3.2-5A), and sedimenting (bottom part of Figure 3.2-5A) in a less dense paint liquid film, further increasing the abundance of LF crystals at the bottom of the layer. While this sedimentation could have an influence on the distribution of LF in the oil matrix (as visible in samples PaWet and PaDry), it probably does not occur when the medium is mixed with LW pigment, as then, the paint matrix density strongly increases (as in sample PaWetPbO_LW).
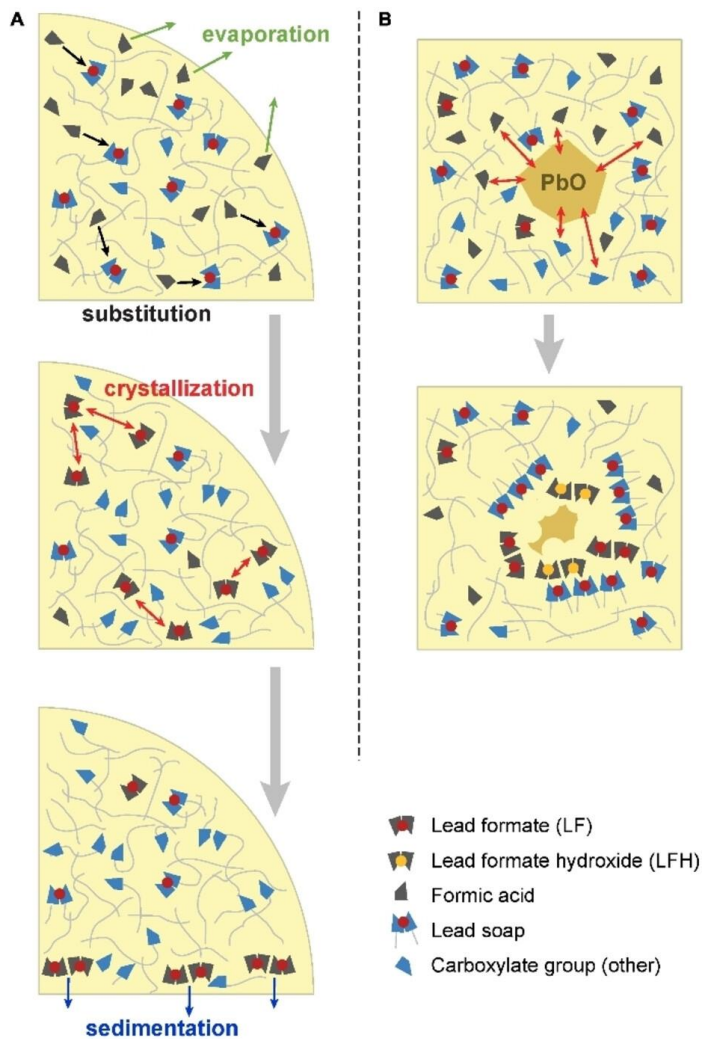
Figure 3.2-5 Schematic of the chemical and physical processes proposed to explain the micro- and macro-distribution of LF in paints. See text for the details. A) Model for the distribution of LF in PaDry and PaWet samples, cross-section of a paint droplet. Green, black, red and blue arrows represent evaporation of formic acid, substitution of formic acid on lead carboxylates, crystallization and sedimentation of LF, respectively. B) model for the distribution of LF and LFH in PaDry_PbO, PaWet_PbO and LO_PbO samples, top view of PbO particles deposited in a paint film. Formic acids and mobile fatty acids migrate, react at the surface of PbO forming LFH, LF, lead soaps, and crystallize. For simplification and readability: i) the additional carbonates (PN, HC···) phases are not represented; ii) possible additional pigments are not represented; iii) to facilitate reading, different colors are used for the different lead-based compounds (PbO, LF, LFH, lead carboxylates); iv) Inter conversion of LFH into LF, lead soaps

into LF, LF and LFH into carbonates is not represented. The presence of hybrid lead oxide/hydroxide/formate/long chain carboxylate species cannot be excluded.

In the case of unreacted PbO particles, a secondary local source of Pb^{II} ions is present in addition to lead soaps (Figure 3.2-5B). In such a case, our models show that an additional, more alkaline form of LF (LFH) can be observed. PbO particles react with formic acid and mobile fatty acids, leading to the local formation and crystallization of LFH, LF and additional lead soaps. The higher alkalinity closer to the center of the PbO particles could explain the distribution of LFH with respect to LF, as observed in Figure 3.2-3. In parallel to the formation of LF, LFH and lead soaps, PbO can also convert into PN and HC by taking up CO_2 and water, explaining the detection of these different components in the paint film and the complex layered structure in the globules. Besides, conversion of one compound into another, for example LFH into LF, lead soaps into LF, LF or LFH into HC cannot be excluded.[22]

An interesting question is still whether the simultaneous observation of LF, LFH, PN, HC and lead soaps in similar regions means that (1) the heterogeneity of the system at the nano- to micro-scale translates into local variations of the thermodynamically favorable conditions for crystallization of the various phases; (2) our analyses reflect the composition of the system at a certain time, but do not account for its final, stable conditions. The kinetics of the formation of LF and associated compounds and their evolution under different environmental conditions and/or conservation treatments will be discussed in a dedicated publication.

Besides, when LW is added as a pigment, it may provide an additional source of Pb^{II} for the formation of LF, further increasing the complexity and heterogeneity of the system. Additional samples containing LW as a single source of Pb^{II} ions are under analysis.

3.2.3   Conclusion

In conclusion, the results obtained on mock-up paints shed new light on the presence and distribution of LF in *The Night Watch*, and the possible reasons for their presence in oil paintings in general. In addition to Pb_3O_4, as studied by Švarcová et al., PbO can also lead to the fast formation of LF in paints, together with LFH, lead soaps, PN and HC. Even if no crystalline PbO phases were detected in *The Night Watch*, and its use as a drier remains hypothetical, the presence and distribution of LF, PN and of newly formed HC together with the local absence of C at both the macro- and micro-scales, as well as the presence of lead fatty carboxylates-rich protrusions support the hypothesis that the oil used for light-toned parts of the painting was treated by an alkaline lead drier. In both *The Night Watch* and the model samples, the distribution of LF crystals at the macro- and micro-scale is highly variable. This distribution can be related to the paint thickness and the presence of a local high concentration of alkaline Pb-species (as simulated with unreacted PbO in model samples) and the competing formation and possible inter-conversion of LF, LFH, lead soaps and lead carbonates. In the case of *The Night Watch*, an additional degree of complexity is added by the fact that the painting has been (re)varnished in the past with an oil-based varnish. In 1756, Van Dijk published a booklet on the paintings in the Amsterdam Town Hall in which he wrote that he removed ′layers of boiled oil and varnish' from *The Night Watch*.[23] Boiled oil was usually prepared with a drier such as PbO. However, Van Dijk's identification of "boiled oil" is only based on his empirical findings during his cleaning and restoration of the painting. Another unknown is to what extent this revarnishing was conducted locally or on the entire paint surface. It may have provided a fresh source of formic acid causing different LF-rich areas to form in the painting in different periods. In particular, the LF present at the surface of sample SK-C-5_070 might

be linked to a reaction between formic acid from this varnish and the LW paint. Additional model samples will be prepared to assess this hypothesis. Lastly, a possible environmental origin of formic acid cannot be excluded, as observed in the corrosion of many metallic artifacts.[13]

Finally, even if LF, as a pure compound, is highly soluble in water ($K_{sp} \approx 2.9 \times 10^{-5}$), the paint matrix seems to protect it from the environment. Accordingly, LF, LFH and other metal formates such as zinc formate, may be detected in many more historical paintings in the future, if more attention is paid to these particular short chain lead carboxylates. However, it should be noted that their detection is challenging. First, the MA-XRPD set-up is only sensitive to surface compounds (up to 10 μm in LW paint) and our models show a lower concentration of LF at the paint film surface. Second, μ-FTIR, a technique widely available for the study of paint cross-sections, is not suited for the detection of LF in lead soap/lead carbonate matrices. SR-μ-XRPD is therefore highly recommended to track LF in fragments from historical paintings, while being careful to use as low an X-ray dose as possible. The formation of lead carboxylates with long fatty acid chains has received a lot of scientific interest; in the light of this work, it will be very important to pay similar attention to the presence of shorter lead carboxylates as they can provide essential information about a painting's history and its conservation state.[18] While until now metal formates have been mainly associated with corrosion and degradation products, it will be interesting to see if LF plays any role (positive or negative) in the stability and optical properties of oil paintings.[13]

3.2.4   Materials and methods

MA-XRPD imaging

The macro-XRPD measurements were performed by means of an in-house built mobile MAXRPD scanner (AXIS, University of Antwerp, Belgium). The device is set-up with a low power X-ray micro source (50W, IµS-Cu, Incoatec GmbH, Germany), which produces a monochromatic and focused X-ray beam (Cu–Kα; 8.04 keV) with a photon flux of 2.9×10^8 photon s^{-1} (focal spot diameter: ca. 140 µm; output focal distance: ca. 20 cm; divergence: 2.4 mrad). A primary beam impingement angle of 10° relative to the surface of the painting is chosen due to geometrical limitations. This causes the beam footprint to become elongated in the horizontal direction so that it is of the order of 0.8 mm in the horizontal and 0.2 mm in the vertical direction. A PILATUS 200K area detector is used to record the 2D diffraction patterns. To reduce the effect of local topography and curvature of the painting surface on the diffraction data, the distance between the artwork and the scanner is automatically adjusted with a laser distance sensor (Baumer GmbH, Germany) at each measurement point. All components are placed on a motorized platform that is capable of moving in the XYZ directions (30 x 30 x 10 cm).

Synchrotron µ-XRPD

P06 beamline (PETRA-III, DESY, DE): The cross-sectioned samples SK-C-5_009 and SK-C- 5_1457 were analyzed with SR-µ-XRPD at beamline P06, a hard X-ray micro- and nano-probe beamline suited for X-ray powder diffraction imaging experiments at the (sub-)micrometric scale.[24] A Kirkpatrick-Baez optical system was used to focus the 21 keV beam to a diameter of 0.5 µm and a flux of 10^{10} photons/s. The sample was mounted on a plastic frame that could be moved in the XYZ directions. An EIGER X 4M detector (Dectris Ltd., Switzerland) was used to collect the diffraction signals. The sample was placed

at a distance of 18 cm in front of the detector, ensuring a sufficiently wide angular range.

ID13 beamline (ESRF, FR): ID13 is an ESRF undulator beamline dedicated to high-lateral- resolution diffraction and scattering experiments using focused monochromatic X-ray beams.[6] Samples, notably the historical cross-section SK-C-5_070, were analysed on the micro-branch end-station. Samples are mounted vertically, perpendicular to the X-ray beam. The energy of the incident beam was chosen around 13.0 keV. The beam was focused to $\sim 2 \times 2$ μm^2 (flux$\sim 2 \times 10^{12}$ ph/s, at I = 128 mA electron beam current; attenuated to $\sim 10^{11}$ ph/s by detuning the undulator) using a compound refractive lens set-up (CRL) mounted in a transfocator. SR-μ- XRPD maps were obtained by raster-scanning the samples and collecting 2D XRPD patterns, in transmission, with a Dectris EIGER 4 M single photon counting detector that acquires frames with 2070×2167 pixels (75×75 μm^2 pixel size) at a rate up to 750 Hz. Azimuthal integration and calculation of crystalline phases by linear fits were performed using dedicated Jupyter Notebooks.[20]

XRPD data processing

For both analytical configurations, the synchrotron diffraction data has been corrected for attenuation effects and processed using XRDUA. The software package PyMCA, ROI Imaging was also used to extract averages and statistical analyses.[20]

μ-FTIR-ATR

μ-FTIR-ATR maps were acquired on two Night Watch cross-sections (SK-C-5_70 and SK-C- 5_0009), using a Perkin Elmer Spectrum 100 FTIR spectrometer combined with a Spectrum Spotlight 400 FTIR microscope equipped with a 16x1

pixel linear mercury cadmium telluride (MCT) array detector. A Perkin Elmer ATR imaging accessory consisting of a germanium crystal was used for ATR imaging. The spectral resolution was 16 cm^{-1}. The mapping area was 300 × 400 µm² in size, with a pixel size of 6.25 µm. Maps were analyzed using the PyMCA ROI imaging package.[20]

3.2.5   Supporting information

I)   <u>Table of the abbreviations used for lead containing phases</u>

Table S 3.2-1 Table of the detected lead containing phases with their abbreviations and composition

Name	Abbreviation	Chemical formula
Lead formate	LF	$Pb(HCOO)_2$
Lead formate hydroxide	LFH	$Pb(HCOO)(OH)$
Plumbonacrite	PN	$Pb_5(CO_3)_3O(OH)_2$
Hydrocerussite	HC	$Pb_3(CO_3)_2(OH)_2$
Cerussite	C	$PbCO_3$
Lead-tin yellow	LTY	Pb_2SnO_4

II) Table reporting areas of *The Night Watch* probed using MA-XRPD containing lead(II) formate (LF)

Table S 3.2-2 Areas of *The Night Watch* probed using MA-XRPD containing LF. Correlations are based on the visual inspection of the distribution images.

map	Location	LF	PN (compared to LF)	HC	C	LTY
D01	Face	Not clear. More on nose (<u>white</u> area) and white collar	<u>Same</u> distribution	Highly concentrated in LF regions, but also present elsewhere	Not correlated	Not detected
D02	Collar	<u>White</u> collar	<u>Same</u> distribution	Same as PN	No correlation	No correlation
D08	Pearls on a hat	White feather and light regions of the hat	<u>Same</u> distribution but low intensity	Highly concentrated in LF regions, but also present elsewhere	Anti-correlated	No correlation
D14	Dead chicken + dress girl	In the <u>pale-yellow</u> dress	Not detected	Concentrated in LF regions, but also present elsewhere (more concentrated in dead chicken)	Anti-correlated	<u>Correlated</u>
D22-23	Arm of the red musketeer	In the <u>white</u> cuff	Not detected	Highly concentrated in LF regions, but also present elsewhere	Anti-correlated	Not detected
D24-26	Face and collar of Sgt. Kemp	<u>White</u> parts of the face + <u>white</u> parts of the collar	Correlated (and present in other regions where LF not detected	Highly concentrated in LF regions, but also present elsewhere	Not correlated	Not detected

D27	Dark background and white collar	White collar	Same distribution	Highly concentrated in LF regions, but also present elsewhere	Anti-correlated	Not detected
D28	Silver neck plate	White parts of the neck plate	Correlated	Highly concentrated in LF regions, but also present elsewhere	Not correlated	Not correlated
D29-30	Hat with feather (large map of D8)	White parts of feathers and hat	Correlated	Highly concentrated in LF regions, but also present elsewhere	Anti-correlated	Not correlated
Total		Systematically white or light	Systematically correlated (not detected in 2 maps)	Systematically correlated; but can also be present outside of LF regions; in this case, correlated with C	4 cases with no correlation; 5 cases with anti-correlation	4 cases with no correlation; 1 case with a correlation
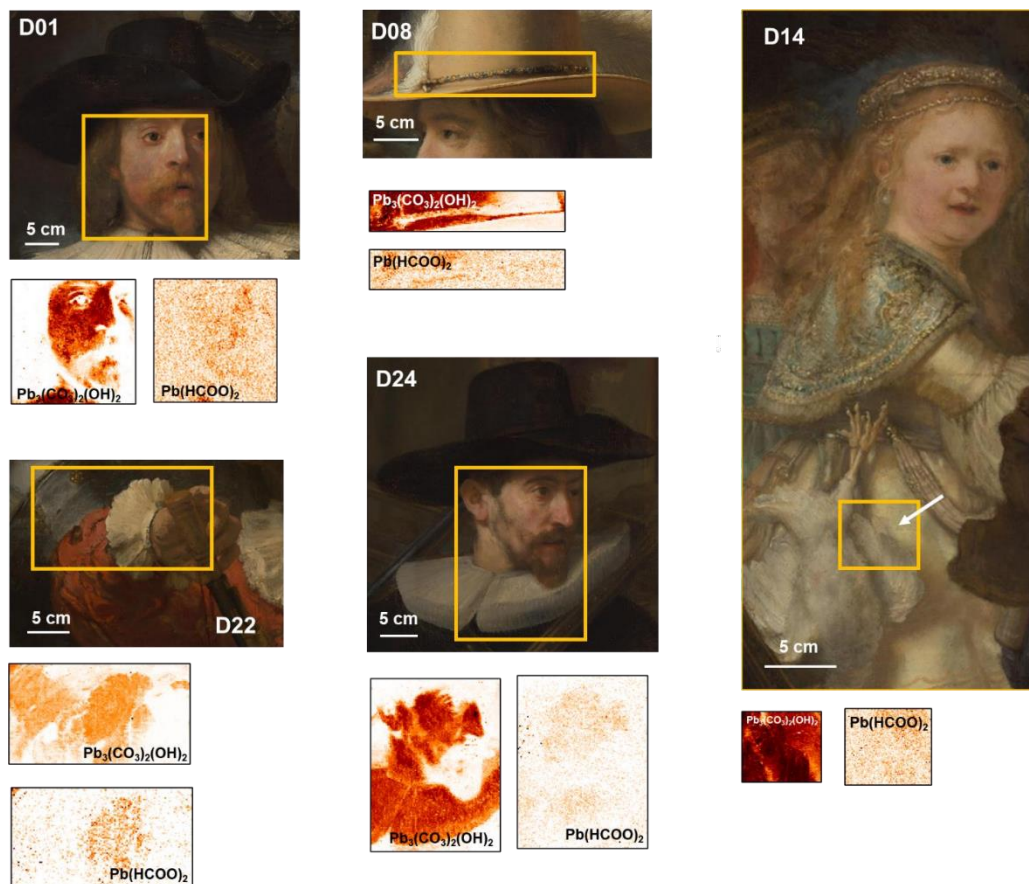
Figure S 3.2-1 Areas of *The Night Watch* probed by MA-XRPD in which LF were detected. For each area, the distributions of HC and LF are presented. The white arrow on area D14 indicates where sample SK-C-5_070 was taken.

IV)   Discrimination of original and neo-formed HC
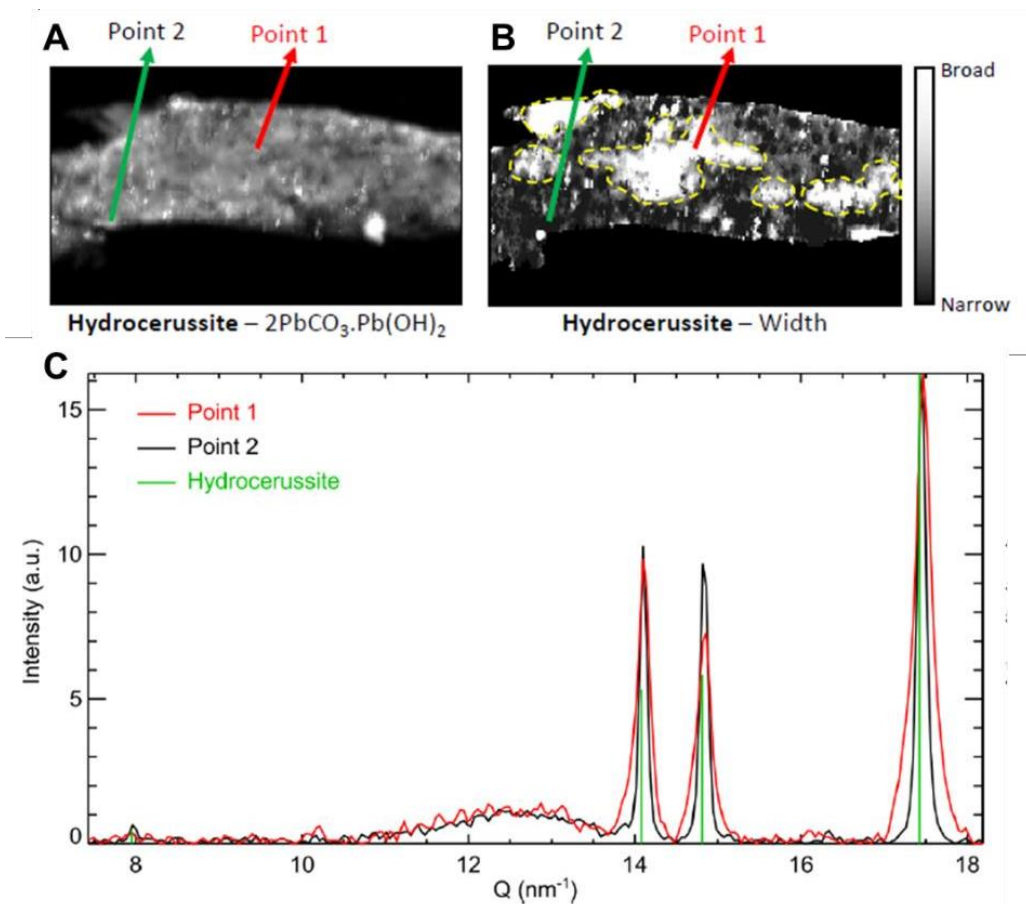
Figure S 3.2-2 A. SR-μ-XRPD distribution of HC for sample SK-C-5_070. B. Plotting of the HC peak FWHM obtained from whole pattern refinement. Broader peaks are present within the protrusion. C. XRPD patterns of HC collected in two points on the sample, inside (point 1, red) and outside (point 2, green) of the protrusion. The FWHM of HC increases within the protrusion, which could indicate an in-situ formation of HC with small crystallite size.

V)   <u>MA-XRPD map of the dog area</u>
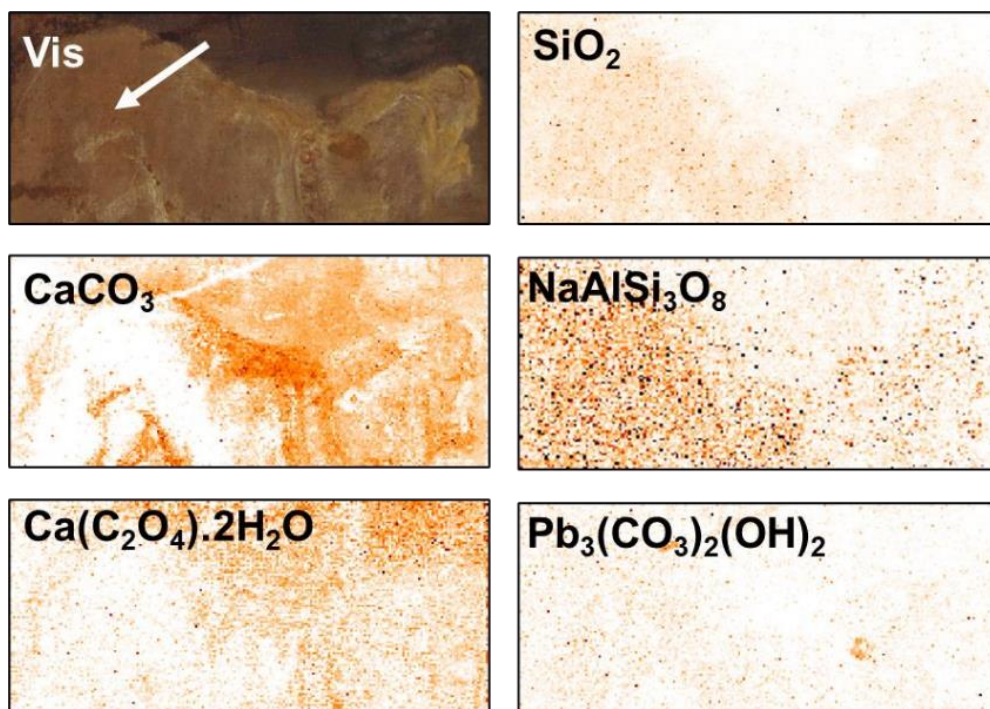
Figure S 3.2-3 MA-XRPD crystalline phases distribution on the area of the Night Watch showing the barking dog. The white arrow indicates the location of sample SK-C-5_009.

VI)   Conversion of LF into Pb(0) under SR beam
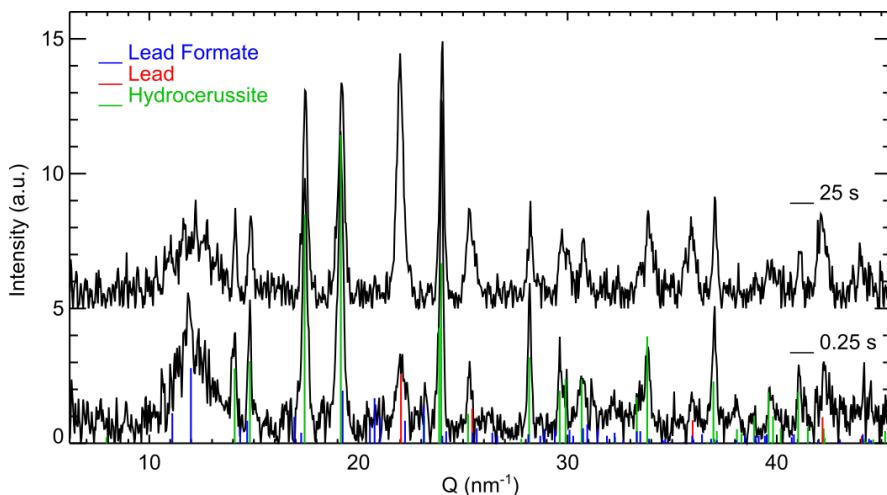
Figure S 3.2-4 Formation of Pb(0) induced by prolonged exposure to the SR beam at P06. The comparison of the pattern collected after 0.25 s and after 25 s of exposure to the SR beam shows a noticeable increase of the Pb(0) signal and a decrease of LF peaks. These patterns were obtained after a previous X-ray imaging experiment was performed on the same area.
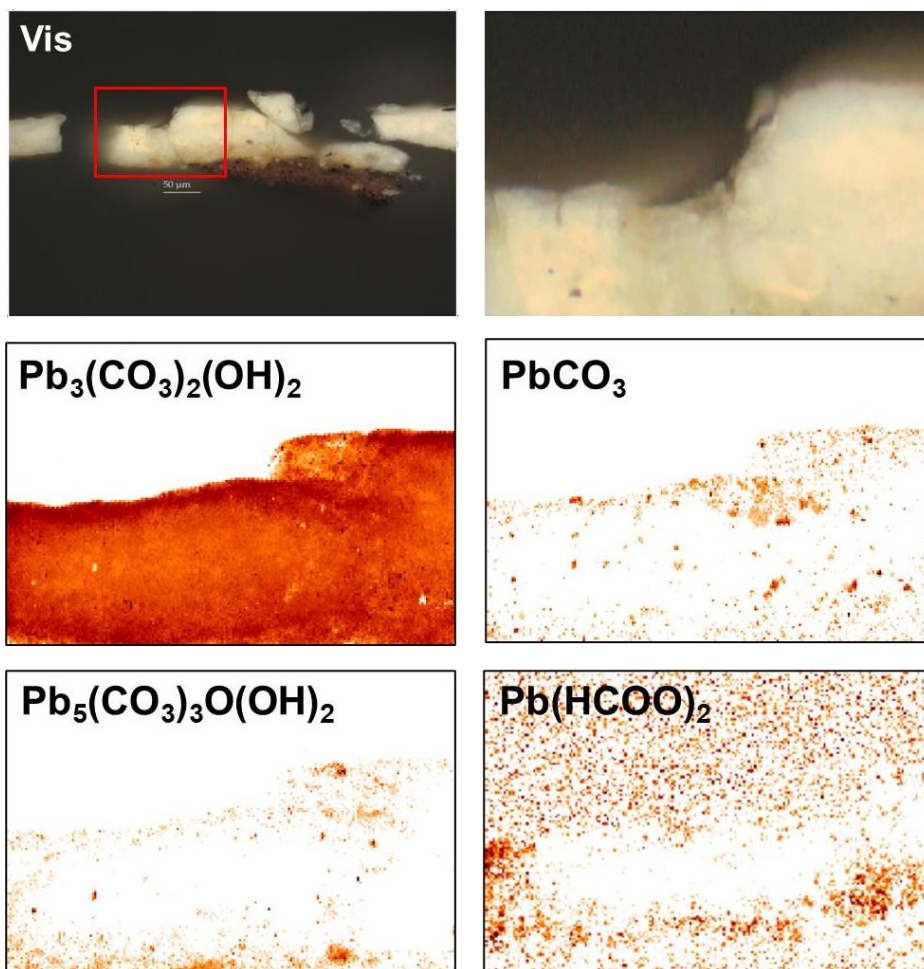
Figure S 3.2-5 SR-μ-XRPD crystalline phases distribution on sample SK-C-5_1457

In sample SK-C-5_009, a precise analysis of the fingerprint wavenumber region revealed subtle differences. Regions of interest (ROI) were defined around specific bands, highlighting the distribution of different molecular groups. Average patterns were acquired over two regions of the protrusion: the red area, highlighted by ROI1 (1484-1583 cm^{-1}), centered on the carboxylates asymmetric stretching (not specific to formate); the green area, highlighted by ROI2 (1319-1350 cm^{-1}), centered on the formate symmetric OCO stretching (ν2 according to the classification of J. Donaldson et al.) and ROI3 (1113-1202 cm^{-1}) was used to map the polyester embedding resin.[25] Comparison of the green spectrum with a reference spectrum of LF (black) shows good agreement.
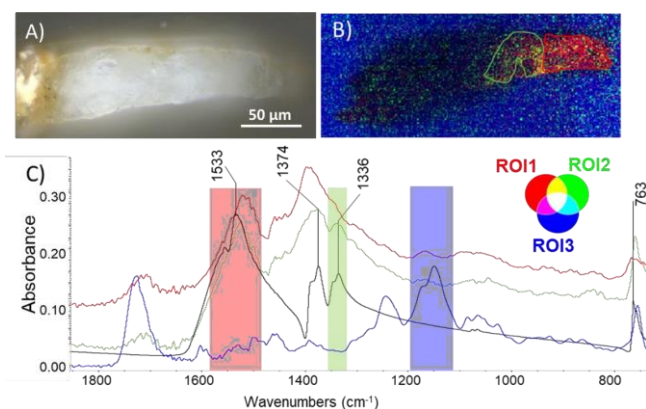
Figure S 3.2-6 A. Visible OM image of sample SK-C-5_009; B. μ-FTIR-ATR intensity maps calculated by the integration of the net intensity of the three ROIs shown in C; C. Average spectra calculated over the green and red areas plotted in B (resp. green and red spectra) and over the resin (blue), and reference FTIR spectrum of a LF powder (black), acquired in ATR mode.

IX) Summary of the SR-μ-XRPD results obtained on the fragments of mockup paints

The summary of these results can be found at the link below.

Table S 3.2-3 Overview of the presence and distribution of different Pb crystalline phases obtained by SR-μ-XRPD maps over model paint film surfaces after ageing.

https://doi.org/10.1002/anie.202216478

X) LF distribution in PaDry and PaDryPbO samples

Thin sections (1-20 μm) of films cured for two years were prepared using a microtome (Leica), by employing the classical embedding in a resin medium approach. Few additional thin sections (2 μm) were prepared for μ-FTIR analyses.[26] For SR-μ-XRPD analyses, resin edges of thin sections (10-20 μm) were glued to the holders to let the analyzed area free from mounting materials.[24] For μ-FTIR analyses, thin sections (1-4 μm) were deposited on BaF_2 crystals and analyzed in transmission using the ID21 Thermo Continuum Microscope, coupled to Nexus Spectrometer (using the internal Globar source). The beam size was set to 25×25 μm² using slits. The maps were acquired with steps of 20×20 μm2 and with 100 scans per spectrum. Maps were analyzed using the OMNIC software from Thermo and the PyMCA ROI imaging package, in particular the Non-Negative Matrix Approximation analysis (NNMA) tool.[20]
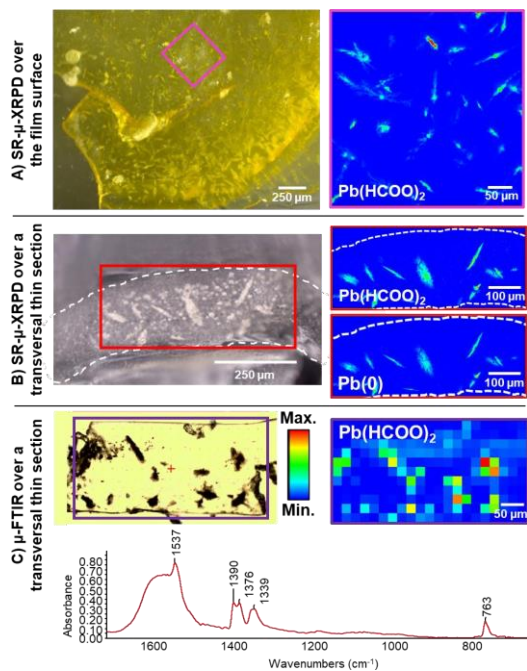
Figure S 3.2-7 Micro-analyses of PaDry cured films after two years of natural drying. A. SR-μ-XRPD distribution map B. SR-μ-XRPD distribution map on a thin section (10 μm) C. μ-FTIR over an embedding free thin section of PaDry after two years of natural ageing
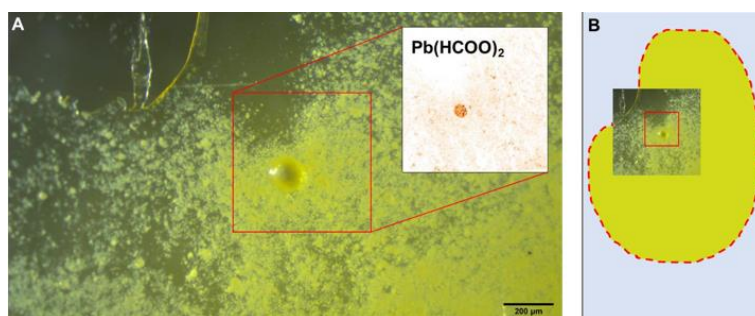
Figure S 3.2-8 A. Visible OM image of sample PaDryPbO cured film after two years of natural ageing. A. Visible OM image of the fragment. B. Scheme of the entire sample PaDryPbO highlighting the edges of the droplet.

XI)   FTIR spectra collected on PaDry curing

Initial stages of LF formation were monitored using ATR-FTIR spectroscopy on

a freshly applied PaDry droplet (Thermo Nexus spectrometer, 120

scans/spectrum, resolution 4 cm^{-1}). This figure compares spectra acquired on a fresh sample (A) and after 17 days of curing at roomtemperature (B). Differences between these two spectra are subtle, and were better highlighted by subtracting the spectra (C). The comparison with the spectrum of a reference LF powder confirms, in addition to curing reactions, the formation of LF.
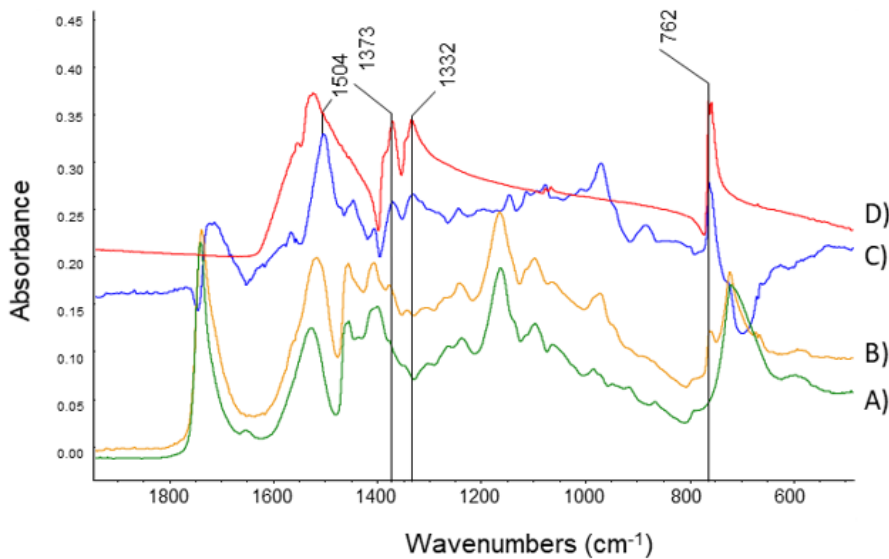
Figure S 3.2-9 ATR-FTIR spectra of A) a fresh drop of PaDry sample and B) after 17 days of natural aging. C) spectrum obtained by subtracting A from B. D) ATR-FTIR spectrum of a reference LF powder.

XII)   Effect of the film thickness on LF distribution
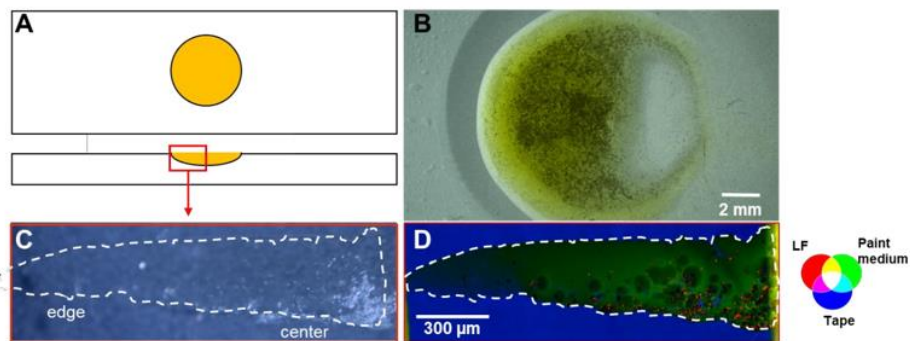
Figure S 3.2-10 Micro-analyses of PaDry droplets deposited on microscope glass slide A) Sample preparation B) Visible OM image of a droplet after 10 months C) Visible OM image of a thin droplet section after 4 months D) Distribution of 3 NNMA components

XIII)   LF distribution in LO_PbO samples
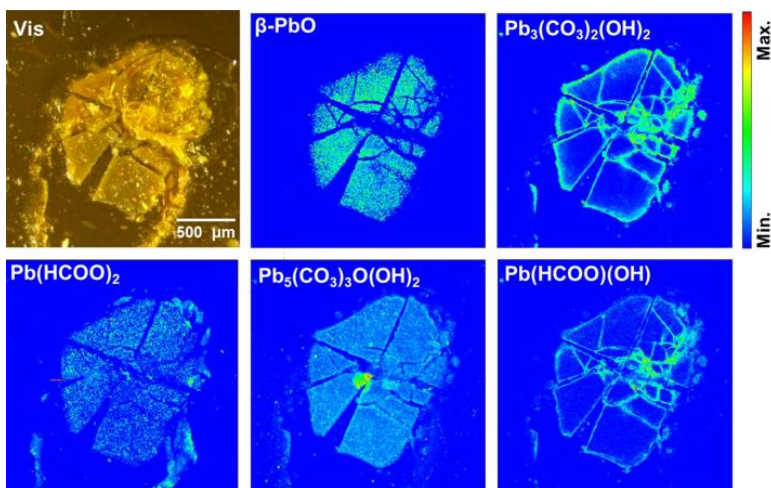
Figure S 3.2-11 SR µ-XRPD crystalline phase distributions on sample LO_PbO

XIV)   XRPD patterns collected on sample PaDryPbO
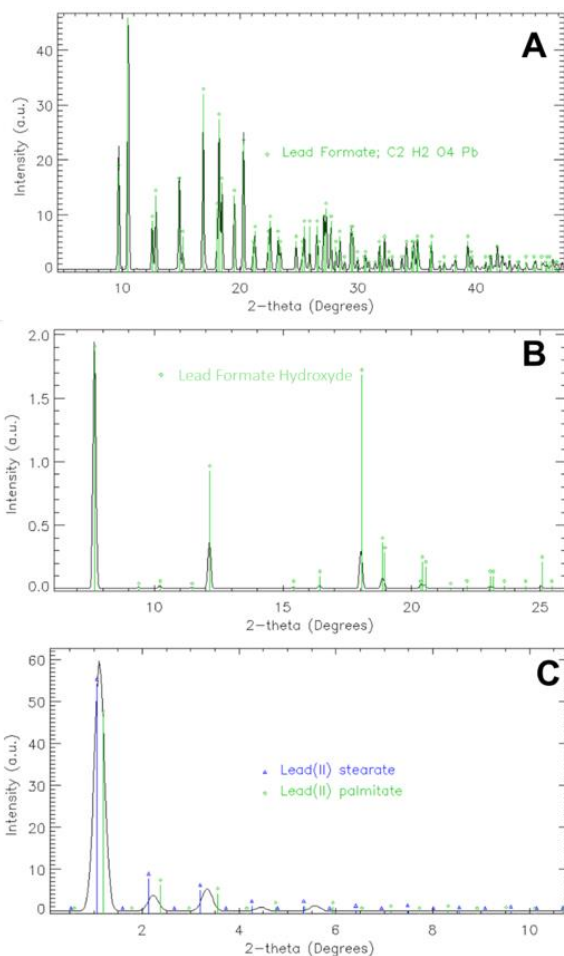
Figure S 3.2-12 XRPD patterns extracted from the SR-µ-XRPD map collected on sample PaDryPbO, allowing the identification of A. LF; B. LFH; C. Pb-soaps. Reference diffraction signals are given for lead(II) stearate and lead(II) palmitate. The experimental pattern shows diffraction peaks located between the peak positions of both references, indicating the presence of a mixed lead soap with a 16- and 18-carbon chain.[6]

XV) Summary of the SR-µ-XRPD results obtained on the thin sections of model paints

The summary of these results can be found at the link below.

Table S 3.2-4 Overview of the presence and distribution of different Pb crystalline phases obtained by SR-μ-XRPD maps over thin sections.

https://doi.org/10.1002/anie.202216478

Acknowledgements

References

(1) https://www.rijksmuseum.nl/en/whats-on/exhibitions/Operation-Night-Watch.

(2) Bomford, D.; Kirby, J.; Roy, A.; Rüger, A.; White, R. *Art in the Making: Rembrandt*; Yale University Press: Yale, 2006.

(3) Gonzalez, V.; Cotte, M.; Vanmeert, F.; Nolf, W.; Janssens, K. X-ray Diffraction Mapping for Cultural Heritage Science: A Review of Experimental Configurations and Applications. *Chem. Eur. J.* **2020**, *26*, 1703–1719.

(4) Gonzalez, V.; Cotte, M.; Wallez, G.; van Loon, A.; de Nolf, W.; Eveno, M.; Keune, K.; Noble, P.; Dik, J. Unraveling the Composition of Rembrandt's Impasto through the Identification of Unusual Plumbonacrite by Multimodal X-ray Diffraction Analysis. *Angew. Chem. Int. Ed.* **2019**, *58*, 5619–5622.

(5) De Meyer, S.; Vanmeert, F.; Janssens, K.; Storme, P. A Mobile Scanner for XRPD-Imaging of Paintings in Transmission and Reflection Geometry. In *6th Interdisciplinary ALMA conference*; Academy of Fine Arts in Prague: Brno, 2017.

(6) Cotte, M.; Gonzalez, V.; Vanmeert, F.; Monico, L.; Dejoie, C.; Burghammer, M.; Huder, L.; de Nolf, W.; Fisher, S.; Fazlic, I.; Chauffeton, C.; Wallez, G.; Jiménez, N.; Albert-Tortosa, F.; Salvadó, N.; Possenti, E.; Colombo, C.; Ghirardello, M.; Comelli, D.; Avranovich Clerici, E.; Vivani, R.; Romani, A.; Costantino, C.; Janssens, K.; Taniguchi, Y.; McCarthy, J.; Reichert, H.; Susini, J. The "Historical Materials BAG": A New Facilitated Access to Synchrotron X-Ray Diffraction Analyses for Cultural Heritage Materials at the European Synchrotron Radiation Facility. *Molecules* **2022**, *27*, 1997.

(7) Cotte, M.; Checroun, E.; Susini, J.; Walter, P. Micro-Analytical Study of Interactions between Oil and Lead Compounds in Paintings. *Appl. Phys. A* **2007**, *89*, 841–848.

(8) Kočí, E.; Rohlíček, J.; Kobera, L.; Plocek, J.; Švarcová, S.; Bezdička, P. Mixed Lead Carboxylates Relevant to Soap Formation in Oil and Tempera Paintings: The Study of the Crystal Structure by Complementary XRPD and SsNMR. *Dalton Trans.* **2019**, *48*, 12531–12540.

(9) Gonzalez, V.; van Loon, A.; WT Price, S.; Noble, P.; Keune, K. Synchrotron Micro-XRD and Micro-XRD-CT Reveal Newly Formed Lead–Sulfur Compounds in Old Master Paintings. *J. Anal. At. Spectrom.* **2020**, *35*, 2267–2273.

(10)   Gliozzo, E.; Ionescu, C. Pigments—Lead-Based Whites, Reds, Yellows and Oranges and Their Alteration Phases. *Archaeol. Anthropol. Sci.* **2022**, *14*, 17.

(11)   Schutte, C. J. H.; Buijs, K. The Infra-Red Spectrum of the Formate Ion. *Spectrochim. Acta* **1964**, *20*, 187–195.

(12)   Baraldi, P. Thermal Behavior of Metal Carboxylates—II. Lead Formate. *Spectrochim. Acta A Mol. Biomol. Spectrosc.* **1981**, *37*, 99–102.

(13)   Eggert, G.; Fischer, A. The Formation of Formates: A Review of Metal Formates on Heritage Objects. *Herit. Sci.* **2021**, *9*, 26.

(14)   Helwig, K.; Thibeault, M.-E.; Poulin, J. Jack Chambers' Mixed Media Paintings from the 1960s and 1970s: Painting Technique and Condition. *Stud. Conserv.* **2013**, *58*, 226–244.

(15)   Keune, K.; Boevé-Jones, G. Its Surreal: Zinc-Oxide Degradation and Misperceptions in Salvador Dalí's Couple with Clouds in Their Heads, 1936. In *Issues in Contemporary Oil Paint*; Springer Cham: Cham, 2014; pp 283–294.

(16)   Švarcová, S.; Kočí, E.; Bezdička, P.; Garrappa, S.; Kobera, L.; Plocek, J.; Brus, J.; Šťastný, M.; Hradil, D. Uncovering Lead Formate Crystallization in Oil-Based Paintings. *Dalton Trans.* **2020**, *49*, 5044–5054.

(17)   Garrappa, S.; Kočí, E.; Švarcová, S.; Bezdička, P.; Hradil, D. Initial Stages of Metal Soaps` Formation in Model Paints: The Role of Humidity. *Microchem. J.* **2020**, *156*, 104842.

(18)   Cotte, M.; Checroun, E.; De Nolf, W.; Taniguchi, Y.; De Viguerie, L.; Burghammer, M.; Walter, P.; Rivard, C.; Salomé, M.; Janssens, K.; Susini, J. Lead Soaps in Paintings: Friends or Foes? *Stud. Conserv.* **2016**, *62*, 2–23.

(19)   Cotte, M.; Checroun, E.; Susini, J.; Dumas, P.; Tchoreloff, P.; Besnard, M.; Walter, Ph. Kinetics of Oil Saponification by Lead Salts in Ancient Preparations of Pharmaceutical Lead Plasters and Painting Lead Mediums. *Talanta* **2006**, *70*, 1136–1142.

(20)   Cotte, M.; Fabris, T.; Agostini, G.; Motta Meira, D.; De Viguerie, L.; Solé, V. A. Watching Kinetic Studies as Chemical Maps Using Open-Source Software. *Anal. Chem.* **2016**, *88*, 6154–6160.

(21)   Hermans, J. J.; Keune, K.; Van Loon, A.; Iedema, P. D. Toward a Complete Molecular Model for the Formation of Metal Soaps in Oil Paints. In *Metal Soaps in Art*; Springer Cham: Cham, 2019; pp 47–67.

(22)   Raychaudhuri, M. R.; Brimblecombe, P. Formaldehyde Oxidation and Lead Corrosion. *Stud. Conserv.* **2000**, *45*, 226.

(23)   Van Dijk, J. *Kunst En Historiekundige Beschryving En Aanmerkingen over Alle de Schilderyen Op Het Stadhuis Te Amsterdam*; Pieter Yver: Amsterdam, 1758.

(24)   Schroer, C. G.; Boye, P.; Feldkamp, J. M.; Patommel, J.; Samberg, D.; Schropp, A.; Schwab, A.; Stephan, S.; Falkenberg, G.; Wellenreuther, G.; Reimers, N. Hard X-Ray Nanoprobe at Beamline P06 at PETRA III. *Nucl.*

Instr. Meth. Phys. Res. A: Accel. Spectrom. Detect. Assoc. Equip. **2010**, *616*, 93–97.

(25)   Donaldson, J. D.; Knifton, J. F.; Ross, S. D. The Fundamental Vibrational Spectra of the Formates of the Main Group Elements. *Spectrochim. Acta* **1964**, *20*, 847–851.

(26)   Pouyet, E.; Lluveras-Tenorio, A.; Nevin, A.; Saviello, D.; Sette, F.; Cotte, M. Preparation of Thin-Sections of Painting Fragments: Classical and Innovative Strategies. *Anal. Chim. Acta* **2014**, *822*, 51–59.

Chapter 4 Identification of degradation products

In this chapter, several case studies are presented that highlight the capacity of reflection MA-XRPD to identify and visualize alteration products formed within the stratigraphy of the painting.

In the first section, the 17th century oil painting *Girl with a Pearl Earring* by Johannes Vermeer was analysed with a combination of transmission and reflection mode MA-XRPD. By employing this scanner in reflection mode, the relative sensitivity for compounds that are present at the paint surface could be increased, establishing it as a highly relevant technique for investigating the degradation processes that are ongoing at paint surfaces. Many of the original

pigments employed by Vermeer could be identified, along with several secondary alteration products: gypsum ($CaSO_4 \cdot 2H_2O$), anglesite ($PbSO_4$), palmierite ($K_2Pb(SO_4)_2$) and weddellite ($CaC_2O_4 \cdot 2H_2O$). The formation of gypsum was linked to the presence of chalk in the upper glaze layer while the formation of palmierite and weddellite is driven by the presence of lake pigments. A paint cross-section taken from an area rich in palmierite was analysed with synchrotron µ-XRPD, which confirmed the presence of this secondary compound at the interface of the upper paint layer with the ground layer. The capacity of MA-XRPD to identify and chart secondary alteration products in a non-invasive manner has only very recently been demonstrated and makes it a highly relevant technique for the assessment of the chemical condition of works of art.

Arsenic-based compounds are the subject of investigation in the second study presented in this chapter: orpiment (As_2S_3) is often described as easily oxidizing upon exposure to light. MA-XRPD imaging on a visually degraded area of a still life painting by the 17th century Dutch painter Martinus Nellius was employed in combination with µ-XRPD imaging of a paint cross section. In this way, the *in situ* formation of secondary metal arsenate and sulfate species and their migration through the paint layer stack they originate from could be visualized. In the areas originally painted with orpiment, it could be shown that several secondary minerals have formed. Closer inspection of the cross-sectioned paint layer stack with µ-XRPD illustrates that arsenate minerals have precipitated at the interface between the orpiment layer and the layer below, rich in lead white.

In the third case study, the visual impact of degradation products on a yellow rose in a 17th century still life painting by Abraham Mignon is discussed. A multimodal combination of chemical and optical imaging techniques, including MA-XRPD and MA-XRF, provided information on both the originally intended

appearance of the flower and its transformation over time. MA-XRPD enabled the correlation of locally formed alteration products with the visual outlook of the paint surface and demonstrated that the formation of lead arsenates from orpiment and the light-induced fading of an organic yellow lake irreversibly changed the artist's intentional light-shadow modeling.

The final part of this chapter concerns the issue of *in situ* oxalate formation in artworks. To investigate the prevalence of metal oxalates, specifically in 15th-16th century Netherlandish oil paintings, a collection of fourteen different paintings were investigated with reflection MA-XRPD in an attempt to draw representative conclusions on which types of oxalates are formed and which pigments are most susceptible for oxalate formation. Calcium oxalates were most frequently identified and were strongly associated with red lake pigments while copper oxalates were commonly found in verdigris-containing zones. This macroscopic approach is part of a wider investigation into the formation of oxalates, including accelerated ageing experiments and historical cross-section analysis, that falls outside the scope of this thesis but which is planned to be published in a peer-reviewed journal at a later date.

4.1 Imaging secondary reaction products at the surface of Vermeer's *Girl with a Pearl Earring* by means of macroscopic X-ray powder diffraction scanning

4.1.1 Introduction

As a master of light and colour, Johannes Vermeer's palette was both limited and distinctive. He made extensive use of the costly pigment ultramarine and used several red pigments, including vermilion and red lakes.[1,2] While the original materials and techniques employed by Vermeer have been extensively studied, questions remain about how those materials might have changed since the work was painted in c. 1665.[3] Degradation phenomena can cause binding media, varnish layers and original pigments to undergo chemical and physical transformations, leading to discolouration or a deterioration of the structural integrity of the paint material. These processes can be initiated by internal factors, for example the chemical interaction of pigments with organic binders, or by external factors, which can range from environmental conditions (humidity and light) to the presence of airborne pollutants in museums.[4–6]

Current methods to investigate the occurrence of degradation processes of pigments at or below the painting surface usually require microscopic paint samples to be taken and prepared as cross-sections. Subsequently these samples can be analysed with laboratory-based techniques, such as scanning electron

microscopy combined with energy-dispersive X-ray spectroscopy (SEM–EDX) and Fourier-transform infrared (FTIR) spectroscopy.[7,8] Synchrotron-based methods such as microscopic X-ray powder diffraction (μ-XRPD) and X-ray absorption near edge structure (μ-XANES) also have been employed, for example to reveal the mechanism behind the conversion of red lead to plumbonacrite and to investigate the degradation of cadmium yellow pigments.[4,9]

A major disadvantage of the aforementioned techniques is that invasive sampling of the original painting is required: an undertaking that is often not permitted or limited to locations on the painting that already show signs of damage. Additionally, relying on a limited number of micrometric samples to draw conclusions about the macroscopic composition of a work of art introduces problems about whether these samples are representative of a wider area. For these reasons, several mobile non-invasive macroscopic imaging techniques have been developed in the past decade. Macroscopic X-ray fluorescence (MA-XRF) has been extensively used to acquire information about the elemental composition of a painting.[10,11] The main limitation of MA-XRF is that it cannot differentiate between compounds with a similar elemental but different molecular composition, as is often the case in degradation processes. More recently, a macroscopic scanning variant of FTIR in reflection mode (MA-rFTIR) has been developed, providing information on the molecular level; however, its application is often limited to paintings without varnish, since the latter absorbs most of the infrared radiation.[12,13] Visible/near infrared reflectance imaging spectroscopy (RIS) has also been frequently used for the investigation of oil paintings and is capable of delivering distribution images based on molecular features from both organic and inorganic compounds.[14,15]

In recent years, macroscopic X-ray powder diffraction (MA-XRPD) has also been successfully converted from a synchrotron-based imaging technique on the microscopic scale to a non-invasive laboratory-based technique on the macroscopic scale that can be deployed in situ in transmission mode, providing information on the bulk composition of the paint stratigraphy.[16] MA-XRPD was successfully employed in transmission mode to visualise the different types of chrome yellow used in Van Gogh's *Sunflowers* (1889, Van Gogh Museum) and to provide information about the orientation of the needle-shaped crystals in his brushstrokes.[17] Furthermore, MA-XRPD has been used to discriminate between pigments applied on the *recto* or *verso* side of an illuminated manuscript by considering the small angular diffraction shift.[18] Finally, MA-XRPD has also been used in reflection mode, which is more suitable for superficial analysis, to demonstrate its potential for detecting crystalline compounds present at or close to the surface of a small mock-up painting and to visualise degradation products at the paint surface of several flower still life paintings.[19,20]

In this article, MA-XRPD will be employed in reflection mode to investigate and explain the presence of secondary alteration products in Vermeer's iconic painting *Girl with a Pearl Earring* (c. 1665, Mauritshuis). The painting was last examined in 1994 using a combination of non-invasive technical photography methods (including infrared and visual light) and invasive microscopic techniques (including SEM–EDX, high-performance liquid chromatography) in order to better understand the composition of the different paint layers.[21,22] Given the advances made in both microscopic and macroscopic analytical imaging methods since 1994, a new research project, *The Girl in the Spotlight,* was initiated. The project *The Girl in the Spotlight* is a Mauritshuis initiative, and involves a team of internationally recognised specialists working within the collaborative framework of the Netherlands Institute for Conservation, Art and

Science (NICAS), with some scientists from other institutions. Within this project, the painting was analysed with a multitude of techniques, including MA-XRF, reflectance imaging spectroscopy and MA-XRPD.

4.1.2 Results and discussion

Identification of original pigments and restorations

Using MA-XRPD, several original pigments that Vermeer used in the upper layer(s) of the stratigraphy have been identified (Figure 4.1-1). The red pigment vermilion (cinnabar, HgS) was used extensively in the lips of the *Girl*, and, mixed with lead white, more sparsely in the flesh tones of her face to create a soft pink colour. Vermeer painted the blue headscarf with ultramarine (lazurite), which he also mixed into the dark yellow paint in her jacket and yellow headscarf. In the bright blue part on the left side of her headscarf, the ultramarine was mixed with lead white, which explains the visible contrast in brightness between the left (lit) and right (shadow) sides.[23] Lead white, a mixture of hydrocerussite $(2PbCO_3 \cdot Pb(OH)_2)$ and cerussite $(PbCO_3)$, has also been used throughout the entirety of the *Girl's* face. In the bright yellow part of her headscarf, MA-XRPD detected lead white while in the darker parts yellow ochre [Goethite, $FeO(OH)$] is found. Finally chalk (calcite, $CaCO_3$), together with quartz (SiO_2), is mainly present in the dark background surrounding the *Girl* and in the dark areas of her headscarf. Previous analyses of cross-sections from the *Girl* have revealed that the dark glaze layer in the background does indeed contain chalk, together with lake pigments (weld and indigo), carbon black and lead white.[22] Because XRPD is restricted to detecting crystalline compounds, the amorphous dyes in the background cannot be identified. However, these dyes are often precipitated on an inert metallic binder such as alum $(KAl(SO_4)_2 \cdot 12H_2O)$, which can be visualised using MA-XRPD. Besides original pigments, several non-original

pigments and fill materials were also identified. These are from the 1994 restoration, or in some cases earlier treatments.[21] Some damages in the *Girl's* face were filled with a putty containing chalk, and a small area was restored with goethite (associated with yellow ochre). Part of the *Girl*'s lead-white containing collar and several smaller areas in the *Girl*'s face have been retouched with a mixture containing titanium white (rutile, TiO_2) and barite ($BaSO_4$). Finally, three secondary alteration compounds were also identified: gypsum ($CaSO_4 \cdot 2H_2O$), weddellite ($CaC_2O_4 \cdot 2H_2O$) and palmierite ($K_2Pb(SO_4)_2$).
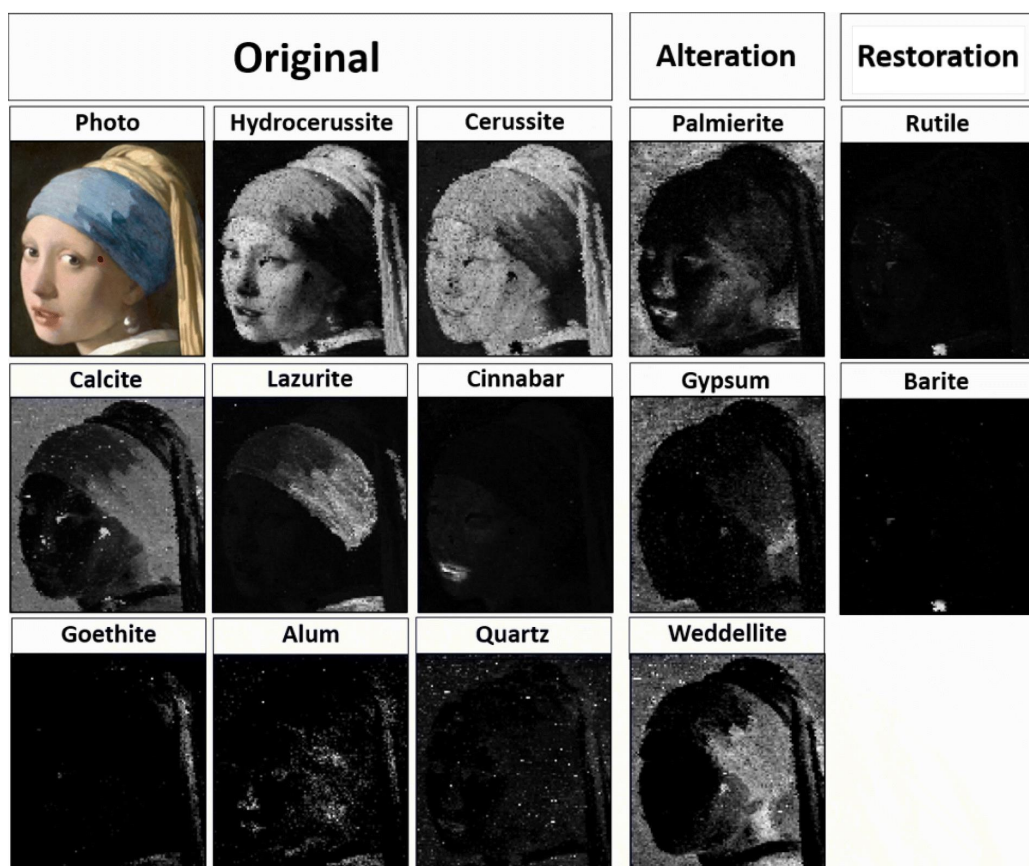
Figure 4.1-1 Results obtained with MA-XRPD. Distribution images obtained with MA-XRPD showing the scaling parameter for every pixel. Higher scaling parameters

are represented by a brighter colour. The position where the paint fragment for μ-XRPD analysis was taken is marked with a red dot.

Superficial sensitivity of reflection mode MA-XRPD

Macroscopic X-ray powder diffraction imaging allows to identify, localise and quantify crystalline compounds in a complex paint matrix. Scanning in reflection mode greatly increases the sensitivity for (thin) surface layers.[20] The X-ray beam impinges upon the painting under a small angle ($\gamma = 10°$) with the painting surface, resulting in a shallow probing depth. This sampling depth d_s varies from 10 μm or less for compounds containing 'heavy' elements (Pb) up until 50 μm for compounds consisting of 'light elements' (Ca) and was calculated using the following equation for the alteration products encountered with MA-XRPD in *Girl with a Pearl Earring* (Table 4.1-1).

$$d_s = \frac{\ln 100}{\mu\rho \left[\frac{1}{\sin(2\theta\text{-}\gamma)} + \frac{1}{\sin\gamma}\right]}$$

Table 4.1-1 Superficial sensitivity of MA-XRPD in reflection mode

Compound	Formula	Indices (hkl)	2θ (°)	d_s (μm)
Palmierite	$K_2Pb(SO_4)_2$	(10-5)	28.42	9
Weddellite	$CaC_2O_4 \cdot 2H_2O$	(020)	14.31	30
Gypsum	$CaSO_4 \cdot 2H_2O$	(021)	20.73	28

To illustrate the increased superficial sensitivity of MA-*r*XRPD, a small region of the painting was also analysed in transmission mode, facilitating a direct comparison between the two modes. In this case a measurement was taken on the *Girl*'s nose in both reflection and transmission mode (Figure 4.1-2). Transmission mode MA-XRPD shows the presence of four compounds: calcite

(chalk, $CaCO_3$), hydrocerussite (lead white, $2PbCO_3 \cdot Pb(OH)_2$), cerussite (lead white, $PbCO_3$) and wax. Hydrocerussite and cerussite are both components of the pigment lead white and together with chalk they constitute the ground layer.[22] Finally, beeswax was found as well. In 1960 the back of the painting was wax-resin lined using beeswax to provide extra support for the original canvas.[22] This clearly demonstrates that transmission mode MA-XRPD provides information about the bulk (e.g. ground layer) composition of the painting. Indeed, vermilion used in the pink flesh tones is not visible in the transmission data. In reflection mode multiple other crystalline components appear: palmierite ($K_2Pb(SO_4)_2$) and weddellite ($CaC_2O_4 \cdot 2H_2O$) are two superficial alteration compounds, while vermilion and cerussite-rich lead white are present in the upper paint layer to provide a pink flesh tone together with chalk. No information on the ground layer is obtained, but several superficial pigments and degradation compounds are revealed instead.
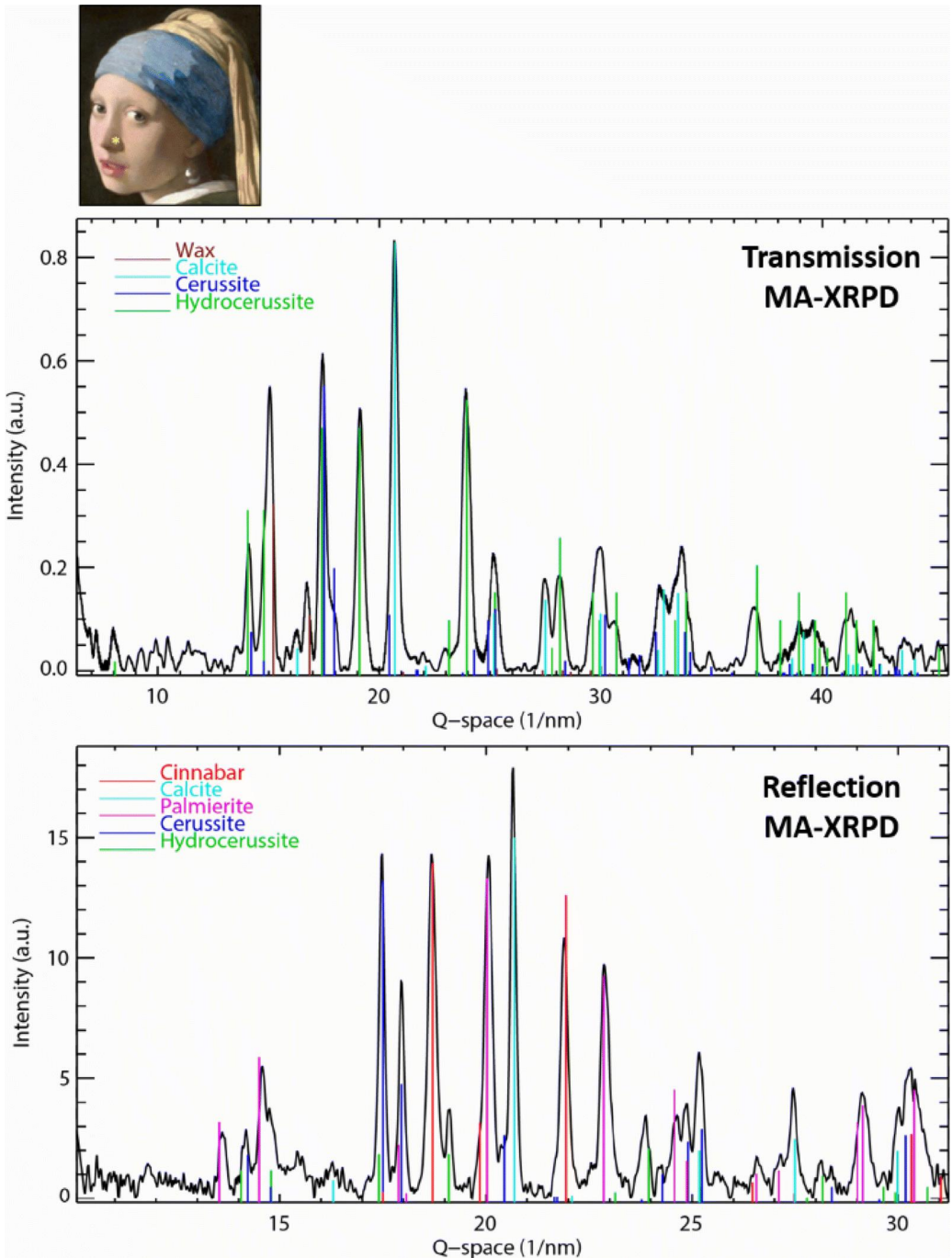
Figure 4.1-2 Comparison between transmission and reflection mode MA-XRPD. A spot measurement was performed using transmission- and reflection mode MA-XRPD

on the nose. The yellow dot indicates the position where the measurement was performed.

Alteration products in *Girl with a Pearl Earring*

MA-*r*XRPD is a useful technique for tracking the formation of secondary reaction products, which are often formed at (or close to) the surface of the painting. Three such compounds were identified on the macroscopic scale (Figure 4.1-1): gypsum ($CaSO_4 \cdot 2H_2O$), weddellite ($CaC_2O_4 \cdot 2H_2O$) and palmierite ($K_2Pb(SO_4)_2$). To further investigate the occurrence of each of these compounds a cross-section extracted from an area on the painting rich in palmierite was analysed with μ-XRPD (Figure 4.1-3). With synchrotron μ-XRPD analysis, microscopic information about all of the individual layers of the paint stratigraphy is obtained, which makes it a highly useful method not only for verification of the macroscopic data but also for providing information on layers beneath the surface.

Photo	Schematic
50 µm	Lead white + red lake Palmierite-containing layer **Ground layer + anglesite** (lead white, chalk)

| Original	Alteration
Hydrocerussite	**Palmierite**
Cerussite	**Anglesite**
Calcite	**Gypsum**
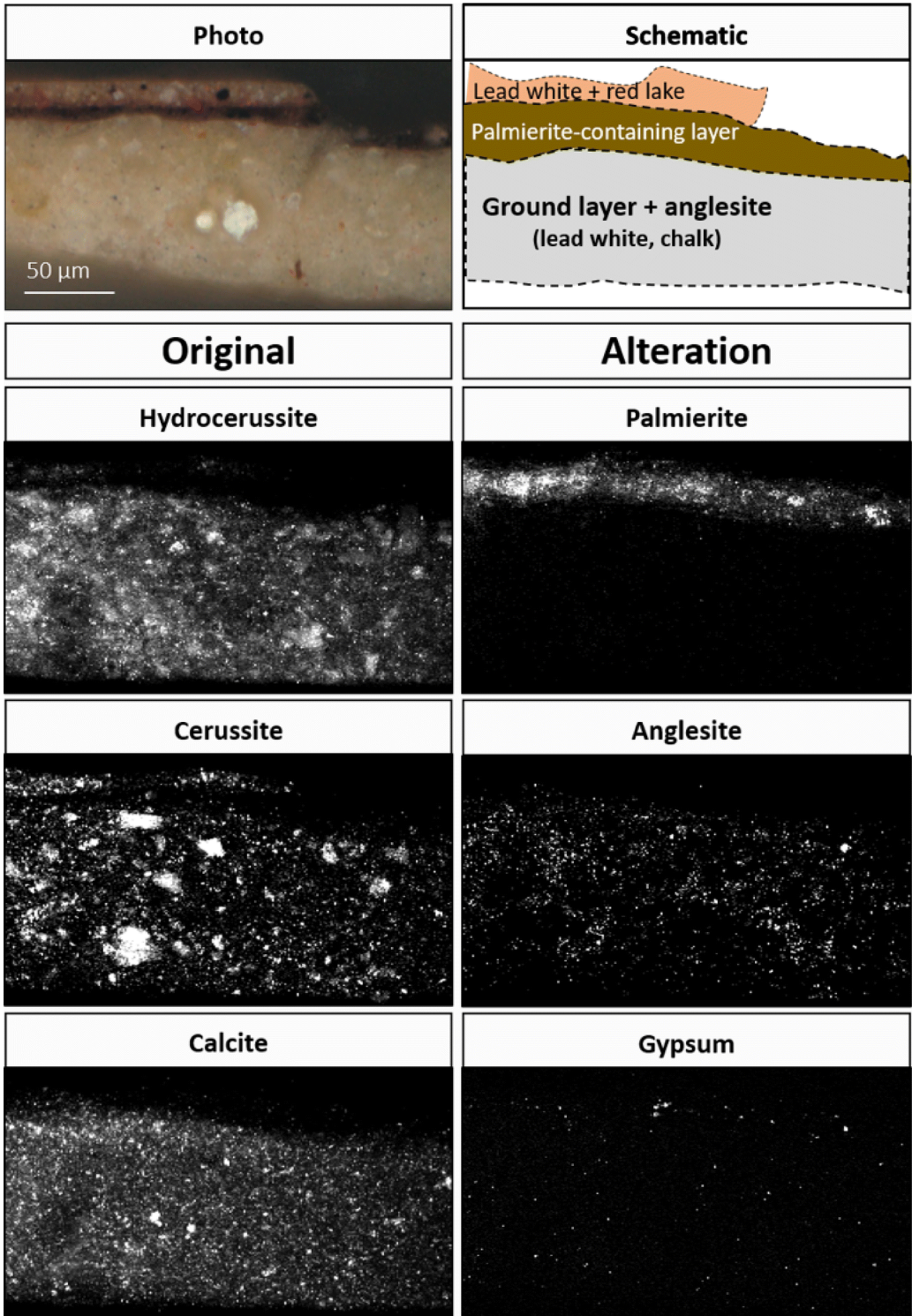
Figure 4.1-3 Results obtained with μ-XRPD. Distribution images obtained with μ-XRPD showing the scaling parameter for every pixel. Higher scaling parameters are represented by a brighter colour.

Two secondary lead sulphates were detected with MA-rXRPD and/or μ-XRPD: palmierite and anglesite (Figure 4.1-1 and Figure 4.1-3). Palmierite has previously been identified as an alteration product in paint fragments from seventeenth-century Dutch paintings by Johannes Vermeer, Jacob Jordaens and Rembrandt, and the authors have also identified it in paintings by Jan Steen, Martinus Nellius and Jan Davidsz de Heem.[20,24–28] Anglesite has previously been found on an ancient bronze inkwell and in paintings by Van Gogh and Memling.[29–31]

In *Girl with a Pearl Earring*, palmierite formed in dark areas, such as the background and the shadow tones of the *Girl*'s face (Figure 4.1-1), and is present in an underlayer between the upper paint layer and the ground layer (Figure 4.1-3). The formation of palmierite requires the supply and migration of three different ions: Pb^{2+}, K^+ and SO_4^{2-}. Figure 4.1-4 shows that sulphur (S–K) and potassium (K–K) are localised in the background of *Girl with the Pearl Earring* and in several areas of the *Girl*'s face. In the facial areas sulphur is mostly associated with the sulphur-containing pigment vermilion however. The distribution of potassium looks similar to the palmierite distribution of Figure 4.1-1. In these areas lead is present as well. It has been proposed that lead ions can be released from lead white from the ground by a reaction with the oil binding medium and can easily diffuse into the upper paint layer(s).[24,28] Additionally lead driers can act as a source of Pb^{2+} ions.[32] Potassium-containing sources include pigments such as smalt and green earth as well as lake substrates such as alum. Potash alum is a frequently used substrate for red lakes and was identified by MA-XRPD as a minor component in several parts of the *Girl*'s face, including

her lips, nose and eyes as well as in the shadow (Figure 4.1-1).[33] Alum can be considered to be a remnant of the synthesis method.[33] In areas where alum is found, there is also a significant presence of palmierite, indicating that potash alum functions here as a source of both potassium and sulphate ions for the local formation of palmierite. However, palmierite was also identified in the background, an area where no red lakes were used but that is nevertheless rich in potassium (Figure 4.1-4). During the 1994 restoration and as part of the current research, the composition of the background was also investigated. The main colourants of the glaze in the background are indigo and weld: blue and yellow dyestuffs that together create a translucent green glaze. While indigo requires no substrate, weld is soluble in oil and therefore needs to be precipitated on a substrate. For yellow lakes in 17th century Dutch paintings a substrate of chalk with a limited amount of alum was often used.[22] The presence of alum in the upper glaze layer was confirmed by FTIR analysis and SEM-EDX.[22] With MA-XRPD, however, only a limited amount of alum is identified in the background, which could suggest that most of the alum has already reacted away to form palmierite. Anglesite on the other hand was not identified with MA-XRPD because its formation is restricted to the ground layer (Figure 4.1-3).
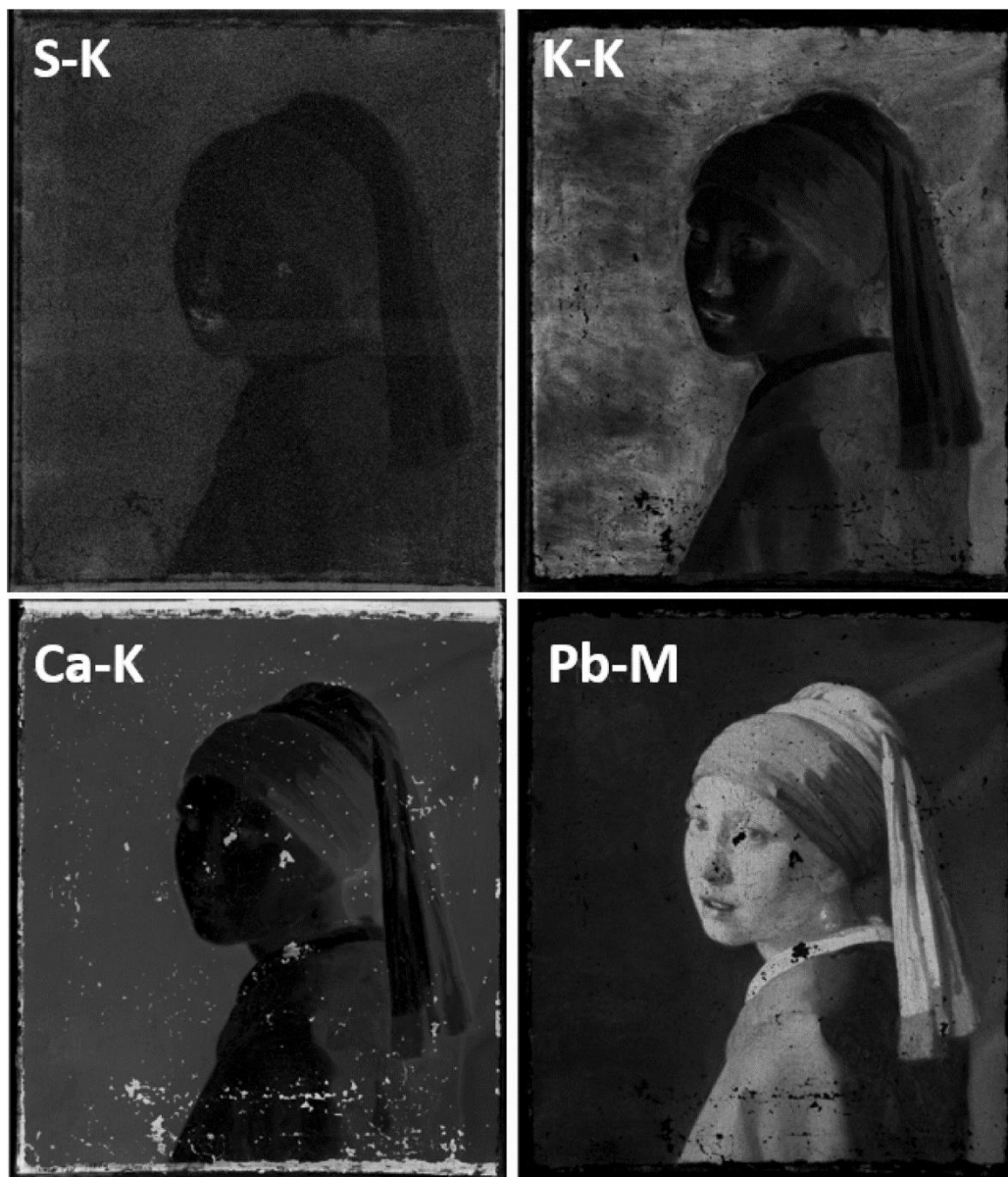
Figure 4.1-4 Results obtained with MA-XRF. Selected distribution images obtained with MA-XRF showing the elemental intensity for every pixel. Higher intensities are represented by a brighter pixel

Next to palmierite, also gypsum was identified with MA-XRPD. Historically gypsum has been used in ground layers by Southern European artists, or as an extender or bulking agent for specific pigments (e.g. orpiment).[34,35] The

superficial presence of gypsum in *Girl with a Pearl Earring* indicates it is likely a secondary reaction product. There is a very small amount of gypsum present in the ground layer, which consists mostly of chalk and lead white (Figure 4.1-3). Gypsum has often been encountered before as a degradation product in black crusts found on historical buildings and monuments as well as an alteration product in oil paintings.[20,36,37] Gypsum can also formed as minor by-product in the manufacturing process of lake pigments on a combined chalk alum substrate.[38] The formation of gypsum requires the presence of both calcium (Ca^{2+}) cations and sulphate (SO_4^{2-}) anions. Figure 4.1-1 shows that gypsum and calcite have a mostly similar distribution, suggesting that chalk from the upper glaze layer (or ground layer) is reacting with sulphate ions, which are supplied by either an external source, for example atmospheric pollutant SO_2, or an internal source, such as alum.

Weddellite was identified as a fourth secondary alteration product, alongside gypsum, palmierite and anglesite. Weddellite has been previously encountered as a degradation product on stone sculptures and gilded paintings, sometimes occurring together with its monohydrated analogue whewellite ($CaC_2O_4 \cdot H_2O$).[39,40] Furthermore, it has been demonstrated that calcium ions have an extremely high propensity to form oxalate salts over a wide pH range, explaining their common occurrence in works of art.[41] Two sources of oxalate ions for the formation of metal oxalates have been described: biological/microbial and chemical. The former is especially relevant for works of art in outdoor conditions, e.g. sculptures and wall paintings.[42] For indoor easel paintings, the potential for microbial growth is limited, yet cases of bacterial colonisation on traditional oil paintings have been reported.[43] More likely in the case of *Girl with a Pearl Earring,* a chemical mechanism is at play in which organic materials such as varnishes, binders and dyes release oxalate ions during

degradation. Figure 4.1-1 shows that weddellite is mostly formed in areas where palmierite has formed as well and where chalk is present. While palmierite requires the presence of the lake substrate alum, the formation of weddellite appears to involve the (degradation of the) organic dye itself and/or the degradation of other organic materials such as binders and varnishes. As part of degradation, the organic compounds release oxalate ions which form the stable calcium oxalate salt by reacting with calcium ions from either the upper glaze or ground layer. In the background area indigo, weld or other organic components used in the translucent green paint are suspected to be responsible for the supply of oxalate ions.

4.1.3   Conclusions

The ability of MA-XRPD to perform non-invasive, superficial and highly specific chemical imaging was demonstrated on a 17th century oil painting made by Johannes Vermeer. Besides the visualisation of a variety of inorganic pigments, several degradation products were identified. A small amount of gypsum was identified in the upper glaze layer of the background, likely the result of chalk reacting with sulphate ions released by internal or external components. Furthermore, two different lead sulphates were encountered, anglesite and palmierite. Anglesite was identified in the ground layer while palmierite was found at the surface in the background and shadow areas. Palmierite is believed to be the reaction product of the lake substrate, alum, and migratory Pb(II) ions. The calcium oxalate weddellite was encountered in similar areas, indicating that possibly the organic dye itself is involved in degradation processes.

The information that is obtained about these degradation compounds using MA- and μ-XRPD warrants further investigation to determine their exact reasons of formation. Especially the role played by organic dyes in the formation of

weddellite and palmierite in oil paintings should be examined more closely using complementary non-invasive imaging techniques capable of visualising amorphous organic compounds such as MA-*r*FTIR or NIR reflectance imaging and by performing accelerated ageing experiments under different environmental conditions.

The chemical distributions shown in this article highlight the added value MA-XRPD brings to the field of cultural heritage for the identification of both inorganic pigments and their secondary reaction products. By combining the data from MA-XRPD with µ-XRPD, superficial information on the macroscopic scale and stratigraphic details on the microscopic scale are acquired, providing insight into both the active area and mechanism of the degradation process. MA-XRPD can therefore be considered as a highly relevant technique for the in situ evaluation of degradation phenomena in a work of art, and could help guide restoration efforts by pinpointing degraded areas suitable for cleaning treatments or sampling.

4.1.4   Materials and methods

<u>Macroscopic X-ray powder diffraction imaging</u>

A laboratory MA-XRPD scanner was used to analyse the painting *Girl with a Pearl Earring.* A monochromatic Cu-K$_\alpha$ (8.04 keV) X-ray source was employed to scan the painting in reflection mode. Due to geometrical limitations dictated by the dimensions of the X-ray source, a primary beam impingement angle of 10° relative to the painting surface was chosen, leading to a beam with an elliptical footprint of approximately 1×0.2 mm^2 (horizontal × vertical). Low energy X-rays are also more easily attenuated by the sample, making this manner of scanning more sensitive for investigating superficial degradation phenomena. The X-ray source (IµS-Cu^{HB}, Incoatec GmbH, DE) generates a photon flux of

2.9×10^8 photons s^{-1}, has a focal diameter of (142 ± 2) μm, a focal distance of (20 ± 1) cm and a divergence of (2.4 ± 0.1) mrad. The painting was placed at a distance of 20 cm from the X-ray source, while the distance between the painting and 2D diffraction detector was kept at 0.5 cm. A Pilatus 200K (DECTRIS Ltd., Germany) detector was oriented at an angle of 40° with the painting surface.

X-ray fluorescence data was simultaneously acquired by means of a Vortex-EX silicon drift detector (Hitachi, JP), positioned with an angle of 45° relative to the *XY*-plane of the painting surface. A set of three motorized stages (25 cm × 10 cm × 10 cm, Newport Corp., US) are responsible for the movements during the scanning procedure. The X-ray source, PILATUS 200K detector and Vortex detector were placed on a motorized platform, capable of moving the setup in the *XZ* plane. The artwork was placed on a motorized easel, capable of moving the painting in the vertical Y-direction (Figure 4.1-5). To correct for topographical variations and curvatures on the painting surface, the *Z*-motor stage, coupled to a laser distance sensor (Baumer Hold., CH), automatically adjusts the distance between the X-ray source and the painting surface. Calibration of the setup was performed with a chalk paint layer on a mock-up canvas.
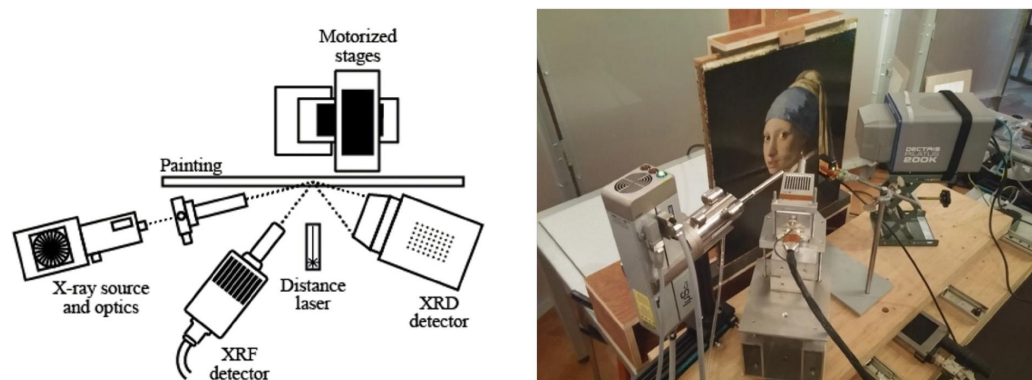
Figure 4.1-5 Schematic and visual photo of the MA-XRPD scanner

In reflection-mode an area encompassing the entirety of the *Girl*'s face (200×224 mm^2) was scanned with an exposure time of 10 s per point and a step size of 2 mm $\times$ 2 mm. This step size is larger than the actual beam footprint (1×0.2 mm^2) but was adopted because of time constraints. The total scan time for this area was approximately 35 h.

The diffraction data was processed using the XRDUA software package and with structural information files obtained from the American Mineralogist Database.[44,45] The data was fitted using a whole pattern refinement procedure. This fitting procedure has been described in detail elsewhere.[18]

Macroscopic X-ray fluorescence imaging

MA-XRF maps of the entire painting were collected in two scan sessions using the Bruker M6 Jetstream.[11] The instrument consists of a measuring head equipped with a 30 W Rhodium-target microfocus X-ray tube, a polycapillary lens, and a 60 mm^2 XFlash silicon drift detector (SDD) with a beryllium window. By slowly moving the measuring head on the *XY* motorised stage, the painting is scanned pixel by pixel. By recording the emitted X-ray fluorescence radiation, the chemical elements present in the paint can be identified. With the Bruker M6, only elements heavier than silicon can be detected. Scans were carried out at 50 kV and a current of 600 µA, with a 400 µm step size, and a dwell time of 125 ms. The distance between the scanning head and the paint surface was set at c. 1 cm, corresponding to an X-ray spot size of c. 300 µm. All data were collected with the Bruker M6 Jetstream software package. The acquired data cubes were then exported as raw files, and processed and stitched using PyMca and the in-house developed Datamuncher software.[46,47]

Microscopic X-ray powder diffraction imaging

A microscopic paint sample collected from a shadow tone of the Girl's face was used to investigate the presence of secondary alteration products as indicated by the MA-XRPD analysis. The cross-section was embedded in Technovit 2000 LC mounting resin (Heraeus Kulzer GmbH, DE) and polished using a sample holder and Micromesh sheets up to grade 12,000 (Micro-Surface Finishing Products Inc., Wilton, Iowa, USA). A Zeiss Axio Imager.A2m microscope equipped with a Zeiss AxioCam MRc5 digital camera was used to examine the polished cross section, prior to SEM–EDX analysis.

The cross-sectioned sample was analysed with μ-XRPD at beamline P06 (PETRA-III, DESY, DE), a hard X-ray micro- and nano-probe beamline suited for X-ray powder diffraction imaging experiments on the (sub-)micrometric scale. A Kirkpatrick-Baez optical system was used to focus the 21 keV beam to a diameter of 0.5 μm and a flux of 10^{10} photons s^{-1}. The sample was mounted on a plastic frame that could be moved in the *XYZ* directions. An EIGER X 4M detector (Dectris Ltd., DE) was used to collect the diffraction signals. The sample was placed at a distance of 18 cm in front of the detector, ensuring a sufficiently wide angular range.

The synchrotron diffraction data has been corrected for attenuation effects and was also processed using XRDUA.

Acknowledgments

Finally, the authors would like to declare that a small subset of the data presented in this article (i.e. the lead white related distributions) has been used in a different article within the context of investigating and quantifying the lead white ratio.

References

(1) Kühn, H. A Study of the Pigments and the Grounds Used by Jan Vermeer. *Report and Studies in the History of Art* **1968**, *2*, 154–175.

(2) Delaney, J. K.; Dooley, K. A.; Van Loon, A.; Vandivere, A. Mapping the Pigment Distribution of Vermeer's Girl with a Pearl Earring. *Herit. Sci.* **2020**, *8*, 4.

(3) Costaras, N. A Study of the Materials and Techniques of Johannes Vermeer. In *Vermeer Studies*; Gaskell, I., Jonker, M., Eds.; Studies in the History of Art; National Gallery of Art: Washington, 1998; pp 144–167.

(4) Monico, L.; Chieli, A.; De Meyer, S.; Cotte, M.; De Nolf, W.; Falkenberg, G.; Janssens, K.; Romani, A.; Miliani, C. Role of Relative Humidity and Cd/Zn Stoichiometry in the Photo-Oxidation Process of Cadmium Yellows in Oil Paintings. *Chem.: Eur. J.* **2018**, *24*, 11584–11593.

(5) Monico, L.; Sorace, L.; Cotte, M.; De Nolf, W.; Janssens, K.; Romani, A.; Miliani, C. Disclosing the Binding Medium Effects and the Pigment Solubility in the (Photo)Reduction Process of Chrome Yellows. *ACS Omega* **2019**, *4*, 6607–6619.

(6) Worobiec, A.; Samek, L.; Krata, A.; Meel, K. V.; Krupinska, B.; Stefaniak, E. A.; Karaszkiewicz, P.; Van Grieken, R. Transport and Deposition of Airborne Pollutants in Exhibition Areas Located in Historical Buildings–Study in Wawel Castle Museum in Cracow, Poland. *J. Cult. Heritage* **2010**, *11*, 354–359.

(7) Schreiner, M.; Melcher, M.; Uhlir, K. Scanning Electron Microscopy and Energy Dispersive Analysis: Applications in the Field of Cultural Heritage. *Anal. Bioanal. Chem.* **2007**, *387*, 737–747.

(8) Prati, S.; Joseph, E.; Sciutto, G.; Mazzeo, R. New Advances in the Application of FTIR Microscopy and Spectroscopy for the Characterization of Artistic Materials. *Acc. Chem. Res.* **2010**, *43*, 792–801.

(9) Vanmeert, F.; Van der Snickt, G.; Janssens, K. Plumbonacrite Identified by X-Ray Powder Diffraction Tomography as a Missing Link during Degradation of Red Lead in a Van Gogh Painting. *Angew. Chem.* **2015**, *127*, 3678–3681.

(10) Alfeld, M.; Janssens, K.; Dik, J.; De Nolf, W.; Van der Snickt, G. Optimization of Mobile Scanning Macro-XRF Systems for the in Situ Investigation of Historical Paintings. *J. Anal. At. Spectrom.* **2011**, *26*, 899–909.

(11) Alfeld, M.; Pedroso, J. V.; van Eikema Hommes, M.; Van der Snickt, G.; Tauber, G.; Blaas, J.; Haschke, M.; Erler, K.; Dik, J.; Janssens, K. A Mobile Instrument for in Situ Scanning Macro-XRF Investigation of Historical Paintings. *J. Anal. At. Spectrom.* **2013**, *28*, 760–767.

(12)   Legrand, S.; Alfeld, M.; Vanmeert, F.; De Nolf, W.; Janssens, K. Macroscopic Fourier Transform Infrared Scanning in Reflection Mode (MA-RFTIR), a New Tool for Chemical Imaging of Cultural Heritage Artefacts in the Mid-Infrared Range. *Analyst* **2014**, *139*, 2489–2498.

(13)   Gabrieli, F.; Dooley, K. A.; Zeibel, J. G.; Howe, J. D.; Delaney, J. K. Standoff Mid-Infrared Emissive Imaging Spectroscopy For Identification and Mapping of Materials in Polychrome Objects. *Angew. Chem.* **2018**, *57*, 7341–7345.

(14)   Cucci, C.; Delaney, J. K.; Picollo, M. Reflectance Hyperspectral Imaging for Investigation of Works of Art: Old Master Paintings and Illuminated Manuscripts. *Acc. Chem. Res.* **2016**, *49*, 2070–2079.

(15)   Alfeld, M.; De Viguerie, L. Recent Developments in Spectroscopic Imaging Techniques for Historical Paintings - A Review. *Spectrochim. Acta Part B* **2017**, *136*, 81–105.

(16)   Vanmeert, F.; De Nolf, W.; De Meyer, S.; Dik, J.; Janssens, K. Macroscopic X-Ray Powder Diffraction Scanning, a New Method for Highly Selective Chemical Imaging of Works of Art: Instrument Optimization. *Anal. Chem.* **2018**, *90*, 6436–6444.

(17)   Vanmeert, F.; Hendriks, E.; Van der Snickt, G.; Monico, L.; Dik, J.; Janssens, K. Chemical Mapping by Macroscopic X-Ray Powder Diffraction of Van Gogh's Sunflowers: Identification of Areas with Higher Degradation Risk. *Angew. Chem.* **2018**, *57*, 7418–7422.

(18)   Vanmeert, F.; De Nolf, W.; Dik, J.; Janssens, K. Macroscopic X-Ray Powder Diffraction Scanning: Possibilities for Quantitative and Depth-Selective Parchment Analysis. *Anal. Chem.* **2018**, *90*, 6445–6452.

(19)   De Meyer, S.; Vanmeert, F.; Janssens, K.; Storme, P. A Mobile Scanner for XRPD-Imaging of Paintings in Transmission and Reflection Geometry. In *6th Interdisciplinary ALMA conference*; Academy of Fine Arts in Prague: Brno, 2017.

(20)   Vanmeert, F.; De Keyser, N.; Van Loon, A.; Klaassen, L.; Noble, P.; Janssens, K. Transmission and Reflection Mode Macroscopic X-Ray Powder Diffraction (MA-XRPD) Imaging for the Noninvasive Visualization of Paint Degradation in Still Life Paintings by Jan Davidsz. de Heem. *Anal. Chem.* **2019**, *91*, 7153–7161.

(21)   Wadum, J. *Vermeer Illuminated: Conservation, Restoration and Research*; V+K Publishing/Inmerc: The Hague: Mauritshuis, 1994.

(22)   Groen, K.; Van der Werf, I.; Van den Berg, K.; Boon, J. Scientific Examination of Vermeer's "Girl with a Pearl Earring." In *Vermeer Studies*; Gaskell, I., Jonker, M., Eds.; Studies in the History of Art; National Gallery of Art: Washington, 1998; pp 168–183.

(23)   Van Loon, A.; Vandivere, A.; Gambardella, A.; Gonzalez, V.; Keune, K.; Haswell, R.; De Groot, S.; Proaño Gaibor, A. N.; Leonhardt, E.; Dooley, K.; Delaney, J. Out of the Blue: Vermeer's Use of Ultramarine in Girl with a Pearl Earring. *Herit. Sci.* **2020**, *8*, 25.

(24)   Van Loon, A.; Noble, P.; Boon, J. J. White Hazes and Surface Crusts in Rembrandt's Homer and Related Paintings. In *ICOM Committee for Conservation 16th Triennial Conference*; Lisbon, 2011.

(25)   Boon, J. J. Chemistry Underneath the Painting Surface: Palmierite Formation in/on a Painting by Johannes Vermeer and by Jacob Jordaens Using Laboratory- and Synchrotron-Aided Spectroscopic Methods. In *Proceedings of Microscopy & Microanalysis*; Indianapolis, 2013.

(26)   Van Loon, A.; Noble, P.; Krekeler, A.; Van der Snickt, G.; Janssens, K.; Yoshinari, A.; Nakai, I.; Dik, J. Artificial Orpiment, a New Pigment in Rembrandt's Palette. *Herit. Sci.* **2017**, *5*, 26.

(27)   Simoen, J.; De Meyer, S.; Vanmeert, F.; De Keyser, N.; Avranovich Clerici, E.; Van der Snickt, G.; Van Loon, A.; Noble, P.; Keune, K.; Janssens, K. Combined Micro- and Macro Scale X-Ray Powder Diffraction Mapping of Degraded Orpiment Paint in a 17th Century Still Life Painting by Martinus Nellius. *Herit. Sci.* **2019**, *7*, 83.

(28)   Price, S.; Van Loon, A.; Keune, K.; Parsons, A.; Murray, C.; Beale, A.; Fred, M. Unravelling the Spatial Dependency of the Complex Solid-State Chemistry of Pb in a Paint Micro-Sample from Rembrandt's Homer Using XRD-CT. *Chem. Commun.* **2019**, *55*, 1931–1934.

(29)   Remazeilles, C.; Conforto, E. A Buried Roman Bronze Inkwell: Chemical Interactions with Agricultural Fertilizers. *Stud. Conserv.* **2008**, *53*, 110–117.

(30)   Van der Snickt, G.; Janssens, K.; Dik, J.; De Nolf, W.; Vanmeert, F.; Jaroszewicw, J.; Cotte, M.; Falkenberg, G.; Van der Loeff, L. Combined Use of Synchrotron Radiation Based Micro-X-Ray Fluorescence, Micro-X-Ray Diffraction, Micro-X-Ray Absorption Near-Edge, and Micro-Fourier Transform Infrared Spectroscopies for Revealing an Alternative Degradation Pathway of the Pigment Cadmium Yellow in a Painting by Van Gogh. *Anal. Chem.* **2012**, *84*, 10221–10228.

(31)   Janssens, K.; Legrand, S.; Van der Snickt, G.; Vanmeert, F. Virtual Archaeology of Altered Paintings: Multiscale Chemical Imaging Tools. *Elements* **2016**, *12*, 39–44.

(32)   Cotte, M.; Checroun, E.; De Nolf, W.; Taniguchi, Y.; De Viguerie, L.; Burghammer, M.; Walter, P.; Rivard, C.; Salomé, M.; Janssens, K.; Susini, J. Lead Soaps in Paintings: Friends or Foes? *Stud. Conserv.* **2016**, *62*, 2–23.

(33)   Kirby, J.; Spring, M.; Higgitt, C. The Technology of Red Lake Pigment Manufacture: Study of the Dyestuff Substrate. *Natl. Gallery Tech. Bull.* **2005**, *26*, 71–87.

(34)   Gettens, R.; Mrose, M. Calcium Sulphate Minerals in the Grounds of Italian Paintings. *Stud. Conserv.* **1954**, *1*, 174–189.

(35)   Keune, K.; Mass, J.; Mehta, A.; Church, J.; Meirer, F. Analytical Imaging Studies of the Migration of Degraded Orpiment, Realgar and Emerald Green Pigments in Historic Paintings and Related Conservation Issues. *Herit. Sci.* **2016**, *4*, 10.

(36)   Toniolo, L.; Zerbi, C. M.; Bugini, R. Black Layers on Historical Architecture. *Environ. Sci. Pollut. Res. Int.* **2009**, *16*, 218–226.

(37)   Siedel, H. Salt Efflorescence as Indicator for Sources of Damaing Salts on Historic Buildings and Monuments: A Statistical Approach. *Environ. Earth Sci.* **2018**, *77*, 572.

(38)   Hermens, E.; Wallert, A. The Pekstok Papers : Lake Pigments, Prisons and Paint-Mills. In *Looking through paintings : the study of painting techniques and materials in support of art historical research*; Hermens, E., Ouwerkerk, A., Costaras, N., Eds.; Leids kunsthistorisch jaarboek XI; Archetype: London, 1998; pp 269–294.

(39)   Cariati, F.; Rampazzi, L.; Toniolo, L.; Pozzi, A. Calcium Oxalate Films on Stone Surfaces: Experimental Assessment of the Chemical Formation. *Stud. Conserv.* **2000**, *45*, 180–188.

(40)   Lluveras, A.; Boularand, S.; Rosell-Roqué, J.; Cotte, M.; Giraldez, P.; Vendrell, M. Weathering of Gilding Decorations Investigated by SR: Development and Distribution of Calcium Oxalates in the Case of Sant Benet de Bages (Barcelona, Spain). *Appl. Phys. A.* **2008**, *90*, 23–33.

(41)   Zoppi, A.; Lofrumento, C.; Mendes, N. F. C.; Castellucci, E. M. Metal Oxalates in Paints: A Raman Investigation on the Relative Reactivities of Different Pigments to Oxalic Acid Solutions. *Anal. Bioanal. Chem.* **2010**, *397*, 841–849.

(42)   Rosado, T.; Milene, G.; Mirao, J.; Candeias, A.; Caldeira, A. T. Oxalate Biofilm Formation in Mural Paintings Due to Micro-Organisms - A Comprehensive Study. *Int. Biodeter. Biodegr.* **2013**, *85*, 1–7.

(43)   Seves, A. M.; Sora, S.; Ciferri, O. The Microbial Colonization of Oil Paintings. A Laboratory Investigation. *Int. Biodeter. Biodegr.* **1996**, *37*, 215–224.

(44)   Downs, R. T.; Hall-Wallace, M. The American Mineralogist Crystal Structure Database. *Am. Mineral.* **2003**, *88*, 247–250.

(45)   De Nolf, W.; Vanmeert, F.; Janssens, K. XRDUA: Crystalline Phase Distribution Maps by Two-Dimensional Scanning and Tomographic (Micro) X-Ray Powder Diffraction. *J. Appl. Crystallogr.* **2014**, *47*, 1107–1117.

(46)   Alfeld, M.; Janssens, K. Strategies for Processing Mega-Pixel X-Ray Fluorescence Hyperspectral Data: A Case Study on a Version of

Caravaggio's Painting Supper at Emmaus. *J. Anal. At. Spectrom.* **2015**, *30*, 777–789.

(47)   Solé, V. A.; Papillon, E.; Cotte, M.; Walter, P.; Susini, J. A Multiplatform Code for the Analysis of Energy-Dispersive X-Ray Fluorescence Spectra. *Spectrochim. Acta Part B* **2007**, *62*, 63–68.

4.2 Combined micro- and macro scale X-ray powder diffraction mapping of degraded orpiment paint in a 17th century still life painting by Martinus Nellius

Contributions of the thesis author: SDM performed the MA-XRPD and SR-μ-XRD data acquisition and analysis together with FV and NDK. The manuscript was written by KJ, SDM, FV and NDK with input from all other co-authors.

4.2.1 Introduction

Photochemically and atmospherically induced alterations in artists' pigments are the result of several degradation processes, some of which are already well known while others are still in need of more detailed investigation and documentation. These alterations can often be visually perceived as color changes, either caused by a change in the oxidation state in the original material or the formation of degradation products or salts, via simple or more complex, multistep reactions.[1–4]

Degradation phenomena, and the subsequent discoloration or loss of structural integrity of paint layers they entail, are often the result of intricate physicochemical processes that are taking place within or at the surface of paint layers. They are triggered by either internal factors, such as the co-presence of mutually incompatible pigment or pigment/binder mixtures, or external factors, such as environmental conditions (relative humidity, light, and temperature), biological activity, volatile organic compounds, pollution or human interventions, or several of these together.[5]

Arsenic-based pigments such as natural orpiment (As_2S_3) or natural realgar (α-As_4S_4) are subject to such modifications and are often described as easily oxidizing upon exposure to light.[6–8]

In a number of recent studies, the oxidation of the arsenic sulfides to As(V)-species has been described.[9,10] In several multicolored flower piece paintings by the 17th century painter Jan Davidz. de Heem, the formation of rare arsenate minerals such as mimetite ($Pb_5(AsO_4)_3Cl$) and schultenite ($PbHAsO_4$) was observed, co-localized with sulfate salts such as palmierite ($K_2Pb(SO_4)_2$), syngenite ($K_2Ca(SO_4)_2 \cdot H_2O$) and gypsum ($CaSO_4 \cdot 2H_2O$).[11]

In one of these studies, the hypothesis is formulated that the resulting arsenate ions can migrate through the paint layer stack before precipitating in the form of rare arsenate minerals.[9]

By employing macroscopic X-ray powder diffraction imaging (MA-XRPD) on a sub area of a still life painting by the 17th century Dutch painter Nellius in combination with microscopic µ-XRPD imaging of a paint cross section taken in the area imaged by MA-XRPD, the in situ formation of secondary metal arsenate and sulfate species and their migration through the paint layer stack they originate in, is studied. The main motivation for performing this study is to gain a better understanding of the spontaneous transformation processes that can affect historical paintings containing arsenic-sulphide based pigments and how such alterations can change the visual outlook and mechanical stability of the affected paint.

The painting and its painter

Since 1898, the painting *Still life with Quinces*, *Medlars and a Glass* (Figure 4.2-1), is part of the collection of the Rijksmuseum acquired by bequest of Dr Daniel Franken Dzn (Amsterdam, 1838–1898).[12]

Figure 4.2-1 Still life with Quinces, Medlars and a Glass by Martinus Nellius (SK-A-1751, Rijksmuseum Amsterdam, The Netherlands) on an oak wood panel measuring

41.4 × 34.1 cm (V × H). Cross indicates sampling location of paint cross-section R36-3. Rectangle indicates area of MA-XRF/XRPD scanning

Martinus Nellius is a Dutch still life painter from the Golden age. Little is known about his life. A first mention of the painter was in 1669 where a fruit piece by 'Niellius' was listed in an inventory in Amsterdam. The birthplace of Nellius is unknown, but one record places the painter in Leiden in 1674. According to Buijsen et al, he moved to The Hague where his presence was recorded for the first time in 1676 and later in October 1719, the date of his death.[13,14]

The oeuvre of Martinus Nellius is rather modest and his works are little studied, consisting of more or less seventeen paintings, mostly signed and a few dated between 1673 and 1694.[15] The format of the paintings is quite consistent: a small rectangle (portrait format) still life painted with a preference for oil on panel with sizes ranging between 20 × 15 cm and 44 × 38 cm. Only four signed paintings are larger in size and were painted on canvas.

Objects that typically reoccur in Nellius' oeuvre, are e.g. half peeled lemons displayed in a Roemer glass or oranges, medlars, quinces, oysters usually visited by flies and butterflies. In the painting discussed in this article, Nellius painted a pair of quinces, remnants of a recently crushed walnut, hazelnuts, medlars and an open quarter of a pomegranate with a Venetian flute glass situated on the left corner of a tabletop. Nellius painted *Still life with Quinces, Medlars and a Glass* on an oak wood panel measuring 41.4 × 34.1 cm. The painting is signed in the lower left corner as '*Nellius Fecit*' but is not dated. A dendrochronology study from 1998 by Dr. Peter Klein from the University of Hamburg places the cut-date not earlier then 1667 and the possible creation of the painting as of 1669.[16] Presumably the painting was created between 1669 and 1719.

In conjunction with the exhibition ''Still life paintings from the Netherlands 1550–1720'' in the Rijksmuseum in 1999, various key still life paintings from the collection, among which the little panel of Nellius, were examined and sampled. In regard to his contemporary painters, such as Jan Davidsz. de Heem and Abraham Mignon, Nellius did not employ a complex elaborate multi-layered painting technique. The subjects were painted with one or two precise paint layers, often beneficially leaving the grey imprimatura base tone visible. A cross-section was taken from the left quince before restoration. It revealed the presence of the arsenic-based yellow pigment orpiment to paint the quinces. Originally, the orpiment must have given the quince a brighter yellow appearance then the now crumbly, dull, greyish and powdery outlook the fruit surface now features. This altered appearance became clear during restoration after varnish removal and was the motivation for the investigations described below.[15]

In art history, the iconological meaning of quinces is associated with immortality while the visiting fly may symbolically refer to the contradiction of immortality, i.e. the transient nature of the fruit itself.[17]

4.2.2 Results and discussion

In Figure 4.2-2, a series of MA-XRF images of the entire painting are shown, as well as two false color composites of the area around the left quince. While the Ca–K, Pb–L and Pb–M images mostly clearly show the painted composition as a whole, they are less informative in a chemical sense. The light green of the foliage can be associated with high levels of Sn and Cu, suggesting that a mixture of lead tin yellow and either a Cu-green (e.g. malachite and/or verdigris) or a Cu-blue (e.g. azurite) was used to obtain this tint of green. The darker greens are also associated with these two elements but show a lower Sn–L intensity, possibly because of the presence of a lake layer (rich in K and Ca) that covers the lighter

green paint below, resulting in a darker appearance. The association of the darker parts of the foliage with higher K signals can clearly be seen in the As, K, Pb composite MA-XRF image of Figure 4.2-2. The yellow parts of the painting (the yellow quince and the pomegranate fragment) have been painted with an As-containing pigment, possibly orpiment (As_2S_3) or realgar (As_4S_4) or a mixture of both. Next to a high K–K signal, the left brown medlar is associated with a high Ca–K intensity, but this signal may originate in part from the ground layer beneath (see further). In the bottom composite image of Figure 4.2-2, it can clearly be seen that slightly shaded edges and ridges of the quince and the crown leaves correspond to higher Ca signals, possibly due to the local presence of bone black. Another source of Ca may be the substrate of the red lakes. None of the depicted fruits, with the exception of the details of the walnut, show elevated Fe–K signals, generally excluding the use of earth pigments. An unclear structure is present in the left upper part of the background for which an Fe-containing paint was used; since this causes the Pb–M signals to be absorbed, this material may be present in a superficial retouching layer. In the area of the quince (and of the walnut), extensive retouching with a Ti-containing pigment (probably TiO_2, see further) has been done. In the K–K, Ca–K, Pb–M, Sn–L and Cu–K images, parts of a two-toned leaf (now hardly visible with the naked eye), positioned just above the quince, can be discerned.
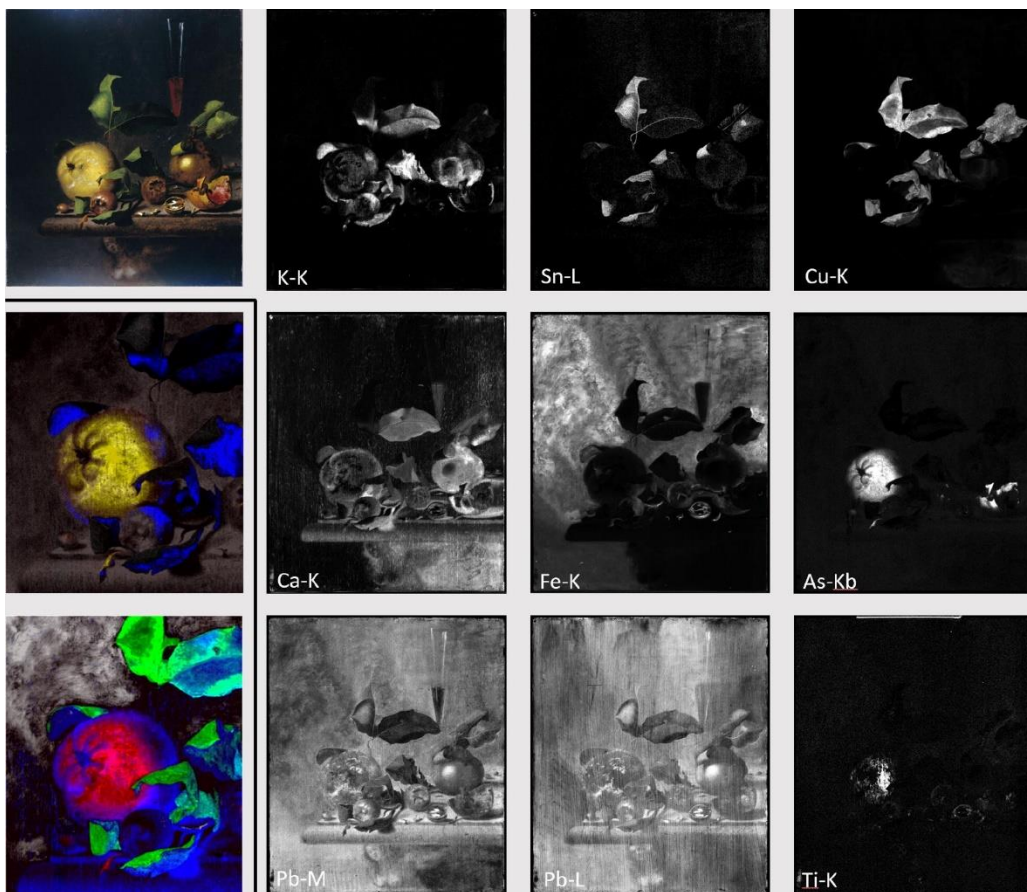
Figure 4.2-2 MA-XRF images of the painting shown in Figure 4.2-1. Top left: optical image; grey scale images show single element distributions, with lighter gray values indicating higher XRF signals. Middle and bottom images of left row show zoomed area of left quince: (middle) composite false color image of As–K (yellow), K–K (blue) and Pb–M (grey); (bottom) composite false color image of As–K$_\beta$ (red), Cu–K (green), Ca–K (blue), and Fe–K (white). Darker parts of the foliage correspond to higher K signals; slightly shaded areas of the quince correspond to higher Ca signals

Macroscopic X-ray powder diffraction mapping of a degraded yellow paint area

In Figure 4.2-3, macroscopic distributions of specific chemical elemental and crystalline phases of a small subarea of the painting are shown. This subarea is indicated in Figure 4.2-1 and corresponds to the upper left corner of the left quince that exhibits a greyish-pale yellow appearance. This quince is suspected

to have had a much more saturated light-yellow color, typical of quinces. Since the X-ray beam impinges the painting under a shallow angle (of around 10°), only the most superficial paint layers (approximately the top 5–10 micrometers) are sampled.[11,18] By combining information of the large scale (Figure 4.2-2) and small scale MA-XRF maps (Figure 4.2-3) with the visual color of the investigated area and with background knowledge on common painters' pigments available in 17th C Amsterdam, already an approximate identification of the pigments employed for painting the quince can be made.

Secondary	Primary materials	Elements

Malachite
$2CuCO_3 \cdot Cu(OH)_2$

Cu-K

Lead-tin yellow
Pb_2SnO_4

Sn-L

P-K

Hydroxyapatite
$Ca_{10}(PO_4)_6(OH)_2$

Gypsum
$CaSO_4 \cdot 2H_2O$

Calcite
$CaCO_3$

Ca-K

Syngenite
$K_2Ca(SO_4)_2 \cdot H_2O$

K-K

Palmierite
$K_2Pb(SO_4)_2$

Hydrocerussite
$2PbCO_3 \cdot Pb(OH)_2$

Cerussite
$PbCO_3$

Pb-M

Schultenite
$PbHAsO_4$

Orpiment
As_2S_3

As-K

S-K

Mimetite
$Pb_5(AsO_4)_3Cl$

Cl-K

MA-XRPD

MA-XRF

183
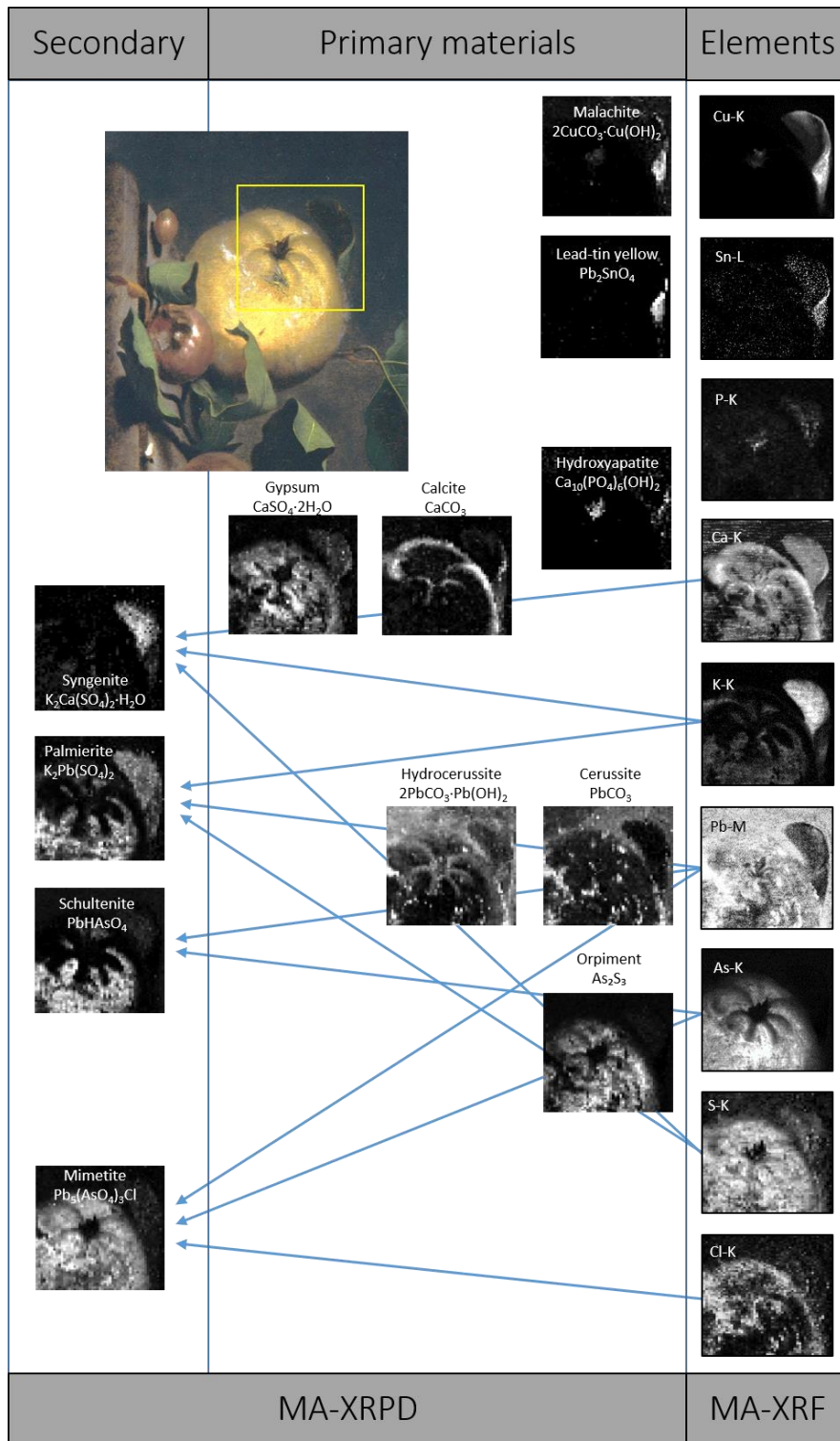
Figure 4.2-3 Elemental and phase specific maps of a sub area (6.5×7 cm^2) of the painting showing part of the left quince and an adjacent leaf. Top panel: MA-XRF maps of various elements; middle panel: MA-XRPD distributions of several crystalline compounds, assumed to have been originally present in the paint; lower panel: MA-XRPD distributions of secondary minerals, formed in situ. Arrows link elemental and secondary mineral distributions

It is clear from the diffraction maps that the resolution of reflection mode MA-XRPD is insufficient to map out fine details such as the insect visiting the quince. The grey/black pigment in this feature is also not detected by XRPD. Some of the lower resolution/small scale MA-XRF maps of Figure 4.2-3 were recorded with an 8.04 keV primary beam during the combined MA-XRF/MA-XRPD scans; these include elemental distributions such as S, P and Cl that could not be detected by the commercial MA-XRF instrument in the conditions used here (polychromatic primary beam of higher energy, 5–22 keV range; and a much shorter dwell time). Several XRF maps (such as those of Ca, K, P, Mn and Fe) allow to visualize the aforementioned two-toned leaf, situated in the upper left corner of the imaged area. The green shade of this leaf has been realized with a pigment that contains Sn, likely lead tin yellow. Some of the darker parts of the scanned area (such as the crown leaves of the quince) are associated with higher P–K levels, suggestive of the use of (phosphate-rich) bone black in these areas. Other dark areas (background, crown leaves) are associated with Mn and Fe (not included in Figure 4.2-3), suggestive of the use of earth pigments (and more in particular umber or Siena earths) to obtain the dark color. The S–K and As–K distributions clearly correspond to the yellow areas and thus very likely with an As-sulfide pigment such as orpiment (the presence of realgar is also consistent with the S and As distributions but the yellow colour makes this less likely). Clearly no lead tin yellow was employed to paint the yellow fruit. The bright areas of the Pb–M map seem to resemble the map of Cl–K, suggesting that a (Pb, Cl) containing compound may be present. In some areas, the Pb–M distribution

is complementary to that of Ca–K, suggesting that a Pb-containing material is present on top of a Ca-containing paint layer. The presence of Ca in the yellow area is not illogical since gypsum is known to have been added to orpiment-based paints.[19] There are, however, significant differences among the S–K and Ca–K distributions. The K–K and Cl–K distributions appear complementary to each other and are not so easily associated with a specific pigment. Together with Ca–K, the K–K map does reflect to some extent the areas on the surface of the fruit where shadows were painted and thus the K–K distribution may reflect (in part) the presence of (red) lakes applied on top of the yellow paint. The same could be true for Ca–K in case a lake was employed precipitated onto a Ca-containing inorganic substrate. Generally speaking, however, the Pb–M, Cl–K, K–K, Ca–K are not easily interpretable in terms of either pigments or other materials present based on their XRF data alone.

A more specific pigment identification is possible when the corresponding MA-XRPD maps are considered (Figure 4.2-3, middle and lower panel) in comparison to the corresponding elemental maps (also shown in Figure 4.2-3, upper panel). The As_2S_3 map clearly confirms the use of only orpiment (i.e. no realgar encountered above the detection limit of MA-XRPD) for painting the yellow fruit. Lead tin yellow (another yellow pigment) is only used in the green of the leaf. Both in the leaf and in the crown leaves of the quince some hydroxyapatite (bone black) is present. The gypsum distribution resembles that of orpiment while that of calcite is largely confined to the (slightly shaded) edges of the quince and ridges around the crown leaves. In this particular area, the hydrocerussite distribution is somewhat similar to that of calcite. Cerussite and hydrocerussite appear to be co-localized in the white highlights that were applied on the yellow surface of the quince.

Next to orpiment, of which the presence in a 17th century painting can be expected/is plausible, also the rare As-containing minerals schultenite ($PbHAsO_4$) and mimetite ($Pb_5(AsO_4)_3Cl$) are found to be present in the general yellow area, but with distributions that are quite different from each other. Consistent with the recent literature on this topic, the rare nature of these minerals strongly suggests that they are secondary products.[9,11] These were not part of the paint employed by Nellius during the creation of the painting and were formed in the course of the past 350 years on or near the surface of the paint as a result of spontaneous chemical transformation processes. Indeed, both orpiment and realgar are known to be light-sensitive, causing their color to fade.[6] For orpiment, a direct photo-oxidation to arsenolite (As_2O_3) takes place, while in the case of realgar an intermediate, pararealgar (As_4S_4), is initially formed.[20–22] Recently it was found that in a subsequent oxidation step arsenolite can be further transformed into soluble arsenates.[9]

Other secondary products that are found on this flower still life are palmierite ($K_2Pb(SO_4)_2$) and syngenite ($K_2Ca(SO_4)_2 \cdot H_2O$), two mixed K-based sulfates with either Ca^{2+} or Pb^{2+} as divalent ions. Both these secondary products are abundantly present in the leaf above the quince where they have the same distribution. In the yellow areas, they are also present but only with a partially similar distribution. In the MA-XRPD data, no indication of the presence of the alum substrate of the lakes (assumed to be a primary material) is visible in this case, suggestion that most or all of it became converted into other sulphates. Both secondary sulfates are less abundantly present in the radial areas around the crown leaves of the quince where there is also less schultenite and less K (see XRF image) present. In turn, somewhat more Ca, corresponding to calcite and gypsum, as well as more hydrocerussite are found in this region. While the cerussite image largely resembles the hydrocerussite distribution, it does not

show a higher abundance in the aforementioned radial areas. The comparison of the Ca-K MA-XRF map with the MA-XRPD map of calcite, bone black (hydroxyapatite), gypsum and syngenite clearly shows the different spatial distribution of these four calcium compounds. The MA-XRPD map of lead tin yellow is quasi identical to the Sn–L MA-XRF map, identifying this traditional yellow pigment as the single Sn-containing compound present. In the brighter green of the leaf, and to a lesser extent in the crown leaves and in the background area, malachite is shown to be present.

Syngenite is a frequently encountered secondary salt, either as a weathering product in black crusts or as efflorescence layers on stone monuments, mural paintings and medieval (K-rich) glass.[23–29] In some cases it has been found below the surface of artworks, such as in a red–orange Baroque bole ground or as a raw material in the plaster of a Chinese wall painting.[30,31] On the other hand, palmierite is less commonly reported as a sulfate salt on stone sculptures, medieval glass windows and wall paintings.[32–34] Palmierite has been encountered in multiple paintings from 17th century Old Masters such as Vermeer, Jordaens and Rembrandt.[35] After migration of Pb^{2+} from lead white to upper paint layers, it can react with K^+ (present in e.g. smalt, lake substrates and earth pigments) and SO_4^{2-} (present in lake substrates, such as potassium alum ($KAl(SO_4)_2 \cdot 12H_2O$), or from environmental SO_2) to precipitate as palmierite.[35–37]

It is noteworthy that the schultenite distribution is quite different from that of the parent pigment orpiment, and similar to that of K and palmierite, suggesting that the formation of schultenite is facilitated when more K is locally present at or just below the surface, e.g. in lake brush strokes. In the very K-rich parts of the scanned areas (especially the leaf above the quince), K also appears to have become the preferred cationic partner for capturing sulfate ions; it would appear

that in the presence of both Ca^{2+} and Pb^{2+} ions (next to K^+), the sulfates syngenite and palmierite coprecipitated.

Although, based on these maps, certain hypotheses on the formation of these various salts can be made, it remains very difficult/impossible to infer information on the depth ordering of the various primary and secondary products that can be identified. Do the secondary arsenate compounds form (i) on top of orpiment, (ii) in the same stratum as their parent compound or (iii) below it? Have the secondary sulfates coprecipitated with schultenite on the surface of the painting or are they located at different depths below the surface. To obtain more information about the sequence of these layers, a paint cross section taken from the central part of the quince was examined.

Microscopic X-ray powder diffraction mapping of a minute paint cross-section

In Figure 4.2-4, two composite false color maps of relevant primary and secondary crystalline compounds obtained by μ-XRPD from a minute paint cross section sampled in the central yellow part of the quince are shown. The sampling position is indicated in Figure 4.2-1. With μ-XRPD, information on the composition of each individual paint layer can be obtained. From these data, and consistent with the MA-XRPD data discussed above, the presence of a number of white/colorless compounds such as calcite and hydrocerussite in well-defined paint strata can be clearly visualized as well of that of yellow orpiment. These compounds can be readily assumed to have been original components of Nellius' paint(s). Again consistent with the MA-XRPD data, the presence of compounds that are likely to be secondary compounds such as palmierite, mimetite and schultenite can now be unambiguously linked to specific layers in the paint stratigraphy. The second lead-arsenate based rare mineral, mimetite

$(Pb_5(AsO_4)_3Cl))$ features a substantially higher Pb:As atomic ratio (5:3) than schultenite (1:1).
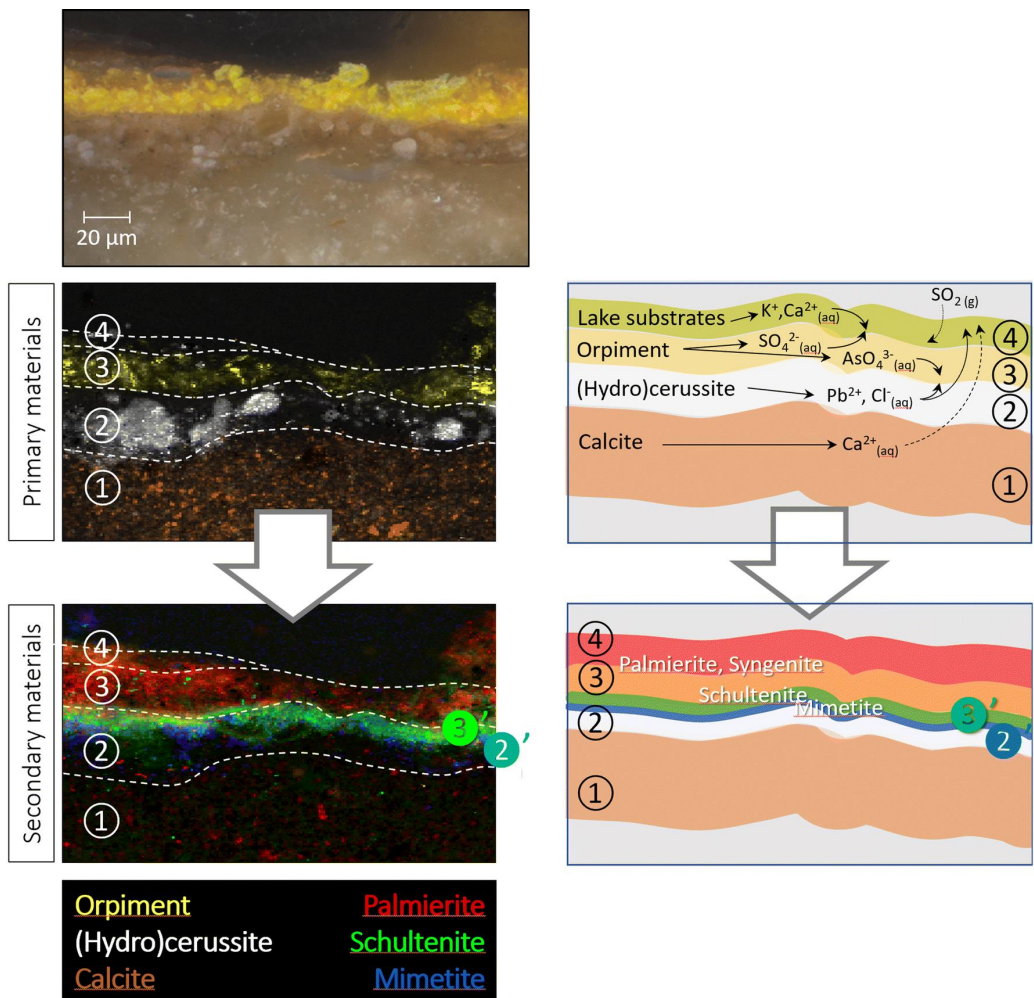
Figure 4.2-4 Optical micrograph of scanned area $(200 \times 110 \ \mu m^2)$ of cross sectioned paint sample R36-3 (top). In-depth distribution of primary compounds obtained by μ-XRPD scanning (see Figure 4.2-1 for sampling location): RGB composite maps of some primary compounds (middle panel) and secondary compounds (lower panel). As a result of the degradation processes that oxidize the original orpiment present in layer ③ and hydrolyze the lead white in layer ②, followed by migration of the resulting arsenate, sulfate, calcium and lead ions, at the interface between layers ② and ③ (indicated as ❷′ and ❸′) but also at the surface of the paint (indicated by ④) secondary compounds such as palmierite, syngenite, schultenite and mimetite precipitate.

Previously, mimetite has been reported on three Hellenistic steles from Alexandria, in several murals and in one case was considered to be a degradation product formed from the interaction between orpiment and red lead (Pb_3O_4).[38–43] Schultenite was recently reported as a degradation product of orpiment, together with arsenolite (As_2O_3), on a colonial American polychromed chest on stand.[9] Fully consistent with the observation of Figure 4.2-4, Vanmeert et al. have recently encountered both arsenates in degraded areas on several paintings by De Heem.[11]

From the depth distributions of a number of primary compounds (Figure 4.2-4), a relatively simple, four-layered structure of the original paint can be inferred, consisting of a ground layer ① containing calcite ($CaCO_3$), covered by a second layer ② containing coarse particles of cerussite ($PbCO_3$) and hydrocerussite ($2PbCO_3·Pb(OH)_2$), which in turn is covered by a yellow layer ③ containing finely ground particles of orpiment (As_2S_3). Inside layers ② and ③, also a few large grains of gypsum ($CaSO_4·2H_2O$) can be observed in the μ-XRPD maps. On top of layer ③, although not discernable by XRPD, a (yellow) lake layer ④ is present e.g. to create the effect of shading on the quince surface. This layer is visible in UV image of this sample (not shown).

It is highly relevant to establish where exactly in the original stratigraphy, the highest local concentration of the secondary products has formed. For the arsenates, unsurprisingly, this is at the interface between the As-rich orpiment layer ③ and the Pb-rich lead white layer ② (labelled ❷′ and ❸′ in Figure 4.2-4). Next to that, inside/near the top layer ④ also some arsenate minerals are present. On the basis of Figure 4.2-4, it is possible to formulate a relatively simple mechanism of formation for the secondary products, consisting of essentially three steps: (i) release of specific ions as a result of (photo)degradation in their

parent paint layers, (ii) migration of these ions towards other layers and (iii) local precipitation of one or more crystalline secondary products. One can imagine that in layers ② and ③, light-induced and other degradation processes in first instance give rise to respectively mobile AsO_4^{3-}, SO_4^{2-} and Pb^{2+} ions while from layer ① Ca^{2+} ions can be released. The chemical transformation to produce the arsenate and sulfate ions from orpiment clearly is an oxidation process since the As(III)-species that are originally present in orpiment become As(V)-species while the sulfidic counter ions become sulfate species, as already described more in detail by Keune et al. and Vermeulen et al.[9,10] This oxidation process can only take place in the presence of moisture and oxygen inside the porous paint, according to the following reactions:

$$2\ As^{3+}_{(s)} + 6\ H_2O_{(l)} + O_{2(g)} \rightarrow 2\ HAsO_4^{2-}{}_{(aq)} + 10\ H^+{}_{(aq)}$$

$$3\ S^{2-}_{(s)} + 12\ O_{2(g)} \rightarrow 3\ SO_4^{2-}{}_{(aq)}$$

$$As_sS_{3(s)} + 6\ H_2O + 13\ O_2 \rightarrow 2\ HAsO_4^{2-}{}_{(aq)} + 3\ SO_4^{2-}{}_{(aq)} + 10\ H^+{}_{(aq)}$$
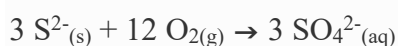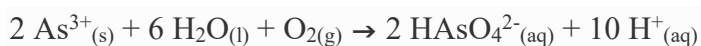
(In the above equations, "$HAsO_4^{2-}$" should be understood to denote all protonated forms of arsenate ions, ranging from the fully protonated H_3AsO_4 to the completely deprotonated AsO_4^{3-}; the average degree of protonation is pH dependent.) The above redox reaction leads to the formation of acidic species and a lowering of the pH of the aqueous phase present in the paint. Either the latter is present as microdroplets of solution inside the porous paint layer (pore water) or as an absorbed layer of water molecules at a (polar) paint surface. In the latter case, the high polarity of the surface of the pigment grains may enhance the reaction rates. Through diffusion or a process of cyclic moisture evaporation/drying and water condensation inside/wetting of the paint layers, the acidic solution that originates in the orpiment layer ③ can reach the lead white layer ② where the dissolution of the lead white can be enhanced above its

'normal' level. The release of Pb^{2+} ions from lead carbonates, in some cases leading to e.g. the in situ formation of lead soaps and other compounds, is a well-known and elaborately studied phenomenon;[35] the acidic groups of the oil binding medium are already sufficient to promote the dissolution of Pb^{2+} ions. This process consumes free protons and involves the release of CO_2:

$$PbCO_{3(s)} + 2\ H^+_{(aq)} \rightarrow Pb^{2+}_{(aq)} + CO_{2(g)} + H_2O_{(l)}$$

$$2\ PbCO_3 \cdot Pb(OH)_{2(s)} + 6\ H^+_{(aq)} \rightarrow 3\ Pb^{2+}_{(aq)} + 2\ CO_{2(g)} + 4\ H_2O_{(l)}$$
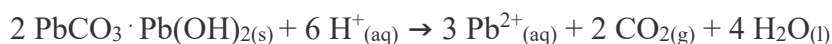
Since the concentration of H_3O^+ ions in the aqueous phase will be the largest at the interface between the orpiment layer ③ and the lead white layer ②, it will be in this contact area (labelled with ❷′ in Figure 4.2-4) that the highest concentration of Pb^{2+} ions in solution will be encountered. The further into the lead white layer the acidic solution diffuses/penetrates, the more it will become neutralized as H_3O^+ ions are replaced by (solvated) Pb^{2+} ions.

At the orpiment–lead white interface area, we hypothesize that two streams of ions may encounter one another: on the one hand solvated arsenate ions that are formed in the orpiment layer and that are migrating towards the lead white layer, while on the other hand solvated Pb^{2+} ions move in the other direction. In this [already partially (?) neutralized] acidic solution, all necessary ions are available to allow precipitation of the arsenate mineral schultenite ($PbHAsO_4$). This precipitation reaction also consumes protons:

$$Pb^{2+}_{(aq)} + HAsO_4^{2-}{}_{(aq)} \rightarrow PbHAsO_{4(s)}$$
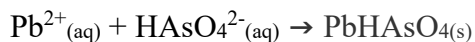
It is interesting to note that slightly below the schultenite layer, i.e. slightly closer to the source of Pb^{2+} ions and slightly more distant from the source of $HAsO_4^{2-}$ ions, possibly at a location where the pH is slightly higher and the acid–

base equilibrium between $HAsO_4^{2-}$ and AsO_4^{3-} favours the presence of AsO_4^{3-}, a second rare arsenate mineral, mimetite ($Pb_5(AsO_4)_3Cl$) has precipitated (labelled ❸′ in Figure 4.2-4):

$$Pb^{2+}_{(aq)} + Cl^-_{(aq)} + 3\ AsO_4^{3-}_{(aq)} \rightarrow Pb_5(AsO_4)_3Cl_{(s)}$$
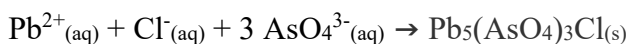
In addition, when we compare the value of the precipitation products of these two minerals ($K_{s,25\,°C} \approx 10^{-23}$–$10^{-24}$ for schultenite and $K_{s,25\,°C} \approx 10^{-76}$–$10^{-83}$ for mimetite) and finally consider that the effect of $[Pb^{2+}]_{aq}$, i.e. the equilibrium concentration of solvated Pb^{2+}-ions in the aqueous phase, on the precipitation behavior is much larger in the case of mimetite than for schultenite, it becomes understandable why mimetite has precipitated closer to lead white layer ② than schultenite. (The source of Cl^- ions required for the formation of mimetite is not easily identified; however, many paintings and painters' materials generally contain an abundance of chlorides and the MA-XRF data of Figure 4.2-3 (Cl–K map) also points out that it is present (at least at the surface). In this case, the lead white, likely produced by means of the Dutch stack process, is considered to be a primary source of Cl.[2–4,11,19,34]

In Figure 4.2-4 we further see that the largest abundance of palmierite (($Na,K)_2Pb(SO_4)_2$), a secondary compound formed by precipitation of solvated Pb^{2+} with SO_4^{2-} and K^+ (and/or Na^+) ions,

$$K^+_{(aq)} + Pb^{2+}_{(aq)} + SO_4^{2-}_{(aq)} \rightarrow K_2PbSO_{4(s)}$$

is situated at the surface (near/in layer ④). Also this phenomenon and in particular the fact that this secondary lead sulfate mineral has not precipitated in the same location as the lead arsenate minerals becomes understandable when the higher solubility (and thus the larger K_s value) of palmierite is taken into consideration ($K_{s,25\,°C} \approx 10^{-10}$–$10^{-8}$). At $[Pb^{2+}]_{aq}$ levels that force the arsenates to

precipitate locally, sulfate ions can still remain in solution and thus have the possibility to migrate over a larger distance. Thus, e.g. as a result of drying/condensation cycles, many (but not all) sulfate ions that were formed (or were originally present) inside orpiment layer ③ may have become transported to the original paint surface (top of layer ③ and/or lake layer, see Figure 4.2-4) where they may have been forced to precipitate because of water evaporation (layer ④). Depending on the available cations, several sulfates may have formed, including palmierite and syngenite. It follows that, if conditions are such that e.g. palmierite is precipitating, then also the less soluble minerals such as schultenite and mimetite will behave similarly, provided all required ions are present in the thin layer of evaporating solution present at the surface. Another relevant difference between the arsenate and sulfate salts is that a possible source of the sulfates is atmospheric SO_2, making formation of the sulfates closer to the paint surface more probable that at greater depths.

Note: The observation that the above-mentioned arsenate minerals are not homogeneously distributed within the As-containing paint layer strengthens our initial assumption that they were formed in situ and were not already present at the time of painting.

4.2.3   Conclusions

We can conclude that by combining information about the lateral distribution of primary and secondary arsenate and sulfate minerals that are formed due to the (photo) degradation of the painters' pigment orpiment, with in-depth information obtained by microscopic analysis of a paint cross section, it is possible to formulate and substantiate a working hypothesis about the multistep mechanism that gives rise to the formation of secondary minerals. A three-step mechanism appears to be consistent with all observations: (i) formation of arsenate and

sulfate ions as a result of (photo)degradation in their parent paint layer which also gives rise to soluble acidic species, (ii) migration of these ions (and the acidic solution they are dissolved in) towards other layers where dissolution of mainly Ca^{2+} and Pb^{2+} ions from calcite and lead white can take place and (iii) local precipitation of Pb-containing arsenate and sulphate minerals both on the interfaces between As- and Pb-rich paint layers and at the paint surface.

This hypothesis permits to design laboratory experiments in which the degradation of orpiment can be realized and studied under controlled circumstances. Analysis of artificially degraded paint mock-up samples, especially at the microscopic level, will then allow to verify the formulated hypothesis.

More in general, the chemical maps discussed in this paper illustrate the added value that MA-XRPD can bring to the field of cultural heritage, not only for the identification of artist's materials, but also for the detection of degradation products and secondary compounds formed inside/at the surface of works of art. We consider that it may become a valuable new tool for in situ monitoring of restoration and cleaning treatments. The information that is provides, and in particular the macroscopic distributions of the alteration products, may also be employed to guide sampling campaigns to strategic areas of the artworks under examination. Nevertheless, it is also obvious that the lateral resolution of MA-XRPD imaging can still be improved to increase the readability of the images.

4.2.4   Materials and methods

The first part of the study involved the examination of the entire painting by means of a commercial MA-XRF instrument.[44] This allowed to pinpoint the areas in which As-containing pigments were present. In a second phase, MA-XRPD imaging experiments were carried out on a small area—see rectangle in Figure

4.2-1—using a mobile MA-XRF/XRPD scanning instrument that was operated in reflection mode.[11,45,46] Within this area, in order to study the in-depth distribution of primary and secondary compounds, a paint sample was taken. The resulting material was prepared as a cross section and analyzed by means of μ-XRPD mapping at the hard X-ray microprobe end station of beamline P06 (PETRA-III facility, Hamburg, Germany).

Large-scale MA-XRF mapping

A commercially available MA-XRF scanner 'M6 Jetstream' from Bruker Nano GmbH (Berlin, Germany) was employed for recording elemental maps of the entire painting. The M6 Jetstream consists of a 30 W Rh-target microfocus X-ray tube with a maximum voltage of 50 kV, a maximum current of 0.6 mA, a polycapillary lens, and a 30 mm^2 X-Flash silicon drift detector that is moved over the surface of the painting by means of an X, Y-motorized stage, enabling a scan area of 80×60 cm^2.[44] A spot size of 150 μm was set for the measurements. The large-scale elemental distribution maps were collected with a step size of 300 μm and dwell time of 50 ms/step, covering the complete surface of the painting (34.1×41.4 cm^2 corresponding to 963×1232 pixels). In the experimental conditions employed for many elements, the detection limits for MA-XRF situate themselves in the range 0.1–1%.

Combined MA-XRF/XRPD mapping

For the reflection mode MA-XRF/XRPD measurements, a self-built system consisting of a low power X-ray micro source (50W, IμS-Cu, Incoatec GmbH, Germany) was employed, delivering a monochromatic (Cu–K$_\alpha$; 8.04 keV) and focused X-ray beam with a photon flux of 2.9×10^8 photon s^{-1} (focal spot diameter: ca. 140 μm; output focal distance: ca. 20 cm; divergence: 2.4 mrad).[11,45,46] An incident angle of 12° was chosen between the primary X-ray

beam and the painting's surface, resulting in an enlarged beam footprint of around 1.5 mm in the horizontal direction; in the vertical direction the beam dimension is around 0.14 mm. Diffraction patterns were recorded with a PILATUS 200K area detector (Dectris Ltd., Switzerland) that was positioned on the front side of the artwork with an angle below 30° between the area detector and the painting. To reduce the effects of local topography and curvature of the painting's surface on the collected diffraction data, the distance between the artwork and the instrument was automatically adjusted with a laser distance sensor (Baumer GmbH, Germany) at each measurement point in the scanning process. This instrument was also equipped with a Vortex-Ex SDD detector (SII, USA), collecting X-ray fluorescence radiation from the front side of the painting. The previously described components were placed on a motorized platform, capable of moving the scanner in the XY (range: 25 cm × 10 cm) plane. The artwork was placed on a motorized easel, capable of moving the painting in the vertical (Z, range: 10 cm) direction. Calibration of several instrumental parameters was performed with a thin calcite paint layer applied on a mockup canvas. During the MA-XRF/XRPD imaging experiment an area of $6.5 × 7$ cm^2 was scanned (see Figure 4.2-1) using a step size of 1 × 1.4 mm in the horizontal and vertical directions. This represents only a small fraction of the total area of the painting. An XRPD acquisition time of 10 s/pixel was employed. The detection limit of MA-XRPD for specific crystalline compounds is rather variable; compounds containing Pb- (or similar heavy elements) are most easily detected while organic crystalline compounds are the most difficult. Mutual overlap of diffraction lines can also strongly influence these values in the negative sense. In the measurement conditions employed, interference-free detection limits are estimated to be of the order of 5–10%.

Micro-XRPD mapping

μ-XRPD data collection was done at the microprobe hutch of the Hard X-ray micro/nanoprobe beamline (P06) of the PETRA III storage ring (DESY, Hamburg, Germany), using a primary photon energy of 21 keV, which is selected by means of a Si(111) double crystal monochromator.[47] A Kirkpatrick-Baez mirror optic was employed to focus the beam, achieving a size of 0.5×0.5 μm^2 (h × v). A Keyence optical microscope equipped with a perforated mirror allowed for positioning of the sample. Diffraction signals were recorded in transmission geometry using an EIGER X 4M area detector (Dectris Ltd., Switzerland). Calibration of the diffraction setup was performed by means of a LaB$_6$ reference sample. The total size of the sample was of the order of 500×600 μm^2 and was embedded in resin and polished prior to analysis. In total an area of 200×110 μm^2 was scanned using a step size of 1×0.5 μm^2 in respectively the horizontal and vertical direction. Diffraction patterns were acquired with 0.25 s/pixel exposure time. This exposure time per pixel is so short that beam damage (e.g. beam induced oxidation of reduced As species) can be excluded.

Data processing

Crystalline phase distribution maps (both macroscopic and microscopic) were obtained by full pattern refinement using the XRDUA software package.[48] The individual diffractograms were fitted to a background term and a linear combination of peak groups.[49] Each peak group contained the Bragg peaks of one crystalline phase and has three parameters that were refined during the fit process: the sample-detector distance, a scaling factor and a width factor. The scaling factor is proportional to the total volume of scattering material for a given phase and is shown in the distribution maps presented in this work. The software

packages PyMCA and DataMuncher were used to create the elemental distribution maps.[50] To avoid overlap between Pb–L and As–K XRF signals, the K_β -line of As was employed for mapping this element.

Acknowledgments

References

(1) Zanella, L.; Casadio, F.; Gray, K. A.; Warta, R.; Ma, Q.; Gaillard, J.-F. The Darkening of Zinc Yellow: XANES Speciation of Chromium in Artist's Paints after Light and Chemical Exposures. *J. Anal. At. Spectrom.* **2011**, *26*, 1090–1097.

(2) Mass, J.; Sedlmair, J.; Patterson, C. S.; Carson, D.; Buckley, B.; Hirschmugl, C. SR-FTIR Imaging of the Altered Cadmium Sulfide Yellow Paints in Henri Matisse's Le Bonheur de Vivre (1905–6) – Examination of Visually Distinct Degradation Regions. *Analyst* **2013**, *138*, 6032–6043.

(3) Van der Snickt, G.; Dik, J.; Cotte, M.; Janssens, K.; Jaroszewicz, J.; De Nolf, W.; Groenewegen, J.; Van der Loeff, L. Characterization of a Degraded Cadmium Yellow (CdS) Pigment in an Oil Painting by Means of Synchrotron Radiation Based X-Ray Techniques. *Anal. Chem.* **2009**, *81*, 2600–2610.

(4) Van der Snickt, G.; Janssens, K.; Dik, J.; De Nolf, W.; Vanmeert, F.; Jaroszewicw, J.; Cotte, M.; Falkenberg, G.; Van der Loeff, L. Combined Use of Synchrotron Radiation Based Micro-X-Ray Fluorescence, Micro-X-Ray

Diffraction, Micro-X-Ray Absorption Near-Edge, and Micro-Fourier Transform Infrared Spectroscopies for Revealing an Alternative Degradation Pathway of the Pigment Cadmium Yellow in a Painting by Van Gogh. *Anal. Chem.* **2012**, *84*, 10221–10228.

(5) Coccato, A.; Moens, L.; Vandenabeele, P. On the Stability of Mediaeval Inorganic Pigments: A Literature Review of the Effect of Climate, Material Selection, Biological Activity, Analysis and Conservation Treatments. *Herit. Sci.* **2017**, *5*, 12.

(6) FitzHugh, E. W. Orpiment and Realgar. In *Artists' Pigments: A Handbook of Their History and Characteristics, vol 3*; Archetype Publications: London, 1997; pp 47–79.

(7) Strbac, N.; Mihajlovic, I.; Minic, D.; Zivkovic, D.; Zivkovic, Z. Kinetics and Mechanism of Arsenic Sulfides Oxidation. *J. Min. Metall. Sect. B Metall.* **2009**, *45*, 59–67.

(8) Muralha, V. S. F.; Miguel, C.; Melo, M. J. Micro-Raman Study of Medieval Cistercian 12–13th Century Manuscripts: Santa Maria de Alcobaça, Portugal. *J. Raman Spectrosc.* **2012**, *43*, 1737–1746.

(9) Keune, K.; Mass, J.; Meirer, F.; Pottasch, C.; van Loon, A.; Hull, A.; Church, J.; Pouyet, E.; Cotte, M.; Mehta, A. Tracking the Transformation and Transport of Arsenic Sulfide Pigments in Paints: Synchrotron-Based X-Ray Micro-Analyses. *J. Anal. At. Spectrom.* **2015**, *30*, 813–827.

(10) Vermeulen, M.; Nuyts, G.; Sanyova, J.; Vila, A.; Buti, D.; Suuronen, J.-P.; Janssens, K. Visualization of As(III) and As(V) Distributions in Degraded Paint Micro-Samples from Baroque- and Rococo-Era Paintings. *J. Anal. At. Spectrom.* **2016**, *31*, 1913–1921.

(11) Vanmeert, F.; De Keyser, N.; Van Loon, A.; Klaassen, L.; Noble, P.; Janssens, K. Transmission and Reflection Mode Macroscopic X-Ray Powder Diffraction (MA-XRPD) Imaging for the Noninvasive Visualization of Paint Degradation in Still Life Paintings by Jan Davidsz. de Heem. *Anal. Chem.* **2019**, *91*, 7153–7161.

(12) van Thiel, P. J. J. *All the Paintings of the Rijksmuseum in Amsterdam: A Completely Illustrated Catalogue, First Supplement 1976-91*; Rijksmuseum: Amsterdam, 1992.

(13) Buijsen, E.; Dumas, C. *Haagse Schilders in de Gouden Eeuw: Het Hoogsteder Lexicon van Alle Schilders Werkzaam in Den Haag 1600-1700*; Waanders: Den Haag, 1998.

(14) van der Willigen, E.; Meijer, F. *A Dictionary of Dutch and Flemish Still-Life Painters Working in Oils: 1525-1725*; Primavera Press: Leiden, 2003.

(15) Wallert, A. *Still Lifes: Techniques and Style: An Examination of Paintings from the Rijksmuseum*; Waanders: Amsterdam, 1999.

(16)   Klein,   P.   Dendrochronology   Report. https://rkd.nl/nl/explore/technical/5003006 (accessed 2019-01-05).

(17)   Meagher, J. Food and Drink in European Painting, 1400-1800. In *Heilbrunn Timeline of Art History*; New York: The Metropolitan Museum of Art, 2000.

(18)   De Meyer, S.; Vanmeert, F.; Janssens, K.; Storme, P. A Mobile Scanner for XRPD-Imaging of Paintings in Transmission and Reflection Geometry. In *6th Interdisciplinary ALMA conference*; Academy of Fine Arts in Prague: Brno, 2017.

(19)   De Keyser, N.; Van der Snickt, G.; Van Loon, A.; Legrand, S.; Wallert, A.; Janssens, K. Jan Davidsz. de Heem (1606-1684): A Technical Examination of Fruit and Flower Still Lifes Combining MA-XRF Scanning, Cross-Section Analysis and Technical Historical Sources. *Herit. Sci.* **2017**, *5*, 38.

(20)   Douglass, D. L.; Shing, C. C.; Wang, G. The Light-Induced Alteration of Realgar to Pararealgar. *Am. Mineral.* **1992**, *77*, 1266–1274.

(21)   Bindi, L.; Popova, V.; Bonazzi, P. Uzonite, As4S5, from the Type Locality: Single-Crystal X-Ray Study and Effects of Exposure to Light. *Can. Mineral.* **2003**, *41*, 1463–1468.

(22)   Kyono, A.; Kimata, M.; Hatta, T. Light-Induced Degradation Dynamics in Realgar: In Situ Structural Investigation Using Single-Crystal X-Ray Diffraction Study and X-Ray Photoelectron Spectroscopy. *Am. Mineral.* **2005**, *90*, 1563–1570.

(23)   Matović, V.; Erić, S.; Kremenović, A.; Colomban, P.; Srećković-Batoćanin, D.; Matović, N. The Origin of Syngenite in Black Crusts on the Limestone Monument King's Gate (Belgrade Fortress, Serbia) – the Role of Agriculture Fertiliser. *J. Cult. Herit.* **2012**, *13*, 175–186.

(24)   Erić, S.; Matović, V.; Kremenović, A.; Colomban, P.; Batoćanin, D. S.; Nešković, M.; Jelikić, A. The Origin of Mg Sulphate and Other Salts Formed on Pure Calcium Carbonate Substrate – Tufa Stone Blocks Built into the Gradac Monastery, Serbia. *Constr. Build. Mater.* **2015**, *98*, 25–34.

(25)   Melcher, M.; Schreiner, M. Leaching Studies on Naturally Weathered Potash-Lime–Silica Glasses. *J. Non Cryst. Solids* **2006**, *352*, 368–379.

(26)   Vettori, S.; Bracci, S.; Cantisani, E.; Riminesi, C.; Sacchi, B.; D'Andria, F. A Multi-Analytical Approach to Investigate the State of Conservation of the Wall Paintings of Insula 104 in Hierapolis (Turkey). *Microchem. J.* **2016**, *128*, 279–287.

(27)   Marszałek, M. Identification of Secondary Salts and Their Sources in Deteriorated Stone Monuments Using Micro-Raman Spectroscopy, SEM-EDS and XRD: Identification of Secondary Salts and Their Sources. *J. Raman Spectrosc.* **2016**, *47*, 1473–1485.

(28)   Newton, R.; Davison, S. Deterioration of Glass. In *Conservation of glass*; Butterworth-Heinemann: Oxford, 1989; pp 135–164.

(29)   Garcia-Vallès, M.; Gimeno-Torrente, D.; Martínez-Manent, S.; Fernández-Turiel, J. L. Medieval Stained Glass in a Mediterranean Climate: Typology, Weathering and Glass Decay, and Associated Biomineralization Processes and Products. *Am. Mineral.* **2003**, *88*, 1996–2006.

(30)   Simova, V.; Bezdicka, P.; Hradilova, J.; Hradil, D.; Grygar, T. X-Ray Powder Microdiffraction for Routine Analysis of Paintings. *Powder Diffr.* **2005**, *20*, 224–229.

(31)   Zeng, Q. G.; Zhang, G. X.; Leung, C. W.; Zuo, J. Studies of Wall Painting Fragments from Kaiping Diaolou by SEM/EDX, Micro Raman and FT-IR Spectroscopy. *Microchem. J.* **2010**, *96*, 330–336.

(32)   Přikryl, R.; Svobodová, J.; Zák, K.; Hradil, D. Anthropogenic Origin of Salt Crusts on Sandstone Sculptures of Prague's Charles Bridge (Czech Republic): Evidence of Mineralogy and Stable Isotope Geochemistry. *Eur. J. Mineral.* **2004**, *16*, 609–617.

(33)   Sterpenich, J. Cristallochimie Des Produits d'altération Des Vitraux Médiévaux: Application Au Vieillissement Des Déchets Vitrifiés. *Bull. Eng. Geol. Environ.* **2002**, *61*, 179–193.

(34)   Cotte, M.; Susini, J.; Solé, V. A.; Taniguchi, Y.; Chillida, J.; Checroun, E.; Walter, P. Applications of Synchrotron-Based Micro-Imaging Techniques to the Chemical Analysis of Ancient Paintings. *J. Anal. At. Spectrom.* **2008**, *23*, 820–828.

(35)   Van Loon, A.; Noble, P.; Boon, J. J. White Hazes and Surface Crusts in Rembrandt's Homer and Related Paintings. In *ICOM Committee for Conservation 16th Triennial Conference*; Lisbon, 2011.

(36)   Boon, J. J.; Oberthaler, E.; Haag, S.; Pénot, S. Mechanical Weakness and Paint Reactivity Observed in the Paint Structure and Surface of The Art of Painting by Vermeer. In *Vermeer, Die Malkunst - Spurensicherung an einem Meisterwerk: Ausstellungskatalog des Kunsthistorischen Museums Wien*; Residenz Verlag: Salzburg, 2010; pp 328–335.

(37)   Boon, J. J. Chemistry Underneath the Painting Surface: Palmierite Formation in/on a Painting by Johannes Vermeer and by Jacob Jordaens Using Laboratory- and Synchrotron-Aided Spectroscopic Methods. In *Proceedings of Microscopy & Microanalysis*; Indianapolis, 2013.

(38)   Kakoulli, I. Late Classical and Hellenistic Painting Techniques and Materials: A Review of the Technical Literature. *Stud. Conserv.* **2002**, *47*, 56–67.

(39)   Leona, M. The Materiality of Art: Scientific Research in Art History and Art Conservation at the Metropolitan Museum. *Metrop. Mus. Art Bull.* **2009**, *67*, 4–11.

(40)   Holakooei, P.; Karimy, A. H. Early Islamic Pigments Used at the Masjid-i Jame of Fahraj, Iran: A Possible Use of Black Plattnerite. *J. Archaeol. Sci.* **2015**, *54*, 217–227.

(41)   Brecoulaki, H. *La Peinture Funéraire de Macédoine: Emplois et Fonctions de La Couleur IVe-IIe s. Av. J.-C.*; De Boccard: Paris, 2006.

(42)   Buisson, N.; Burlot, D.; Eristov, H.; Eveno, M.; Sarkis, N. The Tomb of the Three Brothers in Palmyra: The Use of Mimetite, A Rare Yellow Pigment, in A Rich Decoration: The Tomb of the Three Brothers in Palmyra: The Use of Mimetite. *Archaeometry* **2015**, *57*, 1025–1044.

(43)   Hradil, D.; Hradilová, J.; Bezdička, P.; Švarcová, S.; Čermáková, Z.; Košařová, V.; Němec, I. Crocoite PbCrO4 and Mimetite Pb5(AsO4)3Cl: Rare Minerals in Highly Degraded Mediaeval Murals in Northern Bohemia. *J. Raman Spectrosc.* **2014**, *45*, 848–858.

(44)   Alfeld, M.; Pedroso, J. V.; van Eikema Hommes, M.; Van der Snickt, G.; Tauber, G.; Blaas, J.; Haschke, M.; Erler, K.; Dik, J.; Janssens, K. A Mobile Instrument for in Situ Scanning Macro-XRF Investigation of Historical Paintings. *J. Anal. At. Spectrom.* **2013**, *28*, 760–767.

(45)   Vanmeert, F.; De Nolf, W.; De Meyer, S.; Dik, J.; Janssens, K. Macroscopic X-Ray Powder Diffraction Scanning, a New Method for Highly Selective Chemical Imaging of Works of Art: Instrument Optimization. *Anal. Chem.* **2018**, *90*, 6436–6444.

(46)   Vanmeert, F.; De Nolf, W.; Dik, J.; Janssens, K. Macroscopic X-Ray Powder Diffraction Scanning: Possibilities for Quantitative and Depth-Selective Parchment Analysis. *Anal. Chem.* **2018**, *90*, 6445–6452.

(47)   Schroer, C. G.; Boye, P.; Feldkamp, J. M.; Patommel, J.; Samberg, D.; Schropp, A.; Schwab, A.; Stephan, S.; Falkenberg, G.; Wellenreuther, G.; Reimers, N. Hard X-Ray Nanoprobe at Beamline P06 at PETRA III. *Nucl. Instr. Meth. Phys. Res. A: Accel. Spectrom. Detect. Assoc. Equip.* **2010**, *616*, 93–97.

(48)   De Nolf, W.; Vanmeert, F.; Janssens, K. XRDUA: Crystalline Phase Distribution Maps by Two-Dimensional Scanning and Tomographic (Micro) X-Ray Powder Diffraction. *J. Appl. Crystallogr.* **2014**, *47*, 1107–1117.

(49)   De Nolf, W.; Janssens, K. Micro X-Ray Diffraction and Fluorescence Tomography for the Study of Multilayered Automotive Paints: M-XRF/XRD Tomography for the Study of Multilayered Automotive Paints. *Surf. Interface Anal.* **2010**, *42*, 411–418.

(50)   Alfeld, M.; Janssens, K. Strategies for Processing Mega-Pixel X-Ray Fluorescence Hyperspectral Data: A Case Study on a Version of Caravaggio's Painting Supper at Emmaus. *J. Anal. At. Spectrom.* **2015**, *30*, 777–789.

4.3 Reviving degraded colors of yellow flowers in 17th century still life paintings with macro- and microscale chemical imaging

Adapted from De Keyser, N.; Broers, F.; Vanmeert, F.; <u>De Meyer, S.</u>; Gabrieli, F.; Hermens, E.; Van der Snickt, G.; Janssens, K.; Katrien K. Reviving degraded colors of yellow flowers in 17th century still life paintings with macro- and microscale chemical imaging. Sci. Adv. **2022**, 8, abn6344.

Contributions of the thesis author: SDM performed the MA-XRPD and SR-μ-XRD data acquisition and analysis together with FV and NDK.

4.3.1 Introduction

Over time, artist pigments and binders in oil paintings are inevitably subject to slow deterioration processes induced by external (light, relative humidity, temperature, and solvent exposure) and internal factors (copresence of incompatible pigment mixtures).[1,2] These complex processes take place at the paint surface or within the paint on the microscopic to the molecular level and can affect the physicochemical properties of the paint in an undesirable way. Inherent to the artist's choice of material and technique, degradation entails discoloration and color changes and/or affects the structural integrity of the paint, causing (loss of) transparency, brittleness, delamination, or pronounced microcracking. At an advanced stage, these phenomena can decrease the readability of the artwork and hence conspicuously alter the artists' intention. Notable examples of the degradation of artists pigments are the discoloration of the blue glass pigment smalt in Rembrandt paintings;[3] ultramarine "sickness" in works by Johannes Vermeer, Jan Steen, and Jan Van Eyck;[4] the fading of light-sensitive pigments such as Prussian blues and organic yellow and red lake pigments; and the darkening of chrome yellows and cadmium yellows in

paintings by, for instance, Edvard Munch, Vincent Van Gogh, James Ensor, Pablo Picasso, and other contemporaries.[5,6] Because of pigment degradation, not only can carefully constructed optical effects such as folds in draperies disappear, rendering the object flat, for example, the ultramarine degradation in the blue cloak in Van Eyck's *Three Marys at the Tomb* (1425–1435), but also a reverse optical effect can be formed [for example, *The Bedroom* (1888) by Van Gogh where the fading of the red pigments turned the purple walls blue and the pink floor brown].[7] As paintings are composed of layers of complex heterogenous mixtures of pigments, it is often a combination of various degradation phenomena that affects the current appearance of degraded areas. Thus, to understand a degraded motif (e.g. draperies, flowers, foliage, incarnates, etc.) in itself and in context of the whole painting, a macroscale approach is required.

The capability of non-invasive imaging techniques such as macroscopic x-ray fluorescence (MA-XRF) scanning, reflectance imaging spectroscopy (RIS), and macroscopic reflectance Fourier transform infrared (MA-rFTIR) spectroscopy for the identification of artist's working methods and materials has been demonstrated over the past decades.[8–10] MA-XRF allows for the identification and mapping of chemical elements, while RIS provides complementary molecular information. A more recently developed method, macroscopic x-ray powder diffraction (MA-XRPD) imaging, has proven its potential in the cultural heritage field, specifically in the study of pigment degradation, as it allows for a non-invasive identification of crystalline pigment phases and secondary alteration products, as well as the visualization of their spatial distribution at the paint surface.[11,12] When combined with microscopic imaging modalities [synchrotron radiation micro–x-ray powder diffraction (SR-µ-XRPD)], it becomes a highly valuable tool for obtaining a three-dimensional (3D) understanding of pigment degradation pathways.[13]

In this context, arsenic-based pigments such as orpiment (As_2S_3) and realgar (As_4S_4), used by artists since antiquity, are known to undergo several discoloration phenomena and have severely affected the current appearance of various old master paintings. Paolo Veronese, Tintoretto, and Giorgione used the arsenic pigments in orange draperies, while Dutch and Flemish still life painters such as Adriaen Coorte, Daniël Seghers, Willem Kalf, and Jan Davidsz. De Heem made use of their ideal paint properties in oil to create luminous golden or warm glowing highlights to paint oranges, lemons, yellow flowers, or a sheen of golden metalwork.[14–18] Despite numerous documentary sources with disclaimers warning against their incompatibility with other pigments, poisonous nature, horrible drying property, and change of color, they were still used until the 18th century and now are often found degraded.[19] Earlier studies have pointed out the light sensitivity of these pigments through photo-oxidation with the formation of secondary products such as white arsenolite (As_2O_3) (in case of the yellow pigment orpiment) and bright yellow pararealgar (As_4S_4) (in case of the orange pigment realgar).[15,20] Keune *et al.* found that highly mobile and soluble arsenate (As^{5+}) species, as a result of degradation, migrate through the multilayered paint system.[14] Recently, two rare lead arsenate species, mimetite [$Pb_5(AsO_4)_3Cl$] and schultenite ($PbHAsO_4$), were identified in still life paintings by Jan Davidsz. De Heem and Martinus Nellius and are considered to be degradation (end) products of those soluble mobile arsenates that have precipitated with available Pb^{2+} ions.[13,21] While these studies dealt with the characterization of the arsenic species, this work demonstrates how the multimodal combination of chemical and optical imaging techniques allows us to understand and document the visual impact of arsenic degradation on the optical appearance of the paint and the painting itself with remarkable detail.

As a case study for this research, we focus on the yellow rose in the painting *Still Life with Flowers and a Watch* by Abraham Mignon (1640–1679) from the collection of the Rijksmuseum. Since long, yellow roses have attracted the attention of scholars, as these are considered signature flowers in the circle of the leading 17th century still life painters Jan Davidsz. De Heem (1606–1684), Abraham Mignon, and Daniël Seghers (1590–1661). In addition, several authors identified the presence of natural orpiment as their main constituent pigment, whereas yellow roses have been reported to exhibit varying degrees of degradation.[22–25] Mignon's yellow rose in the Rijksmuseum painting is therefore an exemplary topic for this study, looking flat and poor in color contrast while featuring a crumbling powdery appearance or a conspicuously broken up paint surface. In particular, upon considering the surrounding, better-preserved flowers in the composition, it becomes clear that the rose has lost most of its 3D character.[22,23] Nevertheless, the elemental map of arsenic, supplied by MA-XRF imaging experiments, revealed that the paint layers still hold all details of the once elaborated brushwork used to create the 3D illusion of the flower that is now no longer visible to the naked eye (Figure 4.3-1).

Figure 4.3-1 Pigment degradation in the yellow rose of Abraham Mignon's *Still Life with Flowers and a Watch.* (A) Visual photograph of *Still Life with Flowers and a Watch* of Abraham Mignon (1640–1679), oil on canvas, dated c. 1660–1679, signed *A. Mignon. Fc*, from the collection of the Rijksmuseum (SK-A-268), (B) with a detail of the yellow rose (C) and the corresponding elemental distribution image of arsenic.

The question of why we cannot perceive these details anymore can be raised. This research therefore aims to gain an in-depth 3D understanding of the transformation of the original intended appearance of the yellow rose into its degraded current state by (i) identifying the original pigments and their stratigraphy, to gain a complete understanding of the paint technique, and (ii) characterizing the secondary degradation products on the micro- and macroscale, to better understand the various degradation processes that have occurred. To do this, the painting was analyzed with a range of analytical imaging techniques, which includes high-resolution elemental mapping of the yellow rose with the Bruker M6 MA-XRF scanner, MA-XRPD imaging in reflection mode (Figure S

4.3-1) with x-rays probing superficial paint layers under a shallow angle (10°), and RIS in the visible to near IR (VNIR). To visually correlate the results of the chemical imaging techniques, the yellow rose paint surface was photographed with a 5-μm pixel resolution and studied under the 3D Hirox surface microscope for midrange resolution images. Complementary to the non-invasive analyses, a microsample taken from the yellow rose was examined with scanning electron microscopy combined with energy-dispersive x-ray (SEM-EDX) analysis and with SR-based x-ray powder diffraction at the P06 beamline at PETRA III (DESY). Additional characterization of the original arsenic-based pigment was done using micro–Raman spectroscopy.

4.3.2   Results and discussion

Non-invasive analysis: MA-XRF

MA-XRF imaging enabled mapping the distribution of the elements present in the yellow rose; relevant distribution maps are shown in Figure 4.3-2: for arsenic (A), calcium (B), iron (C), sulfur (D), lead (E), and copper (F). The arsenic, calcium, and sulfur maps demonstrate painterly features for the definition of the flower, while in the iron map, the overall shape of the flower can be discerned. Following Mignon's use of light and shadow in surrounding flowers, the yellow rose would have been illuminated from the upper left. Although the contrast, light, and shadow modeling is no longer visible today, the elemental distribution maps of arsenic and calcium give insight into the original illumination. While the arsenic map visualizes the light striking the flower with intricate details and highlights that were meticulously applied to define the flower petals and stamens, the distribution of calcium appears to correlate with the expected shadow areas. This is particularly visible where one of the upper flower petals casts a shadow on a neighboring petal [see red arrows in Figure 4.3-2A-B].
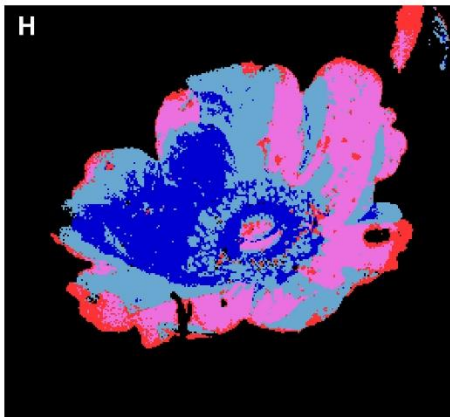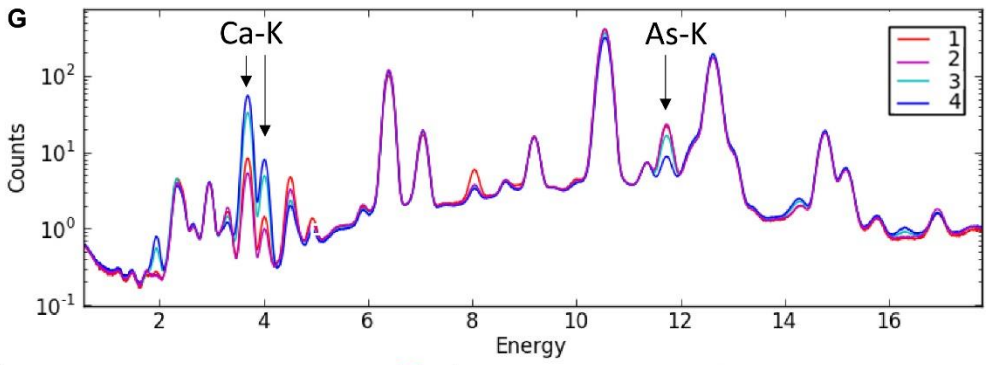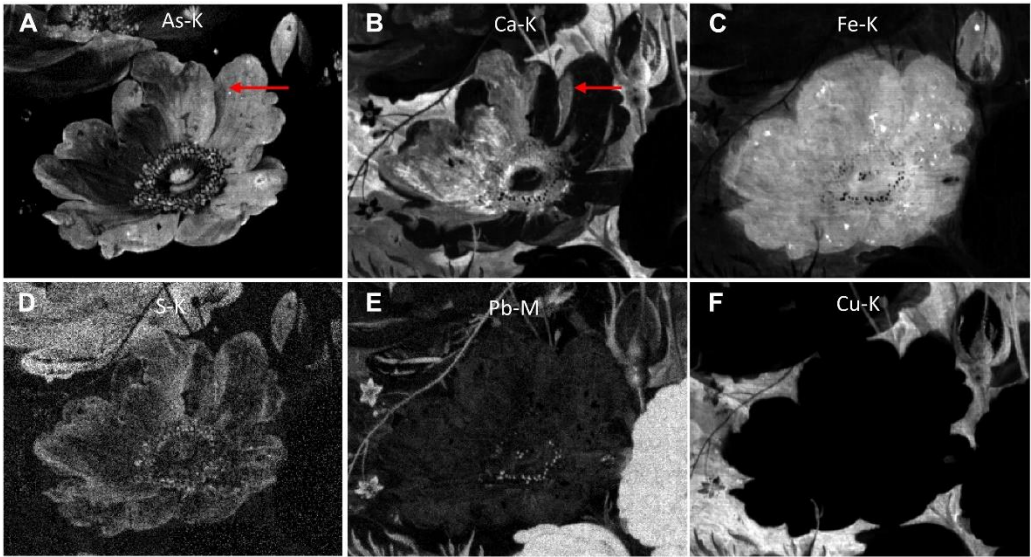
Principal component analysis (PCA) *k*-means clustering
MA-XRF dataset

Cluster 1

Cluster 2
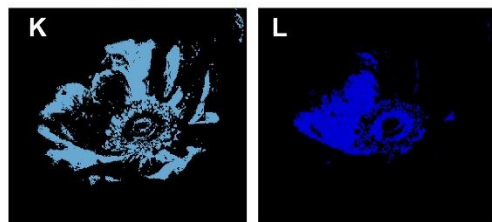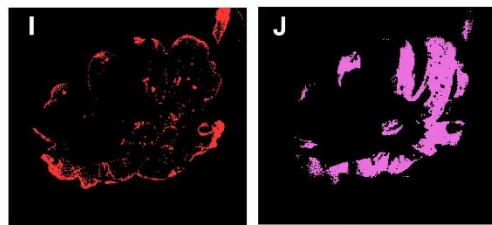
Cluster 3

Cluster 4

Figure 4.3-2 Results from MA-XRF imaging and principal component analysis with *k*-means clustering of the dataset. Detailed elemental distribution images for (A) arsenic, (B) calcium, (C) iron, (D) sulfur, (E) lead, and (F) copper of the yellow rose acquired with a Bruker M6 Jetstream by mapping an area of 193 mm by 235 mm with a step size of 300 μm and a dwell time per pixel of 150 ms. Results from the principal components analysis (PCA) with *k*-means clustering showing the averaged XRF spectra of the clusters 1 to 4 in (G) and the clusters visualized in a composite image (H) and separately (I to L).

In the distribution map of iron, both the rough shape of the flower and an oval shape encompassing the flower are visible. The iron signal does not correspond to any painterly feature in the flower and neither correlates with the arsenic or the calcium map; this suggests that the signal is stemming from a more uniformly applied underpainting underneath the flower. From previous MA-XRF studies on Dutch flower still lives, a single oval-shaped underpainting would be expected here, marking the position of the flower applied in an earlier stage. The iron signal from the lower underpainted layer is attenuated differently by the superimposed layers.[18,25,26] The background around the flower is applied with a copper-rich paint (Figure 4.3-2F) that is blocking the iron signal of the underpaint more than the superimposed calcium and arsenic paint layers constituting the flower. Little white highlights are also present in the center of the flower and were applied with touches of lead white, visible in the lead distribution map (Figure 4.3-2E).

A closer inspection of the MA-XRF dataset was obtained by performing principal component analysis (PCA) followed by *k*-means clustering in PC space. The first six PCs covered most of the variance in the data and were used for image segmentation by *k*-means clustering. Pixels with similar spectra are effectively clustered via this method into *k* groups, resulting in an image segmentation. To achieve additional image segmentation, 13 clusters were selected (without prior knowledge), and the result was improved by a Gaussian mixture model (GMM) using expectation maximization (EM) for clustering (maximum of 1000

iterations) (Figure S 4.3-2). In Figure 4.3-2, the composite image (Figure 4.3-2H) and four separate clusters (Figure 4.3-2I-L) that describe the different pixel types within the yellow rose are presented. The average spectra of the four clusters are reported in Figure 4.3-2G; the largest difference between the four clusters can be explained by the variance in observed arsenic and calcium XRF intensity.

When visualizing the location of these clusters in the composite image (Figure 4.3-2H), it becomes apparent that the PCA with k-means clustering effectively identified pixel groups within the yellow rose that also, under the 3D digital optical microscope, can visually be differentiated on the basis of their tonality, paint surface, particle distribution, and condition. While from a distance, subtle nuances, details, and transitions can hardly be observed in the yellow rose, up close and under the microscope, the differences in optical appearance among the four areas is evident. In Figure 4.3-3B, the areas are indicated on the yellow rose and supplemented with microscopic images taken at medium magnification (×140) under the 3D digital optical microscope (Figure 4.3-3D-G).
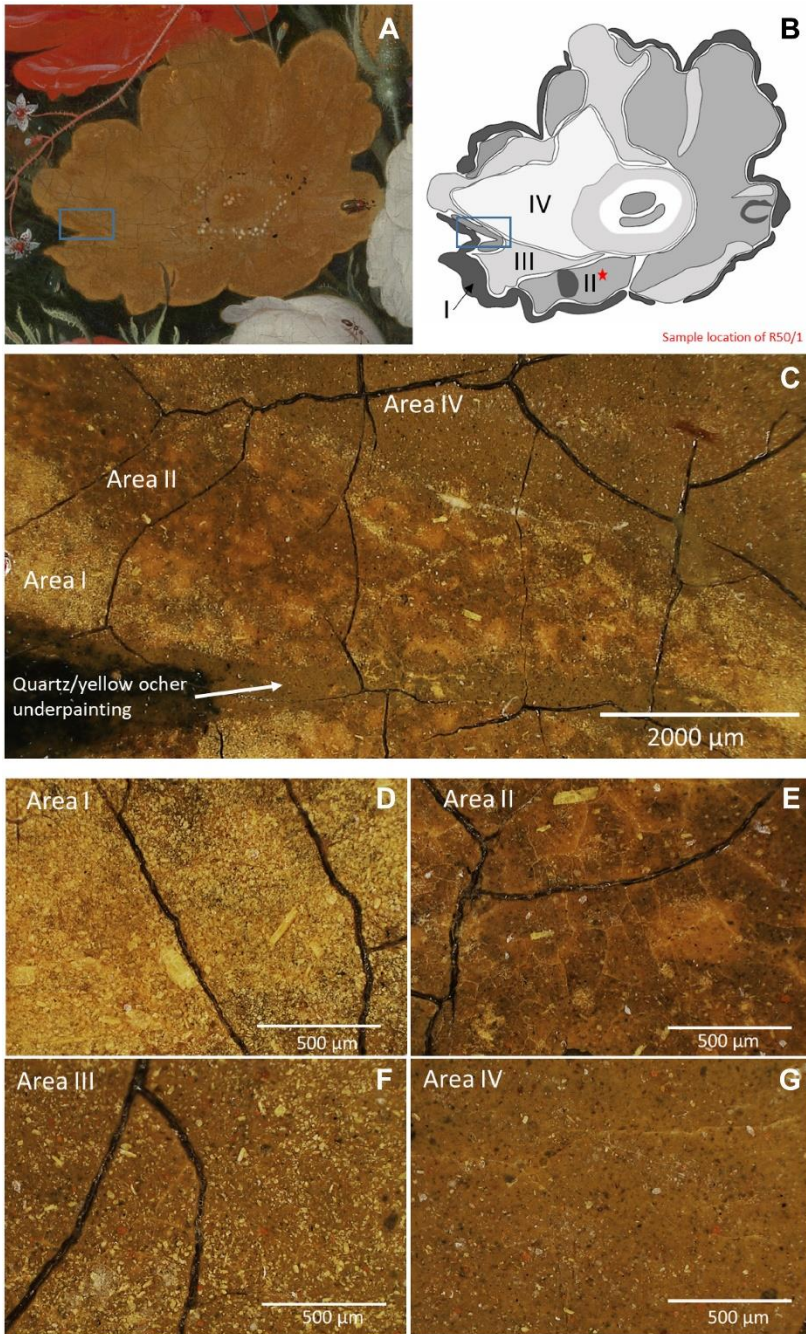
Figure 4.3-3 Comparison of the differences in optical appearance in the yellow rose under the 3D digital optical microscope. (A) Detail of the yellow rose. (B) Schematic overview of the four defined areas (I to IV) and sample location, (C) detail of the rose photographed under low magnification (×35), and corresponding images photographed

under the Hirox microscope with magnification of ×140 for area I (D), area II (E), area III (F), and area IV (G).

Area I, closely corresponding to cluster 1, defines the brighter yellow color around the outline of the yellow rose and the highlight under the little beetle and leaf. Under the microscope, this area (Figure 4.3-3C) is specifically characterized by a clustering of bright yellow pigment particles with a foliated micaceous platelet-like morphology, similar to natural orpiment. The size of the particles (lengthwise) varies from small (c. 20 μm) to coarse (on average, 100 to 200 μm up to even 600 μm for a few particles).

The paint surface indicated as area II (Figure 4.3-3D), correlating with cluster 2, represents most of the paint surface and shows clear signs of degradation. It has a brittle appearance due to a more pronounced microcracking and is affected by superficial paint losses. Visually, the area appears darker in tonality, and under the 3D digital optical microscope, it is perceived as a darkened more transparent paint with fewer bright yellow particles (ranging from 20 to 100 μm).

By eye, the transition between area II and area III in the painting is subtle; however, area III (Figure 4.3-3E), closely corresponding to cluster 3 (Figure 4.3-2K), is lighter gray in tonality, appears less brittle, and is not affected by paint loss. Under the 3D digital microscope, again, the same bright yellow pigment particles are observed but in greater quantity and more evenly distributed over the surface in a transparent layer compared to the sporadically distributed particles observed in area II.

Area IV indicates a region located on the left side of the rose (Figure 4.3-3F) [correlating with cluster 4 (Figure 4.3-2L)] and is visually perceived whiter in tonality with a powdery appearance compared to the neighboring areas. Under the 3D digital optical microscope, mostly white particles and few yellow particles

can be observed in an overall transparent-looking paint film over a coarse-grained underlayer.

Although MA-XRF scanning provides highly specific information on the macroscale, it is not depth selective and elemental information can originate from different levels in the stratigraphy, which has to be taken into account when interpreting the resulted clustering. There is a variable degree of attenuation of the signal, depending on the thickness, atomic number, and density of superimposed materials. For instance, the area on the top where the yellow flower petal was painted over the neighboring red flower erroneously resulted in a different clustering because of attenuation of the iron signal (present in the underpainting) by the superimposed vermilion (HgS) paint of the red flower (Figure S 4.3-2). Although the obtained clusters merely group pixels with similar spectra, rather than showing exact paint mixtures that were used to paint the flower, in this case, the clusters could overall be linked with visually distinct areas of the paint surface and even prelude to the presence of different calcium-based pigments and formed degradation products, which will be discussed in the next paragraph.

Non-invasive analysis: MA-XRPD

To better distinguish the pigments present in the superficial paint layers and identify the formed degradation products (i.e., the different arsenic and calcium phases), MA-XRPD maps of the yellow rose were recorded. The painting was analyzed in reflection mode with monochromatic x-rays impinging the paint surface under a shallow angle (10°), which limits the probing depth to the superficial paint layers of the stratigraphy, ranging between 10 and 50 μm, depending on the material composition.[26,27] An area of 97.5 mm by 109.5 mm was scanned with an exposure time of 10 s per pixel and a step size of 1.5 mm

by 1.5 mm. In Figure 4.3-4, a selection of the relevant MA-XRPD distribution maps is shown. These distributions allowed further interpretation of the aforementioned MA-XRF results (Figure 4.3-2) and microscopic observations of the paint surface (Figure 4.3-3), i.e., by enabling a correlation between specific crystalline pigment phases and degradation products with the MA-XRF clusters and optical areas, respectively.
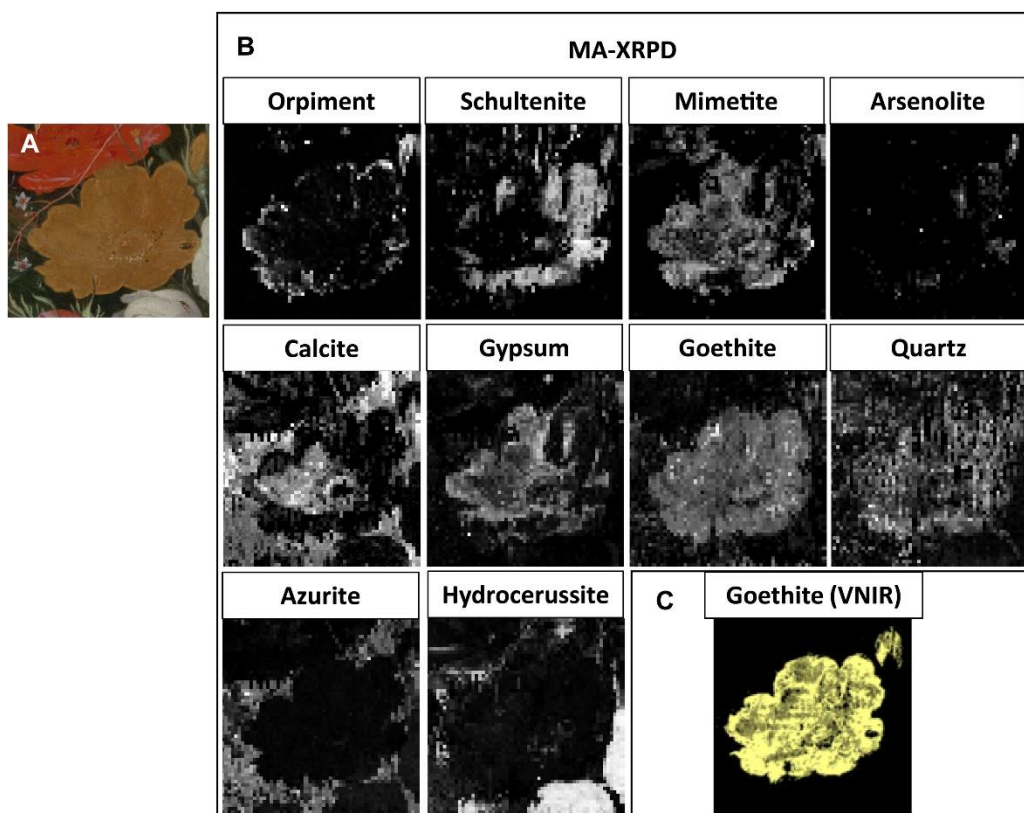
Figure 4.3-4 Results from MA-XRPD in reflection mode and VNIR. (A) Optical photograph of the analyzed area. (B) Distribution images obtained with reflection MA-XRPD, showing the intensity scaling parameter for every pixel. (C) Map obtained with the portion of the spectral endmember showing characteristic features of goethite, contained in the yellow ocher pigment.

The elemental arsenic maps were substantially augmented by MA-XRPD, as no less than four different arsenic-containing crystalline products were identified:

217

schultenite ($PbHAsO_4$), mimetite [$Pb_5(AsO_4)_3Cl$], arsenolite (As_2O_3), and orpiment (As_2S_3) (Figure S 4.3-3), each showing a distinct spatial distribution. In particular, orpiment, schultenite, and mimetite correspond to areas I, II, and III, respectively, while arsenolite can be visually correlated to the white crust formations in area II. In addition, two main calcium-based crystalline products: calcite ($CaCO_3$), and gypsum ($CaSO_4\cdot2H_2O$) were found, with calcite corresponding to the calcium rich area IV, while gypsum matches area III with a similar distribution as mimetite. Last, goethite [$FeO(OH)$] and quartz (SiO_2) are present.

Both mimetite and schultenite are rare arsenate minerals in nature and, consistent with recent literature, can be identified as secondary degradation products in artworks.[13,15,21] Their different spatial distribution in the rose is particularly of interest, as it seems that the distribution of mimetite is correlated to the distribution of gypsum. Local environmental conditions play an important role in the in situ formation of crystalline products in paint layers; the conditions for the formation of mimetite or schultenite depend on several factors. In general, As(V) species, originating from an oxidation reaction of As(III) in orpiment, are predominant under moderate to high oxidation conditions, in this case, a more oxidized paint medium.[28] Mimetite is relatively insoluble and thermodynamically stable, particularly at pH > 5, while schultenite is formed under more acidic conditions.[22] In addition, mimetite also requires the presence of chlorine (Cl^- ions), which are often present in old master paintings and can stem from the use of the Dutch stack process for the manufacture of lead white, can be released during lead soap formation, or can originate from external (atmospheric) sources.[13]

The more abundant presence of gypsum and calcite in area III might be indicative of a more alkaline environment, favorable for the formation of mimetite. Furthermore, we could hypothesize that such a variation in pH could have been caused by a variability in the local concentration of orpiment in the paint matrix, with more orpiment initially present in area II than in area III.

Although MA-XRF scanning is less sensitive to elements with a low atomic number, the elemental distribution of sulfur is consistent with the above-mentioned MA-XRPD results, in particular, showing less S to be present in area II, rich in schultenite, than in the orpiment-rich border of the flower (area I), while the arsenic distribution map shows a comparable arsenic content in areas I and II.[29]

In addition, MA-XRPD mapping provided information regarding the iron-containing pigment in the presumed underlying layer and the distribution of quartz over the whole surface of the flower. In contrast to the elemental map of iron obtained by MA-XRF, the map of goethite, indicative of yellow ocher, shows only the shape of the flower and not the oval shape surrounding it. The copper (azurite containing) background paint covering the ocher blocks the goethite signals from the underlying oval shape.

Complementary to MA-XRPD, RIS in the VNIR spectral region allowed us to map goethite within the painting, giving rise to comparable distribution maps (Figure 4.3-4C). RIS in the visible spectral range detects spectral signatures from pigments that are predominantly present on the surface of the painting based on the electronic transitions related to the color of materials.[30] The VNIR goethite map was obtained on the basis of a spectral endmember showing the typical features for goethite: a reflectance transition edge around 545 nm and absorption bands near 650 and 950 nm (Figure S 4.3-4).[30] Yellow pigments such as orpiment

and non-degraded yellow lake pigments normally can be detected with VNIR; however, in this case, no definite spectral features for their identification could be observed.[31] We attribute this to the fact that, as demonstrated by MA-XRPD analysis, the original yellow pigment at the surface has converted into secondary products and that the yellow lakes faded.

Microscale analysis

A cross-sectioned sample (R50/1), taken from area II of the yellow rose, offered the opportunity to study the buildup, pigment composition, and distribution of secondary degradation products on the microscale. The cross section was studied under the light microscope, and elemental and molecular information was obtained by SEM-EDX analysis, Raman spectroscopy, and transmission mode SR-μ-XRF/XRPD mapping performed at beamline P06 of the PETRA III facility to provide complementary information to the macroscale XRF and XRPD analyses.

In Figure 4.3-5E, the distribution maps of the most relevant crystalline phases are shown; five paint layers could be identified. Unfortunately, since the layered structure of the sample did not align completely to the incoming x-ray beam (because of a slight tilt of the sample in the embedding material), the boundaries between the different strata cannot be easily discerned. However, combined with the corresponding XRF maps (obtained simultaneously during the μ-XRPD analysis) and with the SEM-EDX point and mapping analysis (Figure 4.3-5C), it was nevertheless possible to obtain a full understanding of the (original) sample stratigraphy: a red brownish calcite ground layer (L1) followed by two lead white–containing layers (L2 and L3), a yellow goethite + quartz layer (L4), and a thin, transparent top layer (L5) with one remaining orpiment particle.
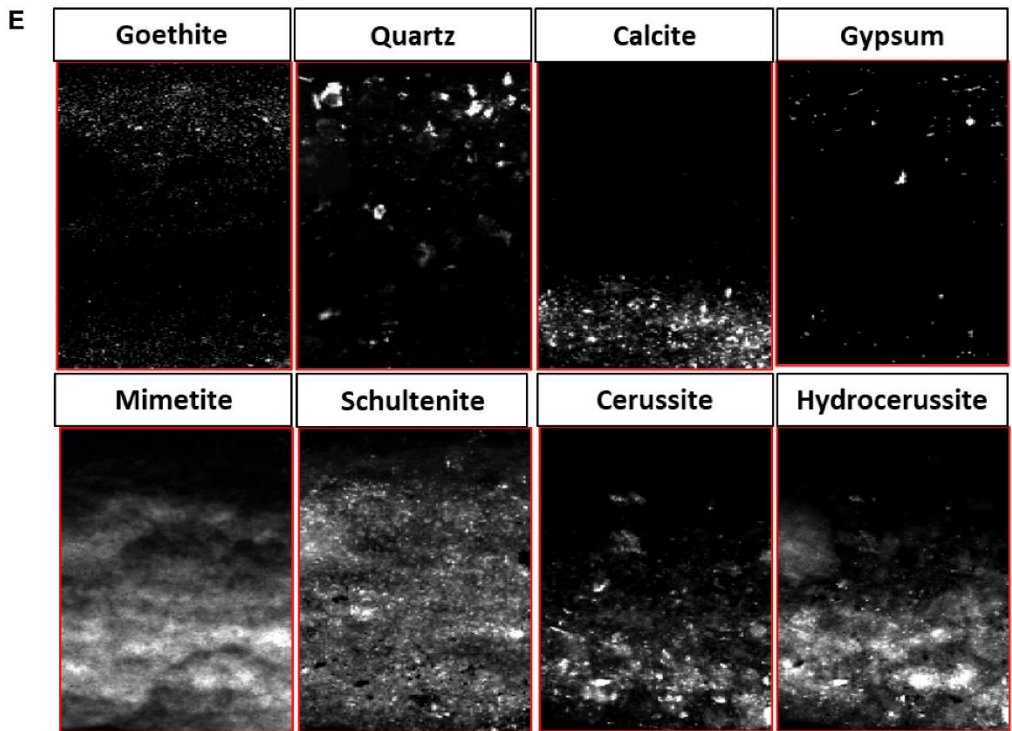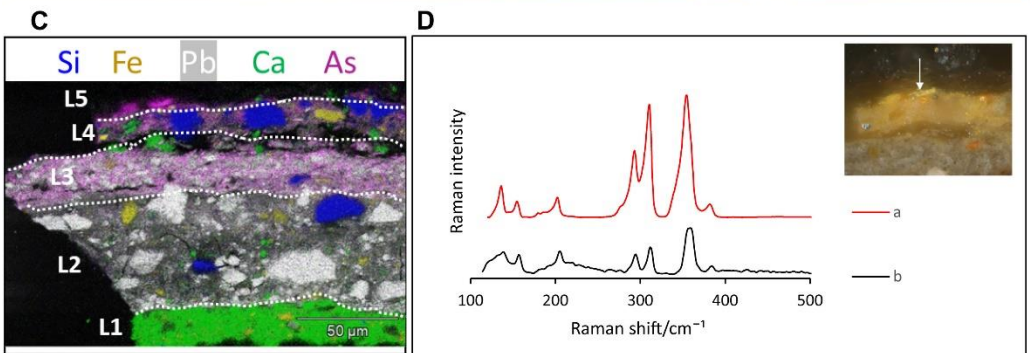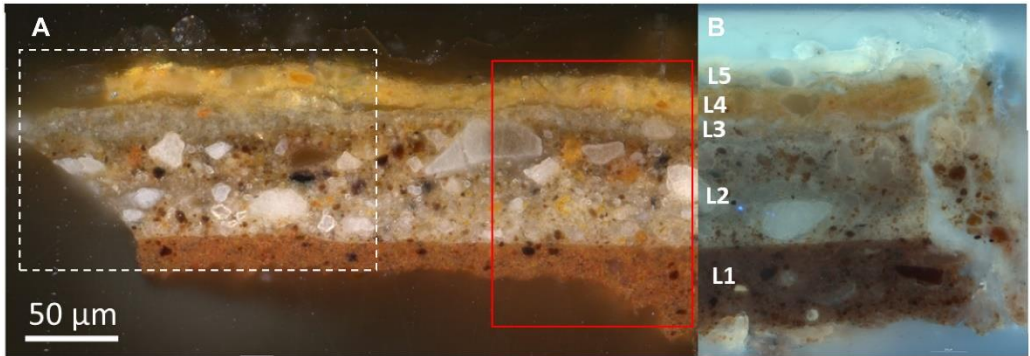
Figure 4.3-5 Results of microscale analysis [light microscopy (LM), SEM-EDX, Raman, and SR-μ-XRPD] of the paint cross section taken from the degraded yellow rose (sample location is indicated in Figure 4.3-3B with a red star). (A) Cross section R50/1 photographed in dark field (A) and UV light (B). The white rectangle indicates the area analyzed by SEM-EDX, with ensuing elemental maps shown in (C) of silicon (Si), iron (Fe), lead (Pb), calcium (Ca), and arsenic (As). The red rectangle indicates the area imaged by SR-μ-XRPD, with ensuing results shown in (E). (D) Identification of natural orpiment of an arsenic sulfide particle (white arrow) in cross section R50/1 with Raman spectroscopy: (a) reference spectrum of natural orpiment (RRUFF ID: R060105) and (b) spectrum collected on an orpiment pigment particle in R50/1. (E) Crystalline pigment phases and secondary products obtained with SR-μ-XRPD mapping at the P06 beamline of PETRA III. The 2D distributions shown are based on the scaling factors obtained through whole-pattern fitting, and the collected diffraction data were corrected for attenuation effects.

The first three layers (L1 to L3) of the cross section are consistently found in other cross sections taken from this still life painting and are consequently not specific for the buildup of the yellow rose. Mignon made use of a gray (L3) on double ground (L1 + 2) as traditionally encountered in 17th century Dutch paintings on canvas.[32] The first red ground (L1) is mainly chalk based (calcite) and consists of earth pigments such as hematite, goethite, and lead white. The second grayish-brown ground (L2), which is approximately 50 μm, is mainly lead white based (cerussite and hydrocerussite) and contains quartz and earth pigments. The third, thin whitish gray layer (L3) consists of primarily lead white (cerussite and hydrocerussite), chalk (calcite), and fine carbon black particles. Layer 4 is a warm yellow paint layer that is approximately 20 μm thick and appears to be mainly composed of coarse quartz (SiO_2) particles, fine-grained goethite, and some lead white, as identified by SR-μ-XPRD and EDX mapping and point analysis. In view of its goethite content, L4 is associated with the iron-rich underpainting layer that was previously inferred from macroscale imaging. Microanalysis on the paint cross section now evidences that the goethite layer is only followed by a thin (semi-)transparent paint layer (L5) in the paint stratigraphy, which aided its detection by the superficial MA-XRPD and RIS

techniques. Layer 5 appears very thin and transparent in bright-field light microscopy but is highly fluorescent under ultraviolet (UV) light (Figure 4.3-5B). The elemental SEM-EDX images and, in particular, additional point analyses revealed a pigmented layer containing quartz, calcite, gypsum, and one arsenic sulfide particle (the only yellow pigment particle present at the far left in layer 5). Both the refractive index of calcite, gypsum, and quartz are close to the binding medium of oil, which partially explains the transparent aspect of this paint layer. Today, the aforementioned Hirox observations exposed the top paint layer (L5) in area II as a darkened, semitransparent, and brittle paint over a coarse-grained brown underlying layer, corresponding to layer 4 in the paint cross section.

Although arsenic seems to be present throughout the paint stack, both SR-µ-XRF mapping and SEM-EDX analysis found only one remaining, intact orpiment grain, i.e., in L5. We therefore hypothesize that the artist included orpiment exclusively in the top paint layer. Micro–Raman spectroscopy identified this grain as natural orpiment, as demonstrated by the characteristic bands of natural orpiment with very strong absorption peaks at 311 and 355 cm^{-1}, strong peaks at 293 cm^{-1}, medium peaks at 154 and 203 cm^{-1}, and weak to very weak peaks at 136 and 106 cm^{-1} (Figure 4.3-5D).[33] Supplementary to MA-XRPD, SR-µ-XRPD imaging did not only allow for the identification of the secondary arsenic products schultenite and mimetite but also permitted to situate their distribution over the layer buildup (Figure S 4.3-5). Both lead arsenates are not located in discrete layers but are found distributed throughout the paint stratigraphy from L2 to L5, in this way, explaining the aforementioned elemental distribution. The ample presence of schultenite and mimetite throughout the stratigraphy is considered to be the result of a multistep degradation process of arsenic sulfide pigments, with soluble arsenate species migrating from L5 through the paint

stratigraphy and locally precipitating into lead arsenate minerals upon encountering suitable Pb^{2+} ions from (saponified) lead carbonate.[13] Preparatory layers L2 and L3 are particularly rich in hydrocerussite and cerussite and thus provide a good lead source for the formation of lead arsenates. The migratory aspect is underpinned by the backscattered electron image (Figure S 4.3-6), revealing the presence of sharp needle-like particles, rich in arsenic and lead, and visible throughout layers 2 to 4.[14]

Painting technique

On the basis of the chemical imaging on the micro- and macroscale and the optical examination of the paint surface, the original painting technique and layer buildup of the yellow rose could be inferred. The flower appears to have been painted after an efficient three-step method that is characteristic for 17th century still life painters. This included first blocking in the position of the flower with a monochrome underpainting and subsequently working up the details by applying (semi)transparent paint, i.e., with glazes for the shadows and lighter scumbles of paint for the sunlit parts.[24] In this manner, Mignon marked the position of the yellow rose with a yellow ocher-based underpaint that provided a midtone base for the superimposed top paint layer. The main body and details of the flower were painted with different orpiment containing paints depending on the desired/intended hue: either exclusively pigmented with orpiment for the bright highlights in area I or with more increasing admixture of gypsum, calcite, quartz, and carbon black for the light midtone of area II and the intermediate shadow tone of area III. In the expected deeper shadows, a more abundant presence of calcite was detected (area IV), which suggest the presence of a yellow lake.

A direct parallel can be drawn from Mignon's painting technique with the contemporary Dutch painters' manual *The Big World Painted Small* by Willem

Beurs, published in 1692 in Amsterdam. Aside from other detailed instructions for various objects in still life paintings, he includes paint instructions for the yellow rose [*geelen eglantier*] and suggests to paint it only with Kings yellow [*koningsgeel*], the artificial equivalent of natural orpiment, for the highlights; a little bit of carbon black and a fugitive yellow lake [*schietgeel*] for the shadows; for the reflections, only a light yellow lake; and for the colors in between, a mixture of Kings yellow and black.

In Mignon's yellow rose, calcite is present in the areas that we assume to have been shadowed, and although it is plausible that chalk was used as a filler for the translucent glaze, it is more likely present as a residual substrate for a now degraded yellow dyestuff, as its use is also prescribed by Beurs. Lake pigments were prepared by the precipitation or adsorption of an organic dyestuff onto an insoluble substrate. For yellow lakes in 17th century paintings, calcium carbonate or chalk is almost predominantly found as a substrate.[34–36] The presence of a yellow lake is generally difficult to prove, as the yellow organic dyestuff has completely faded away as a result of photochemical reaction. However, previous studies have demonstrated that its presence can be indicated by a high concentration of calcium (as a marker for chalk).[37] Chalk in its own right was sometimes used as a paint additive, to give body and translucency to a paint, but typically in combination with other colored pigments. This does not appear to be the case here, given that no other elements or colored pigments seem to correlate with area IV on the basis of the MA-XRF and MA-XRPD results. Thus, this strengthens our hypothesis regarding the use of a degraded yellow lake with a Ca-based substrate.

In area III, a clear amount of gypsum is found, associated to the paint mixtures with orpiment and little calcite. It has been suggested that gypsum can be formed

in situ as a secondary product, as a reaction between calcite and orpiment in the oxidized paint matrix. However, this would entail the presence of smaller (nano-like) particles formed through precipitation, while in this case, bigger crystal particles (2 to 10 μm) are observed inside the paint, which suggest the presence of deliberately added gypsum. Gypsum does not have a considerable color effect in oil, and from paint reconstructions made by the author with natural orpiment, the addition of gypsum also does not influence the color of the bright yellow orpiment. It does however change the optical properties to a more translucent yellow paint, which, applied on a quartz and yellow ocher paint, gives a subtle warm greenish hue. This paint layer thus likely functioned as a pigmented glaze to achieve an intermediate shadow tone required for the smooth transition between area II and area IV. Gypsum is listed by the Italian painter Lomazzo in his *Trattato dell'arte de la pintura* among the pigments that are safe to use with orpiment, and the combined detection with gypsum has also been reported in other paintings by Adriaen Coorte, Jan Davidsz. de Heem, and Martinus Nellius.[13,15,38,39]

Quartz (SiO_2) was identified with SR-μ-XRPD in L4 and L5 of the paint cross section, whereas MA-XRPD found it distributed over the entire surface of the flower (Figure 4.3-4). Quartz is a mineral commonly found in iron and arsenic ores. However, in view of the size of the particles and their abundance, quartz seems to also have been intentionally added to the paint mixture. Under the SEM microscope, the particles show a distinct angular shape characteristic of crushed glass, but EDX spectra of individual particles only presented high signals for silicon and oxygen, excluding the hypothesis of the presence of colorless glass, in which considerable amounts of sodium, potassium, and calcium or minor quantities of magnesium, aluminum, phosphorus, titanium, manganese, or iron are expected.[40] Orpiment is typified in historical sources as a poor drier and an

extremely hard pigment to grind. Authors such as Cennino Cennini, Marshall Smith, Palomino, De Mayerne, and Willem Beurs therefore recommend the addition of glass to improve its drying and grinding properties.[41–45] Although more inert than glass, paint reconstructions and grinding experiments proved that quartz also facilitated the grinding and the drying of the orpiment paint. Another plausible explanation for the presence of quartz in the paint mixtures is that it may have functioned as a transparent, colorless extender to improve the working properties of the paint and/or to change the physico-optical properties of the paint film, increasing its transparency.[46] Quartz or other silica are regularly encountered in paint, but its function is rarely discussed and not yet well understood, for example, in the grounds of Rembrandt paintings and mixed with a red lake in Lorenzo Lotto's *St. Catherine*, dated 1522.[46,47]

Optical changes

The combined analysis augmented with close examination of the paint surface led to important insights on the now degraded state of the yellow rose. As a result of various chemical and physical degradation processes in the paint system, the originally intended optical appearance of the yellow rose drastically changed. The yellow lake, used to paint the shadow areas on the flower, faded, while the orpiment, used in the sunlit area of the flower, degraded and turned the paint layer from bright yellow to transparent. The degradation of the original parent pigment instigated various reactions, which led to the formation of arsenolite, schultenite, and mimetite. Intact orpiment particles are still present around the borders of the yellow rose (area I) and dispersed over the surface of the yellow rose. These are probably the paint areas with the highest concentrations of orpiment, leaving some grains only partially degraded. Arsenolite can be visually correlated to white crust formations on the paint surface as a result of direct photo-oxidation

of the orpiment, while the increased transparency and consequent visual darkening in area II and particularly in area III are caused by the physical breakup of the yellow mineral and subsequent formation of the colorless secondary lead arsenate minerals schultenite and mimetite. The degradation now allows light to penetrate the once opaque top paint layer and be reflected by the underlying dark yellow ocher-based underpainting, leading to an optical darkening effect.

Both pigment mixtures that were used for creating either the shadows on the flower or the bright yellow highlights degraded or faded, and while these paint layers were intentionally already thinly applied, conforming to the painting technique of still life painters, both have caused an increased visibility of the underlying, monochrome yellow ocher paint layer, which is now responsible for the overall color appearance of the rose. This resulted in a flatter (less 3D)–looking flower, as subtle transitions defining the body of the flower can no longer be perceived, which is the reverse optical effect originally intended by Mignon.

4.3.3   Conclusions

In conclusion, a combined micro- and macroscopic approach has been presented in this article to investigate the yellow rose in *Still Life with Flowers and a Watch* by Abraham Mignon. This investigation has led to a considerably improved insight into the bilayer buildup, current condition, and the original intended appearance of this strongly degraded flower.

Degradation of the arsenic pigment orpiment and yellow lake has each caused substantial optical changes. Light-induced fading of the organic yellow dyestuff in the yellow lake glaze has caused the intended shadow areas to turn white because of the remaining calcite-based substrate. The yellow bright pigment orpiment underwent several chemical reactions, leading to the precipitation of lead arsenates schultenite and mimetite and the formation of arsenolite. These

newly formed degradation products visually affected the paint surface. White crust deposits on the paint surface were correlated to arsenolite, while the formation of schultenite and mimetite altered the physical condition and appearance of the paint. The once bright yellow paint transformed into a colorless, transparent, and brittle layer. Although the chemical reactions irreversibly changed the artists' intention, chemical imaging such as MA-XRF scanning made it still possible to recapture the once visible and meticulously applied highlights and shadows of this flower.

From a wider perspective, this paper showcases the potential of SR-µ-XRPD and MA-XRPD to discriminate inorganic degradation products at the micro- and macroscale. MA-XRPD enables us to precisely correlate in situ formed products with what we see on the surface, while SR-µ-XRPD investigations made an in-depth study of this particular degraded multilayered system possible on the microscale. RIS in the VNIR spectral range also provided insight into the optical condition of the now-degraded layers, as their consequent transparency allowed mapping goethite in the underpainting with high spatial resolution.

Ultimately, this interdisciplinary approach uncovered new information on Mignon's artistic practice, and in a broader perspective, our research sheds light on substantial optical changes that might occur for specific surface textures that were painted with a similar pigment palette. Our methodology and all the extracted data that we obtained toward a virtual reconstruction of a degraded motif could be applied to artworks of worldwide renown.

4.3.4   Materials and methods

Light microscopy

A microscopic paint sample (R50/1), taken by A. Wallert in 1999, was reexamined for the purpose of this study.[24] The cross section was taken from a

flower petal of the yellow rose (see figure for the location of the cross section). The cross section was photographed according to the paint sample database protocol of the Rijksmuseum with a Zeiss Axio Imager.A2m microscope (Carl Zeiss Microscopy LLC, USA) equipped with a Zeiss AxioCam Mrc5 digital camera. White light was provided by a light-emitting diode (LED) lamp with a color temperature of 5600 K and a colibri.2 controller for UV fluorescence microscopy (LED, 365 nm). All images were obtained, processed in the image acquisition software Zen 2 pro (blue edition) with extended depth of focus facilities, and observed on a calibrated EIZO ColorEdge CG277 BK computer screen.

SEM-EDX

SEM-EDX was performed on a JEOL JSM-5910LV microscope. Before the analysis, the cross section was coated with a thin layer of gold to improve surface conductivity using a JEOL JFC-1200 Fine Coater (15 s at 45 mA). Backscattered electron images were obtained in high vacuum and point analysis and elemental mapping using the Noran System Six software. The cross section was also studied in low vacuum with the FEI scanning electron microscope. Backscattered electron (BSE) images of the cross section were taken at an acceleration voltage of 5 kV, at a 5.9-mm eucentric working distance with a spot size of 3.

SR-μ-XRPD

To gain more insight into the crystalline pigment phases and secondary degradation products, μ-XRPD mapping was carried out on cross section (R50/1) at the Microprobe hutch of the hard x-ray micro/nanoprobe beamline (P06) of the PETRA III storage ring (DESY, Hamburg, Germany).[48] A Kirkpatrick-Baez mirror optical system was used to focus the beam, achieving a size of 0.5 μm by 0.5 μm (hor. × vert.), using a primary photon energy of 21 keV. A Keyence

optical microscope equipped with a perforated mirror was allowed for positioning of the sample. Diffraction signals were recorded in transmission geometry using an EIGER X 4M area detector (Dectris Ltd., Switzerland), and calibration of the diffraction setup was performed by means of a LaB_6 reference sample.

An area of 100 μm by 180 μm was scanned using a step size of 1 μm in the horizontal direction and 0.5 μm in the vertical direction. An exposure time of 0.25 s per pixel was used to acquire the diffraction patterns.

The in-house developed software package XRDUA was used for the processing of the XRPD data. The obtained 2D distributions shown in this article are based on the scaling factor obtained through whole pattern fitting, and the collected diffraction data were corrected for attenuation effects.[49]

Micro-Raman spectroscopy

Micro–Raman spectroscopy spectra were acquired with a Renishaw InVia Raman microscope with a Peltier-cooled (−60°) charge-coupled device detector (1020 × 256 pixels), using a high-power near-IR solid diode laser of 785 nm (1.12 mW) in combination with a grating of 1200 lines per millimeter (l/mm). A silicon reference sample was used to calibrate the instrument. To avoid damage, the power of the laser was reduced to 0.1% with neutral density filters. The sample was analyzed with a ×100 objective and an exposure time of 2 s and five accumulations. The spectra were acquired, normalized, and corrected for baseline using the Wire 3.4 Raman software.

MA-XRF imaging

Elemental maps of the entire painting and a smaller detail were collected with the commercially available MA-XRF scanner M6 Jetstream from Bruker Nano

GmbH (Berlin, Germany). The M6 Jetstream consists of a 30-W Rh-target microfocus x-ray tube with a maximum voltage of 50 kV, a maximum current of 0.6 mA, a polycapillary lens, and a 30-mm2 X-Flash silicon drift detector that is moved over the surface of the painting by means of an X, Y–motorized stage, enabling a scan area of 80 cm by 60 cm.[50] A spot size of 150 μm was set for the measurements with a working distance of ca. 10 mm from the x-ray snout and the surface of the painting. The entire painting (750 mm by 571 mm) was scanned with a step size of 650 μm and a dwell time 70 ms. For the detail scan (193 mm by 235 mm), including the yellow rose, a step size of 300 μm and a dwell time of 150 ms were used.

The resulting spectral data cubes of the MA-XRF scanning were processed using data analysis software packages Python Multichannel Analyzer and Datamuncher gamma.[51,52] In the ensuing 2D distribution maps, each pixel carries information on the calculated net peak intensities of the emission lines of the element, with a gray scale linear to the detected intensities.

<u>PCA: k–means clustering</u>

For a closer inspection of the MA-XRF dataset, a PCA with subsequent k-means clustering was carried out using the open-source software package XANES-wizard.[53,54] PCA is a well-established dimension-reducing statistical technique, applied for pattern recognition in multivariate datasets.[55,56] PCA using the singular value decomposition approach of the mean-centered data matrix was used to reduce its dimensionality from E to N dimensions by expressing the dataset using only the first N PCs. The first N PCs explain most of the data's variance, and in this case, six pieces were selected (see Supplementary Figures). The distance between data points in the N-dimensional component space (score plot) is a direct measure of the similarity of the XRF spectra and can thus be used

to cluster pixels according to their (Euclidean) distances from the cluster centers (centroid linkage method, *k*-means clustering). Pixels with similar spectra are effectively clustered via this method into *k* groups, resulting in an image segmentation. To achieve a finer image segmentation, $k = 13$ clusters were used. After the *k*-means clustering, the result was improved by a GMM using EM for clustering (maximum of 1000 iterations).

MA-XRPD imaging

The macro-XRPD imaging experiments on the painting *Still Life with Flowers and a Watch* were carried out using an in-house built mobile MA-XRF/XRPD scanning instrument from the AXIS Research Group (University of Antwerp), operating in reflection mode. A monochromatic Cu-K$_\alpha$ (8.04 keV) x-ray source (Incoatec GmbH, Germany) was used with a photon flux of 2.9×10^8 photons/s, a focal diameter of ca. 140 μm, a focal distance of ca. 20 cm, and a divergence of 2.4 mrad. An incident angle of 10° was chosen between the primary x-ray beam and the painting's surface, leading to a beam with an elliptical footprint of approximately 1 mm by 0.2 mm. Opposite the x-ray source a, PILATUS 200K detector (Dectris Ltd., Switzerland) was positioned at an angle of 40° with the painting surface to record the diffraction patterns. To ensure an equal distance between the x-ray source and the painting for every point of the scan, a laser distance sensor (Baumer Hold., Switzerland) was used to automatically correct the position of the setup for topographical variations. The XRPD scanning instrument is also equipped with a Vortex silicon drift detector (Hitachi, Japan) that allows for simultaneously acquiring XRF data. The above-mentioned equipment is fastened to a motorized platform (motor stages from Newport Corp., USA) that allows moving in the *XY* plane. The painting itself was positioned on a motorized stage that allowed movement in the vertical (*Z*) direction. The area

of the yellow rose (97.5 mm by 109.5 mm) was scanned with an exposure time of 10 s per pixel and a step size of 1.5 mm by 1.5 mm.

The recorded XRPD data were processed using the in-house developed software package XRDUA from the AXIS research group (University of Antwerp).[49,57] The obtained 2D distributions shown in this article are based on the intensity scaling factor obtained from the fitting procedure.

<u>Visible-to-near-infrared RIS</u>

VNIR (400 to 1000 nm) diffused reflectance image cubes were acquired using a high sensitivity hyperspectral camera (Surface Optics Corp, 710E model), equipped with a transmission grating-prism spectrometer combined with a backside illuminated EMCCD detector. The imaging camera has a spectral sampling of 2.5 nm, for a total of 260 channels, and produces image cubes with 1024 by 1024 spatial pixels. The spatial resolution at the painting was 0.168 mm, corresponding to 172-mm field of view, and the integration time used was 100 ms. Two light sources Solux 4700K, 50-W lamps (coated to minimize UV and IR light) were used to collect the reflected signal. A step/stare collection approach was used to collect VNIR image cubes of the entire surface of the painting to allow generating a complete image cube. To do this, the camera and lights remained stationary, the painting was moved left-right and up-down on an easel, and a total of 20 cubes (1024 × 1024 pixels) were acquired to have the final VNIR reflectance data cube. The conversion to apparent reflectance was done using a standard protocol, namely flat fielding. A dark image cube (no light allowed into the camera) was collected along with an image cube of the illumination light reflected off a white diffuse reflectance standard (99% reflector, Labsphere, Inc) that was placed in the plane of the painting. The apparent reflectance image cubes were calculated by dividing each raw cube collected of the painting after

subtraction of the dark image cube by the image cube of the dark-subtracted diffuse reflectance standard. The 20 cubes were then stitched and registered to a visible image.[58] The reflectance maps of the endmembers were made using the spectral angle mapper algorithm in the ENVI software (Harris Corp.).

Five-micrometer resolution photography

The detail of the yellow rose (10 cm by 10 cm) was photographed in 5-μm resolution with a Hasselblad H6D-400c MS camera by photographer Carola van Wijk. Six separate images were collected with an 11600×18700 pixel dimension at 300 dpi horizontal and vertical resolution. The separate images were color-calibrated using an ICC profile (Argyll) that was custom-made by photographing a ColorChecker Digital SG (X-rite) color card at the same 5-μm resolution. The color-calibrated images were then digitally assembled into a single image in Photoshop.

High-resolution 3D digital microscopy

The paint surface of the yellow rose was studied and photographed using a Hirox RH-2000 3D digital microscope on a motorized XY stage, equipped with a MXB-2500REZ lens. The microscope can achieve spatial sampling from 4.3 μm per pixel in low range (×35 magnification), 1.13 μm per pixel in mid-range (×140 magnification), and 0.45 μm per pixel in high range (×350 magnification). For the images in this paper, images were taken in mid-range. A white balance was made with a color checker white balance target of the color checker passport from X-rite. The images were photographed under the same light conditions and exposure time.

4.3.5 Supporting information
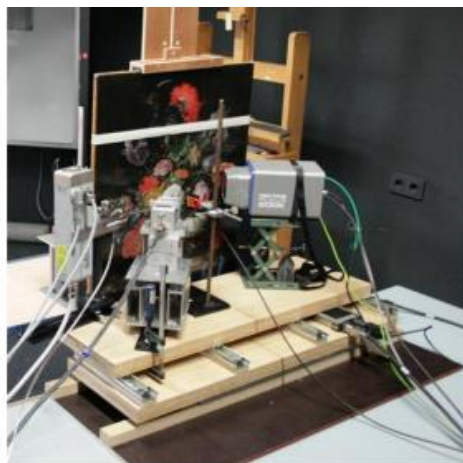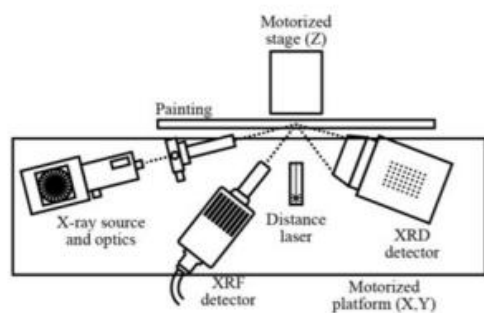
Figure S 4.3-1 Overview of the MA-XRPD scanning instrument. Schematics and corresponding visual photograph of the MA-XRPD scanner in reflection mode. Photo Credit: (left) Steven De Meyer, Frederik Vanmeert and (right) Nouchka De Keyser.
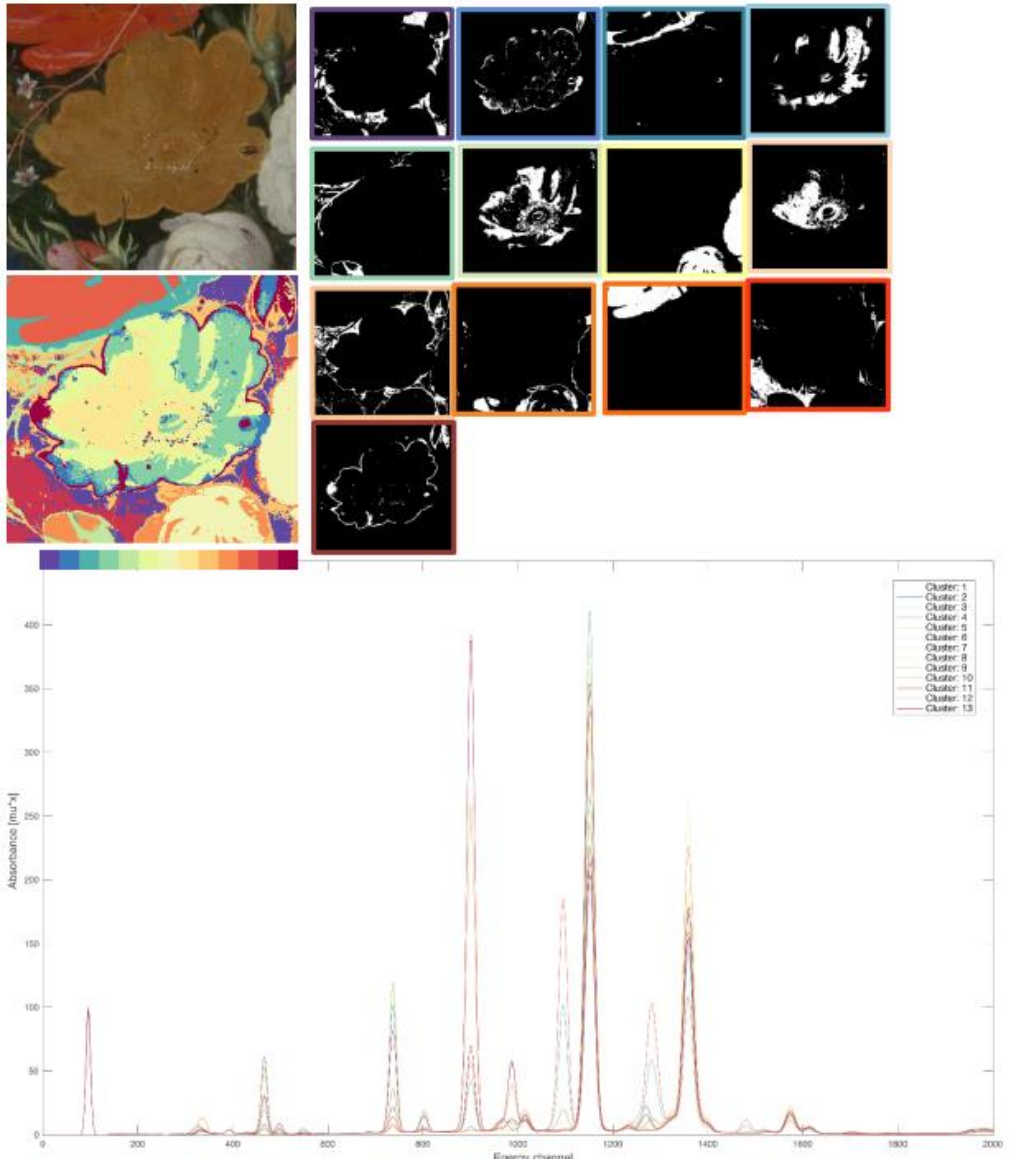
Figure S 4.3-2 Results of the PCA k-means clustering (XANES-Wizard). Composite images of the 13 clusters obtained with Principal Component Analysis and subsequent k-means clustering, improved by a Gaussian Mixture Model (GMM) using Expectation Maximization (EM) for clustering (max 1000 iterations) of the MA-XRF dataset.

2theta	Intensity	FWHM
18.31	1000.0	0.2398
19.92	78.1	0.2398
20.06	58.4	0.2398
20.20	35.1	0.2398
20.62	120.7	0.2398
21.01	67.3	0.2398
23.79	43.3	0.2398
23.97	46.4	0.2398
24.64	93.2	0.2398
25.38	46.4	0.2398
25.77	36.9	0.2398
26.17	285.6	0.2398
26.49	359.0	0.2398
26.98	54.0	0.2398
27.60	46.2	0.2398
27.78	79.9	0.2398
28.20	185.3	0.2398
28.53	73.6	0.2398
28.98	263.3	0.2398
29.57	266.9	0.2398
30.50	59.4	0.2398
31.93	93.4	0.2398
34.87	87.4	0.2398
35.86	57.4	0.2398
36.37	137.5	0.2398
38.14	39.5	0.2398
38.23	46.8	0.2398
39.84	37.7	0.2398
39.98	48.4	0.2398
40.11	53.2	0.2398
40.30	45.5	0.2398
40.50	62.4	0.2398
40.66	57.1	0.2398
40.79	53.0	0.2398
40.94	47.7	0.2398
42.09	48.4	0.2398
42.22	51.5	0.2398

Figure S 4.3-3 XRPD data orpiment. (A) 1D diffractogram of a pixel from the border of the flower with orpiment like particles. (B) 2D XRD pattern showing preferential orientation for the high intensity peak around 18.35. The identification of orpiment was complicated by a strong preferred orientation observed in the 2D XRPD patterns. The preferred orientation is an intrinsic property of certain minerals to orient themselves in certain directions according to a preferred crystallographic plane.(59) Ideally, all crystallites are assumed to be randomly oriented for homogenous debye markers, however, when preferred orientations are observed, anisotropic signals are obtained and some reflection may completely disappear.(5) This complicates the identifica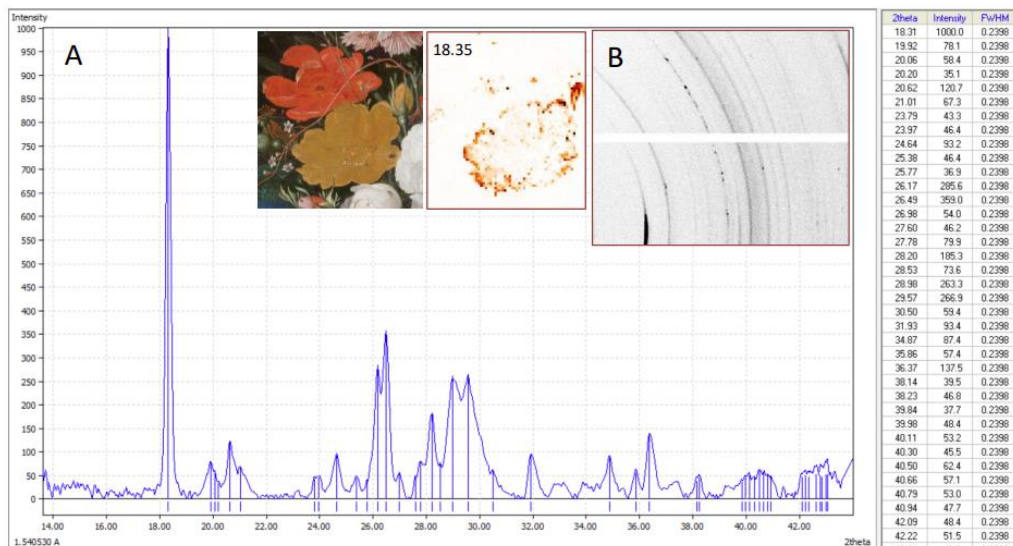tion of the pigment as this can lead to the change in relative intensities of the reflections from other crystallographic planes and increasing intensities of peaks corresponding to the preferred oriented cleavage planes.(59) This was also the case here, where the most intense peak of orpiment was found at 18.35 (corresponding to the literature and XRD reference data (COD, crystallography open database), but the intensities at the other angular positions deviated from the reference data. With our MA-XRPD set-up we also capture a limited azimuthal range with the XRPD detector, which means that there is a great chance that signals showing preferential orientation and thus covering a limited azimuthal range will be lost. Despite the incomplete characterization with XRPD, its distribution corresponded strongly with the defined area I, around the outlines and in certain details of the yellow rose, which is characterized by yellow micaceous, foliated pigment particles, that were identified by Raman as natural orpiment in the cross-section.
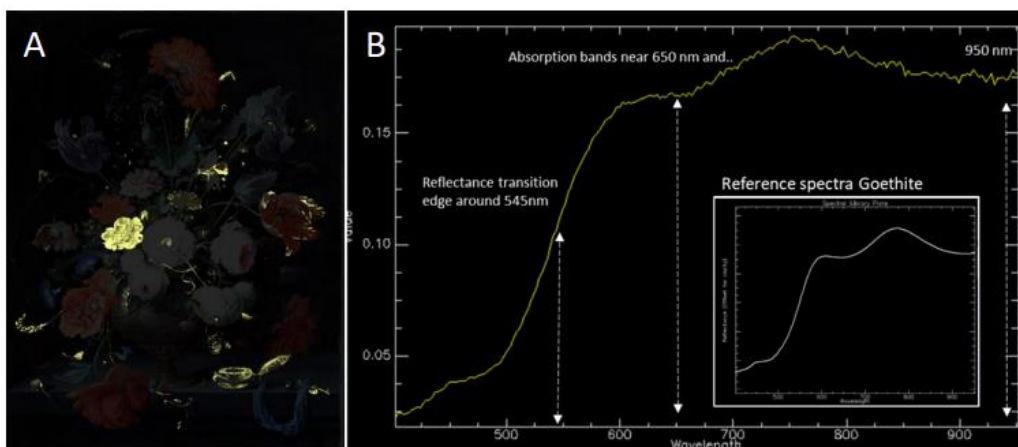
Figure S 4.3-4 Identification and mapping of goethite with Visible-to-near-infrared reflectance imaging spectroscopy of Mignon's Still life with flowers and a Watch. (A) Map obtained with the portion of the spectral endmember (B) showing characteristic features of Fe Hydroxide know as goethite, contained in the yellow ochre pigment.
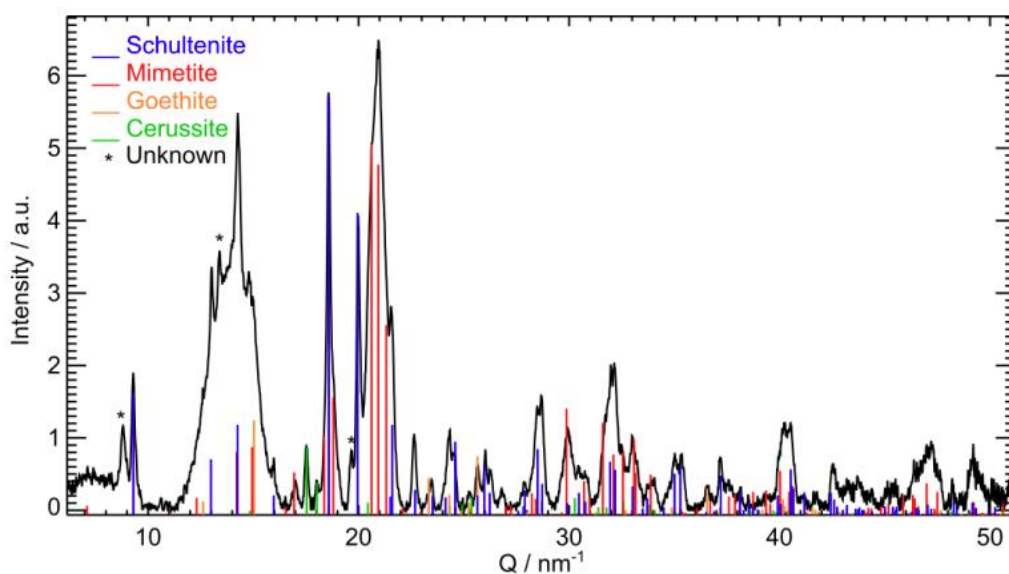
Figure S 4.3-5 Identification of secondary formed arsenic products schultenite and mimetite with SR-μ-XRPD. Diffractogram obtained after median azimuthal integration of an averaged 2D diffraction image (25 pixels) collected with SR-μ-XRPD.
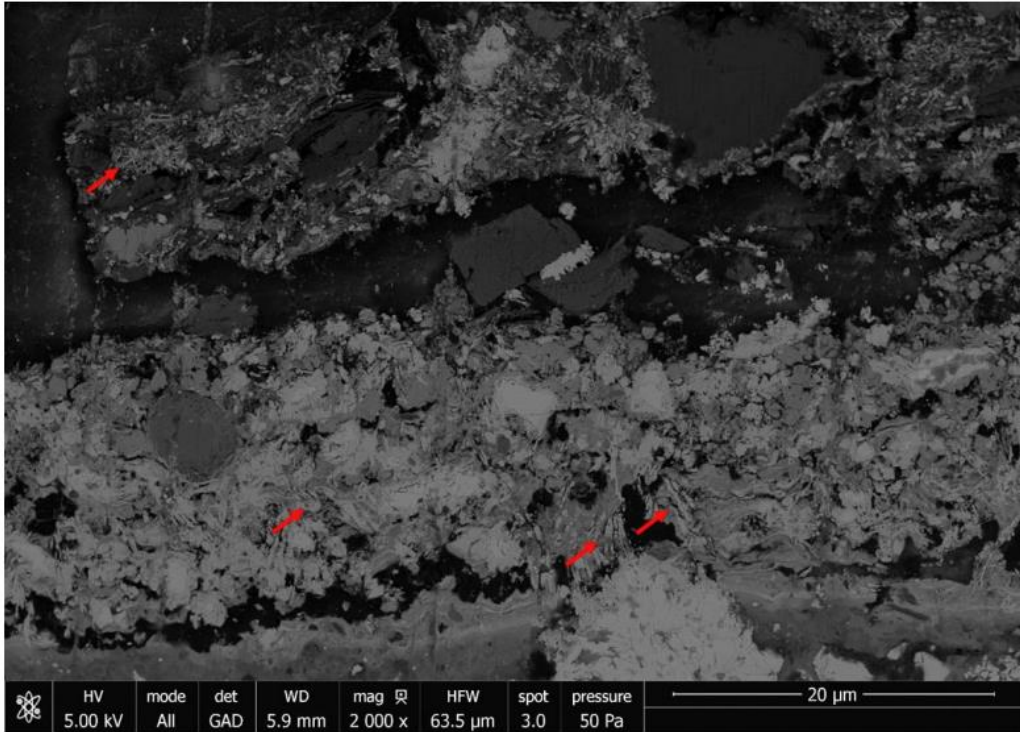
Figure S 4.3-6 Backscattered electron image of cross-section R50/1. The backscattered electron image (BEI) of cross-section R50/1 shows sharp needle like particles (red arrows), rich in arsenic and lead, visible throughout layer 2-4.

Acknowledgements

Author contributions: Data acquisition/analysis was performed by N.D.K., F.V., S.D.M., and K.J. (MA-XRPD and SR-μ-XRPD); N.D.K. and F.G. (RIS); N.D.K. (MA-XRF); and F.B. and N.D.K. (PCA). The manuscript was written by N.D.K. with input (review and editing) from K.K., K.J., G.V.d.S., E.H., and all other authors. All authors contributed to the manuscript.

Competing interests: The authors declare that they have no competing interests.

Data and materials availability: All data needed to evaluate the conclusions in the paper are present in the paper and/or the Supplementary Materials.

References

(1) Baij, L. A Molecular Perspective on the Cleaning of Oil Paintings, Universiteit van Amsterdam, Amsterdam, 2020.

(2) Miliani, C.; Monico, L.; Melo, M. J.; Fantacci, S.; Angelin, E. M.; Romani, A.; Janssens, K. Photochemistry of Artists' Dyes and Pigments: Towards Better Understanding and Prevention of Colour Change in Works of Art. *Angew. Chem. Int. Ed.* **2018**, *57*, 7324–7334.

(3) Van Loon, A.; Noble, P.; De Man, D.; Alfeld, M.; Callewaert, T.; Van Der Snickt, G.; Janssens, K.; Dik, J. The Role of Smalt in Complex Pigment Mixtures in Rembrandt's Homer 1663: Combining MA-XRF Imaging, Microanalysis, Paint Reconstructions and OCT. *Herit. Sci* **2020**, *8*, 90.

(4) Schnetz, K.; Gambardella, A. A.; Van Elsas, R.; Rosier, J.; Steenwinkel, E. E.; Wallert, A.; Iedema, P. D.; Keune, K. Evidence for the Catalytic Properties of Ultramarine Pigment. *J. Cult. Herit.* **2020**, *45*, 25–32.

(5) Vanmeert, F.; Hendriks, E.; Van der Snickt, G.; Monico, L.; Dik, J.; Janssens, K. Chemical Mapping by Macroscopic X-Ray Powder Diffraction of Van Gogh's Sunflowers: Identification of Areas with Higher Degradation Risk. *Angew. Chem.* **2018**, *57*, 7418–7422.

(6) Monico, L.; Cartechini, L.; Rosi, F.; Chieli, A.; Grazia, C.; De Meyer, S.; Nuyts, G.; Vanmeert, F.; Janssens, K.; Cotte, M.; De Nolf, W.; Falkenberg, G.; Sandu, I. C. A.; Tveit, E. S.; Mass, J.; De Freitas, R. P.; Romani, A.; Miliani, C. Probing the Chemistry of CdS Paints in The Scream by in Situ Noninvasive Spectroscopies and Synchrotron Radiation X-Ray Techniques. *Sci. Adv.* **2020**, *6*, eaay3514.

(7) *Research Project REVIGO, "Original Colours of Van Gogh's Paintings."* https://assets.vangoghmuseum.nl/a41553fa-025e-4a8d-9e49-132f267652aa?c=fdacfed0591e798c2daa6b72e18b4abc00da7f192ad37b8ac a211e2a0c6ace30.

(8) Van der Snickt, G.; Dooley, K. A.; Sanyova, J.; Dubois, H.; Delaney, J. K.; Gifford, M.; Legrand, S.; Laquiere, N.; Janssens, K. Dual Mode Standoff Imaging Spectroscopy Documents the Painting Process of the Lamb of God in the Ghent Altarpiece by J. and H. Van Eyck. *Sci. Adv.* **2020**, *6*, eabb3379.

(9) Legrand, S.; Alfeld, M.; Vanmeert, F.; De Nolf, W.; Janssens, K. Macroscopic Fourier Transform Infrared Scanning in Reflection Mode (MA-RFTIR), a New Tool for Chemical Imaging of Cultural Heritage Artefacts in the Mid-Infrared Range. *Analyst* **2014**, *139*, 2489–2498.

(10) Dooley, K. A.; Conover, D. M.; Glinsman, L. D.; Delaney, J. K. Complementary Standoff Chemical Imaging to Map and Identify Artist Materials in an Early Italian Renaissance Panel Painting. *Angew. Chem. Int. Ed.* **2014**, *53*, 13775–13779.

(11)   Vanmeert, F. Highly Specific X-Ray Powder Diffraction Imaging at the Macroscopic and Microscopic Scale, Universiteit Antwerpen, 2019.

(12)   De Meyer, S.; Vanmeert, F.; Vertongen, R.; Van Loon, A.; Gonzalez, V.; Delaney, J.; Dooley, K.; Dik, J.; Van der Snickt, G.; Vandivere, A.; Janssens, K. Macroscopic X-Ray Powder Diffraction Imaging Reveals Vermeer's Discriminating Use of Lead White Pigments in Girl with a Pearl Earring. *Sci. Adv.* **2019**, No. 8, eaax1975.

(13)   Simoen, J.; De Meyer, S.; Vanmeert, F.; De Keyser, N.; Avranovich Clerici, E.; Van der Snickt, G.; Van Loon, A.; Noble, P.; Keune, K.; Janssens, K. Combined Micro- and Macro Scale X-Ray Powder Diffraction Mapping of Degraded Orpiment Paint in a 17th Century Still Life Painting by Martinus Nellius. *Herit. Sci.* **2019**, *7*, 83.

(14)   Keune, K.; Mass, J.; Mehta, A.; Church, J.; Meirer, F. Analytical Imaging Studies of the Migration of Degraded Orpiment, Realgar and Emerald Green Pigments in Historic Paintings and Related Conservation Issues. *Herit. Sci.* **2016**, *4*, 10.

(15)   Keune, K.; Mass, J.; Meirer, F.; Pottasch, C.; van Loon, A.; Hull, A.; Church, J.; Pouyet, E.; Cotte, M.; Mehta, A. Tracking the Transformation and Transport of Arsenic Sulfide Pigments in Paints: Synchrotron-Based X-Ray Micro-Analyses. *J. Anal. At. Spectrom.* **2015**, *30*, 813–827.

(16)   Mench, K.; Pottasch, C. SEM and Microanalysis. In *Historical Technology, Materials and Conservation*; Archetype Publications: London, 2012; pp 100–106.

(17)   Cutts, H.; Harrison, L.; Higgitt, C. The Image Revealed: Study and Conservation of a Mid-Nineteenth Century Ethiopian Church Painting. *Brit. Mus. Tech. Res. Bull.* **2010**, *4*, 1–17.

(18)   Van Dorst, S. Daniël Seghers, Phoenix of Flower Painters. *Hamilton Kerr Inst. Bull.* **2016**, *6*, 29–44.

(19)   Wallert, A. Orpiment and Realgar. *Maltechnik Restauro* **1984**, *90*, 54–57.

(20)   Douglass, D. L.; Shing, C. C.; Wang, G. The Light-Induced Alteration of Realgar to Pararealgar. *Am. Mineral.* **1992**, *77*, 1266–1274.

(21)   Vanmeert, F.; De Keyser, N.; Van Loon, A.; Klaassen, L.; Noble, P.; Janssens, K. Transmission and Reflection Mode Macroscopic X-Ray Powder Diffraction (MA-XRPD) Imaging for the Noninvasive Visualization of Paint Degradation in Still Life Paintings by Jan Davidsz. de Heem. *Anal. Chem.* **2019**, *91*, 7153–7161.

(22)   Vermeulen, M.; Nuyts, G.; Sanyova, J.; Vila, A.; Buti, D.; Suuronen, J.-P.; Janssens, K. Visualization of As(III) and As(V) Distributions in Degraded Paint Micro-Samples from Baroque- and Rococo-Era Paintings. *J. Anal. At. Spectrom.* **2016**, *31*, 1913–1921.

(23)   The Scientific Examination of a Seventeenth Century Masterpiece. *Z. Kunsttechnol. Konserv.* **2007**, *21*, 38–51.

(24)   Wallert, A. *Still Lifes: Techniques and Style: An Examination of Paintings from the Rijksmuseum*; Waanders: Amsterdam, 1999.

(25)   Christensen, A. H.; Hermens, E.; Tempest, H.; Wallert, A. History, Materials and Studio Practice. In *Painting Techniques*; Rijksmuseum: Amsterdam, 2013.

(26)   De Keyser, N.; Van der Snickt, G.; Van Loon, A.; Legrand, S.; Wallert, A.; Janssens, K. Jan Davidsz. de Heem (1606-1684): A Technical Examination of Fruit and Flower Still Lifes Combining MA-XRF Scanning, Cross-Section Analysis and Technical Historical Sources. *Herit. Sci.* **2017**, *5*, 38.

(27)   De Meyer, S.; Vanmeert, F.; Vertongen, R.; van Loon, A.; Gonzalez, V.; van der Snickt, G.; Vandivere, A.; Janssens, K. Imaging Secondary Reaction Products at the Surface of Vermeer's Girl with the Pearl Earring by Means of Macroscopic X-Ray Powder Diffraction Scanning. *Herit. Sci.* **2019**, *7*, 67.

(28)   Magalhaes, M. C. F.; Silva, M. C. M. Stability of Lead(II) Arsenates. *Monatsh. Chem.* **2003**, *134*, 735–743.

(29)   Van der Snickt, G.; Dubois, H.; Sanyova, J.; Legrand, S.; Coudray, A.; Glaude, C.; Postec, M.; Van Espen, P.; Janssens, K. Large-Area Elemental Imaging Reveals Van Eyck's Original Paint Layers on the Ghent Altarpiece (1432), Rescoping Its Conservation Treatment. *Angew. Chem. Int. Ed.* **2017**, *56*, 4797–4801.

(30)   Dooley, K. A.; Gifford, E. M.; Van Loon, A.; Noble, P.; Zeibel, J. G.; Conover, D. M.; Alfeld, M.; Van Der Snickt, G.; Legrand, S.; Janssens, K.; Dik, J.; Delaney, J. K. Separating Two Painting Campaigns in Saul and David, Attributed to Rembrandt, Using Macroscale Reflectance and XRF Imaging Spectroscopies and Microscale Paint Analysis. *Herit. Sci.* **2018**, *6*, 46.

(31)   Aceto, M.; Agostino, A.; Fenoglio, G.; Idone, A.; Gulmini, M.; Picollo, M.; Ricciardi, P.; Delaney, J. K. Characterisation of Colourants on Illuminated Manuscripts by Portable Fibre Optic UV-Visible-NIR Reflectance Spectrophotometry. *Anal. Methods* **2014**, *6*, 1488.

(32)   Stols-Witlox, M. J. N.; Megens, L.; Carlyle, L. "To Prepare White Excellent...": Reconstructions Investigating the Influence of Washing, Grinding and Decanting of Stack-Process Lead White on Pigment Composition and Particle Size. In *The artist's process: technology and interpretation*; Eyb-Green, S., Townsend, J. H., Clarke, M., Nadolny, J., Kroustallis, S., Eds.; Archetype: London, 2012; pp 112–129.

(33)   Vermeulen, M. Natural and Amorphous Arsenic Sulfide Pigments : Characterization, Degradation and Influence of the Binding Medium, Universiteit Antwerpen, Antwerpen, 2017.

(34)   Kirby, J.; Spring, M.; Higgitt, C. The Technology of Red Lake Pigment Manufacture: Study of the Dyestuff Substrate. *Natl. Gallery Tech. Bull.* **2005**, *26*, 71–87.

(35)   Saunders, D.; Kirby, J. Light-Induced Colour Changes in Red and Yellow Lake Pigments. *Natl. Gallery Tech. Bull.* **1994**, *15*, 79–87.

(36)   Hermens, E.; Wallert, A. Looking Through Paintings: The Study of Painting Techniques and Materials in Support of Art Historical Research; Archetype Publications: London, 1998; pp 269–295.

(37)   Van Loon, A. Color Changes and Chemical Reactivity in Seventeenth-Century Oil Paintings, Universiteit van Amsterdam, 2008.

(38)   Harley, R. *Artists Pigments c. 1600-1835: A Study in English Documentary Sources*; Butterworth Scientific: London, 1982.

(39)   Lomazzo, G. P. *Trattato Dell'arte de La Pintura, Libro Terzo: Del Colore, Cap VI*; 1584.

(40)   Spring, M. Colourless Powdered Glass as an Additive in Fifteenth and Sixteenth Century European Paintings. *Natl. Gallery Tech. Bull.* **2012**, *33*, 4–26.

(41)   Cennino, C. *A Treatise on Painting*; BiblioBazaar: London, 1844.

(42)   Smith, M. *The Art of Painting According to the Theory and Practise of the Best Italian, French and Germane Masters*; 1692.

(43)   Velasco, P. Y. *El Museo Pictorico y La Escala Optica*; 1724.

(44)   de Mayerne, T. T. Pictoria, Sculptoria, Tinctoria et Quae Subalkternarum Artium Spectantia; 1620.

(45)   Beurs, W. *De Groote Waereld in't Kleen Geschildert, of Schilderagtig Tafereel van's Weerelds Schilderyen, Kortelijk Vervat in Ses Boeken: Verklarende de Hooftverwen, Haare Verscheide Mengelingen in Oly, En Der Zelver Gebruik. Omtrent de Meeste Vertoningen van de Zigtbare Natuire. Leersaamelijk Den Liefhebbers En Leerlingen Der Ed. Schilderkonst Medegedeelt*; Johannes en Gillis Janssonius van Waesberge: Amsterdam, 1692.

(46)   Lutzenberger, K.; Stege, H.; Tilenschi, C. A Note on Glass and Silica in Oil Paintings from the 15th to the 17th Century. *J. Cult. Herit.* **2010**, *11*, 365–372.

(47)   Groen, K. *Paintings in the Laboratory: Scientific Examination for Art History and Conservation*; Archetype Publications, 2014.

(48)   Schroer, C. G.; Boye, P.; Feldkamp, J. M.; Patommel, J.; Samberg, D.; Schropp, A.; Schwab, A.; Stephan, S.; Falkenberg, G.; Wellenreuther, G.; Reimers, N. Hard X-Ray Nanoprobe at Beamline P06 at PETRA III. *Nucl.*

Instr. Meth. Phys. Res. A: Accel. Spectrom. Detect. Assoc. Equip. **2010**, *616*, 93–97.

(49)   De Nolf, W.; Vanmeert, F.; Janssens, K. XRDUA: Crystalline Phase Distribution Maps by Two-Dimensional Scanning and Tomographic (Micro) X-Ray Powder Diffraction. *J. Appl. Crystallogr.* **2014**, *47*, 1107–1117.

(50)   Alfeld, M.; Pedroso, J. V.; van Eikema Hommes, M.; Van der Snickt, G.; Tauber, G.; Blaas, J.; Haschke, M.; Erler, K.; Dik, J.; Janssens, K. A Mobile Instrument for in Situ Scanning Macro-XRF Investigation of Historical Paintings. *J. Anal. At. Spectrom.* **2013**, *28*, 760–767.

(51)   Alfeld, M.; Janssens, K. Strategies for Processing Mega-Pixel X-Ray Fluorescence Hyperspectral Data: A Case Study on a Version of Caravaggio's Painting Supper at Emmaus. *J. Anal. At. Spectrom.* **2015**, *30*, 777–789.

(52)   Solé, V. A.; Papillon, E.; Cotte, M.; Walter, P.; Susini, J. A Multiplatform Code for the Analysis of Energy-Dispersive X-Ray Fluorescence Spectra. *Spectrochim. Acta Part B* **2007**, *62*, 63–68.

(53)   Liu, Y.; Meirer, F.; Williams, P. A.; Wang, J.; Andrews, J. C.; Pianetta, P. TXM-Wizard: A Program for Advanced Data Collection and Evaluation in Full-Field Transmission X-Ray Microscopy. *J. Synchrotron Rad.* **2012**, *19*, 281–287.

(54)   Meirer, F.; Liu, Y.; Pouyet, E.; Fayard, B.; Cotte, M.; Sanchez, C.; Andrews, J. C.; Mehta, A.; Sciau, P. Full-Field XANES Analysis of Roman Ceramics to Estimate Firing Conditions—A Novel Probe to Study Hierarchical Heterogeneous Materials. *J. Anal. At. Spectrom.* **2013**, *28*, 1870.

(55)   Vogt, S.; Maser, J.; Jacobsen, C. *Journal de Physique IV* **2003**, *104*, 617–622.

(56)   Tsodouos, I.; Papachristodoulou, C.; Stamoulis, K.; Ioannides, K.; Pavlides, S.; Caputo, R.; Chatzipetros, A.; Koukouvelas, I.; Kremastas, E. EGU General Assembly Conference Abstracts; 2013.

(57)   De Nolf, W. Imaging of Crystalline Phase Distributions by Means of Scanning and Tomographic X-Ray Powder Diffraction. PhD thesis, University of Antwerp, Antwerp, 2013.

(58)   Conover, D. M.; Delaney, J. K.; Loew, M. H. Automatic Registration and Mosaicking of Technical Images of Old Master Paintings. *Appl. Phys. A.* **2015**, *119*, 1567–1575.

4.4 Uncovering the prevalence of metal oxalates in 15th-16th century early Netherlandish oil paintings: a macroscopic approach

4.4.1 Introduction

Oil paintings are highly complex chemical systems composed of mixtures of inorganic and organic materials (pigments, oil-based binders, driers, etc.) that can undergo chemical transformations over time due to environmental factors such as light, relative humidity or external pollutants. Historically, the structure of an oil paint layer has been described as a dispersion of pigment particles in a stable, covalently-bound and cross-linked oil network. With scientific advances this vision has changed over time towards the oil paint layer being a reactive metastable mixture of oxidized and ionic compounds in which complex pigment-binder interactions systematically occur.[1–3]

Within this reactive matrix, soaps and metal oxalates are among the most frequently described ionic species.[4–6] Understanding the physicochemical mechanism behind the formation of these compounds is essential for conservation and restoration purposes as they can modify the structural and aesthetic properties of the painting. Metal oxalates have been associated with the formation of thick, opaque insoluble crusts at the painting surface, significantly impacting the painting's appearance.[7] Different theories have been proposed for the formation of the oxalate anion, including microbiological activity for outdoor wall paintings, pigment – varnish interactions and photodegradation of the lipidic binding medium.[8–10] Ageing conditions such as exposure to UV radiation or high relative humidity have also been shown to stimulate the oxidation of fatty acids to dicarboxylic acids.[11] However, direct proof of the formation of the oxalate anion from an oil binder under these environmental conditions is yet missing.

The role of the cation in the oxalate formation mechanism also remains unclear. Several studies have reported a catalytic effect of specific pigments (e.g. zinc white) and different metal oxalates have been identified in paint layers, including copper, cadmium and lead oxalates.[6,8,12,13] Calcium oxalates have been most frequently reported in literature in oil paintings and their origin has typically been attributed to calcium-containing materials in the paint and ground layers or from particulate matter deposited on the paint surface.[5–7]

These questions were further investigated within the context of the MetOx[a] research project, coordinated by the Royal Institute for Cultural Heritage of Belgium (KIK-IRPA); more specifically the project aims to shed light on the mechanism behind the oxalate anion formation in oil films and to investigate which pigments are most susceptible for the formation of metal oxalates. To accomplish these goals a three-pronged methodology approach was chosen based on the multi-instrumental, microanalytical characterization of cross-sections belonging to historical oil paintings, the non-invasive and non-destructive macro-analysis of historical oil paintings and the characterization of the alteration phenomena in different collections of model systems with varying materialities and ageing conditions.

This thesis chapter will focus on the macro-analysis experiments that were carried out during the project. Within the scope of this project the macroscopic imaging provides representative information that is necessary to provide insights into 3 research questions: (a) how widespread is the occurrence of metal oxalates in historical oil paintings, (b) which types of metal oxalates can be identified and

---

[a] BRAIN-be Project n° BR/165/A6/METOX funded by BELSPO

(c) can a correlation be established between metal oxalate formation and specific pigment types.

4.4.2 Results and discussion

In order to answer the aforementioned questions, a series of material and chronological selection criteria were applied. Thus, the project was focused on historical Southern Netherlandish oil paintings and their cross-sections, produced from the 15th to the 16th centuries and mostly belonging to the Royal Museums of Fine Arts of Belgium (RMFAB). Furthermore, mostly surface red, green or blue areas of such paintings and their corresponding samples were studied as previous experience from the researchers involved in this project indicated that metal oxalates were more commonly found in such coloured zones. Despite this focus, differently coloured areas were also investigated using macroscopic techniques.

Based on the methodological criteria, a selection of oil paintings was made. These paintings (Table 4.4-1) were analysed across three different scan campaigns ranging from 2019 to 2021.

Table 4.4-1 List of historical oil paintings analysed with macroscopic imaging techniques for the MetOx project.

Painter name	Painting	Century
Albrecht Bouts	Assumption of the Virgin Triptych	XV
Petrus Christus	Lamentation	XV
Master of the View of St. Gudula	Visitation and St. Simon Stock	XV
	Fragment of St. Ursula	XV
Jan and Hubert Van Eyck	The Ghent Altarpiece (4 panels)	XV
Adriaen Isenbrant	Yaris van de Velde, Mayor of Bruges, and his wife Barbara	XVI
Michiel Coxie	Copy of Van Eyck's polyptych	XVI
Colijn De Coter	Saint Michael	XVI
Master of the Holy Blood	The Holy Trinity	XVI
Master of the Lyversberg Passion	Christ on the cross between two thieves	XVI
Master of the Mansi Magdalene	Adam and Eve	XVI
Wenceslaz Coebergher	The Entombment	XVI

Three macroscopic imaging techniques were employed as part of this investigation: MA-XRF, MA-rFTIR and MA-XRPD. While oxalates were detected homogeneously in the varnish layers with MA-rFTIR (and to a lesser degree) with MA-XRPD, significant variations in the concentration of the oxalates was observed based upon the paint layer they were identified in.

Red lakes: formation of weddellite

All three macroscopic techniques were employed to characterize the pigments and secondary compounds in *The Visitation* by The Master of the View of St. Gudula. The obtained distribution images are shown in Figure 4.4-1. Both MA-XRPD and MA-rFTIR confirmed the presence of calcium oxalate. Calcium oxalate can occur as the monohydrate whewellite ($CaC_2O_4 \cdot H_2O$), the dihydrate weddellite ($CaC_2O_4 \cdot 2H_2O$), the trihydrate caoxite ($CaC_2O_4 \cdot 3H_2O$) or as an

amorphous compound. In this case only the dihydrate weddellite was identified using MA-XRPD while MA-rFTIR is unable to differentiate between the different oxalates. The heterogeneous distribution of weddellite also suggests that the oxalate formation is pigment-dependent and not solely a varnish-related phenomenon. However, the distributions of calcite (the only other calcium-containing compound identified) and weddellite differ significantly, suggesting that weddellite is not necessarily formed in areas rich in chalk. Weddellite appears to be most strongly present within the red dress and, to a lesser extent, within the purple drapery. While weddellite seems co-localized with vermilion, it is actually more likely that the presence of calcium oxalate is correlated with potassium, a potential marker for a red lake substrate, e.g. alum $(KAl(SO_4)_2 \cdot 12H_2O)$ as calcium oxalates have been previously linked to lake substrates in literature.[7]
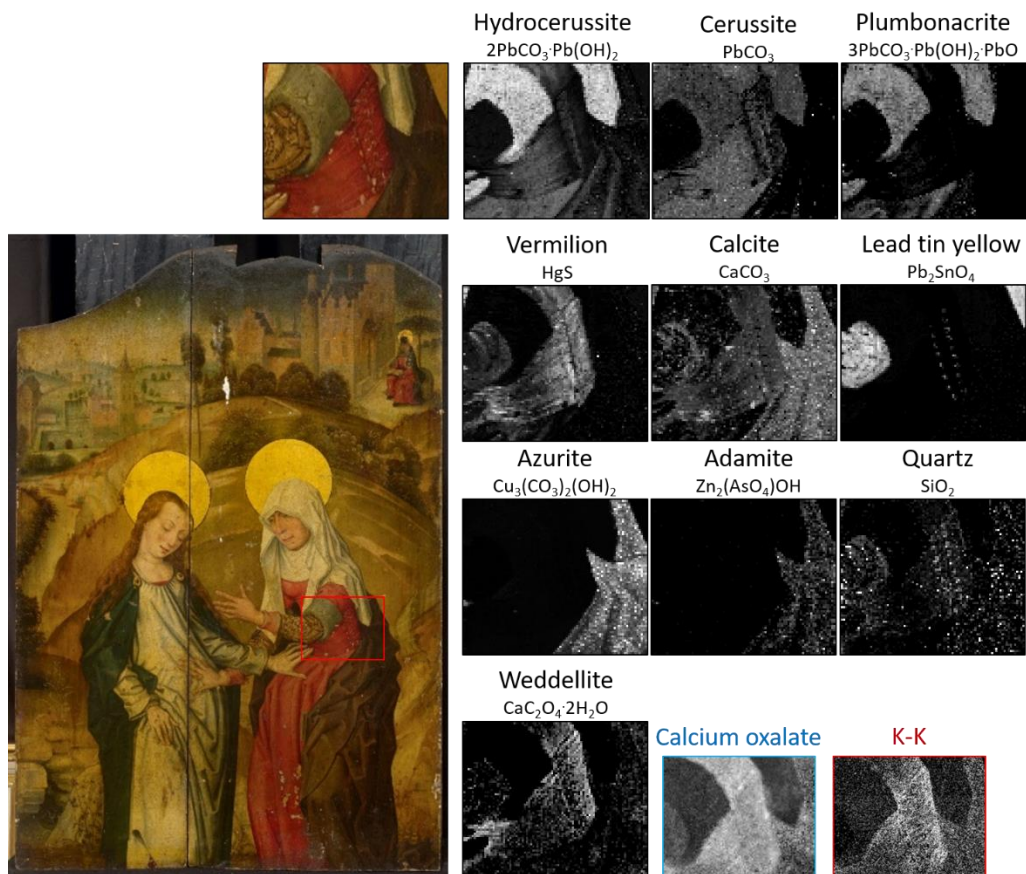
Figure 4.4-1 MA-XRPD distribution images for *The Visitation* panel by The Master of the View of St. Gudula accompanied by relevant distribution images from the MA-XRF (red) and MA-rFTIR (blue) analysis.

This correlation of weddellite and red lake is a recurring phenomenon. Weddellite was detected in 17 out of the 20 red areas that were analyzed with MA-XRPD across 10 different paintings. As lake pigments are amorphous, their presence was determined based on the presence of potassium within the MA-XRF images and/or based on the absence of other red crystalline pigments.

A second example is shown in Figure 4.4-2 which shows the distribution of weddellite in an area of *The Entombment* by Coebergher. In this case the distributions of weddellite and vermilion differ significantly from each other as

weddellite is co-localized with potassium within the very dark red regions of the scanned region. Note that the K-K distribution contains contributions of both red lake and lazurite, the mineral component of ultramarine. A third example is highlighted in Figure 4.4-3. No crystalline compounds were detected within the red drapery, with the exception of an abundance of weddellite and quartz. Previous analyses of red lake dyes have sometimes identified the presence of silicon and quartz.[14,15]
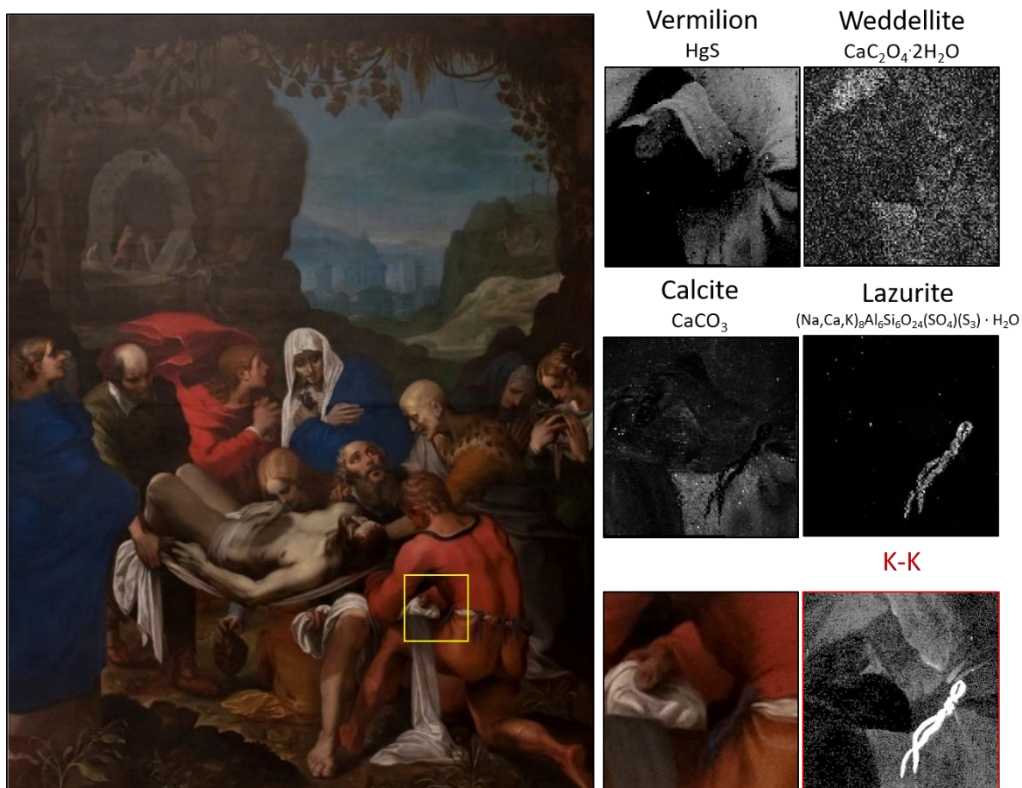
Figure 4.4-2 Relevant MA-XRPD and MA-XRF (red) distribution images for *The Entombment* by Wenceslaz Coebergher.
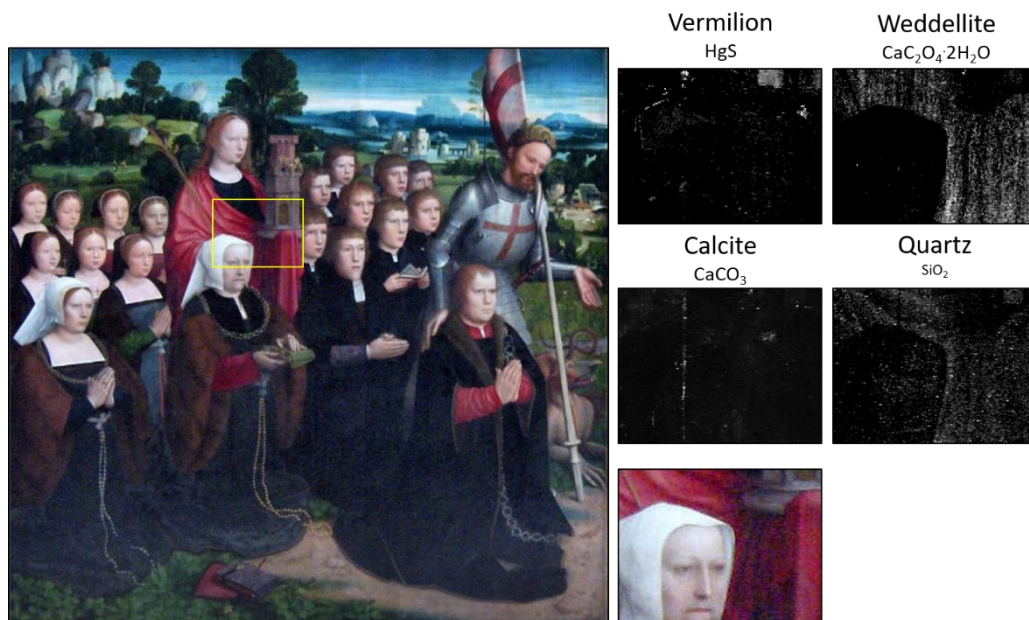
Figure 4.4-3 Relevant MA-XRPD distribution images for *Yaris van de Velde, Mayor of Bruges, and his wife Barbara* by Adriaen Isenbrant.

<u>Verdigris: formation of moolooite and weddellite</u>

Copper oxalate can exist under many forms but moolooite ($CuC_2O_4 \cdot H_2O$) is generally regarded as the most commonly recurring type and has been previously found in cultural heritage artefacts.[16,17] Aside from moolooite no other copper oxalates were detected during these scanning campaigns and moolooite was exclusively identified in green areas. An example of the identification of moolooite is highlighted in Figure 4.4-4, which shows areas on the *Ghent Altarpiece* that were analyzed with MA-XRPD. Both moolooite and lead tin yellow are present in the green zones; the source of the copper ions and the green color is unclear however. This absence of a green crystalline compound suggests the presence of an amorphous copper-containing material in this zone, most likely verdigris. Verdigris refers to a group of copper acetate compounds and was almost exclusively used as the main green pigment in 15th to 17th century Early

Netherlandish oil paintings but fell into disuse due to its instability and the emergence of other green pigments (e.g. Scheele's green, emerald green) in the late 18th century. Because of its poor hiding power in oil media, verdigris was often combined with lead white or lead tin yellow to create a bright green hue that could not be replicated by other green pigments known at the time, such as malachite or green earth.[18] Artificial ageing experiments have shown that crystalline verdigris tends to undergo molecular reorganization over time which may lead to amorphous forms of verdigris.[19] Van Eyck was also known to have used verdigris and µ-Raman confirmed the presence of verdigris in cross-sections taken from similar green areas in the *Ghent Altarpiece*.[20]
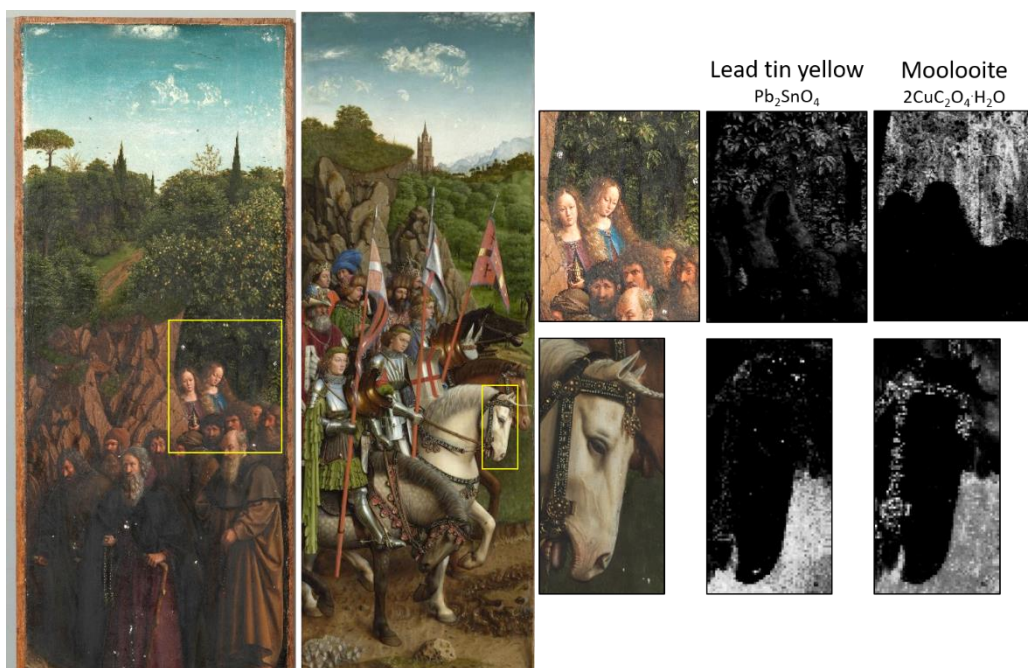
Figure 4.4-4 Relevant MA-XRPD distribution images for *The Knights* and *The Hermits* panels of the *Ghent Altarpi*ece by Jan and Hubert Van Eyck.

Out of the 16 green verdigris-containing areas that were analyzed, 15 areas returned a positive identification for moolooite. Not only was moolooite

frequently identified in the panels of the *Ghent Altarpiece*, it was also identified in verdigris-containing zones in *The Entombment* by Coebergher, *Pietà* by Petrus Christus (Figure 4.4-5), *Assumption of the Virgin* by Bouts and in *Christ on the cross between two thieves* by The Master of the Lyversberg Passion. In areas where the green color was achieved by a mixture of azurite and lead tin yellow, no moolooite was identified, e.g. in *The Visitation* by The Master of the View of St. Gudula. The tendency of verdigris-based oil paint to produce oxalates is likely related to the acetate ligand instability, resulting in high ligand exchange rates when in contact with carboxylate anions.[21]

A second trend that was observed in these green verdigris-containing areas is that calcium oxalate (specifically weddellite) and moolooite are frequently co-localized. Of the 16 verdigris-containing zones investigated, 11 returned a positive identification for both moolooite and weddellite. The superficial presence of calcium oxalate in verdigris-based paint layers hints at a system of cationic migration (of Ca^{2+}) across paint layers: from lower layers to the surface.

Figure 4.4-5 Relevant MA-XRPD distribution images for *Lamentation* by Petrus Christus.

Ultramarine: formation of weddellite

While weddellite was identified primarily in red lakes and (to a lesser degree) in verdigris, based on the previous experience from the researchers involved in this project, also blue areas painted with ultramarine were studied[22]. Weddellite was identified in 4 out of 11 zones in which ultramarine was used as a pigment, limited to Coxie's copy of *The Knights* panel (as shown in Figure 4.4-6) and areas within the original *Ghent Altarpiece* by Jan and Hubert Van Eyck. Figure 4.4-6 also shows that weddellite is not only co-localized with lazurite but that it is also correlated with red zones where a red lake was likely used. Other paintings

(*Lamentation* and *The Entombment*) did not return a positive identification for (calcium) oxalates in ultramarine-containing zones. It has recently been demonstrated that ultramarine has a tendency to induce the photocatalytic degradation of oil paints through a free radical process when exposed to UV light which could accelerate the formation of oxalate anions[23].
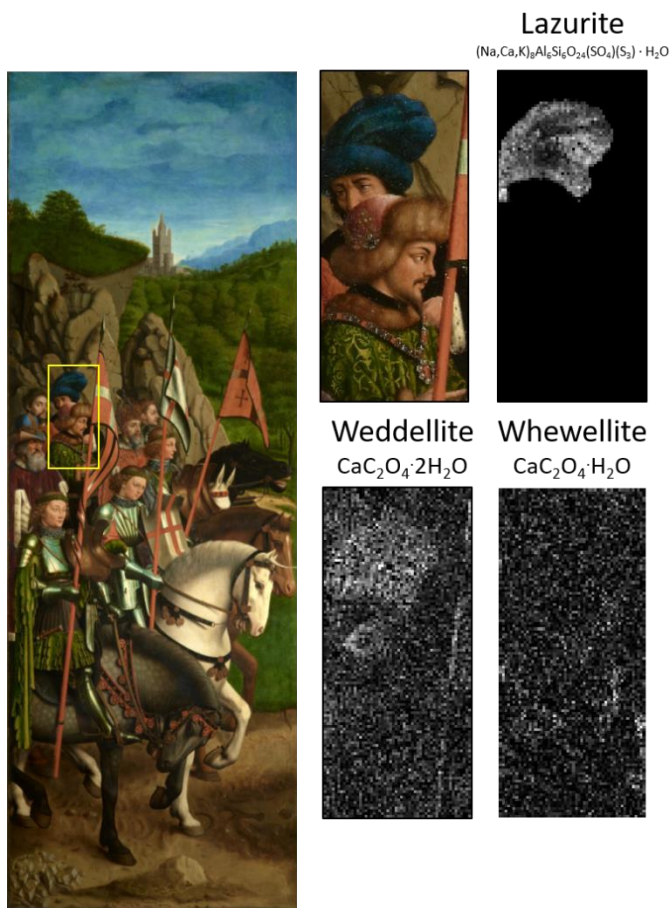
Figure 4.4-6 Relevant MA-XRPD distribution images for the copy of *The Knights* panel by Michiel Coxie.

Weddellite and whewellite

Figure 4.4-6 shows that in this painting also a (very) minor amount of whewellite is present. The monohydrated calcium oxalate seems to be partially localized within the black robe of the man with the blue cap. A small amount of whewellite was also found in *The Hermits* panel of the Ghent Altarpiece in a dark area of the painting. These are the only two instances in which whewellite was identified. Whewellite is regarded to be the most stable form of calcium oxalate at environmental conditions while weddellite can spontaneously and quickly dehydrate into whewellite[24]. However, *in vivo* investigations of renal calculi have found that weddellite becomes the dominant calcium oxalate form at high calcium concentrations while whewellite is preferably formed at high oxalate concentrations[25]. Additional studies which more closely resemble the historical oil paint composition are required to determine the effect of the concentration of calcium and oxalate ions on the preferred formation of weddellite or whewellite.

To investigate the mechanism of metal oxalate formation and the occurrence of weddellite and whewellite, mock-up samples of different oil paints were artificially aged (Figure 4.4-7) and investigated with macro- and microscopic techniques. While the complete results of this investigation are largely outside of the scope of this chapter and thesis (and are scheduled to be published at a later date), one of the findings deserves special consideration as it provides a possible explanation for why weddellite is the dominant oxalate identified with MA-XRPD.

Figure 4.4-7 Mock-up stratigraphic oil paint systems with artificial and natural ageing conditions. Characterisation measurements were realized at different time intervals labelled t_0 to t_8.

A large concentration of calcium oxalates was identified in the madder lake mock-up paint, especially after accelerated ageing. By using a semi-quantitative whole pattern refinement approach, it became possible to observe changes both in the total concentration of calcium oxalates present in the sampled volume as well as in the compositional profile of the calcium oxalates. The madder lake mock-up paint was analyzed at seven different moments in time: before ageing (t_0), after 2, 3, 8 and 11 weeks of artificial ageing after which the mock-up paint was naturally aged and measured after 118 and 147 weeks of time. The mock-up paint was aged by exposure to UV light and a high relative humidity. The weight fraction (relative to the other crystalline compounds in the sample) of weddellite and whewellite is shown in Figure 4.4-8. As there is quartz present in the madder

lake paint, it could be used as an internal standard to quantify the increase in the total amount of oxalates detected.

Before any artificial ageing has occurred, a small amount of whewellite is already present in the madder lake. This is not due to an alteration of the paint film but rather due to its presence in the raw plant materials used for production, as confirmed by XRPD and µ-FTIR analysis of a root sample provided by the pigment producer. After two weeks of ageing we see that the concentration of the oxalates in the sampled volume has risen dramatically by a factor eight: the composition has changed from 90% quartz and 10% oxalates to 20% quartz and 80% oxalates. Additionally, we see that whewellite is the dominant oxalate after two weeks of ageing: the ratio of whewellite to weddellite is 55% to 25%. From this point on the whewellite concentration seems to decline while the weddellite concentration increases. As the total concentration of oxalates seems to remain constant, this suggests that an interconversion from whewellite to weddellite is happening. Initially only whewellite is present but over time the relative amount of weddellite increases. As the artificial ageing process ended, both the formation of calcium oxalates and the interconversion to weddellite seem to slow down. A comparison of the diffractograms of the madder lake sample before and after ageing is shown in Figure 4.4-9. These macroscopic results support the theory that the formation of calcium oxalates is a humidity-mediated photochemical process and provide a possible explanation for the near-exclusive identification of weddellite with MA-XRPD in historical oil paintings.
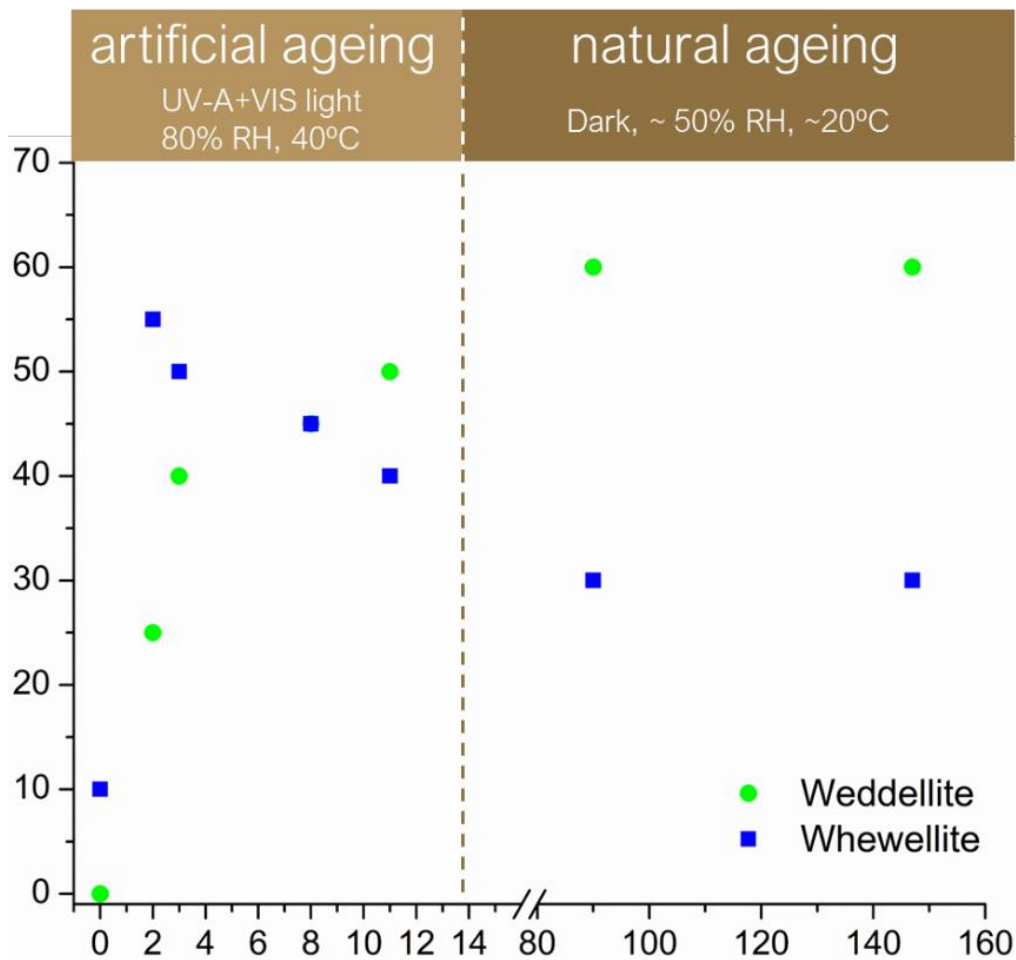
Figure 4.4-8 Weight fractions of weddellite and whewellite relative to all crystalline compounds in the paint mixture during the artificial and natural ageing processes.
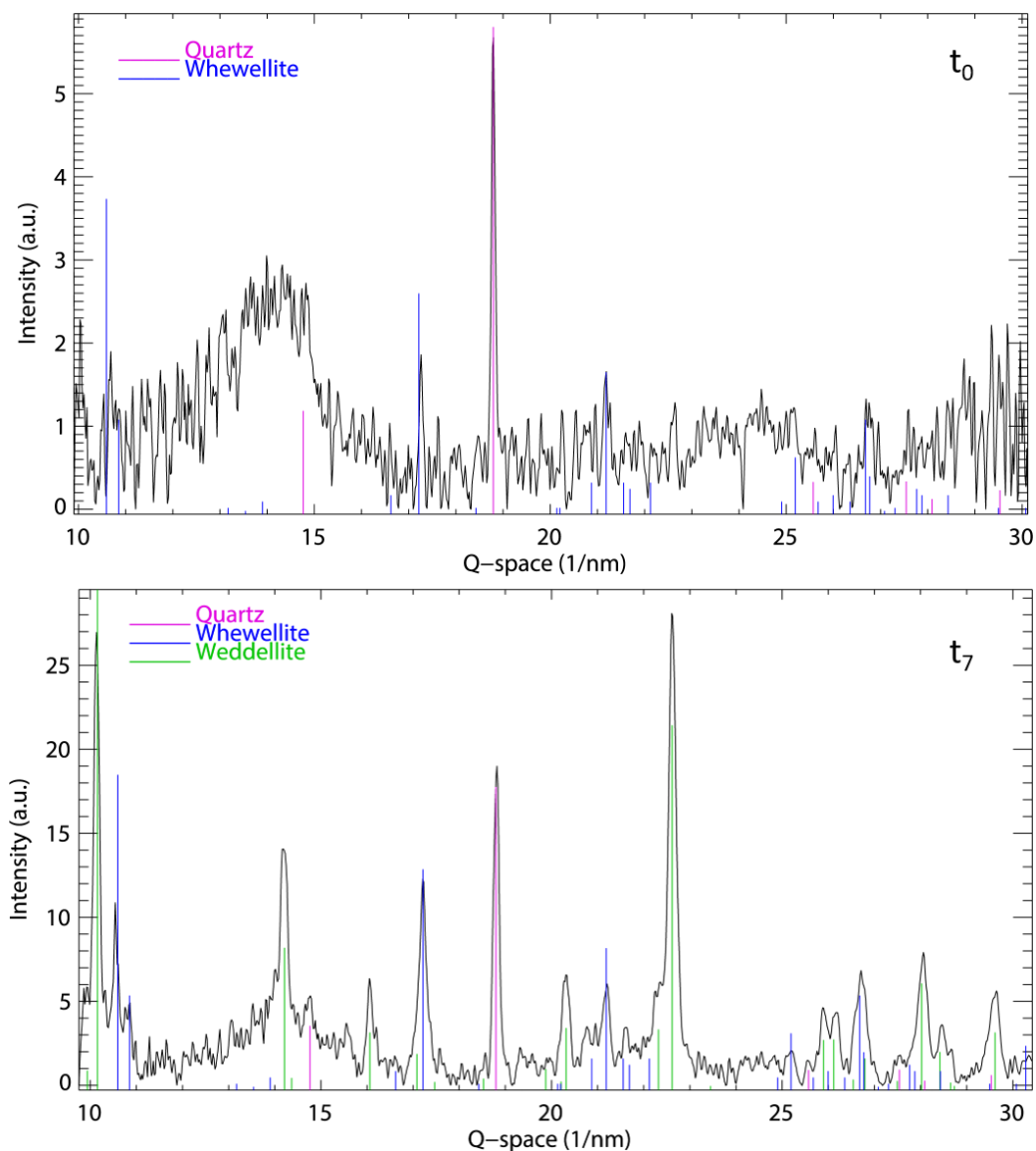
Figure 4.4-9 Diffractograms for the madder lake sample before ageing (t_0) and after 147 weeks of ageing (t_7).

4.4.3 Conclusions

The use of MA-XRPD, in combination with MA-rFTIR and MA-XRF, provided a representative overview of the metal oxalate composition found at the surface in 15th-16th century Netherlandish oil paintings. It confirmed that the

phenomenon of oxalate formation in these paintings is widespread and a clear pattern in the occurrence of metal oxalates and presence of pigments was established. Clear evidence was obtained showing that the oxalate formation at the surface is strongly dependent on the underlying paint layer(s). Calcium oxalates were very frequently identified, primarily in areas containing red lake and (to a lesser degree) in areas containing either verdigris or ultramarine. The composition of the calcium oxalates is strongly dominated by the dihydrate weddellite while the monohydrate whewellite is encountered only very rarely. Artificial ageing experiments on oil paint mock-ups support the theory that weddellite is preferably formed over a longer timescale.

Copper oxalates (moolooite) were also frequently encountered within the selected artworks, exclusively within green verdigris-containing regions. Other copper-containing pigments such as azurite or malachite showed no signs of co-localization with moolooite.

Finally, despite the significant presence of different lead-based pigments (e.g. lead white, lead tin yellow), no lead oxalates were identified with either MA-XRPD or MA-rFTIR. Mentions of lead oxalates in oil paintings in literature are equally rare[6], suggesting that these lead-based pigments in an oil medium are much less likely to form lead oxalates than verdigris or red lakes. It is suspected that the stability of the lead oxalate complex is much lower than for other ligands (e.g. soaps or formates) which were frequently encountered with techniques such as FTIR or ToF-SIMS.

4.4.4 Materials and methods

Figure 4.4-10 The three scanners in action during the 2019 MetOx scanning campaign. From left to right: MA-rFTIR, MA-XRF and MA-XRPD.

All three scanners used during this project were built in-house at the University of Antwerp. The MA-rFTIR scanner consists of a Bruker Alpha FTIR spectrometer with a frontal reflection module mounted on motorized stages $(10x25x10\ cm^3)$ while the MA-XRF scanner uses a XOS X-Beam microtube with a Rh anode anode coupled to a Vortex EX-90 SDD detector on a motor stage of $57x60\ cm^2$. The MA-XRPD scanner employs a Incoatec Cu[HB] X-ray source, a Dectris PILATUS 200K 2D diffraction detector and motor stages (30x30x10 cm^3). A more detailed description of the MA-XRF and MA-rFTIR scanners can be found elsewhere.[26,27] The MA-XRPD scanner is described in more detail in chapter 2 of this thesis.

MA-rFTIR was only used to analyse the two paintings by the Master of the View of St. Gudula as they were unvarnished paintings. One area on a varnished painting by Colijn De Coter was also scanned for the purpose of comparison. The presence of varnish strongly inhibits the detection of metal oxalates from within the paint layers. Despite this limitation, MA-rFTIR is more sensitive than MA-XRPD for the detection of metal oxalates. Based on the availability of paint samples and the MA-XRF results, one or more areas (approx. $10x10\ cm^2$) per

painting were selected for analysis with MA-XRPD. MA-XRF was mostly used as a supporting technique for the interpretation of the MA-XRPD data and for the (indirect) identification of amorphous compounds. In total 40 areas were scanned on 14 paintings by 11 different artists.

Acknowledgements

References

(1) Hermans, J. J.; Keune, K.; Van Loon, A.; Corkery, R. W.; Iedema, P. D. An Infrared Spectroscopic Study of the Nature of Zinc Carboxylates in Oil Paintings. *J. Anal. At. Spectrom.* **2015**, *30*, 1600–1608.

(2) Hermans, J. J.; Keune, K.; Van Loon, A.; Corkery, R. W.; Iedema, P. D. Ionomer-like Structure in Mature Oil Paint Binding Media. *RSC Adv.* **2016**, *6*, 93363–93369.

(3) Bonaduce, I.; Duce, C.; Lluveras-Tenorio, A.; Lee, J.; Ormsby, B.; Burnstock, A.; Van den Berg, K. Conservation Issues of Modern Oil Paintings: A Molecular Model on Paint Curing. *Acc. Chem. Res.* **2019**, *52*, 3397–3406.

(4) Cotte, M.; Checroun, E.; De Nolf, W.; Taniguchi, Y.; De Viguerie, L.; Burghammer, M.; Walter, P.; Rivard, C.; Salomé, M.; Janssens, K.; Susini, J. Lead Soaps in Paintings: Friends or Foes? *Stud. Conserv.* **2016**, *62*, 2–23.

(5) Casadio, F.; Keune, K.; Noble, P.; Van Loon, A.; Hendriks, E.; Centeno, S. A.; Osmond, G. *Metal Soaps in Art - Conservation & Research*; Springer International Publishing AG: Switzerland, 2019.

(6) Salvado, N.; Buti, S.; Nicholson, J.; Emerich, H.; Labrador, A.; Pradell, T. Identification of Reaction Compounds in Micrometric Layers from Gothic Paintings Using Combined SR-XRD and SR-FTIR. *Talanta* **2009**, *79*, 419–428.

(7) Higgitt, C.; Klaassen, L.; Lampens, D. Memling's God the Father with Singing and Music-Making Angels: Oxalate Formation in Old Master Paintings. In *Harmony in Bright Colors: Memling's God the Father with*

Singing and Music-Making Angels restored; Brepols: Turnhout, 2021; pp 192–209.

(8)   Otero, V.; Vilarigues, M.; Carlyle, L.; Cotte, M.; De Nolf, W.; Melo, M. J. A Little Key to Oxalate Formation in Oil Paints: Protective Patina or Chemical Reactor? *Photochem. Photobiol. Sci.* **2018**, *17*, 266–270.

(9)   Rosado, T.; Milene, G.; Mirao, J.; Candeias, A.; Caldeira, A. T. Oxalate Biofilm Formation in Mural Paintings Due to Micro-Organisms - A Comprehensive Study. *Int. Biodeter. Biodegr.* **2013**, *85*, 1–7.

(10)   Poli, T.; Piccirillo, A.; Nervo, M.; Chiantore, O. Interactions of Natural Resins and Pigments in Works of Art. *J. Colloid Interface Sci.* **2017**, *503*, 1–9.

(11)   Bordignon, F.; Postorino, P.; Dore, P.; Tabasso, M. L. The Formation of Metal Oxalates in the Painted Layers of a Medieval Polychrome on Stone, as Revealed by Micro-Raman Spectroscopy. *Stud. Conserv.* **2008**, *53*, 158–169.

(12)   Poli, T.; Piccirillo, A.; Zoccali, A.; Conti, C.; Nervo, M.; Chiantore, O. The Role of Zinc White Pigment on the Degradation of Shellac Resin in Artworks. *Polym. Degrad. Stab.* **2014**, *102*, 138–144.

(13)   Van der Snickt, G.; Janssens, K.; Dik, J.; De Nolf, W.; Vanmeert, F.; Jaroszewicw, J.; Cotte, M.; Falkenberg, G.; Van der Loeff, L. Combined Use of Synchrotron Radiation Based Micro-X-Ray Fluorescence, Micro-X-Ray Diffraction, Micro-X-Ray Absorption Near-Edge, and Micro-Fourier Transform Infrared Spectroscopies for Revealing an Alternative Degradation Pathway of the Pigment Cadmium Yellow in a Painting by Van Gogh. *Anal. Chem.* **2012**, *84*, 10221–10228.

(14)   Zagora, J. SEM-EDX Pigment Analysis and Multi-Analytical Study of the Ground and Paint Layers of Francesco Fedrigazzi's Painting from Kostanje. *CeROArt* **2013**, No. 3.

(15)   Kirby, J.; Spring, M.; Higgitt, C. The Technology of Red Lake Pigment Manufacture: Study of the Dyestuff Substrate. *Natl. Gallery Tech. Bull.* **2005**, *26*, 71–87.

(16)   Frank-Kamenetskaya, O. V.; Zelenskaya, M. S.; Izatulina, A. R.; Vereshchagin, O. S.; Vlasov, D. Yu.; Himelbrant, D. E.; Pankin, D. V. Copper Oxalate Formation by Lichens and Fungi. *Sci. Rep.* **2021**, *11*, 24239.

(17)   Castro, K.; Sarmiento, A.; Martínez-Arkarazo, I.; Madariaga, J. M.; Fernández, L. A. Green Copper Pigments Biodegradation in Cultural Heritage: From Malachite to Moolooite, Thermodynamic Modeling, X-Ray Fluorescence, and Raman Evidence. *Anal. Chem.* **2008**, *80*, 4103–4110.

(18)   Kühn, H.; Roy, A. Verdigris and Copper Resinate. In *Artists' Pigments. A Handbook of Their History and Characteristics, Vol. 2*; Oxford University Press: England, 1993; pp 131–158.

(19) Brostoff, L. B.; Connelly Ryan, C. Tracing the Alteration of Verdigris Pigment through Combined Raman Spectroscopy and X-Ray Diffraction, Part I. *Restaurator* **2020**, *41*, 3–30.

(20) Spring, M. New Insights into the Materials of Fifteenth- and Sixteenth-Century Netherlandish Paintings in the National Gallery, London. *Herit. Sci.* **2017**, *5*, 40.

(21) Gunn, M.; Chottard, G.; Rivière, E.; Girerd, J.-J.; Chottard, J.-C.; Gunn, M.; Chottard, G.; Riviere, E. Chemical Reactions between Copper Pigments and Oleoresinous Media. *Stud. Conserv.* **2002**, *47*, 12.

(22) De Meyer, S.; Vanmeert, F.; Vertongen, R.; van Loon, A.; Gonzalez, V.; van der Snickt, G.; Vandivere, A.; Janssens, K. Imaging Secondary Reaction Products at the Surface of Vermeer's Girl with the Pearl Earring by Means of Macroscopic X-Ray Powder Diffraction Scanning. *Herit. Sci.* **2019**, *7*, 67.

(23) de la Rie, E. R.; Michelin, A.; Ngako, M.; Del Federico, E.; Del Grosso, C. Photo-Catalytic Degradation of Binding Media of Ultramarine Blue Containing Paint Layers: A New Perspective on the Phenomenon of "Ultramarine Disease" in Paintings. *Polym. Degrad. Stab.* **2017**, *144*, 43–52.

(24) Conti, C.; Brambilla, L.; Colombo, C.; Dellasega, D.; Gatta, G. D.; Realini, M.; Zerbi, G. Stability and Transformation Mechanism of Weddellite Nanocrystals Studied by X-Ray Diffraction and Infrared Spectroscopy. *Phys. Chem. Chem. Phys.* **2010**, *12*, 14560.

(25) Daudon, M.; Reveillaud, R. J. Whewellite and Weddellite: Toward a Different Etiopathogenesis. The Significance of Morphological Typing of Calculi. *J. Nephrol.* **1984**, *5*, 195–201.

(26) Van der Snickt, G.; Legrand, S.; Slama, I.; Van Zuien, E.; Gruber, G.; Van der Stighelen, K.; Klaassen, L.; Oberthaler, E.; Janssens, K. In Situ Macro X-Ray Fluorescence (MA-XRF) Scanning as a Non-Invasive Tool to Probe for Subsurface Modifications in Paintings by P.P. Rubens. *Microchem. J.* **2018**, *138*, 238–245.

(27) Legrand, S.; Alfeld, M.; Vanmeert, F.; De Nolf, W.; Janssens, K. Macroscopic Fourier Transform Infrared Scanning in Reflection Mode (MA-RFTIR), a New Tool for Chemical Imaging of Cultural Heritage Artefacts in the Mid-Infrared Range. *Analyst* **2014**, *139*, 2489–2498.

Chapter 5   Conclusions

A large amount of important information is hidden at the surface of a painting. It can provide information on the painterly style used by the artist, the palette he employed, conservation treatments that have taken place or what the current state of preservation is. For this reason, there is a growing demand for non-invasive imaging techniques that can extract this type of information on a macroscopic scale.

In this thesis the possibilities and limitations of a MA-XRPD scanner in reflection mode are investigated in order to assess whether or not this technique is a suitable addition to the existing imaging toolkit used by conservators, restorers and art historians.

A comparison between MA-XRPD in transmission and reflection mode highlighted that both techniques have clear advantages and limitations, depending on the desired information. For information on superficial degradation phenomena or the pictorial composition of the painting, it became clear that only reflection MA-XRPD provides the required superficial sensitivity. Different configurations of equipment were evaluated in order to obtain the best combination of the relevant parameters: spatial resolution, sampling depth, angular range and angular resolution. A final X-ray source – X-ray diffraction detector configuration was established to perform the imaging experiments. A monochromatic IμS-Cu^{HB} X-ray source employing Cu-K$_\alpha$ radiation was chosen as it was determined to be the most suitable choice for combining a high superficial sensitivity with a good spatial resolution and a high flux. This X-ray

source was combined with a 2D diffraction detector, an X-ray fluorescence detector, a laser distance sensor to correct for topographical variations and three motor stages (30 cm x 30 cm x 10 cm) in order to move the scanning platform relative to the painting and perform a point-by-point scan of the desired area of the painting. After integration, identification and whole pattern fitting of the dataset, compound-specific distribution images are obtained. Compared to transmission MA-XRPD, these images are much more representative of the superficial composition of the painting and provide more insight into the pictorial layers, degradation processes and retouched areas. While this is highly useful information, one important limitation remains present however. The sampled volume is highly dependent on the composition of the paint material (e.g. fraction of organic oil, the pigment itself) so accurately gauging the sampling depth is not straightforward and sampling is still relevant to obtain stratigraphic information. Reflection MA-XRPD can be used however as a technique to guide sampling campaigns to areas of interest on a painting to limit the amount of sampling necessary.

In chapter 3 the added value of MA-XRPD compared to already established techniques such as MA-XRF is highlighted with two case studies focused on the composition of the pigment lead white. In the first case study it became possible to differentiate different subtypes of lead white used by Johannes Vermeer to achieve different painterly effects in his masterpiece *Girl with a Pearl Earring*. In this case study it was also demonstrated that MA-XRPD in reflection mode can provide semi-quantitative information on the composition of the crystalline materials in the paint and offers (limited) depth-based information. The second case study revolves around Rembrandt's use of specific lead white *impasto's* containing plumbonacrite and lead formate, two other lead-based compounds, in

The Night Watch. For such a large painting especially, macroscopic imaging techniques are essential to provide guidance for sampling.

Aside from providing information on the painterly style of an artist, MA-XRPD in reflection mode has also proven very useful for investigating degradation phenomena occurring at the paint surface. In Nellius' *Still life with Quinces, Medlars and a Glass* and in Mignon's *Still Life with Flowers and a Watch* two heavily visually degraded areas of the painting were investigated with reflection MA-XRPD and it was revealed that a large amount of arsenic-based degradation compounds had formed over time. By combining the lateral distribution of primary and secondary arsenate and sulfate minerals with in-depth information obtained by microscopic analysis, it was possible to formulate a working hypothesis about the degradation mechanism responsible for the visually degraded appearance of both paintings. Similarly, in *Girl with a Pearl Earring* lead-based degradation compounds were identified that point towards a high reactivity of red lakes in the presence of lead white. In the last case study of this chapter a total of fourteen early Netherlandish oil paintings were analysed to investigate the prevalence of metal oxalates. The use of MA-XRPD, in combination with MA-rFTIR and MA-XRF, provided a representative overview of the metal oxalate composition found at the surface in 15th-16th century Netherlandish oil paintings. It confirmed that the phenomenon of oxalate formation in these paintings is widespread and a clear pattern in the occurrence of metal oxalates and presence of pigments was established.

While the case studies presented in this thesis illustrate the potential of MA-XRPD imaging in reflection mode for the investigation of the painterly style and superficial degradation phenomena, limitations remain present. Despite the superficial sensitivity, no stratigraphic information is obtained which means that

sampling remains very relevant and necessary. Reflection MA-XRPD is also a relatively slow technique compared to e.g. MA-XRF (0.2 s point^{-1}) or MA-rFTIR (2 s point^{-1}) with a measurement time of typically 10 s point^{-1}. Scanning an entire artwork is often not feasible due to time restrictions so a selection of relevant areas has to be made a priori, which is why often a combined approach of MA-XRF and MA-XRPD is preferred. The MA-XRPD scanner is also limited to objects that are mostly flat as (especially) concave and convex objects present challenges for both the data acquisition and the physical dimensions of the scanner. Further improvements of the instrument include upgrading the laser distance sensor to improve the positional accuracy in areas with poorly-reflective surfaces (e.g. black pigments) and exploring methods to speed up the (lengthy) data processing stage. The most significant upgrade would require the incorporation of the next generation of monochromatic laboratory X-ray sources, which provide higher flux values and thus a decrease of the long acquisition times.

Summary

Scientific research into cultural heritage has significantly grown in importance over the past decades. The growing popularity of macroscopic imaging techniques such as X-ray fluorescence or Fourier transform infrared now means that conservators and restorers have access to valuable and highly objective information on the chemical composition of a painting without the necessity for destructive sampling. As many works of art are heterogeneous on the macroscopic scale, it is clear that solely relying on microscopic samples does not provide sufficiently representative information on the condition of a painting and that macroscopic imaging techniques should be considered a crucial part of the analytical toolkit for conservation science.

The main goal of this thesis is to investigate the added value of reflection-mode macroscopic X-ray powder diffraction (MA-XRPD) for scientific and art historical investigations of cultural heritage artefacts. In a first step a prototype scanner was developed after careful consideration of the individual components, e.g. the X-ray source and X-ray diffraction camera. This mobile instrument allows for the analysis of flat objects such as oil paintings with reflection MA-XRPD. In this manner images can be obtained that show the distribution of crystalline components present at or near the surface of the stratigraphy. These crystalline materials can originate from different sources. Original pigments offer insight into the painterly style and palette of the artist, non-original pigments can provide information on past restorations that have been carried out and secondary materials can be formed over time due to interactions of the paint materials with eachother or with external factors such as humidity or light.

MA-XRPD can offer novel insights into different original pigments such as ultramarine, copper sulfates and lead white. Up until the 19th century lead white was the most commonly used white pigment and, depending on the synthesis method, consisted of different compositions of the lead carbonates hydrocerussite ($2PbCO_3 \cdot Pb(OH)_2$) and cerussite ($PbCO_3$). In 'Girl with a Pearl Earring' by Johannes Vermeer the MA-XRPD instrument was used to prove that Vermeer used multiple subtypes of leadwhite to achieve subtle optical effects within this masterpiece. For this purpose, quantitative analysis was performed on the identified lead carbonates. Additionally, the depth sensitivity of MA-XRPD allowed us to gain additional information on the layer structure of the paint without having to sample. In the painting 'The Night Watch' by Rembrandt the lead white composition was also studied in detail and multiple rare lead-based compounds were identified, including plumbonacrite ($3PbCO_3 \cdot Pb(OH)_2 \cdot PbO$) and lead(II)formate ($Pb(HCOO)_2$). These two compounds were linked to the usage of a lead oxide drier (PbO) in the oil paint in certain parts of the painting, which has degraded over time.

Next to information on the artists' palette MA-XRPD is also a suitable technique for assessing the conservation state of an artwork and to investigate the presence of degradation products. For this purpose the MA-XRPD instrument was used to investigate why specific parts of paintings by Martinus Nellius and Abraham Mignon (a yellow fruit and a yellow flower) had visually deteriorated over time. Many different alteration compounds were identified, including lead arsenates which were likely formed from the original yellow arsenic-based orpiment (As_2S_3) pigment. Combined with synchrotron μ-XRPD a hypothesis was proposed for a possible chemical degradation pathway to explain the optical changes in the paint. In the final study MA-XRPD was employed as part of a large scale (14 paintings in total) investigation into the presence of metal oxalates

in early Netherlandish paintings to obtain representative information. Thanks to this research it has become clear that certain pigments (e.g. red lake, verdigris) are very sensitive and will easily form metal oxalates, which is highly valuable information for conservators and restorers.

Samenvatting

Wetenschappelijk onderzoek naar cultureel erfgoed heeft de afgelopen decennia grote stappen voorwaarts genomen. De groeiende populariteit van macroscopische beeldvormende onderzoekstechnieken zoals X-straal fluorescentie of fourier transform infrarood heeft ervoor gezorgd dat conservatoren en restoratoren waardevolle en objectieve informatie kunnen verkrijgen over de chemische samenstelling van een schilderij zonder het schilderij te moeten bemonsteren. Zulke macroscopische technieken bieden ook het voordeel dat ze beter de heterogeniteit van het werk in kaart kunnen brengen dan analyse van een (of meerdere) microscopische verfmonsters.

Voor deze thesis werd onderzocht in welke mate X-straal poeder diffractie (MA-XRPD) in reflectie-geometrie een toegevoegde waarde kan bieden aan wetenschappelijk en kunsthistorisch onderzoek naar cultureel erfgoed. In een eerste stap werd een prototype scanner gebouwd na een zorgvuldige overweging van verschillende componenten zoals een X-stralen buis of een X-straal diffractie camera. Dit transporteerbaar instrument laat toe om vlakke schilderijen te analyseren met reflectie MA-XRPD. Zo kunnen beelden bekomen worden die de verdeling weergeven van kristallijne materialen die zich aan het oppervlak van het schilderij bevinden. Deze kristallijne materialen kunnen van verschillende oorsprong zijn. Het kan gaan om originele pigmenten die inzicht bieden in de schilderstijl en het kleurenpalet van de artiest, niet-originele pigmenten die wijzen op uitgevoerde restoraties of secundaire materialen die gevormd zijn door chemische reacties van de verfmaterialen onderling of onder invloed van externe factoren zoals vochtigheid of UV licht.

MA-XRPD kan zo nieuwe inzichten bieden in verscheidene originele pigmenten zoals ultramarijn, kopersulfaten en loodwit. Loodwit was tot de 19[de] eeuw een veelvoorkomend pigment dat, afhankelijk van de syntheseprocedure, bestond uit verschillende verhoudingen van de loodcarbonaten hydrocerussiet ($2PbCO_3.Pb(OH)_2$) en cerussiet ($PbCO_3$). In 'Meisje met de parel' van Johannes Vermeer werd de MA-XRPD scanner gebruikt om aan te tonen dat Vermeer verschillende subtypes loodwit gebruikte om subtiele optische effecten aan te brengen. Hiervoor werd een kwanitatieve analyse uitgevoerd van de aanwezige loodcarbonaten in het werk. Ook werd aangetoond dat de dieptegevoeligheid van reflectie MA-XRPD informatie kan verschaffen over de laagopbouw van het schilderij zonder bemonstering op basis van de positie van de diffractiesignalen. Ook in het schilderij 'De Nachtwacht' van Rembrandt van Rijn werd de loodwitcompositie uitvoerig bestudeerd met MA-XRPD. Hier werden twee zeldzame loodcomponenten aangetroffen, plumbonacriet ($3PbCO_3.Pb(OH)_2.PbO$) en lood(II)formaat ($Pb(HCOO)_2$), die uiteindelijk werden geïdentificeerd als reactieproducten ten gevolge van het gebruik van lood(II)oxide (PbO) als droogmiddel in de olieverf.

Naast kunsthistorische informatie over het verfgebruik van een schilder is MA-XRPD ook een erg geschikte techniek om informatie te bekomen over de conservatietoestand van een schilderij door mogelijke degradatieproducten op te sporen. De scanner werd ingezet om te onderzoeken waarom een gele bloem in een werk van Abraham Mignon en een geel fruitstuk in een werk van Martinus Nellius hun glans en details verloren hadden. Heel wat degradatieproducten werden aangetroffen in deze gebieden, waaronder loodarsenaten. In combinatie met synchrotron μ-XRPD kon een chemische hypothese worden gevormd die de visuele toestand van deze voorwerpen verklaart. In een laatste studie werd aangetoond dat MA-XRPD ook gebruikt kan worden om op grote schaal

representatieve informatie te vergaren over reeksen schilderijen. Zo werden 14 schilderijen geanalyseerd van Nederlandische schilders in de 15de-16de eeuw om de vorming van metaaloxalaten in kaart te brengen. Zo werd duidelijk dat in deze werken pigmenten zoals rode lak en verdigris erg gevoelig zijn voor degradatie en aanleiding geven tot de vorming van verscheidene metaaloxalaten.

Publications

1. M. Vermeulen, J. Sanyova, K. Janssens, G. Nuyts, S. De Meyer, K. De Wael, *The darkening of copper- or lead-based pigments explained by a structural modification of natural orpiment: a spectroscopic and electrochemical study*, Journal of Analytical Atomic Spectrometry, 32 (2017) 1331-1341. DOI: 10.1039/c7ja00047b

2. J. Salvant, J. Williams, M. Ganio, F. Casadio, C. Daher, K. Sutherland, L. Monico, F. Vanmeert, S. De Meyer, K. Janssens, C. Cartwright, M. Walton, *A Roman Egyptian Painting Workshop: Technical Investigation of the Portraits from Tebtunis, Egypt*, Archaeometry, 60 (2018) 815-833. DOI: 10.1111/arcm.12351

3. L. Monico, A. Chieli, S. De Meyer, M. Cotte, W. De Nolf, G. Falkenberg, K. Janssens, A. Romani, C. Miliani, *Role of relative humidity and Cd/Zn stoichiometry in the photo-oxidation process of cadmium yellows (CdS/Cd$_{1-x}$Zn$_x$S) in oil paintings*, Chemistry, A European Journal, 24 (2018) 11584-11593. DOI: 10.1002/chem.201801503

4. S. De Meyer, F. Vanmeert, R. Vertongen, A. Van Loon, V. Gonzalez, J. Delaney, K. Dooley, J. Dik, G. Van der Snickt, A. Vandivere and K. Janssens, *Macroscopic x-ray powder diffraction imaging reveals Vermeer's discriminating use of lead white pigments in Girl with a Pearl Earring*, Science Advances, 5 (2019) eaax1975. DOI: 10.1126/sciadv.aax1975

5. J. Simoen, S. De Meyer, F. Vanmeert, N. De Keyser, E. Avranovich, G. Van der Snickt, A. Van Loon, K. Keune, K. Janssens, *Combined Micro-*

and Macro scale X-ray powder diffraction mapping of degraded Orpiment paint in a 17th century still life painting by Martinus Nellius, Heritage Science 7 (2019) 83. DOI: 10.1186/s40494-019-0324-4

6. A. van Loon, A. Vandivere, J.K. Delaney, K.A. Dooley, S. De Meyer, F. Vanmeert, V. Gonzalez, K. Janssens, E. Leonhardt, R. Haswell, S. de Groot, P. D'Imporzano and G.R. Davies, *Beauty is skin deep: the skin tones of Vermeer's Girl with a Pearl Earring*, Heritage Science, 7 (2019) 102. DOI: 10.1186/s40494-019-0344-0.

7. S. De Meyer, F. Vanmeert, R. Vertongen, A. van Loon, V. Gonzalez, G. van der Snickt, A. Vandivere and K. Janssens, *Imaging secondary reaction products at the surface of Vermeer's Girl with the Pearl Earring by means of macroscopic X-ray powder diffraction scanning*. Heritage Science 7 (2019) 67. DOI: 10.1186/s40494-019-0344-0.

8. L. Monico, L. Cartechini, F. Rosi, A. Chieli, C. Grazia, S. De Meyer, G. Nuyts, F. Vanmeert, K. Janssens, M. Cotte, W. De Nolf, G. Falkenberg, I.C.A. Sandu, E.S. Tveit, J. Mass, R.P. de Freitas, A. Romani, C. Miliani, *Probing the chemistry of CdS paints in The Scream by in situ noninvasive spectroscopies and synchrotron radiation X-ray techniques,* Science Advances, 6 (2020) eaay3514. DOI: 10.1126/sciadv.aay3514

9. A. Marchetti, R. Saniz, D. Krishnan, L. Rabbachin, G. Nuyts, S. De Meyer, J. Verbeeck, K. Janssens, C. Pelosi, D. Lamoen, B. Partoens, K. De Wael, *Unraveling the Role of Lattice Substitutions on the Stabilization of the Intrinsically Unstable $Pb_2Sb_2O_7$ Pyrochlore: Explaining the Lightfastness of Lead Pyroantimonate Artists' Pigments.* Chemistry of Materials, 32 (2020) 2863-2873. DOI: 10.1021/acs.chemmater.9b04821

10. T. Christiansen, M. Cotte, W. de Nolf, E. Mouro, J. Reyes-Herrera, S. de Meyer, F. Vanmeert, N. Salvadó, V. Gonzalez, P.E. Lindelof, K. Mortensen, K. Ryholt, K. Janssens and S. Larsen, *Insights into the composition of ancient Egyptian red and black inks on papyri achieved by synchrotron-based microanalyses*. Proceedings of the National Academy of Sciences of the USA, 127 (2020) 75, 2004534117. DOI: 10.1073/pnas.2004534117

11. V. Beltran, A. Marchetti, S. De Meyer, G. Nuyts, K. De Wael, *Geranium lake pigments: The role of the synthesis on the structure and composition.* Dyes and Pigments, 189 (2021) 109260. DOI: 10.1016/j.dyepig.2021.109260

12. E. Al-Emam, V. Beltran, S. De Meyer, G. Nuyts, V. Wetemans, K. De Wael, J. Caen, K. Janssens, *Removal of a Past Varnish Treatment from a 19th-Century Belgian Wall Painting by Means of a Solvent-Loaded Double Network Hydrogel*. Polymers, 13 (2021) 2651. DOI: 10.3390/polym13162651

13. A. Marchetti, V. Beltran, G. Nuyts, F. Borondics, S. De Meyer, M. Van Bos, J. Jaroszewicz, E. Otten, M. Debulpaep, K. De Wael, *Novel optical photothermal infrared (O-PTIR) spectroscopy for the noninvasive characterization of heritage glass-metal objects*. Science Advances 8 (2022) 6769. DOI: 10.1126/sciadv.abl6769

14. L. Monico, S. Prati, G. Sciutto, E. Catelli, A. Romani, D. Quintero Balbas, Z. Li, S. De Meyer, G. Nuyts, K. Janssens, M. Cotte, J. Garrevoet, G. Falkenberg, V. Tardillo Suárez, R. Tucoulou and R. Mazzeo, *Development of a multi-method analytical approach based on the combination of synchrotron radiation X-ray micro-analytical techniques*

and vibrational micro-spectroscopy methods to unveil the causes and mechanism of darkening of "fake-gilded" decorations in a Cimabue painting, J. Anal. At. Spectrom., 37 (2022) 114-129. DOI: 10.1039/D1JA00271F

15. N. De Keyser, F. Broers, F. Vanmeert, S. De Meyer, F. Gabrieli, E. Ermens, G. Van der Snickt, K. Janssens, K. Keune, Reviving degraded colors of yellow flowers in 17th century still life paintings with macro- and microscale chemical imaging. Science Advances, 8 (2022) eabn6344. DOI: 10.1126/sciadv.abn6344

16. V. Gonzalez, I. Fazlic, M. Cotte, F. Vanmeert, A. Gestels, S. De Meyer, F. Broers, J. Hermans, A. van Loon, K. Janssens, P. Noble and K. Keune, Lead(II) Formate in Rembrandt's Night Watch: Detection and Distribution from the Macro- to the Micro-scale. Angewandte Chemie – International Edition (2023). DOI: 10.1002/anie.202216478